SIMILARITY STRUCTURE OF AN AXISYMMETRIC VISCOUS VORTEX
WITH VARIABLE CIRCULATION

By

Hsin-Chih Chen

A DISSERTATION

Summitted to
Michigan State University
in partial fulfillment of the requirements
for the degree of

DOCTOR OF PHILISOPHY

Department of Chemical Engineering

1987

ABSTRACT

SIMILARITY STRUCTURE OF AN AXISYMMETRIC VISCOUS VORTEX
WITH VARIABLE CIRCULATION

By

Hsin-Chih Chen

Vortex flows occur in many engineering operations. Recent interest in oil-water separation by using hydrocyclones has increased the need for a better understanding of the flow structure of a viscous swirling core flow. Experimental observations in confined vortex chambers show that a locus of zero axial velocity divides an inner region from an outer region of the flow field and that the swirl component of the velocity field in the outer region can be represented by the empirical expression $u_\theta = Kr^N$, $-1 \leq N < 0$. The total viscous dissipation of the vortex is unbounded for $-1 \leq N \leq -2/3$ and bounded for $-2/3 < N < 0$. The core region of the vortex is studied theoretically by constructing a class of similarity solutions which satisfy the boundary layer equations and the free-vortex-like swirl condition in the outer region. The flow model is used to analyze the behavior of a dispersed phase in the core by using the equilibrium orbit theory for particle - fluid separation.

The model predicts three types of flow behavior in the vortex core : reverse flow, undulated flow, and jet-like flow. The flow regime is uniquely determined by specifying the empirical index N, and a local spin parameter related to the distribution of vorticity on the axis. Most significantly, the theory predicts the existence and location of a 'mantle' (surface of zero radial velocity) within the core region of the

vortex. The theory is qualitatively and quatitatively consistent with recent experimental studies of the viscous core using laser doppler anemometry. The particle - fluid separation study explains the difficulty of capturing very fine particles near the axis of a viscous vortex.

To my family

ACKNOWLEDGMENTS

The author would like to express his deepest gratitude to Professor Charles A. Petty for his guidance and encouragement throughout this research and in preparation of this manuscript.

Thanks are also due Professors John Foss, K. Jayaraman, and Chang-Yi Wang for their useful comments and criticism. Special thanks are given to my friend Spring Wu for her help and moral support. Special thanks are also given to my wife, Emmy Chen, for her many encouragements, moral support, and help during this study.

The author gratefully acknowledges the Department of Chemical Engineering for finacial support. Partial support of this work by the national Science Foundation (Grant NO. CPE-80-15537) and the Exxon Foundation is appreciated.

TABLE OF CONTENTS

LIST OF TABLES

TABLE

LIST OF FIGURES

FIGURE

NOTATION

a	$= \dfrac{u_z(0,z)}{K\delta^N}$, dimensionless centerline axial velocity
a^o	= Initial guess for a
b	$= \dfrac{2\left(\dfrac{\partial u_\theta}{\partial r}\right)\Big\vert_{r=0}}{K\delta^{N-1}}$, local spin parameter
c	= M(0), dimensionless excess pressure on the axis
c^o	= Initial guess for c
D	= Total dissipation
d_p	= Particle diameter
E	$= \rho u_c^2\left(\dfrac{a^2}{2} - c\right)$, excess mechanical energy of the fluid on the axis
$\hat{E}$	$= \dfrac{E}{\rho u_c^2}$, dimensionless excess mechanical energy on the axis
$F(\eta)$	= Dimensionless tangential velocity profile $\left(= \dfrac{r u_\theta}{\delta u_c} \right)$
F_a	= Asymptotic behavior of F
F_c	= Centrifugal force acting on the particles
F_v	= Viscous drag on the particles

F_z	$= 2\pi \int_0^{\tilde{\delta}} (\rho u_z^2 - P) r dr$, axial component of the average force acting on $\pi\tilde{\delta}^2$
$\hat{F}_I$	= Dimensionless inertia force
$\hat{F}_P$	= Dimensionless pressure force
$\hat{F}_V$	= Dimensionless viscous force
$\hat{F}_z$	$= F_z/(2\pi\delta^2 \rho u_c^2)$, dimensionless macroscopic axial force
$G(\eta)$	= Dimensionless axial velocity profile ($= \dfrac{u_z}{u_c}$)
G_a	= Asymptotic behavior of G
$h(\eta)$	= Dimensionless stream function ($= \dfrac{\psi(r,z)}{u_c(z)\delta^2}$)
h_a	= Asymptotic behavior of h
K	= Circulation constant
$M(\eta)$	= Dimensionless pressure drop profile $(P/\rho u_c^2)$
M_a	= Asymptotic solution of M
N	= Exponent of free-vortex-like flow
$P(r,z)$	$= p^o - \rho g z - p(r,z)$
p^o	$= p(\infty,z) = p(r,\infty)$
$\hat{\Delta p}$	$= (p(\delta_a,z) - p(0,z))/\rho u_c^2$, dimensionless pressure drop

Q - $2\pi \int_0^{\tilde{\delta}} u_z r dr$, volumetric flow rate across the area $\pi\tilde{\delta}^2$

$\hat{Q}$ - $Q/(2\pi\delta^2 u_c)$, dimensionless volumetric flow rate

Q_o - Inlet flow rate

r - Radial distance

r_E - Radial position of equilibrium orbit

Re_F - Inlet Reynolds number

Sk - Intrinsic Stoke's number

T_z - $2\pi \int_0^{\tilde{\delta}} [\rho r u_\theta] u_z r dr$, axial torque over the cross section $\pi\tilde{\delta}^2$

$\hat{T}_z$ - $T_z/(2\delta\pi\delta^2\rho u_c^{\ 2})$, dimensionless axial torque

$u_r(r,z)$ - Radial velocity profile

$u_z(r,z)$ - Axial velocity profile

u_c - $K\delta^N$, velocity scale

u_F - Inlet velocity

u_o - $u_z(0,z)$, centerline axial velocity

$u_\theta(r,z)$ - Tangential velocity profile

u_{pr} - The radial component of the particle velocity

Y_1 - $M(\eta)$

Y_2	- $h(\eta)$
Y_3	- $G(\eta)$
Y_4	- $G'(\eta)$
Y_5	- $F(\eta)$
Y_6	- $F'(\eta)$
$\underline{Y}_a$	- Asymptotic solution of $\underline{Y}$
$\underline{Y}_d$	- Small purturbation from the asymptotic solution of $\underline{Y}$
z	- Axial distance from singular point
z^o	- Axial position on the axis where the pressure is zero
z_o	- Singularity point
$\tilde{z}$	- Reference coordinate for experimental data
z_E	- Axial position of equilibrium orbit
$\hat{z}_E$	- Axial position of equilibrium orbit on the axis
Z_1	- Y_1
Z_2	- $Y_2/\tilde{\eta}^2$
Z_3	- Y_3
Z_4	- $\tilde{\eta}Y_4$
Z_5	- $Y_5/(\tilde{\eta}^{N+1})$
Z_6	- $Y_6/(\tilde{\eta}^N)$

Greek

Γ	-	Circulation
$\delta(z)$	-	$(\nu z/K)^{1/(N+2)}$, length scale
$\tilde{\delta}$	-	Surface of viscous core, (equivalently, δ_a for Model I and $\delta^*(z)$ for Model II)
$\delta^*(z)$	-	Size of the inner region where $u_z(r,z) = 0$
$\delta_a(z)$	-	Surface of viscous core for Model I where asymptotic solutions appear
ϵ	-	Accuracy parameter
η	-	$r/\delta(z)$, dependent variable
η^*	-	δ/δ^*, dimensionless size of viscous core for Model II
η_a	-	r/δ_a, dimensionless size of viscous core for Model I
$\tilde{\eta}$	-	$\begin{cases} \eta_a , & \text{Model I} \\ \eta^* , & \text{Model II} \end{cases}$
$\tilde{\eta}^o$	-	Initial guess of $\tilde{\eta}$
μ	-	Molecular viscosity of the fluid
ν	-	Molecular kinematic viscosity of the fluid
ν_e	-	"eddy" viscosity
ξ	-	$\eta/\tilde{\eta}$, rescaled domain where $0 \le \xi \le 1$
ρ_f	-	Density of the continuous fluid phase
ρ_p	-	Density of the particle

τ_p = $\frac{1}{18} \frac{d_p^2}{\nu} (1 - \frac{\rho_p}{\rho_f})$, particle relaxation time

$\tau_{r\theta}$ = Shear stress (see Appendix D)

$\tau_{\theta z}$ = Shear stress (see Appendix D)

Φ = $2\pi \int_0^{\tilde{\delta}} (\underline{\underline{\tau}} : \nabla \underline{u}) r dr$, dissipation integral

$\hat{\Phi}$ = $\Phi/(2\pi\mu u_c^2)$, dimensionless dissipation

ψ = Stream function

ω_z = Axial component of vorticity

CHAPTER 1

INTRODUCTION

1.1 Motivation For This Study

Vortex flows occur in many engineering operations such as swirl atomization, cyclone separation, and flame stabilization (see Gupta et al., 1984). They also appear frequently as natural phenomena in the form of tornadoes and vortical flows in large scale hydraulic systems (Lugt, 1983; Swift et al., 1980). The shedding of concentrated vortex structures from aircraft wings is another important example which has been studied extensively. A common feature of all these flows is that the angular momentum of the fluid changes significantly over relatively small radial distances. This produces some unique features such as large spanwise pressure gradients and flow reversals.

This research is motivated by recent experimental studies of Dabir [1983], Escudier and Zehnder [1982], and Escudier et al. [1980, 1982] on confined vortex flows, and the theoretical results of Long [1961], Burggraf and Foster [1977], and Bloor and Ingham [1975, 1984]. Applications of swirling flows to oil - water separations by Colman and Thew [1980] as well as by Listewnik [1984] have provided additional interest in the class of swirling flows analyzed in this dissertation.

Experimental measurements of axial and tangential velocity components in a flooded 3" - hydrocyclone using laser doppler anemometry show the following general features (Dabir, 1983).

(a). The vortex flow near the axis is approximately axisymmetric,

$$\underline{u} = u_r(r,z)\underline{e}_r + u_\theta(r,z)\underline{e}_\theta + u_z(r,z)\underline{e}_z \quad (1.1)$$

(b). The axial velocity near the axis may be either positive (forward flow) or negative (reverse flow) depending on the total volumetric flow rate of the feed (see Figure 1.1).

(c). For forward flow conditions, two types of axial profiles are possible : at very high flow rates, a jet-like (or parabolic) profile occurs; and, at lower flow rates, an undulated profile occurs.

(d). A surface of zero axial velocity divides an inner region from an outer region of the flow field. This occurs even if the underflow rate (see Figure 1.1) is zero.

(e). The size of the inner region, defined by the surface $r = \delta^*(z)$ for which $u_z(r,z) = 0$, increases in the direction of decreasing magnitude of the centerline axial velocity. The growth of this region is not linear in the coordinate z :

$$\delta^*(z) \propto z^A , \quad 0 < A < 1. \quad (1.2)$$

(f). For most flow situations, the decay of the centerline velocity was algebraic in z with a weaker dependence than z^{-1} :

$$|u_z(0,z)| \propto z^B, \ -1 < B < 0. \quad (1.3)$$

(g). The swirl velocity in the outer region (i.e., $r \geq \delta^*(z)$) is essentially independent of z and consistently shows the following behavior with r :

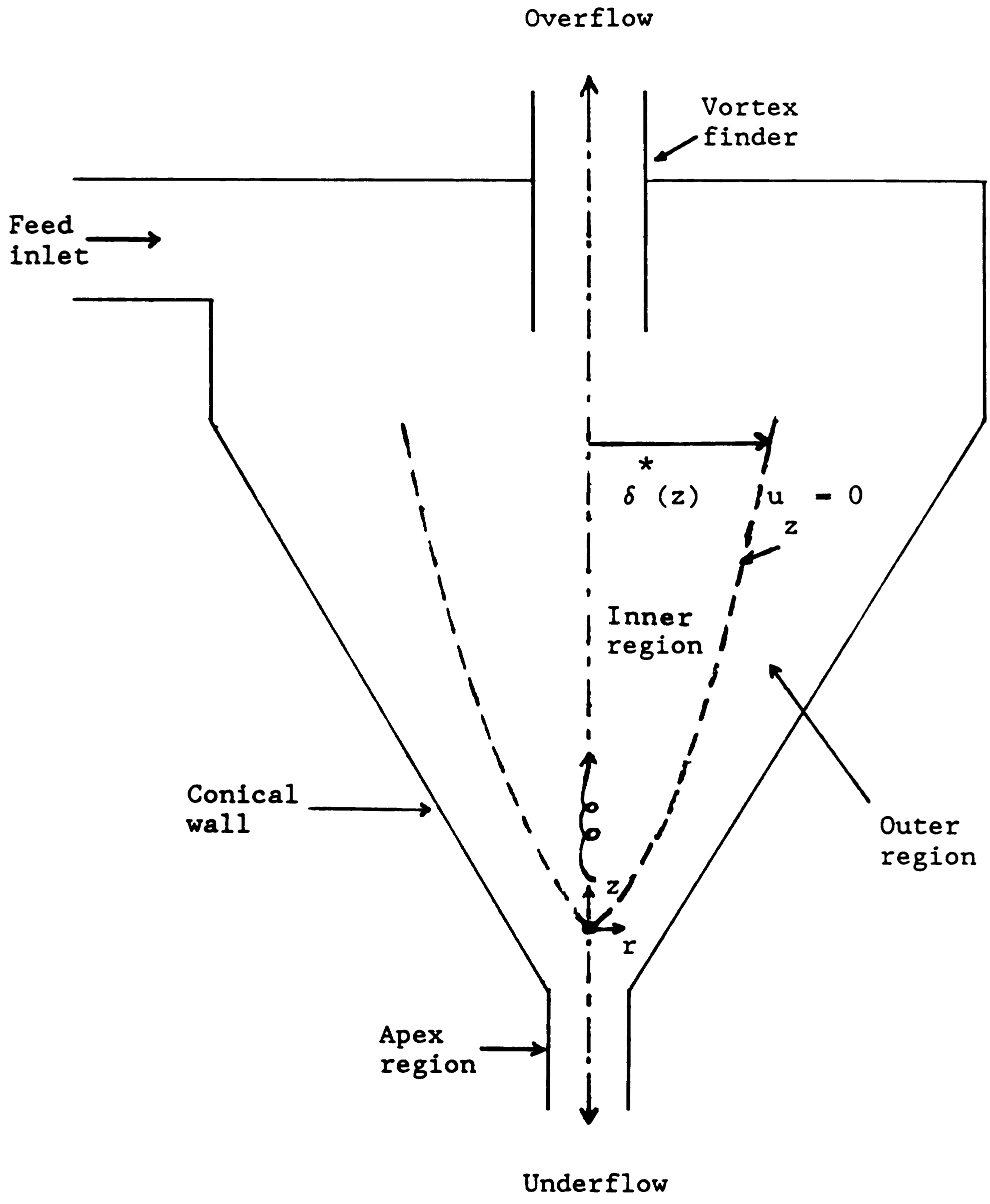

Figure 1.1 Viscous vortex region of a hydrocyclone

$$u_\theta \propto r^N, \ -1 < N < 0. \tag{1.4}$$

Thus, the usual free-vortex structure (i.e., $u_\theta \propto 1/r$) associated with many theoretical studies is not observed experimentally.

(h). The swirl velocity near the axis has a forced-vortex character (i.e., $u_\theta \propto r$).

Some important preliminary conclusions about the flow structure in the inner region follow from the above experimental observations. Because $\delta^*(z)$, $|u_z(0,z)|$, and $u_\theta(\delta^*(z),z)$ all have an algebraic dependence on the independent variable z, a similarity theory based on an appropriate scaling hypothesis may describe a portion of the flow field. Obviously, such a theory would have severe limitations and could not explain the complex flow phenomenon which occurs deep in the apex region of hydrocyclones (see Figure 1.1), near the end wall of a cylindrical vortex chamber, or near the ground of a tornado (Long, 1961). However, other physical effects related to swirling flows could be studied using this theoretical approach.

Experimental observations (a) and (g) are especially noteworthy and dictate the direction of the theoretical development. For axisymmetric flows, the circulation Γ on the closed circuits $2\pi r$ is

$$\Gamma = 2\pi r u_\theta(r,z). \tag{1.5}$$

$\Gamma/2\pi$ also represents the axial component of the angular momentum of the fluid about the axis. If the flow field has a similarity structure, then an instrinsic length and velocity scale must exist for which

$$r u_\theta(r,z) = \delta(z) u_c(z) F(\eta) \tag{1.6}$$

where

$$\eta = r/\delta(z). \tag{1.7}$$

Therefore, Eq. (1.5) becomes

$$\Gamma = 2\pi\delta(z) u_c(z) F(\eta) \tag{1.8}$$

Thus, experimental observations (e) and (f) imply that the circulation on surfaces of constant η (i.e., similarity surfaces) has the following dependence on the axial coordinate,

$$\Gamma \propto z^{A+B} \tag{1.9}$$

Therefore, if $A + B \neq 0$, the vortex has the feature of <u>variable circulation on similarity surfaces</u>.

In his study of a viscous vortex, Long [1961] developed a class of similarity solutions to a boundary layer approximation of the Navier - Stokes equations. Long's vortex, which is defined on an infinite domain (i.e., $0 \leq r \leq \infty$), has an asymptotic velocity field given by

$$\underline{u} \xrightarrow{r \gg 0} -\frac{\nu}{r}\underline{e}_r + \frac{K}{r}\underline{e}_\theta + \frac{K}{\sqrt{2}\, r}\underline{e}_z \tag{1.10}$$

where ν is the kinematic viscosity of the fluid (or a constant 'eddy' viscosity if the vortex is turbulent) and K is a constant defined by

$$\lim_{r \to \infty} u_\theta = K/r, \; K > 0. \tag{1.11}$$

The solutions developed by Long are consistent with experimental observations (a), (b), (c), and (h); however, as indicated by Eq. (1.10), the axial velocity surrounding the vortex is always positive and decreases to zero very slowly ($u_z \propto 1/r$). For confined vortex chambers, a reverse annular flow (i.e., observation (d)) surrounding the vortex generally occurs. Long noted that this also occurs for unbounded flows such as tornadoes and that the asymptotic result given by Eq. (1.10), although an exact solution to the Navier - Stokes equations, was probably too restrictive.

Although Long's vortex shows the qualitative properties expressed by observations (e), (f), and (g), it requires $N = -1$ (see Eq. (1.11)), $B = -1$, and $A = 1$. Unfortunately, these exponents are not observed experimentally. However, Long's vortex has the interesting feature that the circulation is constant on similarity surfaces (see Eq. (1.9))

Similarity scaling also implies that the viscous dissipation per unit volume on surfaces of constant η will depend on the axial coordinate as follows

$$\Phi_v = \underline{\underline{\tau}} : \nabla \underline{u} \propto \left(\frac{u_c}{\delta} \right)^2 \propto (z^{B-A})^2. \tag{1.12}$$

Thus, Long's vortex has the property that $\Phi_v \propto z^{-4}$. However, the data of Dabir [1983] suggest that

$$B - A > -2,$$

so experimental flows do not appear as dissipative as Long's vortex. If Φ_v is integrated over the entire flow domain, then the total viscous dissipation is infinite for Long's vortex, but is bounded for similarity flows having the property that $-1/2 < B < 0$. This intriguing theoretical possibility partly motivates this study.

In the past decade, Thew and his colleagues at Southampton University (U.K.) have made some progress on removing oil from water more efficiently by using a cyclone separator. They (see Colman et al., 1980) were able to obtain 99% separation for a drop size of 55 microns. However, the efficiency apparently drops off sharply when particle sizes become less than 40 microns. What causes the efficiency to drop at smaller particle sizes? Is this phenomenon a result of the specific design of the cyclone or is it an intrinsic property of all vortex flows? This research intends to examine this question by studying the behavior of a dispersed phase in a viscous vortex. Hopefully, this theory will provide new insights on how to improve the separation efficiency for hydrocyclone separators.

1.2 Objectives

The primary objective of this research is to apply the techniques of boundary layer theory to investigate the similarity structure of a special class of swirling flows related to the experimental observations (a) - (h). Two models will be studied. Model I, which has the feature of constant circulation on similarity surfaces, is used to understand the flow structure induced by a free vortex defined by Eq. (1.10). This model was previously studied by Long [1961] and by Burggraf and Foster [1977]. Model II, which has the feature of variable circulation on similarity surfaces, is used to understand the flow structure induced by a more general vortex in the outer region with the conditions that

$$u_z(r,z) = 0 \text{ for } r = \delta^*(z), \text{ and} \qquad (1.13)$$

$$u_\theta = Kr^N, \text{ for } r \geq \delta^*(z). \tag{1.14}$$

Eqs. (1.13) and (1.14) are primarily motivated by experimental observations (d) and (g) discussed in Section 1.1.

A second objective of this study relates to the experimental results. It is intended to demonstrate how the model can be used to characterize selected experimental flows. The major goal here is to compare the qualitative flow behavior between theoretical predictions and experimental results. It is also intended to compare the similarity scaling of the centerline velocity and angular momentum as well as entrainment rates.

The study also examines the application of the flow model to oil - water separation in hydrocyclones. The goal here is to investigate the major effects of particle properties and fluid properties on the separation of very fine light particles in vortex flows. Hopefully, an explanation for the anomalous low separation efficiency associated with very fine particles can be identified. If successful, this research should provide a new basis for the design of cyclone separators.

1.3 Methodology

Chapter 2 contains a review of relevant experimental and theoretical studies of swirling flows related to this research. Particular attention is focused on the flow behavior in a confined vortex chamber. Long's vortex and related geophysical flows are also examined. Experimental observations for different flow behavior provide useful information to explore the efficacy of the theoretical results.

Chapter 3 uses a boundary layer approximation of the Navier - Stokes equations with constant physical properties to develop an axisymmetric similarity model for a vortex flow. Two models are studied in this chapter. Model I, which considers a vortex flow with constant circulation, reexamines Long's vortex (see Long, 1961) in more detail than originally presented by Long and later by Burggraf and Foster [1977]. Model II considers a vortex flow with variable circulation. This feature reflects more realistically the actual behavior of vortex flows and, thereby, provides a basis for understanding experimental observations.

Chapter 4 presents some *a priori* theoretical predictions about the flow behavior near the axis. It also provides, for the first time, criteria for transition between different flow regimes. A physical interpretation of these results follows directly from the mechanical energy balance.

In Chapter 5, a numerical algorithm is developed which solves the nonlinear two-point boundary value problems representing the two vortex models. Standard library subroutines are used to integrate the differential equations and to search for a consistent set of boundary conditions.

Chapters 6 and 7 present the solutions for Model I and Model II for a wide range of conditions. Both chapters focus on quantitative predictions for the velocity and pressure fields. The macroscopic properties of the flow are also calculated and summarized in these chapters. The mechanical energy balance and force balance on the axis are used to develop a physical understanding of the complex helical flows calculated.

Comparisons between theoretical and experimental results show that Model II is consistent with some experimental data. Chapter 8 examines the similarity scaling of both the centerline axial velocity and the angular momentum. The chapter also includes estimates of some important properties for specific experimental flows.

The potential application of this research to oil - water separation in hydrocyclones is discussed in Chapter 9. An equilibrium orbit hypothesis is used to study the effect of the flow structure on the motion of oil droplets in water. The effect of particle size, specific gravity, and other physical parameters on equilibrium orbits will be discussed.

Finally, the conclusions of this study and the recommendations for further research are presented in Chapter 10.

CHAPTER 2

LITERATURE REVIEW

2.1 Experimental Studies

The major objective of this study, as discussed in Chapter 1, is to investigate the structure of vortex flows with variable circulation. In this case, the tangential velocity in the outer region is commonly expressed by

$$u_\theta = Kr^N, \quad r >> 0 \tag{2.1}$$

where $-1 \leq N < 0$. For a free vortex, $N = -1$. N can be determined from the swirl velocity profile in the outer region. Fortein and Dijksman [1953], Escudier et al. [1980,1982], and Dabir [1983] have all shown that N has the value near -0.75 and appears to be insensitive to the flow rate and the contraction ratio of the vortex chamber. However, Knowles et al. [1973] reported a much flatter tangential velocity in the outer region ($N = -0.3$). Near the axis, the tangential velocity profile has the same form as a forced vortex, whereas in the outer region, the tangential velocity always has a free-vortex-like behavior (i.e., Eq.(2.1)).

Many experimental studies about swirling vortex flows have been conducted in the last 30 years. One of the most important findings is the existence of flow reversal phenomenon. In an earlier study of swirling flow in a circular pipe, Nuttal [1953] found that three types of flow patterns occur for Reynolds number in the range 10,000 to 30,000. In his study, the Reynolds number is defined as

$$Re_F = \frac{D_F u_F}{\nu}$$

where D_F is the inlet diameter of the pipe, u_F is the inlet velocity, and ν is the molecular kinematic viscosity. As the swirl component of the velocity increases, the flow changes from a one-celled to a two-celled and, finally, to a three-celled vortex structure. Reverse flows are characteristic of these flows. Although this finding is important, Nuttal gave neither a physical nor a theoretical explanation for this phenomenon.

In a study of flow through a conical nozzle, Binnie and Tear [1956] showed that reverse flows also exist in a cone, but they only observed a two-celled vortex structure. Binnie [1957] also investigated the different flow patterns in the low Reynolds number range by injecting swirling water into a circular pipe, he found that the transition from a single-celled vortex structure to a three-celled structure depends not only on the Reynolds number but on the ratio of swirl to axial flow. One very important conclusion, which Binnie did not emphasize, is that the reverse flow was induced by increasing the swirl component for a fixed Reynolds number.

In his measurements of velocity profiles using an optical technique based on flow visualization, Kelsall [1952] observed a surface of zero axial velocity which increases with axial position. Bradley and Pulling

[1959] also observed this phenomenon. Moreover, they reported that this surface was insensitive to operating variables and had a diameter of 0.43 times the cyclone diameter. For a flooded hydrocyclone (or more generally, a confined vortex chamber), Dabir [1983], Knowles [1973], Escudier et al. [1980,1982], have noted that the surface of zero axial velocity increases in diameter in the direction of decreasing magnitude of the centerline axial velocity. The growth of the vortex core is a nonlinear function of the axial coordinate. Dabir, also observed that this surface (zero axial velocity) divides the inner region of upward flow from an outer region of downward flow, even when the underflow rate (see Figure 1.1) is zero.

The magnitude of the radial velocity in the core flow was also measured by Kelsall (with an air core) and Knowles (without an air core). It is not surprising to find that this number is very small compared with the axial and tangential components of the velocity. In the study of a hydrocyclone with an air core, Bradley and Pulling (see p.15, Bradley, 1965) found that a locus of zero radial velocity, or "mantle", exist in the cylindrical section and terminates at a level in the conical section of the cyclone. For the study of a flooded hydrocyclone, an outward radial flow in the inner region and inward radial flow in the outer region was noted by Knowles (see Figure 8, Knowles et al., 1973). This phenomenon was also observed by Ohasi and Maeda (see p.38, Svarvosky, 1984) and by Dabir (see Figure 5.11, Dabir, 1983). It is interesting that the outward radial flow in the inner region has only been observed in flooded hydrocyclones.

The most recent velocity measurements have been done by using Laser Doppler Anemometry (LDA) (see Durst et al., 1976; Escudier et al., 1980, 1982; Dabir, 1983; and Thew et al., 1980). More recently, Escudier et al. [1980,1982], in their study of confined turbulent vortex flows by using a laser doppler anemometry and a flow visualization technique, showed that different flow patterns occur depending on the contraction ratio of the vortex chamber (D_o/D) and the Reynolds number. Transition from jet-like core behavior to wake-like behavior (including undulated and flow reversal) occurs either as the Reynolds number or the ratio D_o/D increases. Another interesting result is that the maximum swirl velocity ($u_{\theta,max}$) increases significantly as D_o/D decreases. These two results imply that jet-like flow behavior corresponds to larger values of $u_{\theta,max}$ than wake-like flow.

In the measurement of velocity profiles in a 3" flooded hydrocyclone by using laser doppler anemometry, Dabir and Petty [1984a,1984b] have revealed that multiple reverse flows occur in the vortex core if using a 2:1 contraction vortex finder. The occurance of jet-like and reverse flows strongly depends on the size and shape of the geometry. The radial velocity calculated from their data showed that an outward flow (positive radial velocity) occurs near the axis for flooded hydrocyclones. A large number of relative experimental observations were also found. These include the approximate axisymmetric structure, a reversal annular flow surrounding the surface of zero axial velocity, a non-linear growth of the viscous core ($r = \delta^*(z)$) in the direction of decreasing centerline axial velocity, and a free-vortex-like swirl velocity in the outer region.

Long [1956], in his earlier experiments on withdrawing water through a hole at the centre of a bottom plate, observed that : (1) An intense narrow vortex formed when water was extracted from a sink of a slowly rotating cylinder; (2) When the steady draining vortex is achieved from an initial slow rotation, the circulation was almost independent of radius outside the core; (3) The core seemed to spread almost linearly with increasing axial distance. These observations, which imply that $N = -1$, motivated Long's theoretical study.

The features of vortex flows, in many aspects, are similar to those reported in a swirling jet. Chigier and Chervinsky [1967] indicated that the distribution of the axial and swirl velocities were similar at least for moderate swirl numbers. The swirl number, as represented by S, is usually defined as

$$S = \frac{T_z}{F_z(d_o/2)}$$

where

$$T_z = 2\pi\int_0^\infty \rho u_\theta u_z r^2 dr$$

$$F_z = 2\pi\int_0^\infty (\rho u_z^2 + p - p_\infty) r dr$$

are, resp., the global axial torque and the global axial force. $d_o/2$ is the nozzle radius. For a swirling jet, T_z and F_z are independent of z. Consequently, S is independent of z. Experimentally, many researchers including Kerr and Fraser [1965], Chigier and Beer [1964], Rajaratnam [1976], Vu and Gouldin [1982], Rhode and Lilley [1983], Gouldin et al. [1985], Ramas and Somer [1985], have proved that swirl has a large scale effect on the flow fields in many aspects : entrainment, jet growth, flow recirculation, and flame stabilization. In general, the effects of introducing swirl on jets are to cause an increase in jet width, rate of axial velocity decay, and rate of entrainment. The mean - flow terms show a very simple and direct relationship between swirl magnitude and radial pressure gradient. Since the radial pressure gradient is mainly balanced by the centrifugal force, the stronger swirling flow generates a large radial pressure gradient. In the case of low S, the axial velocity distribution remains almost Gaussian, with the maximum velocity on the axis of the jet. As the swirl number reaches a critical number (approximately 0.6, see p.167, Gupta et al., 1984), the axial adverse pressure gradient becomes strong enough to produce flow separation and reversal. The axial velocity profile changes from the initial near plug flow at the nozzle exit to Gaussian profile at the downstream. Meanwhile, the swirl velocity profile changes from a solid body rotation to a Rankine free - forced vortex type.

2.2 Theoretical Studies

The flow structures within the vortex core have been investigated for some time. Early studies were reported by Burgers [1948] and Rott [1958]. The Burgers' vortex has the velocity field :

$$\underline{u} = - a_1 r \underline{e}_r + \left(\frac{\Gamma_\infty}{2\pi r} \right) [1 - e^{-a_1 r^2/2\nu}] \underline{e}_\theta + 2a_1 z \underline{e}_z \qquad (2.2)$$

where a_1 and Γ_∞ are constants. This vortex has been widely used in the study of theoretical vortex models. However, the vortex has the disadvantage of having an artificially assumed axial velocity $u_z \propto z$

which approaches infinity as $z \to \infty$ and leads to a stagnation point at the origin without physical justification.

Sullivan [1959], Donaldson [1956], Donaldson and Sullivan [1960], and Donaldson and Snedeker [1962] improved Burgers' vortex by considering the velocity field as the form of :

$$u_r = u_r(r), \quad u_\theta = u_\theta(r), \quad u_z = zf(r) \tag{2.3}$$

Their solutions represents a rather large class of three - dimensional, viscous vortex motions. They found ,in addition to Burgers' one-celled vortex, three - dimensional one-celled and two-celled vortices. However, in their work, the interaction between the vortex and the ground boundary layer flow is neglected. The Sullivan vortex is, however, of considerably interest to meterologists because two-celled structures have been found in tornadoes. An extensive review of confined vortex flows was reported by Lewellen [1971].

Long [1958,1961], motivated by his early experimental observations (see Section 2.1), studied an intense vortex in an unbounded viscous fluid. Unlike Burgers' and Sullivan's vortices, Long's vortex has the velocity field at the outer region as :

$$\underline{u} = -\frac{\nu}{r}\underline{e}_r + \frac{K}{r}\underline{e}_\theta + \frac{K}{\sqrt{2}\,r}\underline{e}_z \quad , \quad r >> 0 \tag{2.4}$$

All three components of the velocity are independent of z in the outer region. Furthermore, the tangential velocity is a free vortex. Long's vortex is one of the first models proposed to describe tornadoes. It shows that the various flow structures can be determined by a single parameter. Long's vortex also shows the characteristics of constant circulation on similarity surfaces (i.e., constant η). An interesting feature is that the macroscopic axial force in Long's vortex does not uniquely determine the flow behavior. It is noteworthy that the quasi - cylindrical approximation, in which variations in the axial direction are taken to be small compared with variations in the radial direction, was adopted by Long as well as by Bloor and Ingham [1975, 1984], and Qing [1983].

Long's theoretical work initialed many studies about geophysical vortices. A review these concentrated vortex flows was reported by Hall [1966]. Another type of sink vortex was studied by Pedley [1969]. In his study of a so called bath-tub vortex, Pedley considered a point sink with strength $4\pi Q$ situated on the axis and a uniform circulation at large radius. The flow is irrotational (i.e., vorticity equals zero) at large radius and must be rotational at some region around the sink, so that steady vortices will ultimately be set-up. Although the theoretical study of geophysical vortices is far from satisfactory due to few experimental observations, some progress has been achieved in the last 25 years. An excellent review of geophysical vortices was reported by Morton [1966,1969]. Geophysical vortices, such as tornadoes, waterspouts and dust devils, which have narrow vortex cores, terminate at a lower boundary, and are maintained dynamically aloft by some convective system which prevents the lower pressure core from filling with upper air. More theoretical treatments have dealt with the lower part of tornadoes, which have been regarded as steady vortices (see Morton, 1966). Long's vortex, as he recognized, cannot be applied to tornado as close to the ground. Therefore, to improve Long's vortex, many researchers have tried to treat the effect of the ground boundary.

Serrin [1972], adopted the same equations as Long, but assumed the no-slip condition at the surface and allowed a singularity at the origin. He proved that there can exist only three types of motion. In the first type, the radial velocity is directed inward along the boundary and upward along the axis. In the second type, the radial velocity moves inward along the boundary and downward on the axis, with a compensating outward flow at an intermediate angle. In the third type of motion, the radial velocity is outward near the plane and downward on the central axis. In the study of conical vortices, Yih et al. [1982] found a class of exact solutions of the Navier - Stokes equations. Their solutions include different angles of cones which extend the right rectangular angle of Serrin. Wu [1986], in his recent study, has considered a conical turbulent swirling vortex with variable eddy viscosity. He argued that if the eddy viscosity varies only in the boundary layer near the core or surface, the solution outside the layer will approach to one of the laminar solutions of Yih et al. or that of Serrin. He also found that for a class of deliberately chosen "eddy" viscosity functions, a steady turbulent vortex can satisfy both the regularity condition at the core and the adherence condition at the surface, except at the singular point.

In a further study of vortex breakdown of Long's vortex, Burggraf and Foster [1977] showed that breakdown (reverse flow) occured when the global axial force, F_z, was less than a critical number. They also found that Long's F_z is about 3 % lower than their calculations. Foster and Duck [1982], in the study of stability analysis of Long's vortex, pointed out the most dangerous mode in Long's vortex are those with positive azimuthal wave number n, and that the growth rates increase with n at least for the values of $0 \leq n \leq 6$ computed.

In a cyclone chamber, where vortex core flow are characteristized by a reverse annular flow , Bloor and Ingham [1975,1984] have made a systematic analysis. To investigate the core flow structure, they first solved for the basic flow in the outer region by using an inviscid, rotational flow (i.e., vorticity is not equal to zero). From this information, they were able to solve for the velocity profile in the core flow. In order to have solutions which satisfy the momentum equation, Bloor and Ingham assumed that the "eddy" viscosity could be expressed as $\mu \propto z^{-2}$.

Qing [1983], in his study of velocity and turbulence distributions within a cyclone, concluded that different radial distributions of u_r and ν_e have only a slight influence on the radial distribution of u_θ, but strongly affect the shear - stress distribution ($\tau_{r\theta}$). However, in his model u_θ is only a function of r, which he recognized as too restrictive. It is noteworthy that Qing adopted, for the first time, a continuous "eddy" viscosity profile which consists of different models of ν_e for different regions of the vortex.

Another interesting and important theory about the outer region of a confined chamber has been developed by Petty [1985]. The flow in the outer region could be Beltrami for which the velocity and vorticity vectors are colinear. Mathematically, Beltrami flow can be expressed as :

$$\underline{\omega} \propto \underline{u}$$

where $\underline{\omega}$ represents the vorticity vector and $\underline{u}$ represents the velocity vector. For axisymmetric and inviscid flows, if the velocities in the outer region are also Beltrami, then the tangential velocity profile is approximately

$$u_\theta \propto r^{-3/4}.$$

The result is very interesting and important because the value of N (= -0.75) is consistent with most of the experimental data (see Chapter 8).

CHAPTER 3

MATHEMATICAL FORMULATION

3.1 Vortex Models

The balance of linear momentum and the continuity equation for a constant property Newtonian fluid govern the behaviour of the vortex flows studied in this research. For steady, axisymmetric, swirling flows, the velocity and pressure fields depend only on the cylindrical coordinates r and z :

$$\underline{u} = u_r(r,z)\underline{e}_r + u_\theta(r,z)\underline{e}_\theta + u_z(r,z)\underline{e}_z \tag{3.1}$$

$$p = p(r,z). \tag{3.2}$$

If the axial transport of momentum by viscous forces is neglected, then the boundary layer equations governing $\underline{u}$ and p over the spatial domain $0 \le r \le \tilde{\delta}(z)$, $0 < z < \infty$ are (see Long, 1961)

$$\rho \frac{u_\theta^2}{r} = \frac{\partial p}{\partial r} \tag{3.3}$$

$$\rho u_r \frac{\partial}{\partial r}(ru_\theta) + \rho u_z \frac{\partial}{\partial z}(ru_\theta) = \mu r \frac{\partial}{\partial r}\left(\frac{1}{r}\frac{\partial}{\partial r}(ru_\theta)\right) \tag{3.4}$$

$$\rho u_r \frac{\partial u_z}{\partial r} + \rho u_z \frac{\partial u_z}{\partial z} = -\frac{\partial p}{\partial z} + \rho g_z + \frac{\mu}{r}\frac{\partial}{\partial r}\left(r\frac{\partial u_z}{\partial r}\right) \tag{3.5}$$

$$\frac{1}{r}\frac{\partial}{\partial r}(ru_r) + \frac{\partial}{\partial z}u_z = 0. \tag{3.6}$$

Eq. (3.3) assumes that the radial component of the velocity is small and that the large centrifugal force per unit volume, $\rho u_\theta^2/r$, causes the radial pressure drop. The axial pressure gradient in Eq. (3.5) is an important and unique aspect of vortex models examined. It is also noteworthy that Eq. (3.4), which is the tangential component of the equation of motion, can also be interpreted as a transport equation for the axial component of angular momentum.

Eqs. (3.3) - (3.6) govern the behaviour of the three components of $\underline{u}$ and the pressure. Because of the viscous nature of the fluid and the axisymmetric assumption, the boundary conditions on the axis (i.e., r = 0 and z > 0) are

$$u_r(0,z) = 0 \tag{3.7}$$

$$u_\theta(0,z) = 0 \tag{3.8}$$

$$\left.\frac{\partial u_z}{\partial r}\right|_{r=0} = 0 \tag{3.9}$$

Far from the axis, the tangential component of the velocity equals the experimental expression discussed in Chapter 2 :

$$u_\theta = Kr^N, \ \tilde{\delta}(z) \le r \le \infty. \tag{3.10}$$

The surface defined by $(r,z) = (\tilde{\delta}(z),z)$ is not known *a priori*, but must be calculated for each vortex model studied. If Eqs. (3.4) - (3.6) are each integrated over the cross sectional area $\pi\tilde{\delta}^2(z)$, then the following macroscopic balance equations result for the axial component of the angular momentum, the axial thrust, and the volumetric flow rate

$$\frac{dT_z}{dz} = -2\pi\tilde{\delta}^2 \left[(u_r - \frac{d\tilde{\delta}}{dz} u_z)\rho u_\theta - \tau_{r\theta} \right] \Bigg|_{r=\tilde{\delta}} \tag{3.11}$$

$$\frac{dF_z}{dz} = -2\pi\tilde{\delta} \left[(u_r - \frac{d\tilde{\delta}}{dz} u_z)\rho u_z - \tau_{rz} + \frac{d\tilde{\delta}}{dz} P \right] \Bigg|_{r=\tilde{\delta}} \tag{3.12}$$

$$\frac{dQ}{dz} = -2\pi\tilde{\delta} \left[u_r - \frac{d\tilde{\delta}}{dz} u_z \right] \Bigg|_{r=\tilde{\delta}} \tag{3.13}$$

In the above equations,

$$P = p^o - \rho gz - p(r,z), \tag{3.14}$$

$$T_z = 2\pi \int_0^{\tilde{\delta}} [\rho r u_\theta] u_z r dr , \tag{3.15}$$

$$F_z = 2\pi \int_0^{\tilde{\delta}} [\rho u_z^2 - P] r dr , \tag{3.16}$$

$$Q = 2\pi \int_0^{\tilde{\delta}} u_z r dr . \tag{3.17}$$

T_z represents the axial component of the macroscopic torque on the cross section $\pi\tilde{\delta}^2$ induced by the swirling flow; F_z is the axial component of the average force acting on $\pi\tilde{\delta}^2$; and, Q is the volumetric flow rate across this area. The above equations show what properties of the flow acting on the surface $(\tilde{\delta}(z),z)$ determine the variation of T_z, F_z, and Q in the axial direction.

Two models of a viscous vortex are studied. Model I, previously analyzed by Long [1961] and Foster (see esp., Burggraf and Foster [1977]), is defined by Eqs. (3.3) - (3.6), Eqs. (3.7) - (3.9), Eq. (3.10) with $N = -1$, and the following two auxiliary conditions :

$$\lim_{\bar{\delta} \to \infty} F_z < \infty, \text{ finite macroscopic force;} \tag{3.18}$$

$$\lim_{r \to \infty} P = 0, \text{ hydrostatics at infinity.} \tag{3.19}$$

A sufficient condition for Eq. (3.18) is

$$\rho u_z^2 = P, \text{ for } \delta_a(z) \le r \le \infty,\ z \ge 0. \tag{3.20}$$

Figure 3.1 shows the definition of the coordinate system and the boundary conditions for vortex Model I.

As previously discussed in Chapter 1 and 2, many vortex flows are characterized by a reverse (or downward) annular flow far from the axis. In Chapter 7, a vortex is studied which approximates this behavior by assuming that a surface of zero axial velocity surrounds the axis. Model II accomodates this physical possibility by imposing specific boundary conditions on a finite surface of similarity rather than the asymptotic conditions defined by Eqs. (3.18) - (3.20).

Therefore, on a surface defined by $(r,z) = (\delta^*(z),z)$, which is not known a priori, Model II assumes that

1. the axial component of the velocity is zero; and
2. the tangential velocity is given by Eq. (3.10) for $-1 \le N < 0$ and $\delta^*(z) \le r \le \infty$.

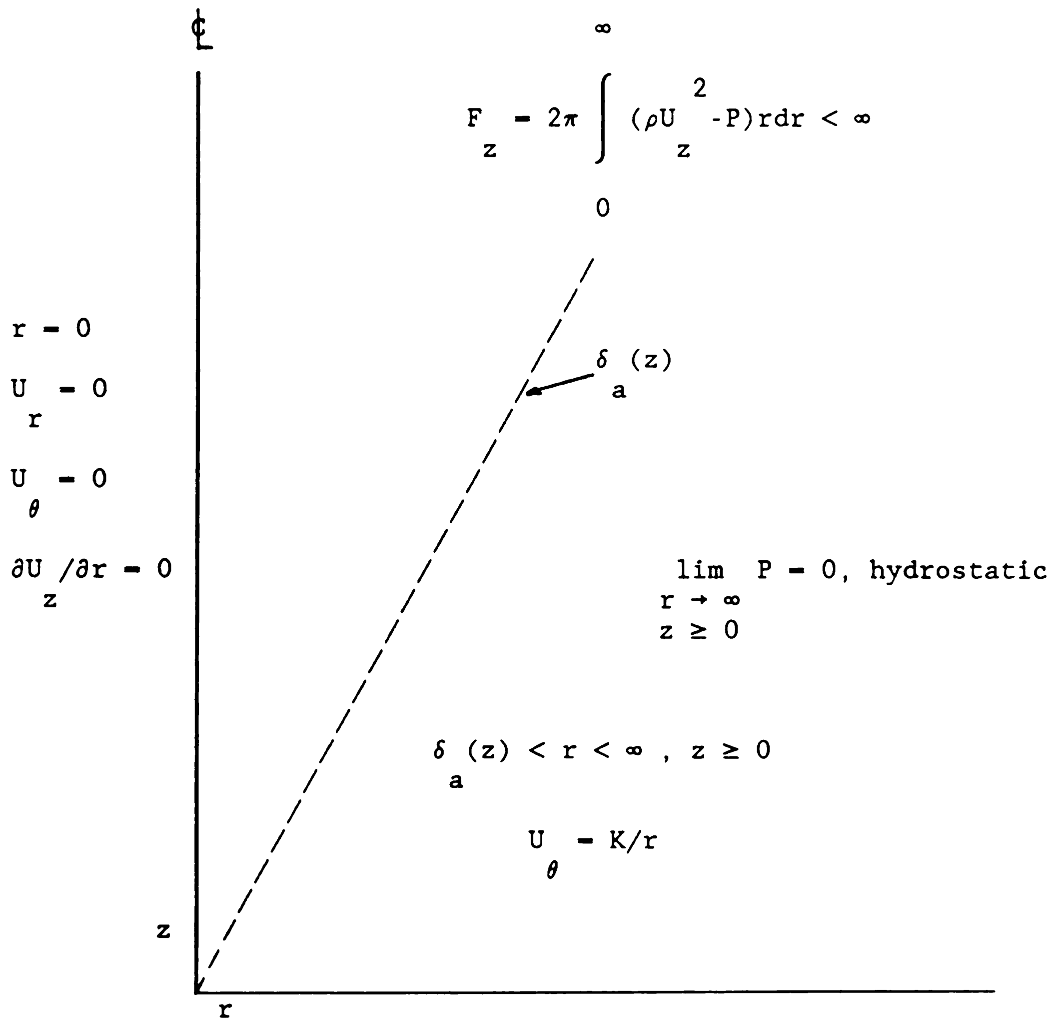

Figure 3.1 Coordinate system and physical boundary condition for the vortex Model I

Although the velocity and pressure fields for $r > \delta^*(z)$ are not specified explicitly, we still assume continuity of viscous stresses, velocity, and pressure across the surface $(\delta^*(z),z)$. Thus, the auxiliary conditions which define Model II are

$$u_\theta = Kr^N, \quad -1 \le N < 0, \quad \delta^*(z) \le r \le \infty \tag{3.21}$$

$$u_z(\delta^*(z),z) = 0 \tag{3.22}$$

$$\tau_{r\theta}(\delta^*(z),z) = \mu K(N-1)[\delta^*(z)]^{N-1} \tag{3.23}$$

$$\tau_{\theta z}(\delta^*(z),z) = 0 \tag{3.24}$$

The other components of the viscous stress are related to the radial and axial components of the velocity (see Appendix D). The behaviour of the outer flow (i.e., $r > \delta^*(z)$) must be consistent with the predicted behaviour of the core flow ($0 \le r \le \delta^*(z)$, $z > 0$). Figure 3.2 shows the definition of the coordinate system and the boundary conditions for vortex Model II.

3.2 Similarity Conditions

Because the three-dimensional flow studied is axisymmetric (see Eq. (3.1)), the radial and axial components are closely coupled through the continuity equation. A convenient way to satisfy Eq. (3.6) automatically is to use a stream function to represent u_r and u_z,

$$u_r = -\frac{1}{r}\frac{\partial\psi}{\partial z} \tag{3.25}$$

$$u_z = +\frac{1}{r}\frac{\partial\psi}{\partial z} \tag{3.26}$$

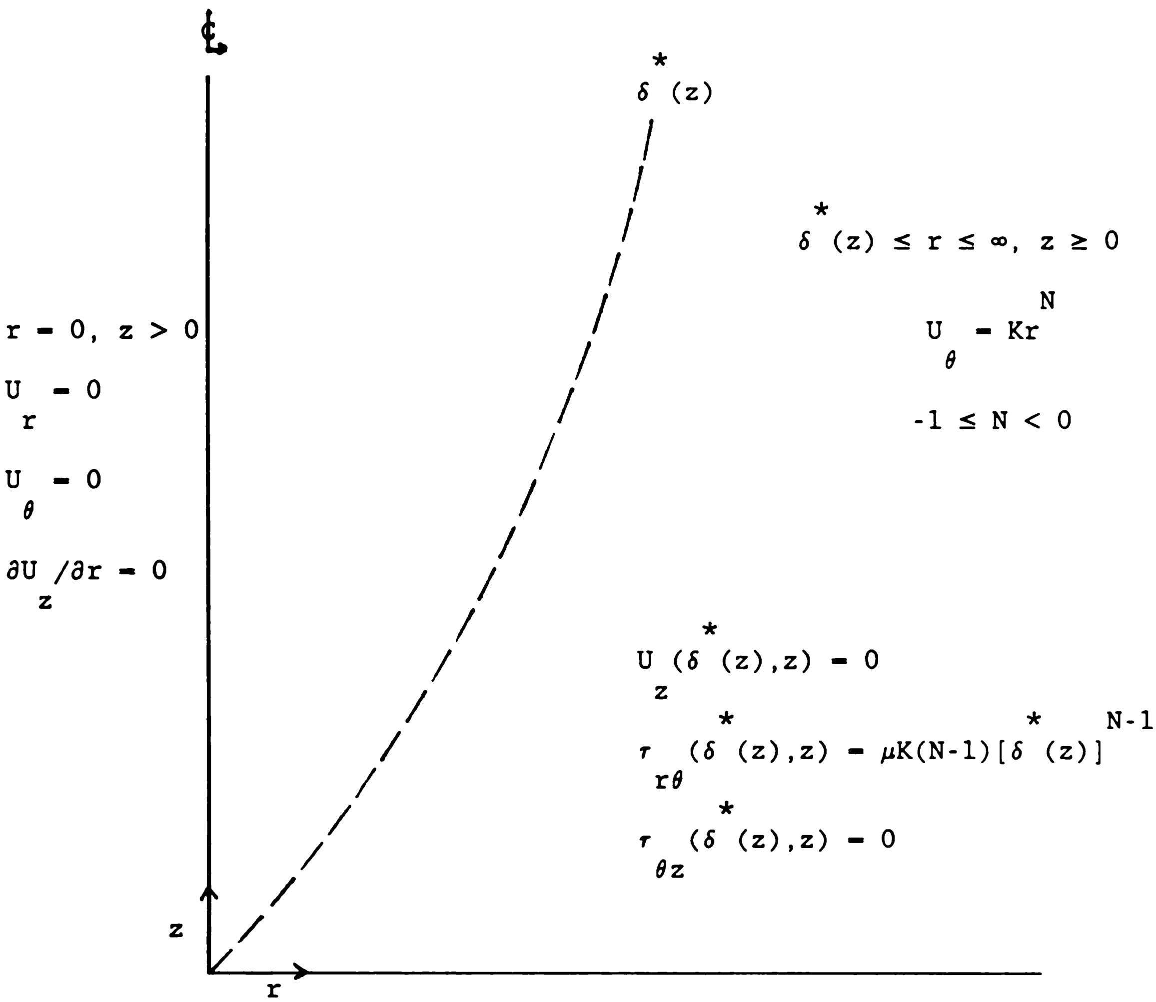

Figure 3.2 Coordinate system and physical boundary condition for the vortex Model II

Boundary conditions on $\psi(r,z)$ stem from the previous conditions on u_r and u_z and will be explicitly noted momentarily. First observe, however, that the boundary surface at $(r,z) = (r,0)$ and at $(r,z) = (\infty,z)$ have similar conditions on $u_\theta(r,z)$. This observation suggests the following representations for the three dependent variables

$$P(r,z) = \rho u_c^2(z)M(\eta) \tag{3.27}$$

$$ru_\theta(r,z) = \delta(z)u_c(z)F(\eta) \tag{3.28}$$

$$\psi(r,z) = \delta^2(z)u_c(z)h(\eta) \tag{3.29}$$

where

$$\eta = r/\delta(z) \tag{3.30}$$

In the above expressions, $\delta(z)$ and $u_c(z)$ represent, resp., intrinsic length and velocity scales. These are determined as part of the solution to a specific vortex model.

Inserting Eqs. (3.27) - (3.29) together with Eqs. (3.26) and (3.27) into Eqs. (3.3) - (3.5) yields

$$F = -\eta^3 M' \tag{3.31}$$

$$\alpha_1 hF' + \alpha_2 h'F = \eta F'' - F' \tag{3.32}$$

$$-\alpha_1 hG' + \alpha_3 h'G = 2\alpha_3 \eta M - \alpha_4 \eta^2 M' + \eta G'' + G' \tag{3.33}$$

where

$$G = \frac{u_z(r,z)}{u_c(z)} = \frac{1}{\eta}\frac{dh}{d\eta} \tag{3.34}$$

and

$$\alpha_1 = \frac{d}{dz} \left(\frac{u_c \delta^2}{\nu} \right)$$

$$\alpha_2 = \delta \frac{d}{dz} \left(\frac{u_c \delta}{\nu} \right)$$

$$\alpha_3 = \delta^2 \frac{d}{dz} \left(\frac{u_c}{\nu} \right)$$

$$\alpha_4 = \frac{u_c \delta}{\nu} \frac{d\delta}{dz}$$

The coefficients α_1, α_2, α_3, and α_4 must be constants. However, all the α's are not independent inasmuch as

$$\alpha_2 = \alpha_1 - \alpha_4$$

and

$$\alpha_3 = \alpha_1 - 2\alpha_4 .$$

Therefore, a necessary condition for similarity is that

$$\frac{d}{dz} \left(\frac{u_c \delta^2}{\nu} \right) = \text{constant, and} \tag{3.35}$$

$$\frac{u_c \delta}{\nu} \frac{d\delta}{dz} = \text{constant.} \tag{3.36}$$

It follows directly from (3.35) and (3.36) that

$$u_c \propto \delta^N \quad \text{and} \quad \delta \propto (z)^{\frac{1}{N+2}} .$$

The physical constants K and ν can be used to scale $u_c(z)$ and $\delta(z)$. Thus,

$$u_c = K\delta^N , \tag{3.37}$$

and

$$\delta = \left(\frac{\nu z}{K} \right)^{1/(N+2)} . \tag{3.38}$$

With these results, the α - coeffients become

$$\alpha_1 = 1$$

$$\alpha_2 = \frac{N+1}{N+2}$$

$$\alpha_3 = \frac{N}{N+2}$$

$$\alpha_4 = \frac{1}{N+2} .$$

Eqs. (3.31) - (3.33) can now be written as

$$M' = - \frac{F^2}{\eta^3} \tag{3.39}$$

$$\eta F'' - F' + F'h = \frac{N+1}{N+2} Fh' \tag{3.40}$$

$$\frac{d}{d\eta} \left[\eta G' - \frac{1}{N+2} \eta^2 M + hG \right] = \frac{2(N+1)}{N+2} \left[G^2 - M \right] \eta \tag{3.41}$$

$$h' = \eta G . \tag{3.42}$$

When N = -1, the set of equations given above reduce to a model previously studied by Long [1961] and reexamined in Chapter 6. The boundary conditions for the sixth order system will be presented in Section (3.4) after the asymptotic behaviour of the solution has been developed. Meanwhile, Figure 3.3 illustrates the shape of the surfaces of constant η in the r,z - plane. The dependent variables $M(\eta)$, $F(\eta)$, and $h(\eta)$ are constants on these surfaces. Note that for the special

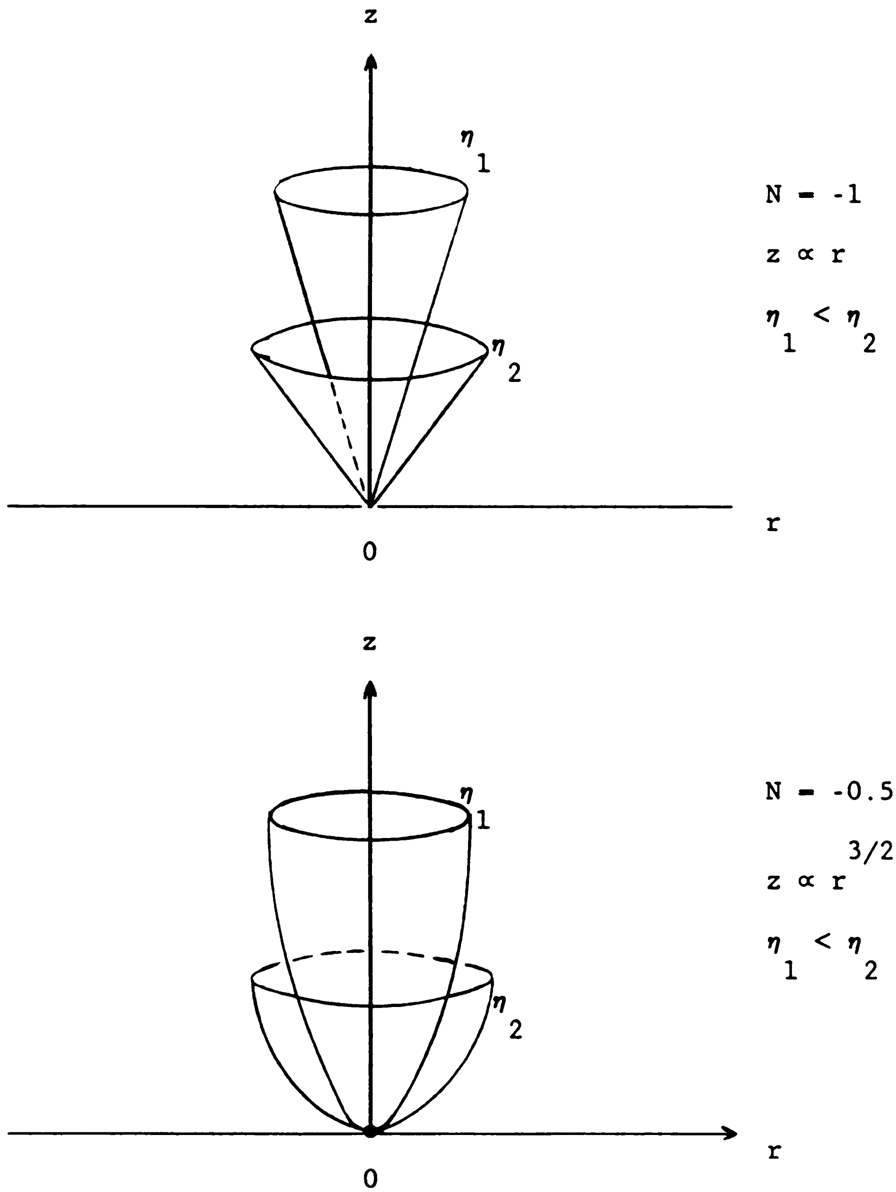

in general : $z \propto r^{2+N}$

Figure 3.3 Surfaces of Similarity (constant value of $\eta = r/\delta(z)$)

case N = -1, the similarity surfaces form a family of cones. For $-1 < N < 0$, the surfaces have a parabolic-like shape.

It follows from Eqs. (3.37) and (3.38) that for a fixed value of η, the dependent variables (see Eqs. (3.27) - (3.29)), depend on the axial coordinate as follows

$$P(r,z) \propto (z)^{2N/(N+2)}$$

$$ru_\theta(r,z) \propto (z)^{(N+1)/(N+2)}$$

$$\psi(r,z) \propto z$$

As illustrated in Figure 3.4, the stream function is proportional to z for $-1 \leq N < 0$. This result implies that the entrainment rate, defined by Eq. (3.13), is constant on surfaces of constant η inasmuch as

$$Q = 2\pi \int_0^{\delta_a} u_z r dr$$

$$= 2\pi \int_0^{\delta_a} \frac{1}{r}\frac{\partial\psi}{\partial r} r dr$$

$$= 2\pi\psi(\delta_a(z), z)$$

$$= 2\pi\nu z h(\eta) \ .$$

This results by letting $\psi(0,z) = 0$ which implies that $h(0) = 0$.

Figure 3.4 also shows that the axial component of the angular momentum, ru_θ, is constant on surfaces of similarity for N = -1 only. However, for $-1 \leq N < 0$, the pressure field is unbounded for $z \to 0$ on surfaces of constant η.

By inserting Eq. (3.29) into Eqs.(3.25) and (3.27), it follows that

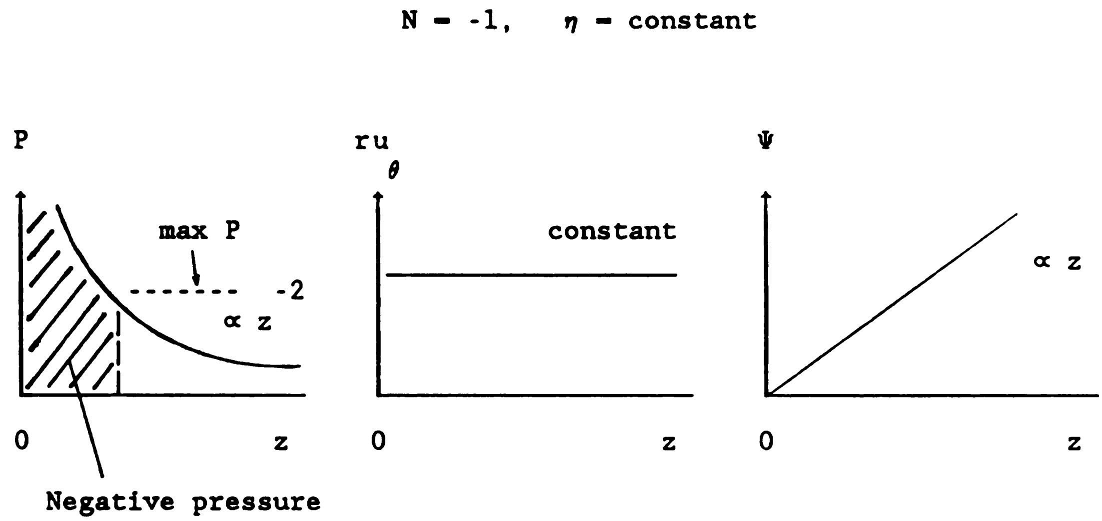

Figure 3.4 Qualitative behavior of the dependent variables on the similarity surfaces

$$u_r = K\delta^N \frac{d\delta}{dz} \left[h' - (N+2)\frac{h}{\eta} \right] \tag{3.44}$$

$$u_z = K\delta^N \frac{h'}{\eta} \quad . \tag{3.45}$$

Thus, for constant values of η, Eqs. (3.44) and (3.45) show that

$$u_r \propto z^{-1/(N+2)} \quad \text{and} \quad u_z \propto z^{N/(N+2)} \quad .$$

As $z \to 0$ for constant η, both the radial and axial components of the velocity become unbounded; however, as $z \to \infty$, these components decay to zero.

Both vortex models studied in Chapters 6 and 7 are subject to the same conditions on the axis. The physical boundary conditions given by Eqs. (3.7) - (3.9) imply that the similarity functions defined by Eqs. (3.27) - (3.29) must satisfy the following conditions :

$$\lim_{\eta \to 0} \left[h' - (N+2) \frac{h}{\eta} \right] = 0 \tag{3.46}$$

$$\lim_{\eta \to 0} \left[\frac{F}{\eta} \right] = 0 \tag{3.47}$$

$$\lim_{\eta \to 0} \left[\frac{h''}{\eta} - \frac{h'}{\eta^2} \right] = 0 \tag{3.48}$$

These results, and $h(0) = 0$, will restrict the behaviour of the swirling flow near the centerline of the vortex and will be explored further in Chapter 4.

3.3 Asymptotic Behaviour

The asymptotic condition on the tangential velocity expressed by Eq. (3.10) implies that $F(\eta)$, defined by Eq. (3.28), has the following behaviour for large values of η

$$F \rightarrow F_a = \eta^{N+1}, \quad \frac{\delta_a(z)}{\delta(z)} = \eta_a \leq \eta \leq \infty \ . \tag{3.49}$$

Thus, for $N = -1$, $F_a = 1$ and the axial component of the angular momentum is bounded; however, for $-1 < N \leq 0$, F_a becomes unbounded for $\eta \rightarrow \infty$.

Because $P(\infty,z) = 0$, $M(\infty) = 0$ also (see Eqs. (3.51) and (3.27)). Therefore, by integrating Eq. (3.31) with $F = F_a$, it follows that

$$M \rightarrow M_a = \frac{\eta^{2N}}{(-2N)} \ , \quad \eta_a \leq \eta \leq \infty. \tag{3.50}$$

If Eq. (3.20) holds, then

$$G_a^{\,2} = M_a \ , \quad \eta_a \leq \eta \leq \infty \ . \tag{3.51}$$

Thus,

$$G_a = \frac{h_a{'}}{\eta} = \frac{\eta^{N}}{\sqrt{-2N}} \ , \quad \eta_a \leq \eta \leq \infty \ . \tag{3.52}$$

Eq. (3.52) can be integrated to give

$$h \rightarrow h_a = \frac{\eta^{N+2}}{(N+2)\sqrt{-2N}} + \gamma \ , \quad \eta_a \leq \eta \leq \infty \ . \tag{3.53}$$

With $G_a^{\,2} = M_a$, Eq. (3.41) reduces to

$$\eta G_a{}' - \frac{1}{N+2}\, \eta^2 G_a{}^2 + h_a G_a = \text{constant}. \tag{3.54}$$

Inserting Eqs. (3.52) and (3.53) into Eq. (3.54) yields

$$(\ \gamma + N\ )\ \frac{\eta^N}{\sqrt{-2N}} = \text{constant}\ . \tag{3.55}$$

This equation is satisfied by setting the arbitrary constant of integration to zero and $\gamma = -N$. Thus, Eq. (3.53) becomes

$$h_a = \frac{\eta^{N+2}}{(N+2)\ \sqrt{-2N}} - N\ ,\ \eta_a \le \eta \le \infty\ . \tag{3.56}$$

For $N = -1$, Eq. (3.40) is balanced. This is not suprising because the free vortex (i.e., $u_\theta = K/r$) is an exact solution to Eq. (3.4). However, because the empirical swirl velocity employed in this study (see Eq. (3.10)) is not a solution to Eq. (3.4), the asymptotic functions given by Eqs. (3.49), (3.50), and (3.56) only satisfy the radial and axial components of the boundary layer equations and the continuity equation. If F_a and h_a are introduced into Eq. (3.40), then

$$[\ \frac{N+1}{N+2}\ F_a h_a{}' - \eta F_a{}'' + F_a{}' - F_a{}' h_a] = (N+1)\ \eta^N\ . \tag{3.57}$$

This result shows that the tangential balance of linear momentum is satisfied for $N = -1$ only. Thus, similarity solutions on the <u>unbounded domain</u>, which simultaneously satisfy all three component equations of the momentum balance and Eq. (3.10) with $-1 < N < 0$, do not exist.

<u>3.4 Boundary Value Problem Studied</u>

The physical boundary conditions given by Eqs. (3.7) - (3.9) require the following restrictions on the similarity functions at $\eta = 0$ (also see Eqs. (3.46) - (3.48)) :

$$h'(0) = 0 \tag{3.58}$$

$$F'(0) = 0 \tag{3.59}$$

$$h'''(0) = 0 \tag{3.60}$$

Moreover, Eqs. (3.28) and (3.43) also require

$$F(0) = 0 \tag{3.61}$$

$$h(0) = 0 \tag{3.62}$$

These conditions are satisfied by both vortex Models studied.

Eqs. (3.49), (3.50), and (3.56) with $N = -1$ define the asymptotic behaviour of a vortex with bounded circulation (Model I). Eqs. (3.39) - (3.42) with $N = -1$ govern the behaviour of Model I for $0 \leq \eta \leq \eta_a$. The constant η_a is calculated as part of the solution.

Model II also satisfies Eqs. (3.58) - (3.62) and the differential equations (3.39) - (3.42) for $0 \leq \eta \leq \eta^*$. However, as previously mentioned, similarity solutions on the unbounded domain for $-1 < N < 0$ do not exist (see Eq. (3.57)). Eqs. (3.21) - (3.24), which completes the mathematical definition of Model II, require the following restrictions on the similarity functions at $\eta = \eta^* = \delta^*(z)/\delta(z)$:

$$F(\eta^*) = (\eta^*)^{N+1} \tag{3.63}$$

$$h'(\eta^*) = 0 \tag{3.64}$$

$$\left.\frac{dF}{d\eta}\right|_{\eta^*} = (N+1)(\eta^*)^N \tag{3.65}$$

Eq. (3.65) stems from either Eqs. (3.23) or (3.24). This can be seen by first writing the stress components in terms of the similarity function $F(\eta)$ as follows

$$\tau_{r\theta} = \mu r \frac{\partial}{\partial r} \left(\frac{u_\theta}{r} \right) = \mu K \delta^{N-1} \frac{1}{\eta^2} \left[\eta \frac{dF}{d\eta} - 2F \right]$$

$$\tau_{\theta z} = \mu \frac{\partial}{\partial r} (u_\theta) = - \mu K \delta^{N-1} \frac{d\delta}{dz} \frac{1}{\eta} \left[\eta \frac{dF}{d\eta} - (N+1)F \right]$$

The above two expressions apply for $0 \le r \le \delta^*(z)$. Eq. (3.65) follows directly by setting $r = \delta^*(z)$ and using the continuity conditions given by Eqs. (3.23) and (3.24).

Table 3.1 summarizes the basic elements of the two vortex models studied and Table 3.2 lists the properties calculated for each model. The two models are qualitatively different inasmuch as the macroscopic axial thrust induced by the flow for Model I is constant (i.e., $\delta u_c = K$ for $N = -1$) whereas this property varies with axial position for Model II (see Chapter 6 and 7).

Table 3.1 Mathematical models

	Differential Equations	Domain	Conditions at $\eta = 0$	Edge Conditions
Model I : Vortex Flows with Constant Circulation	Eqs. (3.40) – (3.43) with $N = -1$	Infinite $0 \le \eta \le \infty$	Eqs. (3.59) – (3.63)	$\eta_a \le \eta \le \infty$ $F = 1$ $M = 1/(2\eta)$ $h = \eta/\sqrt{2} + 1$
Model II : Vortex Flows with Variable Circulation	Eqs. (3.40) – (3.43) $-1 \le N < 0$	Finite $0 \le \eta \le \eta^*$	Eqs. (3.59) – (3.63)	$\eta = \eta^*$ $F = (\eta^*)^{N+1}$ $h' = 0$ $F' = (N+1)(\eta^*)^{N+1}$

Table 3.2 Physical properties calculated for the two vortex models

Property	Equations	Comment
Similarity scales:		
Length	$\delta = \left(\frac{\nu z}{K} \right)^{\frac{1}{N+2}}$	$N = -1$ Model I
Velocity	$U_c = K\delta^N$	$-1 \leq N < 0$, Model II
Angular momentum	$rU_\theta = \delta U_c F$	
Radial pressure difference	$P = \rho U_c^2 M$	$\eta = r/\delta(z)$
Stream function	$\psi = \delta^2 U_c h$	$0 \leq \eta \leq \eta_a$, Model I
Tangential velocity	$U_\theta = U_c \frac{F}{\eta}$	
Axial velocity	$U_z = U_c \frac{h'}{\eta}$	$0 \leq \eta \leq \eta^*$, Model II
Radial velocity	$U_r = U_c \frac{d\delta}{dz} \left(h' - (N+2)\frac{h}{\eta} \right)$	
Axial thrust	$\frac{F_z}{2\pi\rho(\delta U_c)^2} = \int_0^{\tilde{\eta}} (G^2 - M)\eta d\eta$	$\tilde{\eta} = \eta_a$, Model I
Axial torque	$\frac{T_z}{2\pi\rho\delta(\delta U_c)^2} = \int_0^{\tilde{\eta}} FG\eta d\eta - \frac{N+2}{2N+3} [h(\tilde{\eta}) + (N-1)]\tilde{\eta}^{N+1}$	
Flow rate	$\frac{Q}{2\pi\delta^2 U_c} = \int_0^{\tilde{\eta}} G\eta d\eta = h(\tilde{\eta})$	$\tilde{\eta} = \eta^*$, Model II
Pressure drop	$\frac{p(\tilde{\delta},z) - p(o,z)}{\rho U_c^2} = \int_0^{\tilde{\eta}} \frac{F^2}{\eta^3}\eta d\eta = M(0) - M(\tilde{\eta})$	

CHAPTER 4

SOLUTION BEHAVIOR NEAR THE AXIS

4.1 General Solution

The solution to Eqs. (3.39) - (3.42) for small values of η can be developed using Taylor series representations for M, F, and h. In general,

$$M(\eta) = M(0) + M'(0)\eta + \frac{1}{2!} M''(0)\eta^2 + \cdots \tag{4.1}$$

$$F(\eta) = \underline{F(0)} + \underline{F'(0)}\eta + \frac{1}{2!} F''(0)\eta^2 + \cdots \tag{4.2}$$

$$h(\eta) = \underline{h(0)} + \underline{h'(0)}\eta + \frac{1}{2!} h''(0)\eta^2 + \cdots \tag{4.3}$$

The coefficients underlined in Eqs. (4.2) and (4.3) are zero because of boundary conditions (3.58), (3.59), (3.61), and (3.62). All of the coefficients multiplying odd powers of the independent variable are zero because of local symmetry about $\eta = 0$. Because Eqs. (3.39) - (3.42) are invariant if $\eta \rightarrow -\eta$, $M(\eta) = M(-\eta)$; $F(\eta) = F(-\eta)$; and, $h(\eta) = h(-\eta)$. Thus, the power series representations through fourth order can be expressed as

$$M_o = c + c_1\eta^2 + c_2\eta^4 + \cdots \tag{4.4}$$

$$F_o = \frac{b}{2}\eta^2 + b_1\eta^4 + \cdots \tag{4.5}$$

$$h_o = \frac{a}{2}\eta^2 + a_1\eta^4 + \cdots\cdot \tag{4.6}$$

The coefficients a_1, b_1, c_1, c_2, --- can be related to a, b, and c by inserting Eqs. (4.4) - (4.6) into Eqs. (3.39) - (3.42) and equating like forms of the independent variable. This gives

$$a_1 = \frac{N}{8(N+2)} \left(\frac{a^2}{2} - c \right) \tag{4.7}$$

$$b_1 = - \frac{ab}{16(N+2)} \tag{4.8}$$

$$c_1 = - \frac{b^2}{8} \tag{4.9}$$

$$c_2 = \frac{ab^2}{64(N+2)} \tag{4.10}$$

The general solution near the axis depends on the empirical index N and the coefficient a, b, and c. The asymptotic behavior for $\eta >> 0$ (see Model I, Chapter 3) will determine three of the four coefficients (a, b, c, η_a); the remaining coefficient can be used to parameterize the behaviour of the vortex (see Chapter 6, 7). Figure 4.1 portrays the mathematical meaning of these coefficients and provides the interesting *a priori* observation that as 'b' increases the angular momentum changes from zero to its asymptotic value over smaller spatial domains. Thus, the vortex becomes more 'concentrated' about the axis. In Chapters 6 - 7, the limiting behavior of the solution for small values of η will be connected to the asymptotic behavior for the two vortex models defined previously (see Table 3.1).

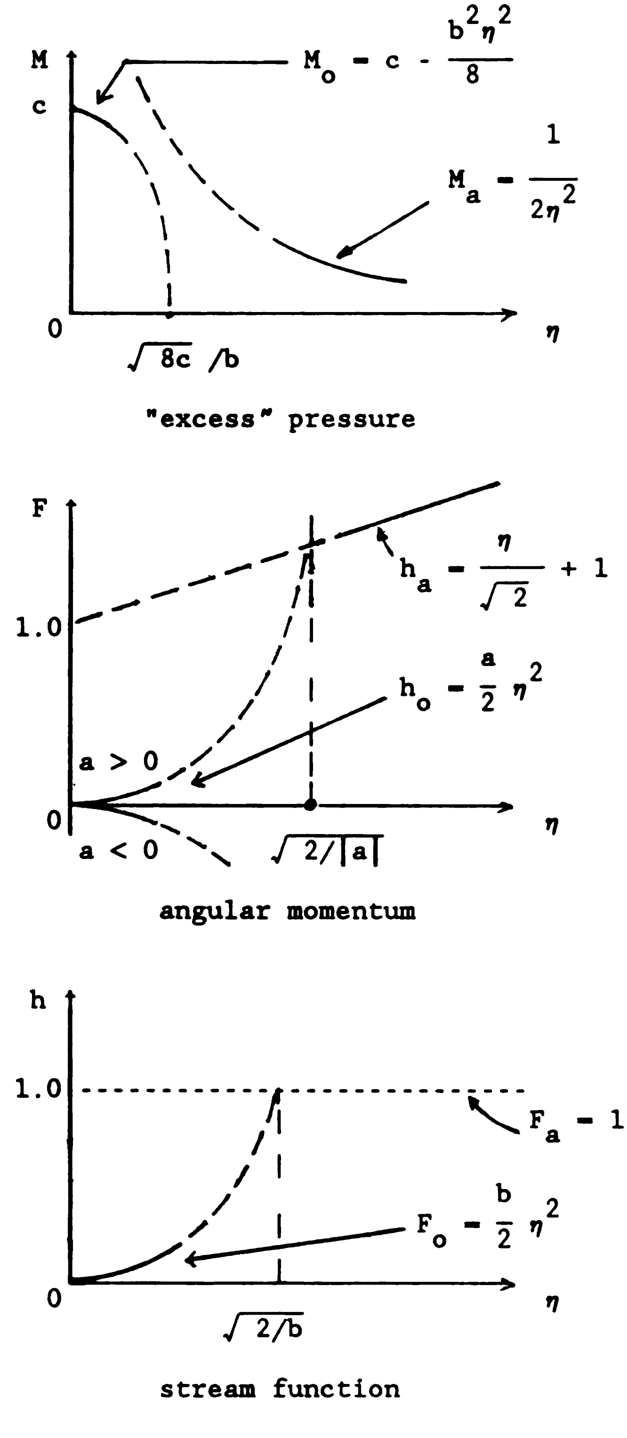

Figure 4.1 Geometric meaning of the expansion coefficients

4.2 Different Flow Regimes

The local behavior of the axial and radial velocity near the 'axis' (i.e., small values of η) is determined by the coefficient 'a'. Because (see Eq. (4.6))

$$h_o = \frac{a}{2}\eta^2 + \frac{N}{8(N+2)}\left(\frac{a^2}{2} - c\right)\eta^4 + \cdots\cdot \tag{4.11}$$

it follows that (see Table (3.2))

$$u_z(r,z) = K\left(\frac{\nu z}{K}\right)^{\frac{N}{N+2}}\left[a + \frac{N}{2(N+2)}\left(\frac{a^2}{2} - c\right)\eta^2 + \cdots\cdot\right] \tag{4.12}$$

and

$$u_r(r,z) = \nu\left(\frac{\nu z}{K}\right)^{-\frac{1}{N+2}}\left[-\frac{N}{2(N+2)}a\eta + \frac{(2-N)N}{8(N+2)^2}\left(\frac{a^2}{2} - c\right)\eta^3 + \cdots\right] \tag{4.13}$$

Eq. (4.12) shows that the transition from forward flow (i.e., $u_z(0,z) > 0$) to backward, or reverse, flow (i.e., $u_z(0,z) < 0$) within the vortex is determined by the sign of the coefficient 'a'. Therefore,

> transition from forward to reverse flow on the axis of a vortex corresponds to $a = 0$.

Likewise, Eq. (4.13) shows that for $-1 \le N < 0$

> forward flow around the axis is accompanied by an outward radial flow (i.e., $u_r > 0$); and

reverse flow around the axis is accompanied by
an inward radial flow (i.e., $u_r < 0$) .

Whereas $-\infty < a < +\infty$, the coefficient b on the other hand is always positive. This follows from Eq. (4.5) and Eq. (3.28) which shows that

$$u_\theta(r,z) = K \left(\frac{\nu z}{K} \right)^{\frac{N}{N+2}} \left[\frac{b}{2} \eta + \cdots \right] \tag{4.14}$$

Positive values of 'b' correspond to counter clockwise rotation about the axis; negative values of 'b' correspond to clockwise rotations. Because Eqs. (3.3) and (3.4) are invariant to a sign change in u_θ, only counter clockwise rotations are considered. The empirical parameter K in Eq. (1.1) is positive.

As noted earlier, large values of 'b' will give a 'concentrated' vortex motion about the axis. Because of the physical interpretation of 'b' as a measure of the frequency of the forced vortex motion about the axis and because of its clear qualitative effect on the flow (see Figure 4.1), the global solution will be parameterized by this dimensionless group. Note that

$$b = \frac{2 \left(\frac{\partial u_\theta}{\partial r} \right) \Big|_{r=0}}{K \left(\frac{\nu z}{K} \right)^{(N-1)/(N+2)}} , \tag{4.15}$$

which is a relatively easy property to measure experimentally (see Chapter 9). This alone justifies its use in the theoretical development as an independent parameter.

The parameter 'c', which represents the dimensionless 'excess' pressure on the axis (see Table 3.2), is always positive for Model I because (see Eq. (3.39))

$$c = M(0) - M(\tilde{\eta}) + \int_0^{\tilde{\eta}} \frac{F^2}{\eta^3}\, d\eta > 0 \tag{4.16}$$

For Model II, computer experiment for the range of b studied in this research (see Chapter 7) shows c is positive for any value of N. For small values of η,

$$P(r,z) = \rho K^2 \left(\frac{\nu z}{K} \right)^{\frac{2N}{N+2}} \left[c - \frac{b^2}{8} \eta^2 + \frac{ab^2}{64(N+2)} \eta^4 + \cdots \right] \tag{4.17}$$

Note that

$$\left. \frac{\partial^2 P}{\partial r^2} \right|_{r=0} < 0 ,$$

so for a fixed cross section (constant z), the pressure on the axis always corresponds to a local minimum (maximum for P). Because $c > 0$, $P(0,z)$ is positive and always decreases with increasing z. Therefore,

$$\left. \frac{\partial}{\partial z} (p + \rho g z) \right|_{r=0} = cK\mu \frac{(-2N)}{N+2} \left(\frac{\nu z}{K} \right)^{\frac{N-2}{N+2}} > 0 . \tag{4.18}$$

Eq. (4.18) shows that forward flow on the axis is always against an adverse pressure gradient. There will always be a region, $0 < z < z^o$, near the singularity point for which the pressure is less than zero. z^o can be calculated from Eq. (3.27) by replacing u_c with Eq. (3.37) and letting $p(0,z^o) = 0$. Thus, negative values of $p(0,z)$ occur on the axis for $z < z^o$, where

$$z^o = \left[\frac{p^o - \rho g z^o}{c \rho K^2} \right]^{\frac{N+2}{2N}} \frac{K}{\nu} \quad . \tag{4.19}$$

Because $-1 \leq N < 0$, it follows from Eq. (4.19) that z^o increases as c increases inasmuch as $p^o \gg \rho g z^o$. For $N = -1$, $z^o \propto c^{0.5}$ whereas for $N = -0.75$, $z^o \propto c^{5/6}$. For $N = -1$, Eq. (4.19) reduces to

$$z^o = K \left(\frac{\rho}{p^o - \rho g z^o} \right)^{0.5} \frac{K}{\nu} (c)^{0.5} \tag{4.20}$$

For jet-like, forward flow with $c \approx 0.1$, z^o is about 0.08 m for a gas vortex with a backpressure (i.e., $p^o - \rho g z^o \approx p^o$) of 14.7 psi ($1.01 \times 10^6$ g-cm^2/sec^2), $K \approx 3050$ cm^2/sec (see Boysan et al.,1982 and Table 8.5), $\rho \approx 0.0013$ g/cm^3, and $K/\nu \approx 231$. However, for a liquid vortex with $N = -0.75$ (see Dabir, 1983 and Table 8.5), $c = 0.1$, $p^o \approx 14.7$ psi, $K \approx 270$ cm^{1-N}/s (see Table 8.2), $\rho = 1.0$ g/cm^3, and $K/\nu \approx 342$ cm$^{-(1+N)}$, the onset of negative pressures occurs at $z^o \approx 0.056$ m.

The behaviour of the axial velocity near the axis depends on the relative values of 'a' and 'c'. Figure 4.2 illustrates four flow patterns consistent with Eq. (4.12). With the exception of Flow IV, all of these features have been observed experimentally (see Chapter 2) and calculated theoretically (see Chapter 6, 7). Table 4.1 gives the conditions for transition between these flow regimes. The qualitative behaviour for the radial flow follows directly from Eq. (4.13) and is also noted for each transition.

The sign of the 'excess' mechanical energy, E, of the fluid on the axis relates directly to the flow structure illustrated in Figure 4.2. The value of E at r = 0 can be calculated as follows

$$E = \frac{1}{2}\,\rho[u_z(0,z)]^2 + [p(0,z) - (p^o - \rho gz)] \tag{4.21}$$

By using the results listed in Table 3.2, the above expression can be written as

$$E = \rho u_c^{\,2}\left(\frac{a^2}{2} - c\right) . \tag{4.22}$$

Thus, forward, jet-like flows (Type I) as well as reverse, undulating flows (Type IV) correspond to <u>positive</u> value of the 'excess' mechanical energy on the axis; <u>negative</u> values of E give a wake-like behaviour which includes both undulated (Type II) and reverse, jet-like flows (Type III). Transition between Type I and II flows correspond to E = 0.

4.3 Mechanical Energy Balance On The Axis

A mechanical energy balance consistent with the approximate boundary layer equations, defined by Eqs. (3.3) - (3.6), has the

	Jet-like Behavior	Undulated Behavior	
Forward Flow $U_z > 0$ at $r = 0$ $a > 0$	I 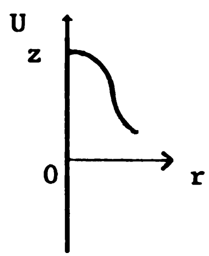 at $r = 0$ $\partial^2 U_z/\partial r^2 < 0$ $c < a^2/2$	II 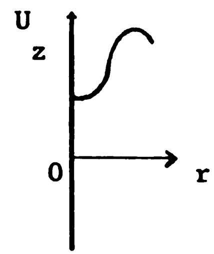 at $r = 0$ $\partial^2 U_z/\partial r^2 > 0$ $c > a^2/2$	at $r = 0$ $\partial U_r/\partial r > 0$ Outward Radial Flow
Reverse Flow $U_z < 0$ at $r = 0$ $a < 0$	III 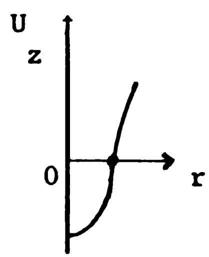 at $r = 0$ $\partial^2 U_z/\partial r^2 > 0$ $c > a^2/2$	IV 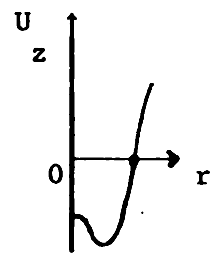 at $r = 0$ $\partial^2 U_z/\partial r^2 < 0$ $c < a^2/2$	at $r = 0$ $\partial U_r/\partial r < 0$ Inward Radial Flow

Figure 4.2 Classes of vortex flows allowed by the similarity model

Table 4.1 Criteria for transition between flow regimes

Transition	Criteria	Comment
I $\leftrightarrow$ II	$a > 0, \quad c = \frac{a^2}{2}$	Forward, Outward Flow
II $\leftrightarrow$ III	$a = 0, \quad c \geq 0$	Inward Flow
III $\leftrightarrow$ IV	$a < 0, \quad c = \frac{a^2}{2}$	Backward, Inward Flow
IV $\leftrightarrow$ I	$a = 0, \quad c = 0$	Impossible for Nonzero angular momentum ; see Eq. (4.16).

interesting feature that the viscous dissipation is zero on the axis. Thus, the change in E (see Eq. (4.21)) along the axis is governed by the following equation

$$\left.\frac{DE}{Dt}\right|_{r=0} = u_z(0,z)\,\frac{\partial E(0,z)}{\partial z} = \lim_{r \to 0} \frac{1}{r}\frac{\partial}{\partial r}\, r(\tau_{r\theta}u_\theta + \tau_{rz}u_z) \tag{4.23}$$

The term on the right-hand-side of Eq. (4.23) represents the rate of work done on the fluid per unit volume by viscous force. By using the definitions of $\tau_{r\theta}$ and τ_{rz} (see Appendix D) as well as the boundary conditions on the axis, the above expression simplifies to

$$\left.\frac{DE}{Dt}\right|_{r=0} = \mu \left.\left(\frac{\partial^2 u_z}{\partial r^2}\, u_z \right)\right|_{r=0} \tag{4.24}$$

Eq. (4.24) and the results listed in Table 3.2 yield

$$\left.\frac{DE}{Dt}\right|_{r=0} = -\left(\frac{-2N}{N+2} \right) \frac{\rho u_c^3}{z}\, a\left(\frac{a^2}{2} - c \right) \tag{4.25}$$

where u_c is defined by Eq. (3.37). For $N = -1$, Eq. (4.25) reduces to an earlier result reported by Long [1961] :

$$\left.\frac{DE}{Dt}\right|_{r=0} = -2\,\frac{\rho K^6}{\nu^3 z^4}\, a\left(\frac{a^2}{2} - c \right) .$$

Eqs. (4.22) and (4.25) can be combined with the conclusion that on the axis

$$\left.\frac{DE}{Dt}\right|_{r=0} = -\left(\frac{-2N}{N+2}\right)\frac{u_c}{z}\,aE(0,z)\ . \tag{4.26}$$

Figure 4.3 illustrates the relationship between the direction of flow on the axis ($a < 0$, backward; $a > 0$, forward), the mechanical energy of the fluid on the axis, and the rate of change of mechanical energy due to convection. Thus, the four types of structures shown in Figure 4.2 can also be classified by using energy considerations.

Figure 4.3 shows that for Type I and Type III vortices the fluid on the axis moves faster than the surrounding fluid. In this case, energy is transfered to the slower moving fluid by viscous work. On the other hand, Type II and Type IV vortices have the feature that the fluid on the axis moves slower than the sourrounding fluid so, in this case, energy is transfered to the axis by viscous work. Transition between the various flow regimes is characterized by

$$\left.\frac{DE}{Dt}\right|_{r=0} = 0\ . \tag{4.26}$$

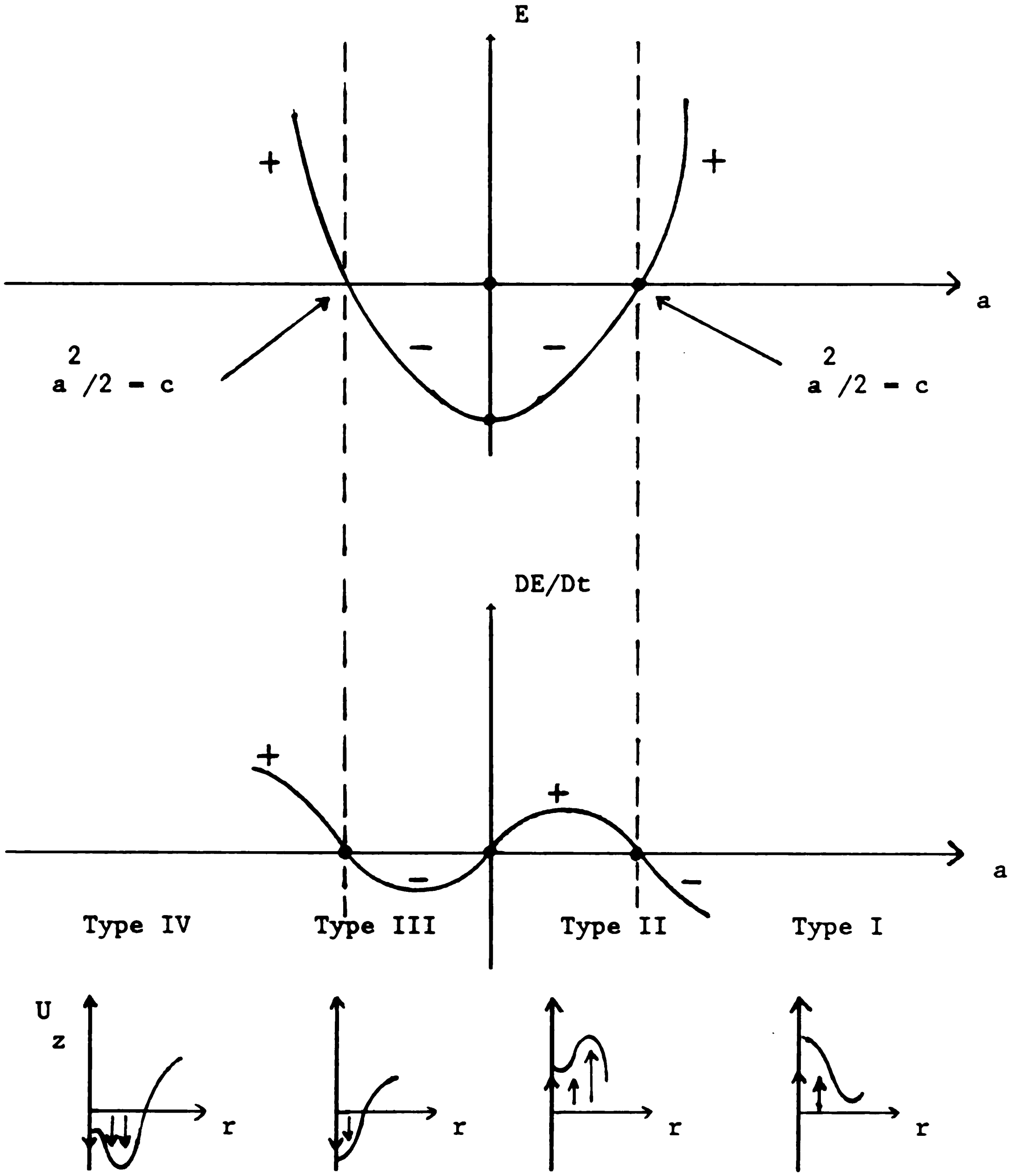

Figure 4.3 Classification of vortex flows based on the mechanical energy balance

CHAPTER 5

SOLUTION METHODOLOGY

5.1 Transformation To A System Of First Order Equations

Eqs. (3.39) - (3.42) can be rewritten as a system of first order ordinary differential equations by introducing the following dependent variables : $Y_1 = M$; $Y_2 = h$; $Y_3 = G$; $Y_4 = G'$; $Y_5 = F$; and, $Y_6 = F'$. The resulting equations are listed in Table 5.1 along with the power series representations of $Y_i(\eta)$ for small values of η (Eqs. (5.1) - (5.12)).

The equations can be expressed more concisely using vector notations:

$$\underline{Y}' = \underline{f}(\underline{Y},\eta). \tag{5.13}$$

Solutions to Eq. (5.13) depend on the three parameters a, b, and c discussed in Chapter 4. These coefficients determine the trajectory of $\underline{Y}(\eta)$ near $\eta = 0$ inasmuch as

$$\underline{Y}(0) = c\underline{e}_1 + a\underline{e}_3 \text{ , and} \tag{5.14a}$$

$$\lim_{\eta \to 0} \frac{d\underline{Y}}{d\eta} = \frac{N}{N+2}\left(\frac{a^2}{2} - c\right)\underline{e}_4 + b\underline{e}_6 \tag{5.14b}$$

$\underline{e}_i$ denotes the ith unit base vector in a 6 - dimensional Euclidean space. Eq. (5.14a) follows directly from Eqs. (4.4) - (4.6) and the

Table 5.1 Representation of the vortex motion as a system of first order equations

Similarity variable	New variable	Differential equations	Series expansion about the axis
Pressure, M	Y_1	$Y_1' = -\dfrac{Y_5^2}{\eta^3}$ (5.1)	$Y_1 = c + c_1\eta^2 + c_2\eta^4 + \ldots$ (5.7)
Stream function, h	Y_2	$Y_2' = \eta Y_3$ (5.2)	$Y_2 = a\eta^2 + a_1\eta^4 + \ldots$ (5.8)
Axial velocity, G	Y_3	$Y_3' = Y_4$ (5.3)	$Y_3 = a + 4a_1\eta^2 + \ldots$ (5.9)
G'	Y_4	$Y_4' = -\dfrac{Y_4}{\eta} + \dfrac{2}{N+2} Y_1 - Y_3^2 - \dfrac{1}{N+2}\dfrac{Y_5^2}{\eta^2} - \dfrac{Y_2Y_4}{\eta} + 2\dfrac{N+1}{N+2}(Y_3^2 - Y_1)$ (5.4)	$Y_4 = 8a_1\eta + \ldots$ (5.10)
Angular momentum, F	Y_5	$Y_5' = Y_6$ (5.5)	$Y_5 = \dfrac{b}{2}\eta^2 + b_1\eta^4 + \ldots$ (5.11)
F'	Y_6	$Y_6' = \dfrac{Y_6}{\eta} - \dfrac{Y_2Y_6}{\eta} + \dfrac{N+1}{N+2} Y_3Y_5$ (5.6)	$Y_6 = b\eta + 4b_1\eta^3 + \ldots$ (5.12)

definition of $G(\eta)$ (see Eq. (3.34)). The parameter 'a' and 'c' must be calculated as part of the solution; however, 'b' can be specified and, as indicated by Eq. (5.14b), determines the initial trajectory of $Y_6(\eta)$.

The asymptotic behavior of $\underline{Y}(\eta)$ for large values of η follows directly from the analysis developed in Section 3.3 and the definition of $\underline{Y}(\eta)$. These specific results are listed in Table 5.2 and apply to the vortex on an unbounded domain (Model I). The bounded vortex, defined by Table 3.2, satisfies the conditions at η^* shown in Table 5.2 (Model II). The set of first order equations were used to calculate the components of $\underline{Y}(\eta)$ and the integral properties for each model over their respective domains once 'a', 'c', and η_a (η^* for Model II) were found (see Section 5.2). Eq. (5.13) was integrated numerically using the computer program listed in Appendix B.

For Model I, the stream function far from the axis is given by

$$h \rightarrow h_a = \frac{\eta}{\sqrt{2}} + 1, \quad \eta_a \leq \eta \leq \infty.$$

The numerical solution approaches this theoretical result, but eventually runs "parallel" to it depending on the precision in determining the parameters 'a' and 'c'. This offset error, which occurs for $\eta \geq \eta_a$, is more apparent with h than the other similarity variables. This can be understood from a perturbation analysis.

If $\underline{Y}_d$ represents a small perturbation from the asymptotic solution, then

Table 5.2 Boundary conditions on the vortex models

Variable	Condition at $\eta = 0$	Model I $\eta_a \le \eta \le \infty$	Model II $\eta = \eta^*$
$Y_1 = M$	c	$\frac{1}{2\eta^2}$	---
$Y_2 = h$	0	$\frac{\eta}{\sqrt{2}} + 1$	---
$Y_3 = G$	a	$\frac{1}{\sqrt{2}\,\eta}$	0
$Y_4 = G'$	0	$-\frac{1}{\sqrt{2}\,\eta^2}$	---
$Y_5 = F$	0	1	$(\eta^*)^{N+1}$
$Y_6 = F'$	0	0	$(N+1)(\eta^*)^N$

$$\underline{Y} = \underline{Y}_a + \underline{Y}_d. \tag{5.15}$$

Inserting this decomposition into Eq. (5.13) and neglecting nonlinear terms yields a linear equation for $\underline{Y}_d$:

$$\frac{d\underline{Y}_d}{d\eta} = \left(\frac{\partial \underline{f}}{\partial \underline{Y}} \right)_{\underline{Y}=\underline{Y}_a} \cdot \underline{Y}_d \tag{5.16}$$

The six first - order, linear differential equations represented by Eq. (5.16) are

$$\frac{dY_{1d}}{d\eta} = - \frac{2}{\eta^3} Y_{5d} \tag{5.17a}$$

$$\frac{dY_{2d}}{d\eta} = \eta Y_{3d} \tag{5.17b}$$

$$\frac{dY_{3d}}{d\eta} = Y_{4d} \tag{5.17c}$$

$$\frac{dY_{4d}}{d\eta} = - \left(\frac{1}{\sqrt{2}} + \frac{2}{\eta}\right) Y_{4d} - \frac{\sqrt{2}}{\eta} Y_{3d} + \frac{1}{\sqrt{2}\,\eta^3} Y_{2d} + 2Y_{1d} - \frac{2}{\eta^2} Y_{5d} \tag{5.17d}$$

$$\frac{dY_{5d}}{d\eta} = Y_{6d} \tag{5.17e}$$

$$\frac{dY_{6d}}{d\eta} = - \frac{1}{\sqrt{2}} Y_{6d} \tag{5.17f}$$

The above six equations are not fully coupled. For instance, it follows directly from Eq. (5.17f) that

$$Y_{6d} \propto e^{-\eta/\sqrt{2}} \quad ,$$

so Y_6 approaches its asymptotic behavior exponentially. This is also the case for Y_{5d} and Y_{1d}. However, Eqs. (5.17b) - (5.17d) have a different behavior. Because Y_{1d} and Y_{5d} decay exponentially, the general solution for Y_{2d} - Y_{4d} can be expressed as

$$Y_{2d} \propto \eta^{q},$$

$$Y_{3d} \propto q\eta^{q-2}, \text{ and}$$

$$Y_{4d} \propto q(q-2)\eta^{q-3}.$$

Substituing Y_{2d} - Y_{4d} into Eq. (5.17d) and neglecting the term which decays exponentially, implies that

$$q = 1.$$

Therefore, the perturbation variables Y_{2d} - Y_{4d} approach their asymptotic behavior algebraically :

$$Y_{2d} \propto \eta$$

$$Y_{3d} \propto \frac{1}{\eta}$$

$$Y_{4d} \propto \frac{1}{\eta^2} \quad .$$

As $\eta \to \infty$, Y_{2d} remains proportional to η. Y_{3d} and Y_{4d}, on the other hand, decay to zero.

Because $Y_{2d} \propto \eta$, the offset error between Y_2 and Y_{2a} for large values of η is determined by the accuracy of the solution defined by

$$E_i < \epsilon, \ i = 3,5,6 \text{ (see Eq. (5.29))}.$$

For instance, if $\epsilon = 0.0001$, numerical calculations show that Y_{2d} is less than $0.005Y_{2a}$; however, if $\epsilon = 0.001$, Y_{2d} is about $0.04\ Y_{2a}$. The difference between these results illustrates that the control of ϵ is very important. In order to have an accuracy of Y_2 within $0.99Y_{2a}$ for $\eta \geq \eta_a$, ϵ must be 0.0001.

5.2 Elements Of The Shooting Method

Although the two vortex models studied have different conditions surrounding their cores, the mathematical structure of each problem and the solution strategy have a common methodology. Both models are represented as a system of differential equations on a finite domian ξ. The actual values of 'a', 'c', and η_a (η^* for Model II) for a given value of 'b' and N were found by rescaling the two - point boundary value problem and using a shooting method. The rescaled problem is

$$\frac{d\underline{z}}{d\xi} = \hat{\underline{f}}(\underline{z}, \xi; N, \tilde{\eta}), \ 0 < \xi \leq 1$$

where

$$\xi = \frac{\eta}{\tilde{\eta}} \ , \qquad \tilde{\eta} = \begin{cases} \eta_a \ , & \text{Model I} \\ \eta^* \ , & \text{Model II} \end{cases}$$

Table 5.3 defines the component equations and boundary conditions. Only three of the six conditions listed under Model I for $\xi = 1$ are independent. The conditions at $\xi = 0$ are the same for both vortex models.

The solution of both vortex models involves a three dimensional search for vectors with components $(a,c,\tilde{\eta})$. The above two - point boundary value problem was solved by using a "shooting" method. Figure 5.1 illustrates the four elements of the algorithm and a brief discussion of each component follows. The Fortran program which implements the algorithm is listed in Appendix B.

A. Initial Guess

The program designed here has been used successfully for a wide range of initial guesses : a^o, c^o, and $\tilde{\eta}^o$. These parameters satisfy $-\infty < a^o < \infty$, $0 < c^o < \infty$, and $0 < \tilde{\eta}^o < \infty$ for $-1 \le N < 0$ and $0 < b < \infty$. If one solution is known, then the next solution for a value of (b,N) near the original one can be found by using the previous solution as an initial guess. In Chapters 3 and 4, the behavior of F for small and large values of η has been discussed. Because F approaches its asymptotic behavior exponentially (see Figure 6.3 and the previous section), it seems reasonable to consider the intersection point of these two curves as an initial guess for $\tilde{\eta}$. In Figure 4.1, this value of $\tilde{\eta}$ equals to $\sqrt{2/b}$. With $\tilde{\eta}^o = \sqrt{2/b}$, an *a priori* relationship between

Table 5.3 Representation of the rescaled vortex models

Rescaled variable	Expansion about $\xi = 0$	Differential equations $0<\xi<1$ $\tilde{\eta} = \eta_a$, Model I; $\tilde{\eta} = \eta^*$, Model II	Boundary conditions at $\xi = 1$ Model I	 Model II
$Z_1 = Y_1$	$Z_1 = c + c_1\tilde{\eta}^2\xi^4 + \ldots$	$\dot{Z}_1 = -\tilde{\eta}^{2N}\dfrac{Z_5^{\,2}}{\xi^3}$ (5.18)	$1/(2\eta_a^{\,2})$	---
$Z_2 = Y_2/\tilde{\eta}^2$	$Z_2 = \frac{a}{2}\xi^2 + a_1\tilde{\eta}^2\xi^4 + \ldots$	$\dot{Z}_2 = \xi Z_3$ (5.19)	$(\eta_a/\sqrt{2}+1)/\eta_a^{\,2}$	---
$Z_3 = Y_3$	$Z_3 = a + 4a_1\tilde{\eta}^2\xi^4 + \ldots$	$\dot{Z}_3 = Z_4$ (5.20)	$1/(\sqrt{2}\eta_a)$	0
$Z_4 = \tilde{\eta}Y_4$	$Z_4 = 8a_1\tilde{\eta}\xi + \ldots$	$\dot{Z}_4 = -\dfrac{Z_4}{\xi} - \tilde{\eta}^2\left[\dfrac{2N}{N+2}Z_1 - \dfrac{N}{N+2}Z_3^{\,2} + \dfrac{\tilde{\eta}^{2N}}{N+2}\dfrac{Z_5^{\,2}}{\xi^2} + \dfrac{Z_2Z_4}{\xi}\right]$ (5.21)	$-1/(\sqrt{2}\eta_a)$	---
$Z_5 = Y_5/(\tilde{\eta})^{N+1}$	$Z_5 = \frac{b}{2}\tilde{\eta}^{1-N}\xi^2 + b_1\tilde{\eta}^{3-N}\xi^4 + \ldots$	$\dot{Z}_5 = Z_6$ (5.22)	1	1
$Z_6 = Y_6/\tilde{\eta}^N$	$Z_6 = b\tilde{\eta}^{1-N}\xi + 4b_1\tilde{\eta}^{3-N}\xi^3 + \ldots$	$\dot{Z}_6 = \dfrac{Z_6}{\xi} + \tilde{\eta}^2\left[\dfrac{N+1}{N+2}Z_5Z_6 - \dfrac{Z_2Z_6}{\xi}\right]$ (5.23)	0	N+1

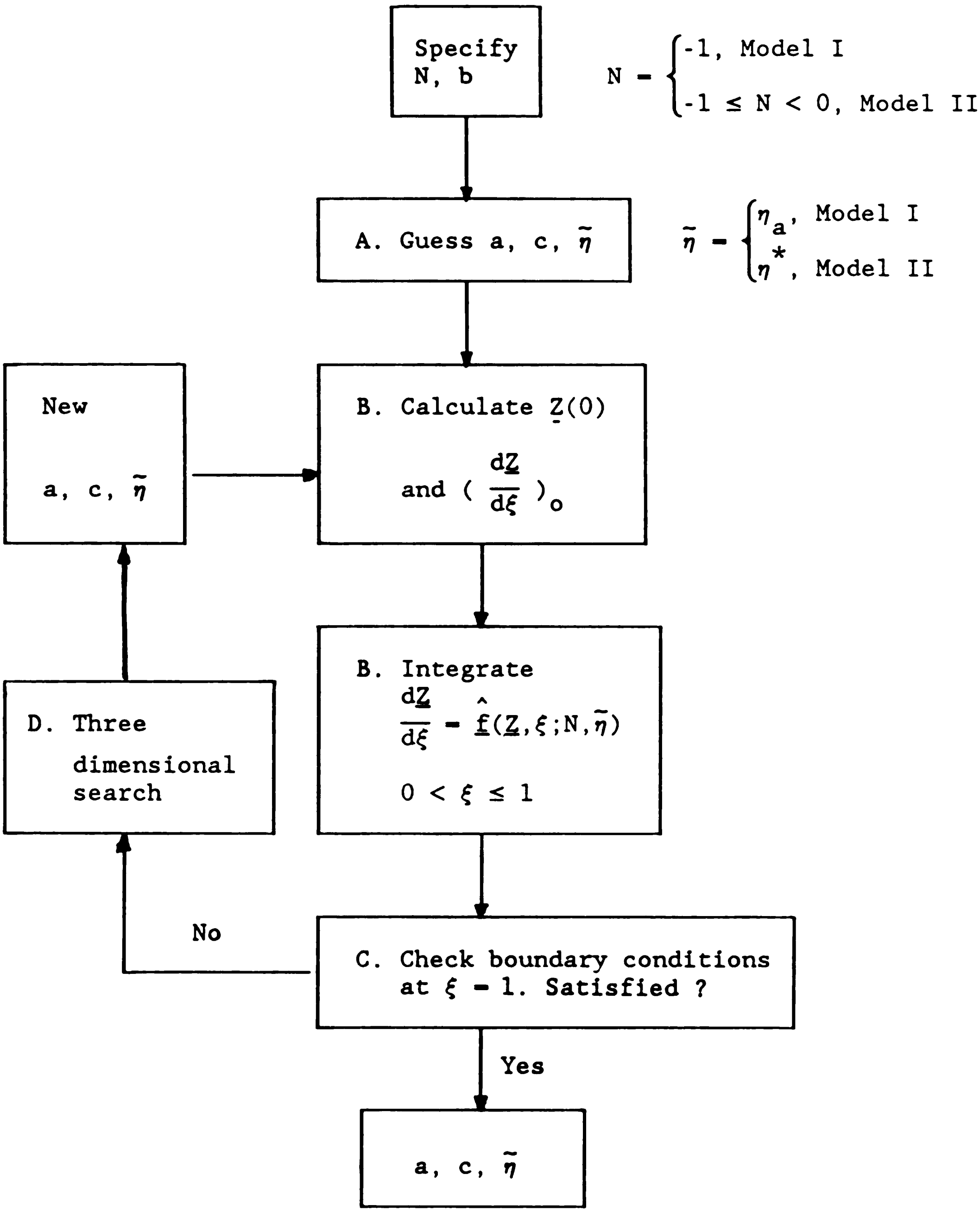

Figure 5.1 Solution strategy based on a shooting method

a^o, b, and c^o for N = -1 follows by assuming $M_o(\sqrt{2/b}) \approx M_a(\sqrt{2/b})$. The result is

$$c^o = b/2 - a^o/16. \tag{5.24}$$

Eq. (5.24) is consistent with the general behavior of (a,b,c) for large values of b. Numerical studies indicate that c is roughly proportional to b. Therefore, with

$$c^o = b/3, \tag{5.25}$$

Eq. (5.24) gives

$$a^o = 8b/3. \tag{5.26}$$

Unfortunately, $\tilde{\eta}^o \approx \sqrt{2/b}$ is not a good initial guess for $\tilde{\eta}$ and is replaced by the empirical result

$$\tilde{\eta}^o = [8\sqrt{2/b}]^{-N} \tag{5.27}$$

Eqs. (5.25) - (5.27) provide good initial guesses for Models I and II at large values of b (say b > 0.10) for any N.

Figure 5.2 illustrates how the initial guess of $(a,c,\tilde{\eta})$ affects the convergence of the algorithm. The initial guess, denoted by point 1 in Figure 5.2, is obtained from Eqs. (5.25) - (5.27). The solid line shows how the algorithm searches for the solution. After six iterations, the value of (a,c,η^*) is very close to the solution. It took another 6 iterations to satisfy the criteria ($\epsilon \leq 0.0001$) and reach the solution (point 12). The initial points denoted by (*) will not converge to the solution. These points give a rough idea of the size of the domain of convergence for $b = 0.3$. Although the projected values of points 4 and 5 on Figure 5.2 appear close to a nonconvergent point, the corresponding value of c for the two points, as indicated, are different.

B. Trajectory for $\underline{Z}(\xi)$

For small values of ξ, the Taylor series expansion defines the solution in the vicinity of $\xi = 0$. The differential equations are integrated numerically from $\xi = 0.001$ to 1 by using the DGEAR subroutine (IMSL,1984). The required input conditions for the algorithm are listed in Appendix B. The DGEAR subroutine solves the set of differential equations by the ADAMS predictor - corrector method. (see Gear, 1971; Lapidus, 1971). The integration only reguires values of $\underline{Z}(0.001)$ and $\dot{\underline{Z}}(0.001)$ to start. The algirithm continues until the end point $\xi = 1$ is reached. DGEAR subroutine is also designed to solve "stiff" differential equations. In this purpose, it is more powerful than other algorithm.

The effect of step size $\Delta\xi$ on the behavior of M, F, and h is important. It was found that these three functions do not change much (three significant figures) between using 1000 steps ($\Delta\xi = 0.001$) and 100 steps ($\Delta\xi = 0.01$) over the domain $0 \leq \xi \leq 1$ for $(a,b,c,\tilde{\eta}) =$

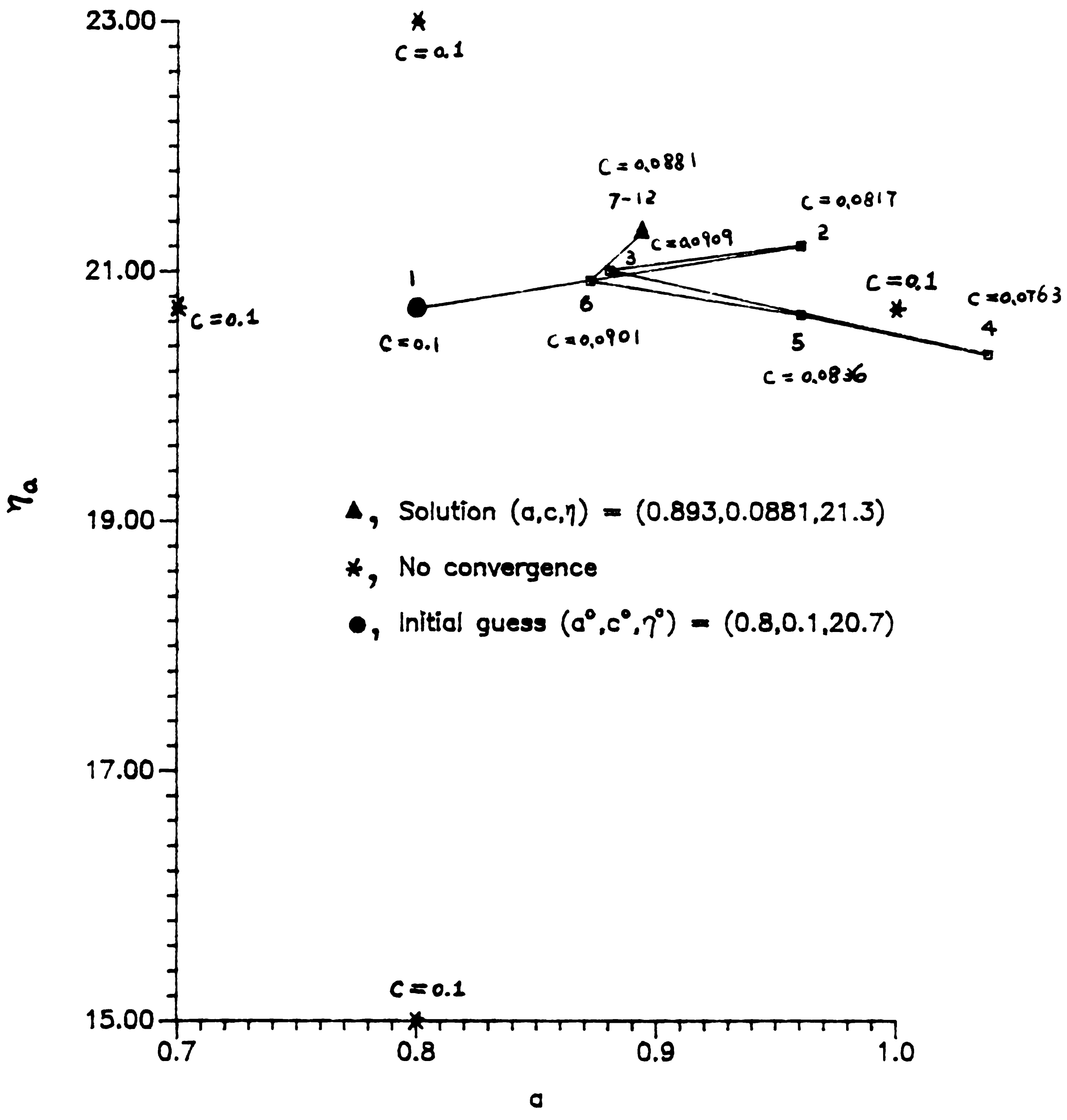

Figure 5.2 Domain of convergence for the three dimensional search with b = 0.3 (Model II, N = −1.0)

(0.893,0.3,0.0881,21.3). $\Delta\xi = 0.001$ gave satisfactory results for all values of the parameters studied.

C. Criteria for Convergence

Let $\underline{Z}^A(\xi)$ represent an approximate numerical solution to the boundary value problem. The accuracy of the solution is determined by how close the boundary conditions at $\xi = 1$ are satisfied. If $\underline{E}$ denotes a three dimensional vector whose components represent the difference between the desired boundary conditions at $\xi = 1$ and the approximate results based on a given value of $(a,c,\tilde{\eta})$, then a solution to the two point boundary value problem occurs when

$$E_i(\underline{x}) < \epsilon \qquad \text{for } i = 1,2,3 \tag{5.28}$$

where ϵ is an accuracy parameter.

The components of $\underline{E}$ are defined by

$$\underline{E} \rightarrow \begin{bmatrix} E_1 \\ E_2 \\ E_3 \end{bmatrix} = \begin{bmatrix} |z_3{}^A(1) - z_3(1)| \\ |z_5{}^A(1) - z_5(1)| \\ |z_6{}^A(1) - z_6(1)| \end{bmatrix} \tag{5.29}$$

$\underline{E}$ depends on a three dimensional vector $\underline{x}$, where

$$\underline{x} \rightarrow \begin{bmatrix} x_1 \\ x_2 \\ x_3 \end{bmatrix} = \begin{bmatrix} a \\ c \\ \tilde{\eta} \end{bmatrix} \tag{5.30}$$

In this research, the three boundary conditions $z_3(1)$, $z_5(1)$, and $z_6(1)$ are used for both Models I and II. The results showed that once these three boundary conditions are satisfied for Model I, the other asymptotic conditions are automatically satisfied.

For Model I, three boundary conditions will uniquely determine all six dependent variables (see Table 5.3). But these three boundary conditions connot be arbitrarily chosen from the six asymptotic functions. Three groups are separated directly by Eqs. (5.18) - (5.23). The first group contains only z_1 and z_5 (Eq. (5.18)). The second group contains z_2, z_3, and z_4 only (Eqs. (5.19) - (5.21)) since z_1 and z_5 in Eq. (5.21) will automatically drop out at $\xi = 1$ and $N = -1$. The last group includes z_6, z_5, z_3, and z_2 (Eqs. (5.22) and (5.23)). Therefore, three different boundary conditions must be chosen from these three groups. One is chosen from either $z_1(1)$ or $z_5(1)$, the other is chosen among $z_2(1)$, $z_3(1)$, and $z_4(1)$, and the last one is $z_6(1)$ since z_6 only appears in the last group. In this research, $z_3(1)$, $z_5(1)$, and $z_6(1)$ are chosen for Model I in correspondence with Model II. For Model I, z_5 and z_6 become asymptotic much sooner (i.e., small values of η) than z_3.

Figure 5.3 illustrates how the accuracy parameter, ϵ, affects the solution, (a,c,η^*), for Model II. For large values of ϵ ($\epsilon \approx 0.1$ - 0.002), (a,c,η^*) changes significantly. When ϵ is small enough ($\leq$ 0.001), the values of (a,c,η^*) become stable. In order to have three significant figure accuracy for a, c, and η_a, ϵ must be less than 0.0001.

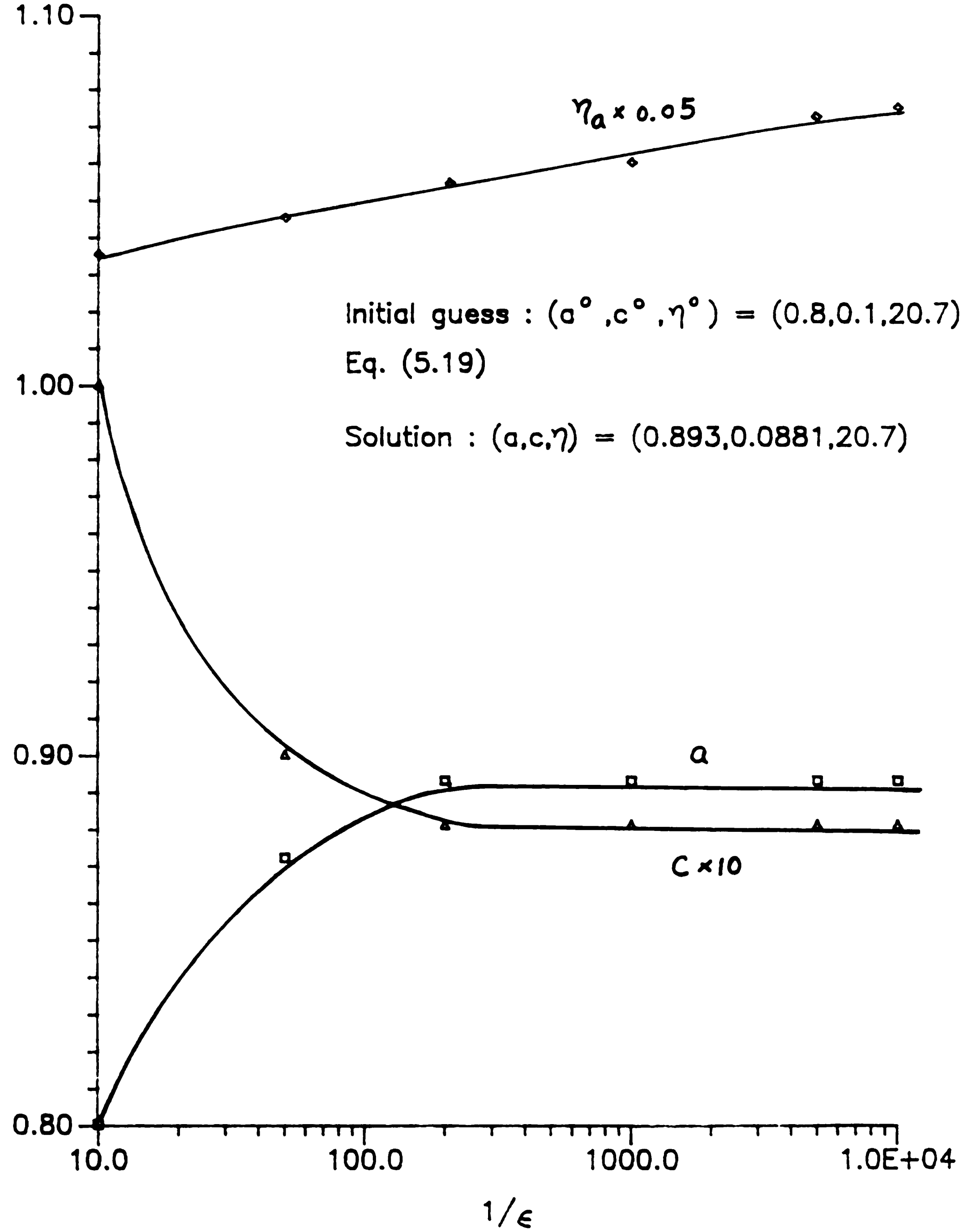

Figure 5.3 The effect of accuracy parameter ϵ on the behavior of the solution for b = 0.3 (Model II, N = −1.0)

D. Method for Updating $(a,c,\tilde{\eta})$

If the criteria in step C are not satisfied, the program will call ZSCNT subroutine in IMSL (see IMSL, 1984). This subroutine uses a secant method to solve a system of non-linear equations (Phillip, 1959), $\underline{E}(\underline{x}) = \underline{0}$. When an initial guess is specified, the ZSCNT subroutine uses a point nearby to search for a better solution. Figure 5.4 shows how the next solution "vector" is obtained for a one dimensional problem. If the initial guess of x^{k-1} is given, the subroutine calculates $E(x^{k-1})$ and uses an arbitrary point nearby x^k to find $E(x^k)$. A new guess for x (i.e., x^{k+1}) is determined from (see Figure 5.4)

$$x^{k+1} = \frac{x^k E(x^{k-1}) - x^{k-1} E(x^k)}{E(x^{k-1}) - E(x^k)}$$

The process is repeated until $E(x^n) < \epsilon$. For a system of non-linear algebraic equations, the algorithm is similar but more complex (see Phillip, 1959). The search for $(a,c,\tilde{\eta})$ continues until the desired accuracy (see Eq. (5.28)) is obtained.

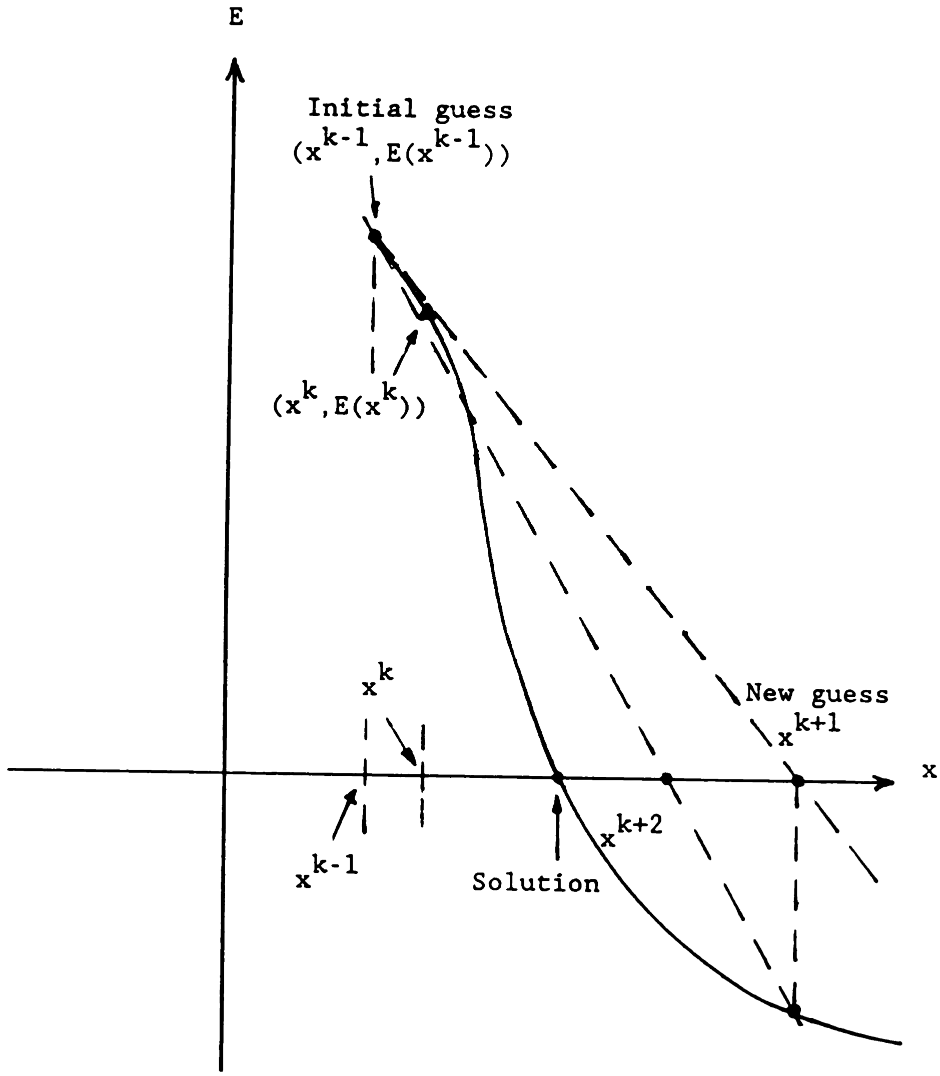

Figure 5.4 ZSCNT search for a one dimensional problem

CHAPTER 6

MODEL I : VORTEX FLOW WITH CONSTANT CIRCULATION

In Chapter 4, qualitative criteria were developed for different flow behavior near the axis. In this chapter, quantitative results for swirling flows governed by Model I (see Section 3.1) are developed. The major goal is to investigate the general behavior of the velocity and pressure fields. A comparison with Long's vortex is presented in Section 6.3. The behavior of macroscopic properties and their significance on the flow behavior will also be discussed (Section 6.4). Finally, an interpretation of the various flow structures is presented in Section 6.5 using the mechanical energy balance and the axial force balance on the axis.

6.1 General Behavior Of The Solution

Figure 6.1 shows the relationship between b and the parameters a, c, and η_a. When b increases, a and c increase but η_a decreases. A smaller viscous core (i.e., small η_a) occurs at larger values of b. Therefore, when the rotation around the axis increases, the core size decreases and the vortex becomes more concentrated.

Three flow regimes have been identified quantitatively, depending on the value of b. The transition values of b between flow reversal and undulated and between undulated and jet-like behavior are 0.042 and 0.136, respectively. The flow structure is determined uniquely by K, ν,

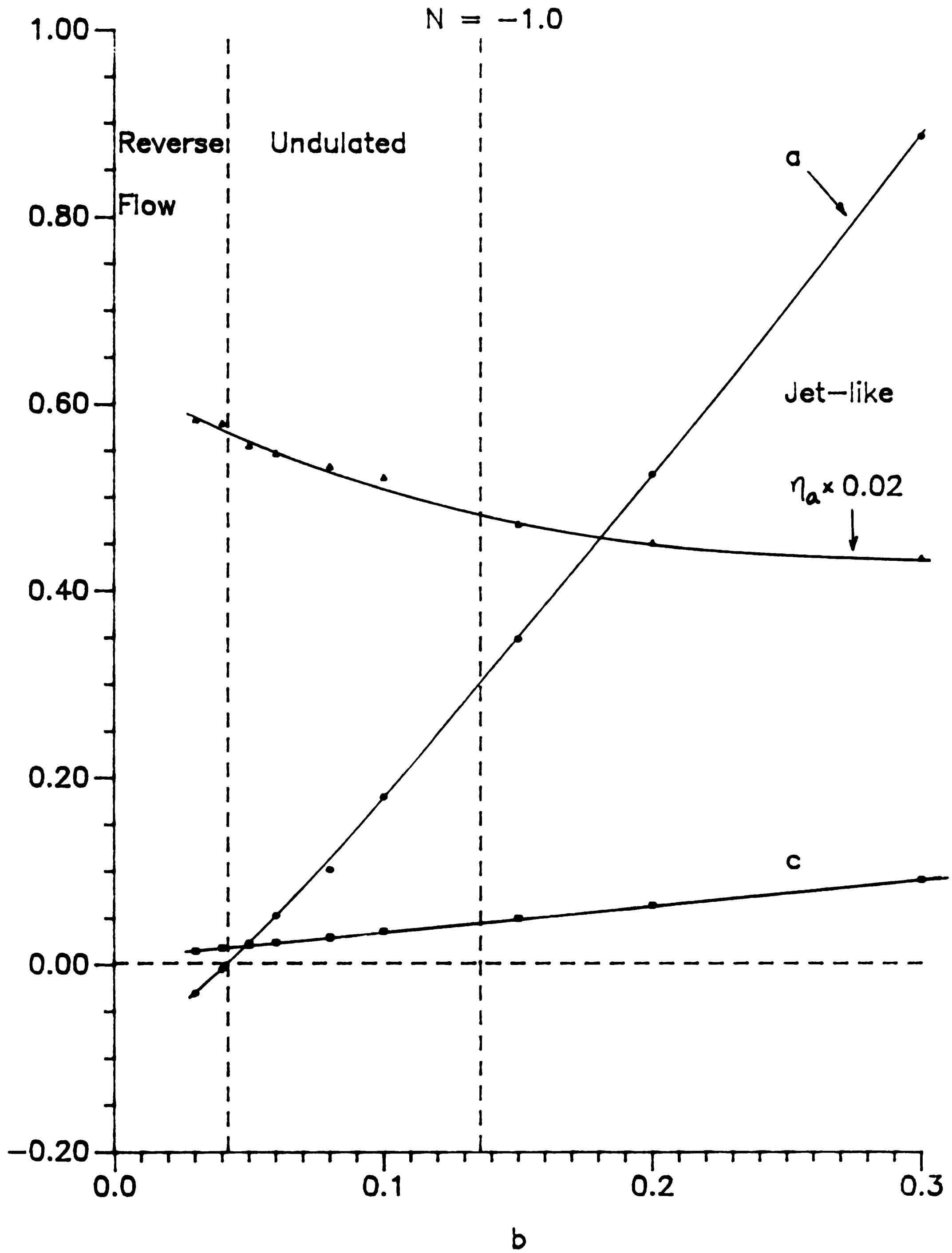

Figure 6.1 The behaviour of the solution for Model I

N and one of the four parameters (a,b,c,η_a) (see Table A.1 in Appendix A). The general behavior of the three dependent variables M, F, and h are plotted on Figures 6.2 - 6.4. The derivatives of M, F, and h at the axis are zero and all of these functions follow their asymptotic behavior for large values of η. These two features stem directly from the boundary conditions (see Table 5.2).

The effect of b on M is significant (see Figure 6.2). For constant η, M increases as b increases. Because M_a, which represents the asymptotic values of M for $\eta > \eta_a$, is independent of b, the "pressure" drop across the vortex (i.e., $M(0) - M(\eta_a)$) increases with b. Thus, coherent vortex structures require relatively large radial pressure drops. Note also that $M \approx M_a$ for $\eta \approx 10$, which is significantly smaller than η_a. This result was anticipated by the analysis of Section 3.3.

Figure 6.3 shows that F obtains its asymptotic value for $\eta \approx 15$, provided $b \geq 0.03$. For large values of b, $F \approx F_a$ for $\eta \ll \eta_a$ also. Thus, if M and F alone were used to control the numerical search (see Section 5.2), then a significant error in η_a would occur (see Section 6.3).

For the same value of η within the core region, larger values of b yield larger values of F. In other words, the circulation for fixed η increases as the rotation around the axis increases (strong vortex) :

$$\Gamma = \oint \underline{u} \cdot \underline{e}_\theta r d\theta = 2\pi K F(\eta;b)$$

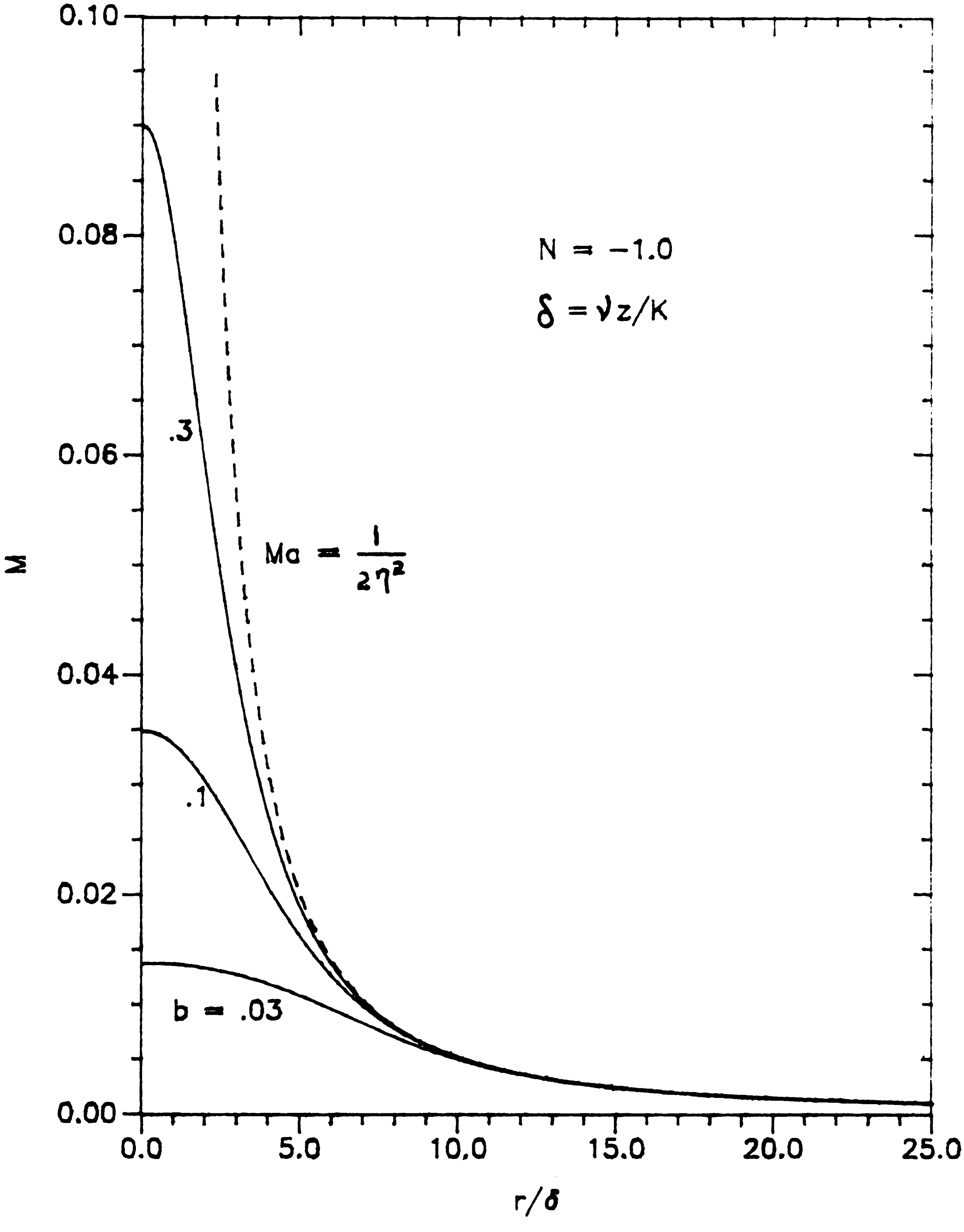

Figure 6.2 The effect of b on the behaviour of M for Model I

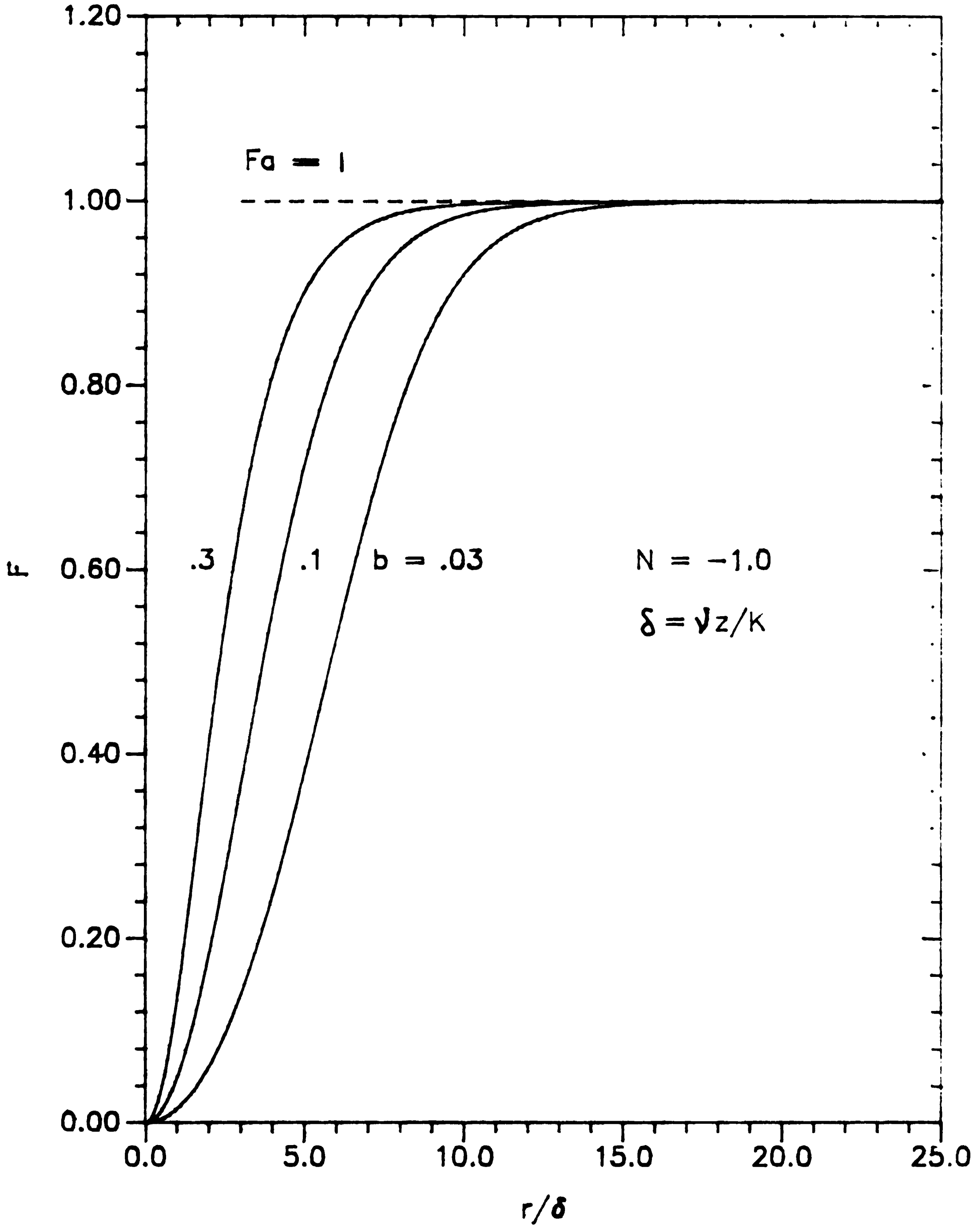

Figure 6.3 The effect of b on the behaviour of F for Model I

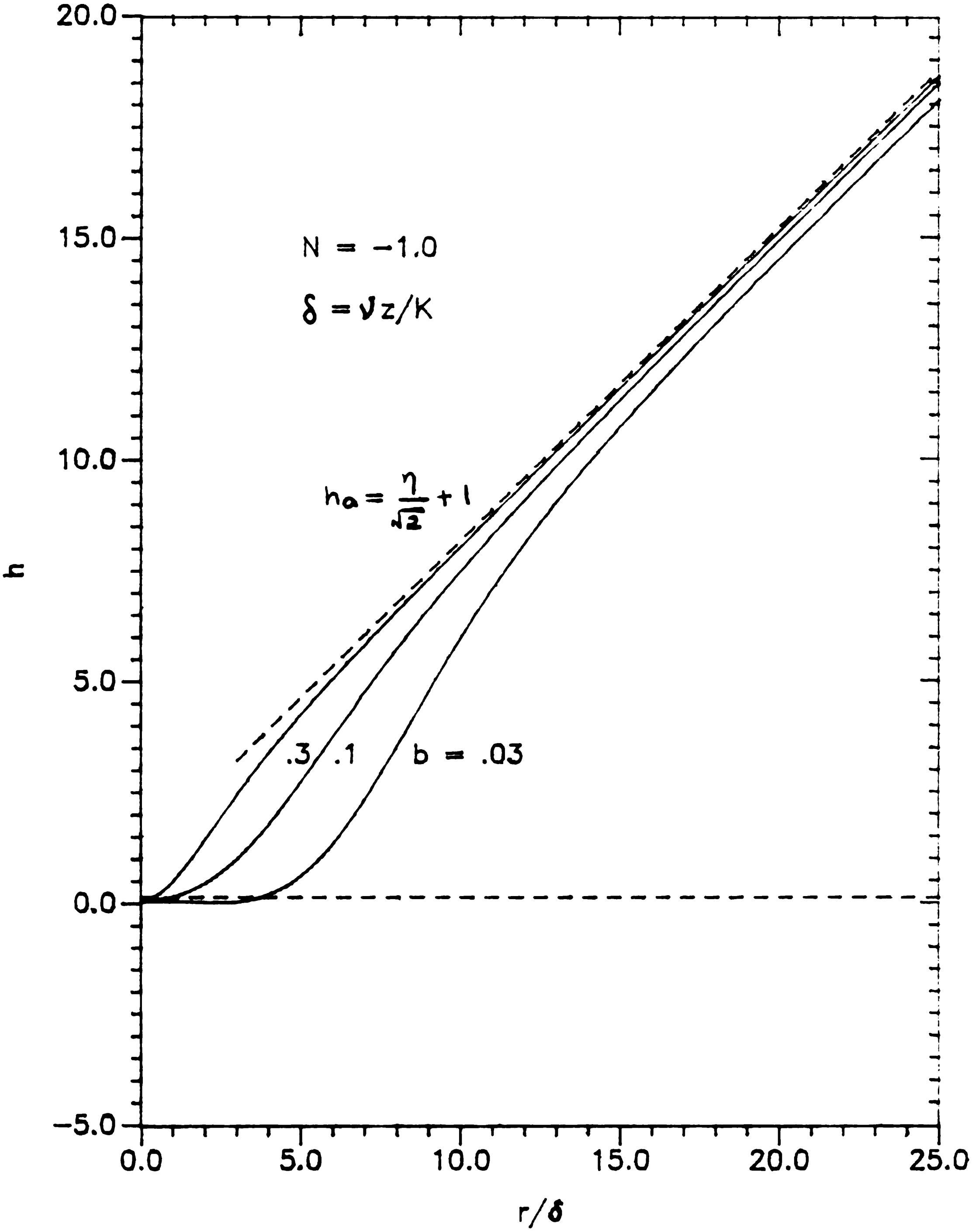

Figure 6.4 The effect of b on the behaviour of h for Model I

The behavior of the dimensionless stream function h, which relates directly to the axial and radial components of the velocity, deserves special attention. Figure 6.4 shows that for reverse flow (b = 0.03), h is negative for small values of η. This was expected based on the analysis of Section 4.1 (see Figure 4.1). For b = 0.03, note that h = 0 when $\eta \approx 4$. Because $h(\eta)$ also represents the local entrainment rate (see Table 3.2), h(4) = 0 means that the local volumetric flow rate across a surface of fixed z and $0 \le r \le 4\delta(z)$ is zero. This also implies that $u_z(r,z)$ must be zero for some values of r between 0 and $4\delta(z)$, if b = 0.03.

For the other two values of b (b = 0.1, 0.3), h is always positive. For very large values of b (see Figure 6.8), h can overshoot h_a for $\eta < \eta_a$. For $\eta > \eta_a$, h parallels h_a with a very small, and controllable offset. As discussed in Chapter 5, the offset always exists because the allowable error in the numerical search for a, c, and η_a is always larger than zero (see Eq. (5.28)). This constant offset error does not affect the velocity components (see Section 5.2).

Another result is that h increases as b increases for fixed η. Thus, a "strong" (i.e., large b) vortex has a larger local volumetric flow rate (fixed η) than a relatively "weak" vortex. However, because a "weak" vortex has a larger value of η_a (see Figure 6.1), the global or macroscopic flow rate through a "weak" (i.e., small b) vortex is large compared to the flow rate through a "strong" vortex.

6.2 Behavior Of Velocity Field

The tangential velocity profiles for different values of b, shown in Figure 6.5, have a Rankine-type structure with a forced vortex behavior near the axis and a free vortex behavior in the outer region of the core. For $\eta > \eta_a$, $u_\theta = K/r$. For large values of b, the region of solid body rotation (i.e., forced vortex) shrinks. The peak tangential velocity shifts to smaller values of η and becomes larger as b increases. If the size of a vortex is defined as the radial position where u_θ is a maximum (see, esp., Donaldson and Sullivan, 1960), then as b increases from 0.03 to 0.3, the size of the vortex decreases by a factor of 2.5, whereas η_a only decreases by a factor of 1.4 over this range of b. An interesting observation in Figure 6.5 for b = 0.03 is that the zero <u>local</u> entrainment rate (h(4) = 0 in Figure 6.4) occurs within the forced vortex region (see Figure 6.5).

Figure 6.6 shows three different axial flow profiles for different values of b. This result is consistent with many experimental observations (Escudier, 1980, 1982; Dabir, 1983). When b increases, the flow changes from a reverse flow on the axis to an undulated flow and, finally, to a jet-like flow. In the flow reversal region, it is observed that $u_z = 0$ at $\eta \approx 2.5$ for b = 0.03. Thus, the fluid moves downward toward the singular point for $\eta < 2.5$ and moves upward for $\eta > 2.5$. This observations also follows directly from Figure 6.4 inasmuch as $h'(2.5) = 0$. Note also that for b = 0.3, the magnitude of u_z near the axis is larger but falls below the axial velocity of the weaker vortices in the outer region. However, all the axial profiles approach $K/(\sqrt{2}\ r)$ for $\eta > \eta_a$. It follows from Figures 6.5 and 6.6 that the local

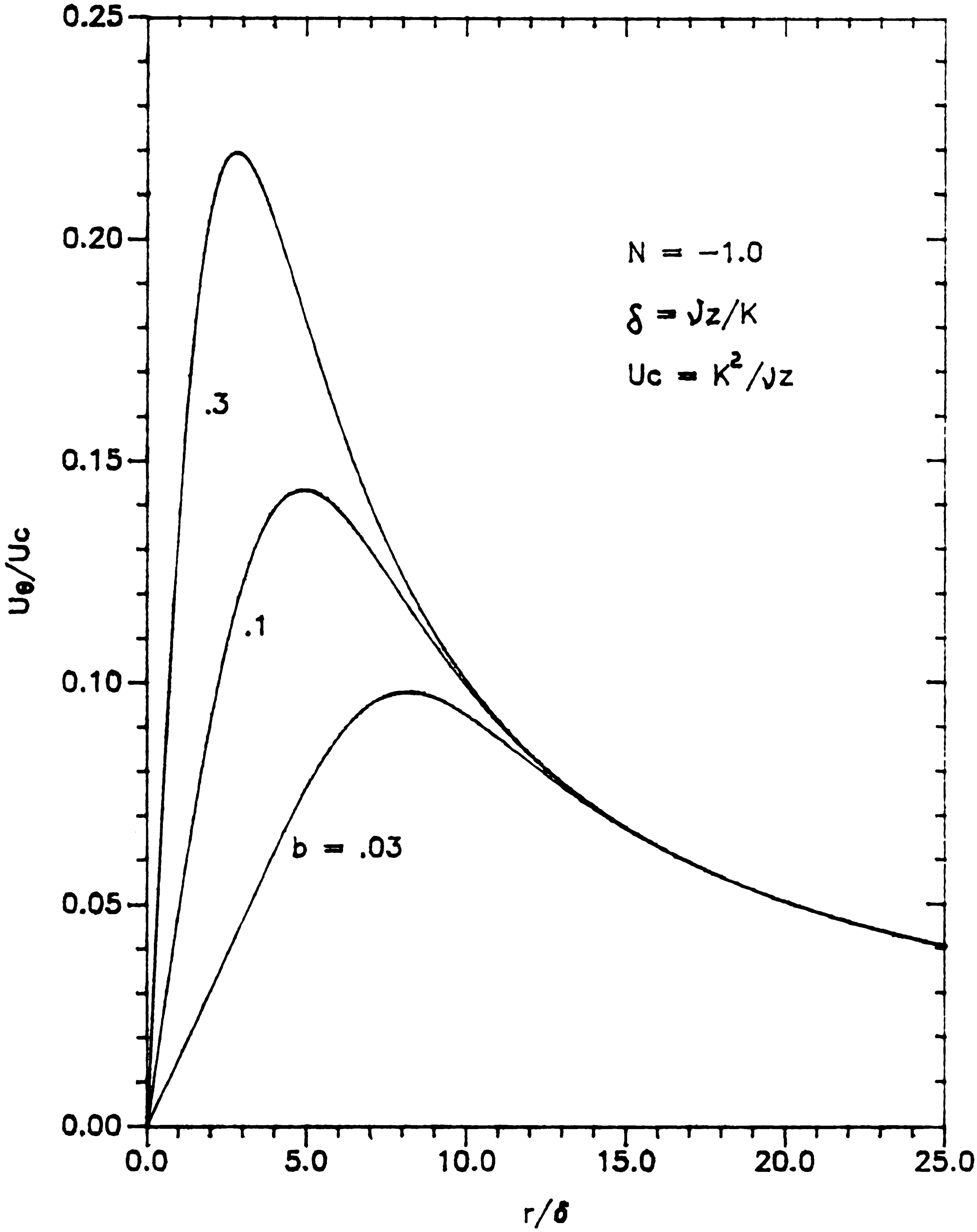

Figure 6.5 The effect of b on the tangential velocity profile for Model I

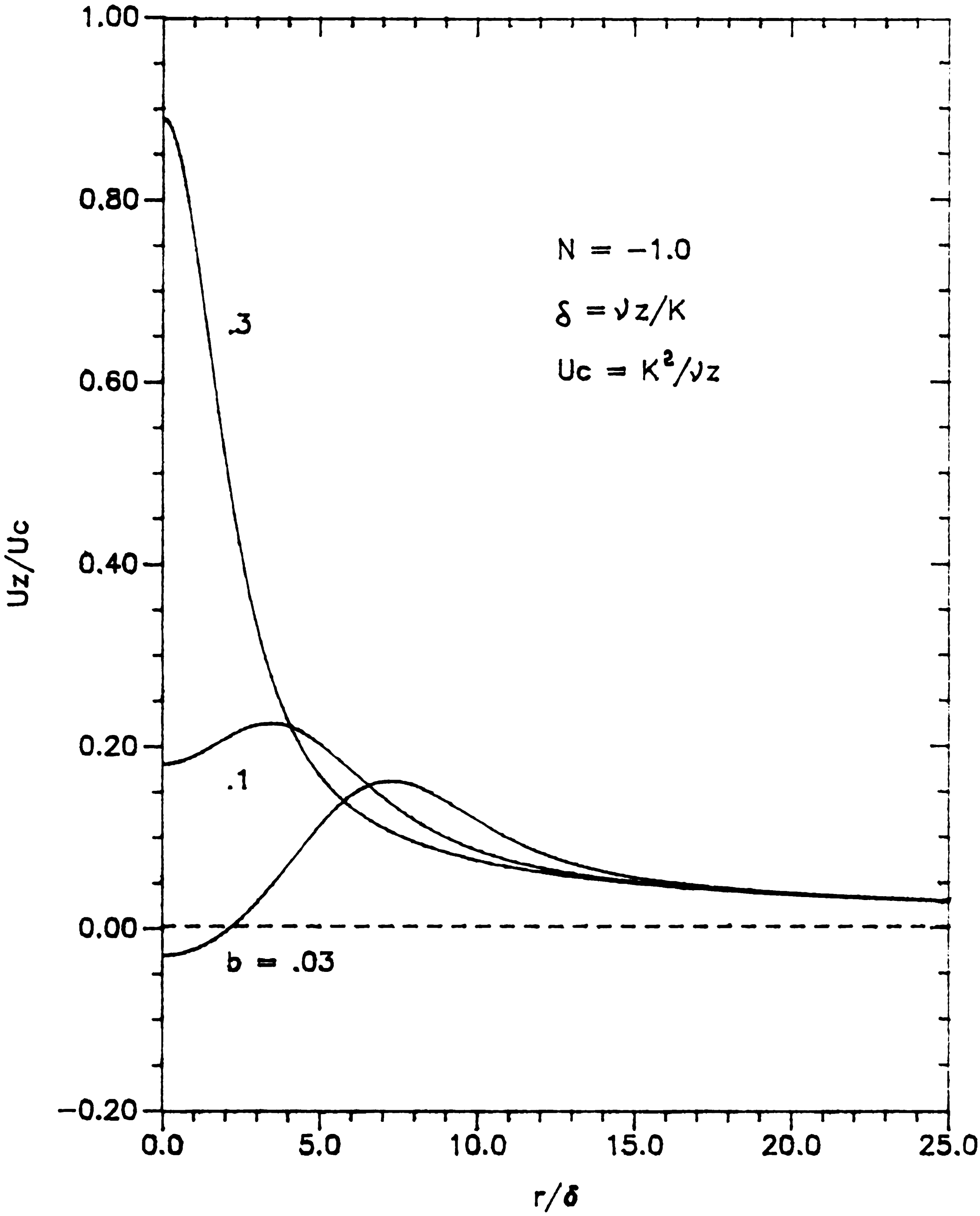

Figure 6.6 The effect of b on the axial velocity profile for Model I

peak of u_z for b = 0.1 and 0.03 occurs at slightly smaller values of η than the peak of u_θ.

The radial velocity profiles in Figure 6.7 exhibit many important features. As predicted in Chapter 4, an outward radial flow ($u_r > 0$) occurs around the axis for forward flow and an inward radial flow ($u_r < 0$) occurs around the axis for reverse flow. For all values of b, a zero radial component of the velocity always exists for a nonzero value of η. As previously discussed in Chapter 2, a surface characterized by $u_r = 0$ is often called a "mantle". Because the flow at infinity must move radially inward toward the core ($u_r = -\nu/r$ for $\eta > \eta_a$), two internal mantles exist in the reverse flow regime due to the inward radial flow near the axis. For the forward flow regime (either undulated or jet-like), however, there is only one mantle. The inner mantle in the reverse flow case appears at very small values of η ($\eta = 2.0$ for b = 0.03), and causes the flow within $\eta < 2.0$ to move downward toward the singular point.

In forward flow, the size of the mantle decreases as b increases, which implies that the stronger rotation around the axis will force the fluid to move into a much smaller core area. This phenomena is very important for the application developed in Chapter 9.

6.3 Comparison With Long's Vortex

As discussed in Chapter 5, the computer algorithm employed in this study used a three dimensional search for a, c, and η_a until the asymptotic conditions were satisfied. This was accomplished by controlling the allowable error on $Z_3(1)$, $Z_5(1)$ and $Z_6(1)$ (see Section

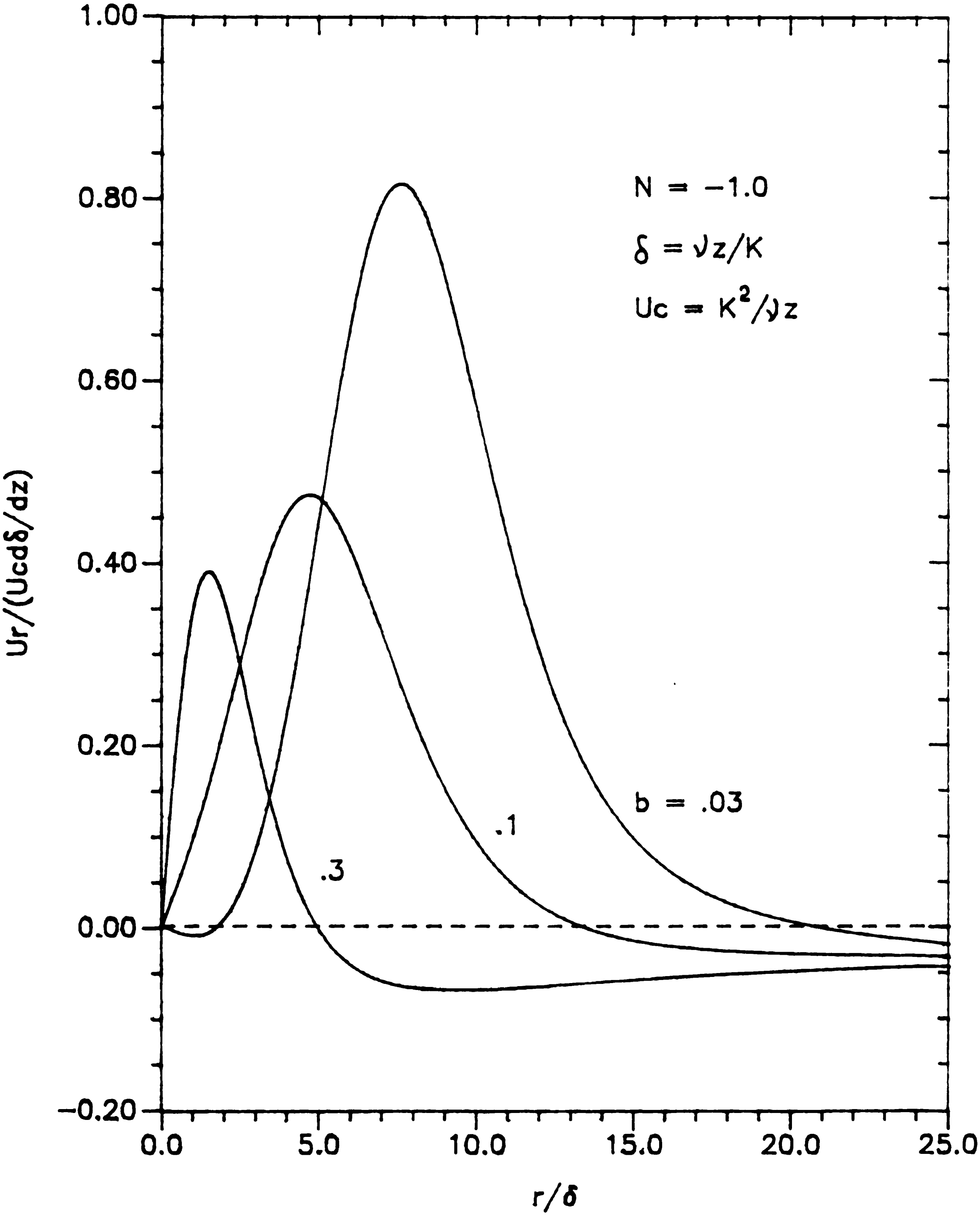

Figure 6.7 The effect of b on the radial velocity profile for Model I

5.2). In contrast, the solution methodology used by Long [1961] determined the values of a and c by only controlling the asymptotic error of Y_1 and Y_5 (equivalently, $Z_1(1)$ and $Z_5(1)$). The value of η_a was determined by the asymptotic behavior of h, but, as illustrated in Figures 6.2 - 6.4, Y_1 and Y_5 (M and F) obtain their asymptotic behavior for smaller values of η than h. Thus, Long's procedure effectively determines η_a inaccurately. Basically, his solution does not satisfy the asymptotic condition on h.

Using the tabular values of a, b, and c found by Long (two decimal accuracy), the differential equation for $\underline{Y}(\eta)$, defined by Table 5.1, was integrated using the computer algorithm listed in Appendix B. For b = 3.82, Figure 6.8 compares the stream functions calculated using Long's solution and the solution developed in this study. The results are the same for small values of η, but differ significantly for large η. Although the difference between (a,c) is small (only 1% difference), the behavior of h at large values of η is much different. Because h is very sensitive to the values of a and c, controlling the numerical error of h_a is very important.

A similar comparison between the radial velocity profiles calculated using Long's parameter and the set developed here is given in Figure 6.9. The radial velocity for large values of η is very sensitive to h. For small values of η ($\eta < 3.0$), both solutions are the same, but differ significantly when η become larger. However, both solutions show the existence of an internal mantle near the axis.

6.4 Macroscopic Properties

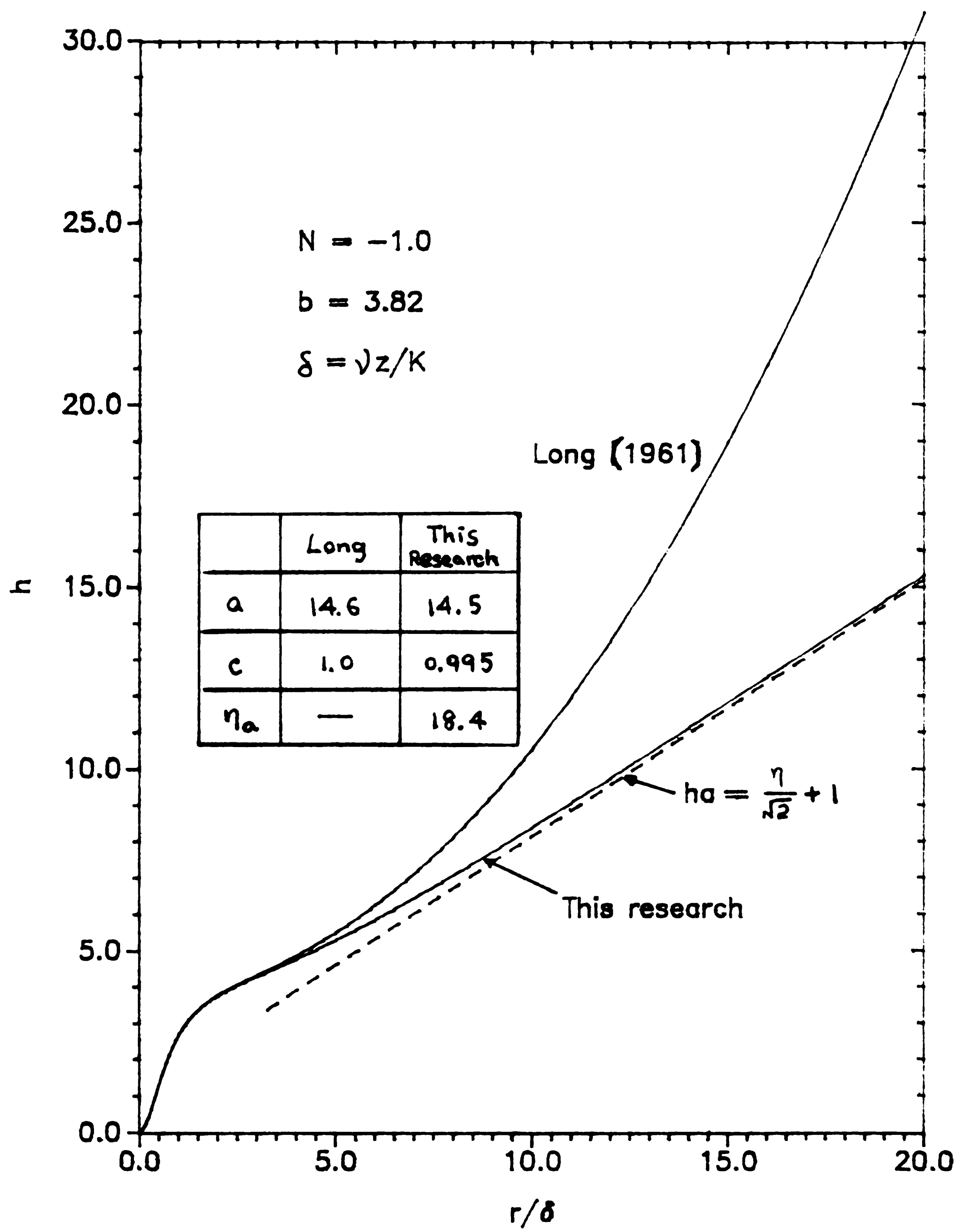

Figure 6.8 Comparison between Model I and Long's vortex for the stream function

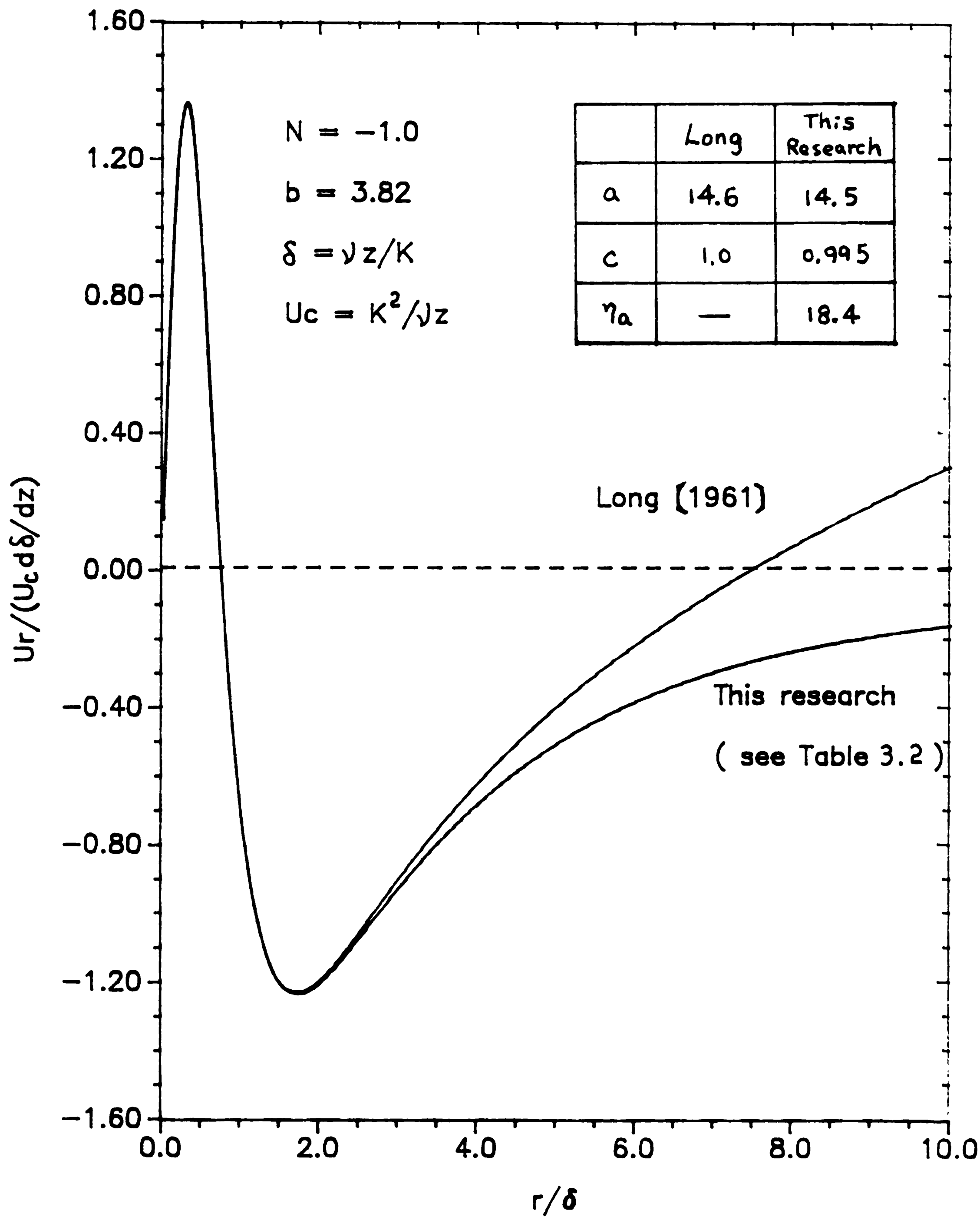

Figure 6.9 Comparison between Model I and Long's vortex for the radial velocity profile

The macroscopic properties discussed in Chapter 3, including axial thrust, axial torque, flow rate, and pressure drop, can also be used to quantify vortex flows. The values for the macroscopic axial thrust computed in this research (see Figure 6.10) agree with the study by Burggraf and Foster [1977] and are a little larger than reported by Long (see Figure 6.10). A minimum value of $\hat{F}_z$ occurs at $b \approx 0.04$; $\hat{F}_z$ increases significantly for very large and small values of b.

The large values of the axial thrust at small and large values of b are due to different mechanisms. For small values of b, the vortex core becomes large and the axial momentum decreases. Thus, the large values of $\hat{F}_z$ mainly come from the area integration (see Eq. (3.16)). On the other hand, for large values of b, the vortex core becomes small and the axial momentum increases significantly (jet-like flow). In this case, the large value of $\hat{F}_z$ stems directly from the large convective transport of axial momentum (see Eq. (3.16)).

The macroscopic axial thrust does not uniquely determine the flow behavior (see Figure 6.10). For $N = -1.0$, reverse flows exist for $b < 0.043$ and jet-like flows exist for $b > 0.136$. Between these two values of b, the axial velocity has an undulated flow behavior. For $\hat{F}_z$ larger than 0.75, either flow reversal or jet-like flow will occur (see Figure 6.10). For $\hat{F}_z$ less than 0.75 but larger than 0.60, either reverse or undulated flow occurs. If $\hat{F}_z$ is between 0.6 and 0.58, only undulated flows exist. Below 0.58, however, no steady state similarity solutions exist.

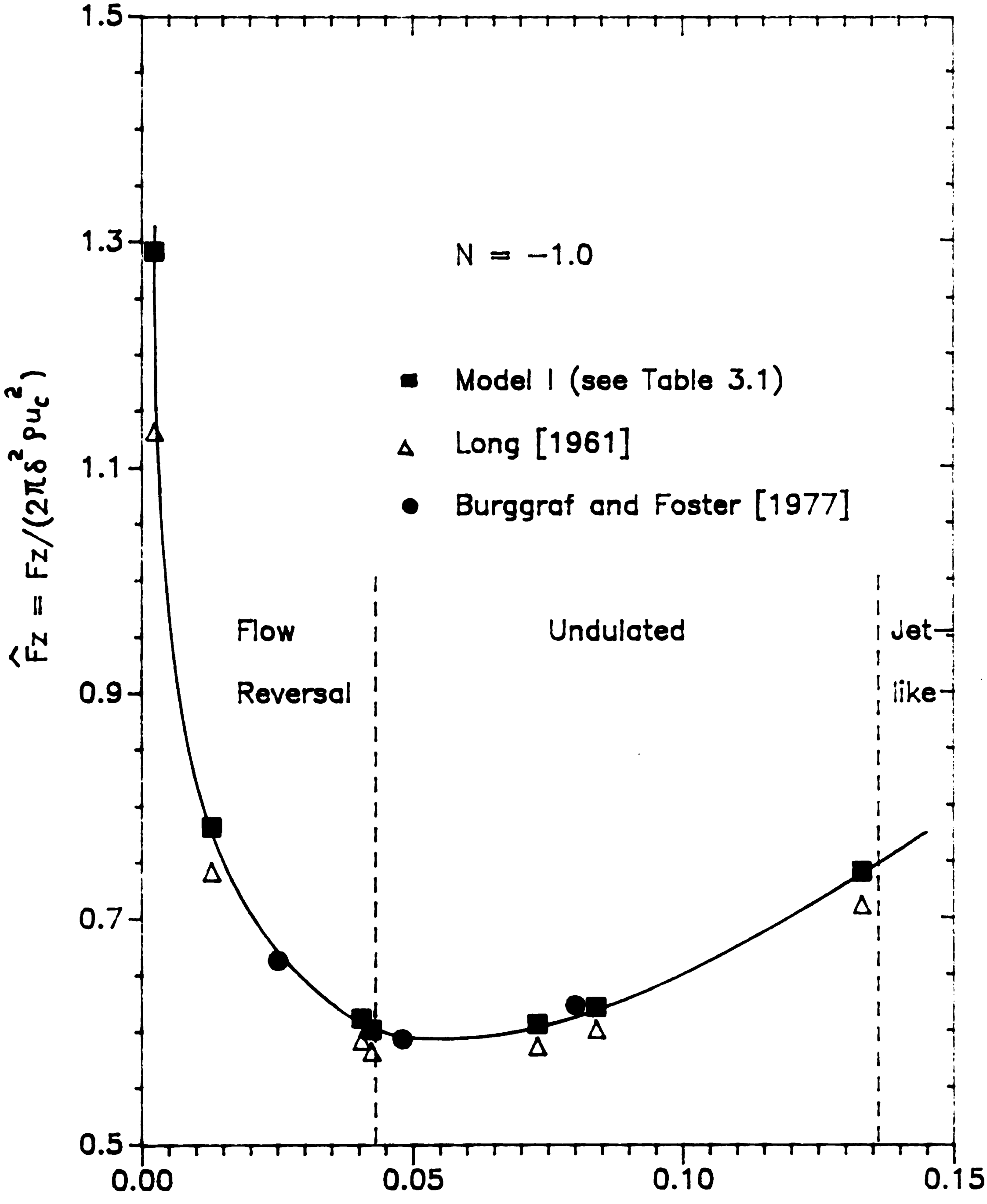

Figure 6.10 The effect of b on the macroscopic axial force for Model I

The macroscopic axial torque and volumetric flow rate decrease monotonically as b increases in the range of $0 < b \leq 0.30$ (see Figures 6.11 and 6.12). For $b = 10.0$, the axial torque is about 10 and the volumetric flow rate (dimensionless) is about 12. Unlike the axial thrust, the large velocity associated with jet-like flows does not make the axial torque or volumetric flow rate unbounded for large values of b. Instead, it appears (numerically) that these two properties may approach a nonzero lower bound. However, for small values of b, the large cross sectional area associated with the flow reversal makes both T_z and Q, like F_z, unbounded (see Figures 6.11 and 6.12).

For the study range of $0 < b \leq 10$, if the axial torque has a value larger than 10, then only one value of b and, therefore, only one type of flow is possible; however, if the axial torque is less than 10, a steady state similarity solution may not exist (see Figure 6.11). Similarly, if the dimensionless macroscopic volumetric flow rate is larger than 12, then this parameter uniquely determines the flow behavior (see Figure 6.12). Transition from flow reversal to undulated flow corresponds to $\hat{T}_z = 19.0$ and $\hat{Q} = 21.0$. Transition between undulated and jet-like behavior occurs for $\hat{T}_z = 15.5$ and $\hat{Q} = 17.5$.

Figure 6.13 shows that the macroscopic pressure drop $\hat{\Delta p}$ uniquely determines the flow structure. Note that $\hat{\Delta p}$ increases monotonically as b increases with an almost constant slope. Moreover, for $\hat{\Delta p}$ less than 0.017, reverse flow exist and for $\hat{\Delta p}$ between 0.017 and 0.045, undulated flow behavior occurs. Finally, for $\hat{\Delta p} > 0.045$, the axial velocity on

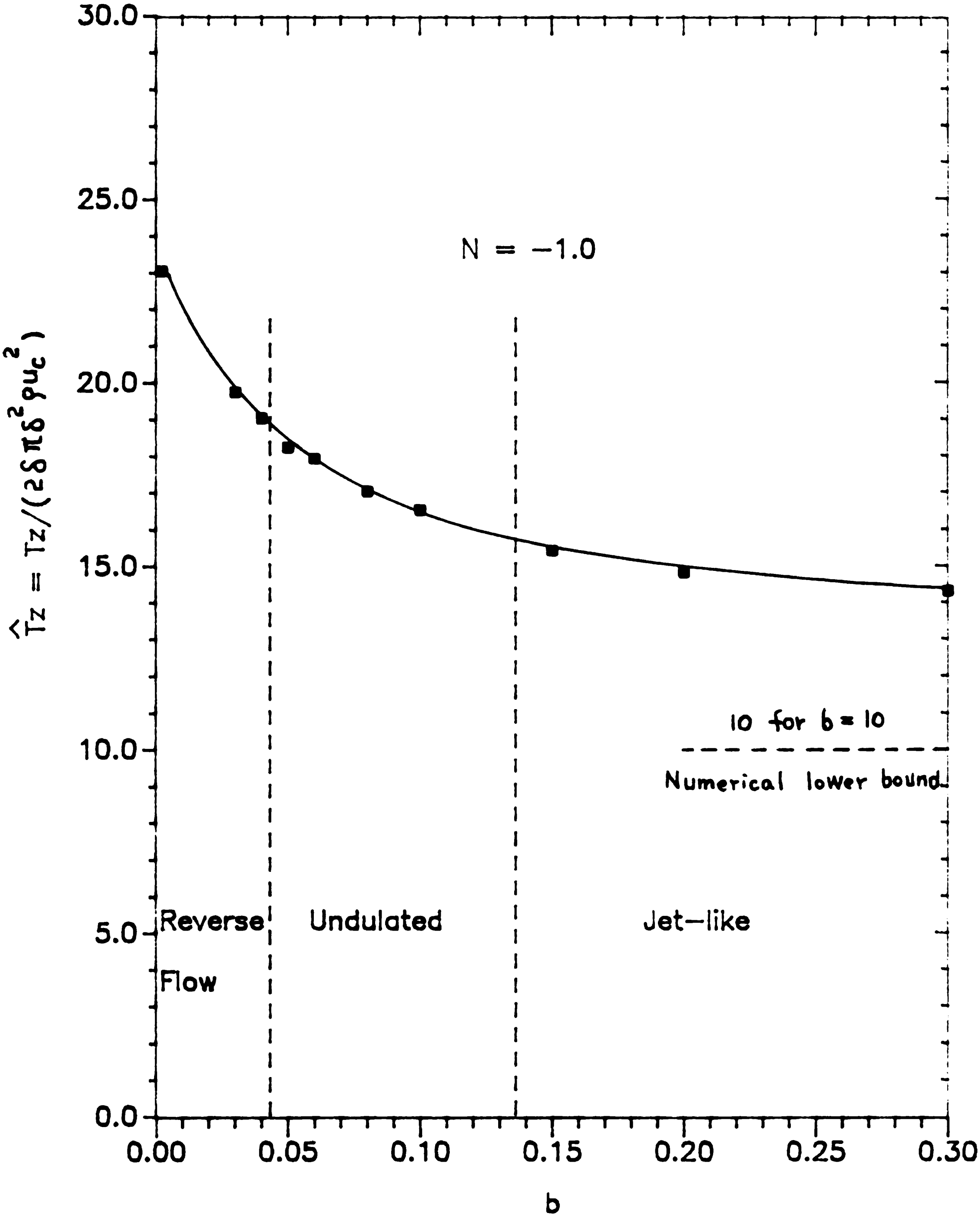

Figure 6.11 The effect of b on the macroscopic axial torque for Model I

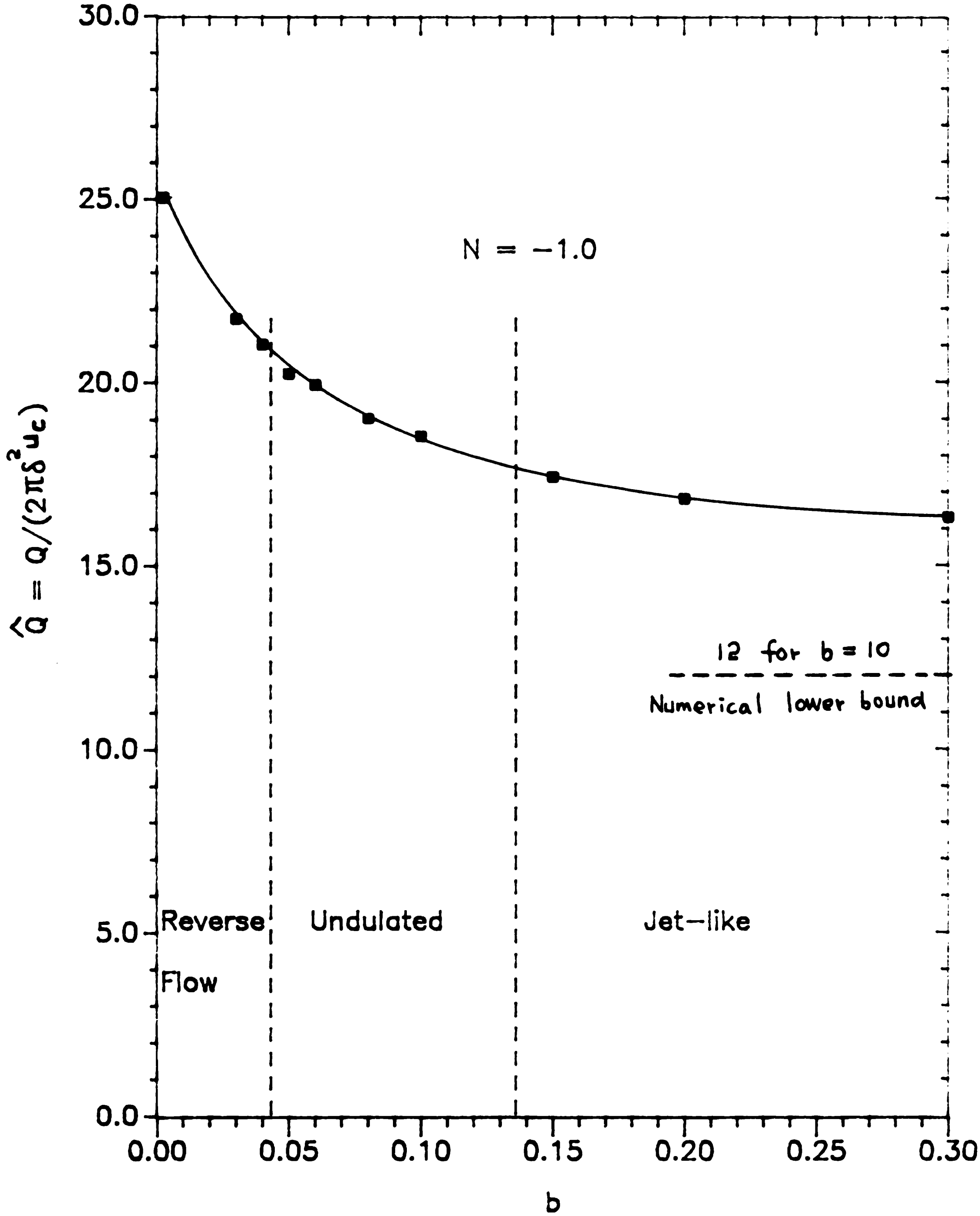

Figure 6.12 The effect of b on the volumetric flow rate for Model I

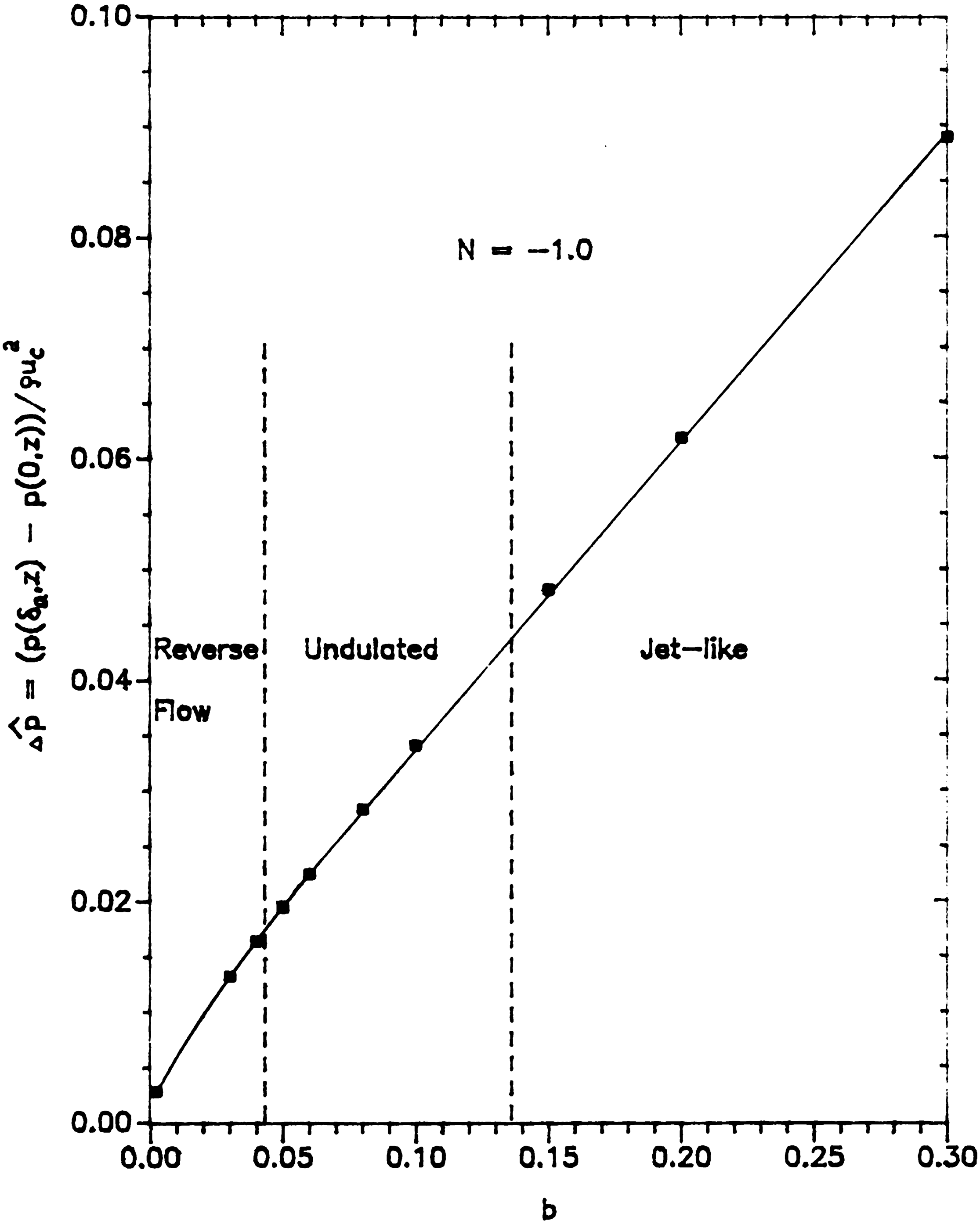

Figure 6.13 The effect of b on the macroscopic pressure drop for Model I

the centerline has a jet-like behavior. Thus, once ν, K, and N (=-1) have been specified, the vortex flow with bounded circulation is uniquely determined by either assigning a numerical value to the local spin parameter 'b' or to the global dimensionless pressure drop $\Delta\hat{p}$ ($0 < \Delta\hat{p} < \infty$). This conclusion was not developed by Long [1961] or by Burggraf and Foster [1977]. They only noted the "unexpected" result that $\hat{F}_z$ did not uniquely determine the flow, as it does for other nonrotating flow problem. Here an explanation for the behavior of $\hat{F}_z$ has been given and more significantly, a macroscopic parameter has been identified which controls the flow behavior.

6.5 Discussion

In Chapter 4, the "excess" mechanical energy of a fluid particle on the axis was examined qualitatively. This property (see Eq. (4.21)) and its substantial time derivative are related to the dimensionless parameters 'a' and 'c' as follows

$$\hat{E} = \frac{E}{\rho u_c^2} = \frac{a^2}{2} - c$$

and

$$\frac{D\hat{E}}{D\hat{t}} = \frac{\delta^2/\nu}{\rho u_c^2}\frac{DE}{Dt} = -2a\hat{E}$$

Figure 4.3 illustrates the relationship between $\hat{E}$ and $D\hat{E}/D\hat{t}$ for four different flow regimes. Although an undulated, reverse flow regime was identified theoretically in Chapter 4 (Type IV pattern, see Figure 4.3), this flow behavior was not observed numerically, for $0.002 \le b \le 10$.

Additional physical understanding of the three flow structures for a vortex with bounded circulation ($N = -1$) results by examining the axial component of the force balance. The force acting on a fluid element situated on the axis includes contributions from inertial, pressure, and viscous effects. Thus, by setting $r = 0$ in Eq. (3.5), it follows that

$$\hat{F}_I + \hat{F}_P + \hat{F}_V = 0$$

where

$$\hat{F}_I = \frac{-[\rho u_z(\partial u_z/\partial z)]\Big|_{r=0}}{\rho u_c^2 \delta(d\delta/dz)} = a^2$$

$$\hat{F}_P = \frac{\left.\dfrac{\partial P}{\partial z}\right|_{r=0}}{\rho u_c^2 \delta(d\delta/dz)} = -2c$$

$$\hat{F}_V = \frac{\left[\dfrac{\mu}{r}\dfrac{\partial}{\partial r}(r\partial u_z/\partial r)\right]\Big|_{r=0}}{\rho u_c^2 \delta(d\delta/dz)} = -a^2 + 2c$$

The dimensionless "excess" mechanical energy, $\hat{E}$, can also be expressed in terms of these dimensionless forces as

$$\hat{E} = \frac{\hat{F}_I + \hat{F}_P}{2} = -\frac{\hat{F}_V}{2}$$

It is noteworthy that $\hat{F}_I$ and $\hat{F}_P$ do not change sign for $0 < b < \infty$ inasmuch as $a^2 \geq 0$ and c is always positive (see Figure 6.1). Thus, a fluid particle on the axis moving in the positive z direction (forward flow) must overcome an adverse pressure gradient ($\hat{F}_P < 0$).

Figure 6.14 shows how the individual terms in the force balance and the energy balance evaluted on the axis change with b. These results show that the three flow structures (jet-like, undulated, flow reversal) have the following features :

Type I (jet-like, forward flow)

$$F_I > 0,\ F_P < 0,\ F_V \leq 0,\ \hat{E} \geq 0,\ \frac{D\hat{E}}{Dt} \leq 0$$

Type II (undulated, forward flow)

$$F_I \geq 0,\ F_P < 0,\ F_V \geq 0,\ \hat{E} \leq 0,\ \frac{D\hat{E}}{Dt} \geq 0$$

Type III (jet-like, reverse flow)

$$F_I \geq 0,\ F_P < 0,\ F_V > 0,\ \hat{E} < 0,\ \frac{D\hat{E}}{Dt} \leq 0$$

For the flow reversal regime (Type III), the "excess" potential energy is much larger than the kinetic energy of the fluid ($\hat{E} < 0$) and as the fluid particle moves toward the singularity the energy deficit of the particle increases due to the transfer of energy from the axis to the surrounding fluid by viscous work ($D\hat{E}/D\hat{t} \leq 0$). The pressure force

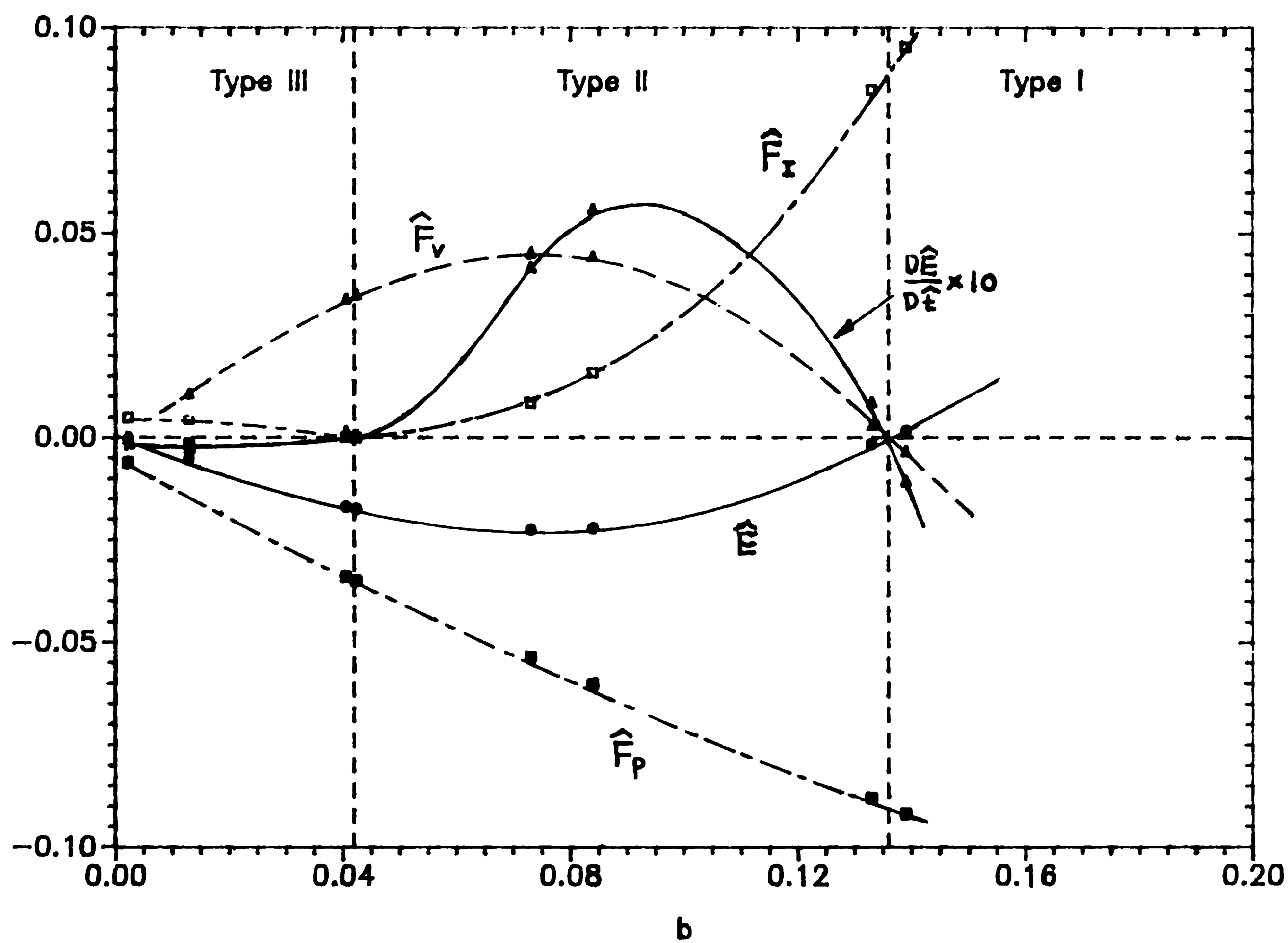

Figure 6.14 The effect of b on the energy of a fluid particle on the axis

acting on the fluid element is small and is balanced by a positive inertial and viscous forces. Transition from Type III to Type II behavior occurs when F_I goes to zero and the viscous and pressure forces balance. At this point, $(a,b,c,\eta_a) = (0,0.042,0.0174,28.6)$ with $\hat{E} < 0$ and $D\hat{E}/D\hat{t} = 0$.

$\hat{E}$ is less than zero for a Type II flow pattern, but as the fluid moves away from the singular point $\hat{E}$ increases due to energy transfer from the surrounding fluid to the axis by viscous work ($D\hat{E}/D\hat{t} > 0$). In this regime, F_P is balanced by positive viscous and inertial forces ($F_V > 0$, $F_I > 0$). Transition from Type II to Type I behavior occurs where F_V goes to zero and the pressure and inertial forces balance. At this point, $(a,b,c,\eta_a) = (0.301,0.136,0.0449,24.2)$ with $\hat{E} = 0$ and $D\hat{E}/D\hat{t} = 0$.

When $b > 0.136$, a jet-like flow behavior occurs (Type I). The kinetic energy term now dominates the "excess" potential energy (i.e., $\hat{E} > 0$); however, as the fluid particle moves toward the hydrostatic condition at $z = \infty$, its "excess" energy decreases ($D\hat{E}/D\hat{t} < 0$) because the high speed fluid on the axis transfers energy to the surrounding fluid by viscous work. The viscous force acting on the particle in this regime is negative so the large inertial force is countered by the adverse pressure and the viscous drag.

The relatively large adverse pressure force acting on the axis for large values of b is due directly to the centrifugal force and the hydrostatic boundary condition for $z \to \infty$.

CHAPTER 7

MODEL II : VORTEX FLOW WITH VARIABLE CIRCULATION

In Chapter 6, quantitative results for swirling flows with constant circulation (Model I) were presented. In this chapter, Model II (see Section 3.1), which includes the effect of N, will be discussed. An interesting aspect of these flows is that the dissipation integral (see Section 7.5) is bounded for $-2/3 < N < 0$. A comparison between Model I and Model II for $N = -1$ is given in Section 7.1 and, in Section 7.2, the effect of N on the three different flow regimes is developed. The behavior of the velocity and pressure fields for $-1 < N < 0$ is presented in Section 6.3 and 6.4; and, the effect of N on the macroscopic properties will be discussed in Section 7.5. These theoretical results will be compared with experimental data from several different laboratories in Chapter 8.

7.1 Comparison Between Models I And II For N = -1

Model II for $N = -1$ is similar to Model I. Model II, however, includes the effect of N. Because N is generally not equal to -1 (see Figure 8.2), Model II was developed in order to understand certain experimental results for confined vortex flows. As discussed in Chapter 3, the major difference between Model I and Model II is that the axial velocity for Model II is zero for $(r,z) = (\delta^{*}(z), z)$. Also, for N >

-2/3, the growth of the viscous core near the singular point keeps the dissipation integral bounded. Figure 7.1 shows that a jet-like flow around the axis occurs for both models when N = -1 and b = 0.30. The small difference in the axial velocity at $\eta = 0$ is due to differences in the values of 'a' determined for each model (a = 0.886 for Model I and 0.893 for Model II). The computed values of $\tilde{\eta}$ for the two models differ only slightly : $\eta_a = 21.7$ whereas $\eta^* = 21.3$. It is also apparent that the axial velocity has an asymptotic behavior ($u_z \propto 1/r$) at $\eta = \eta_a$ for Model I, but is zero at $\eta = \eta^*$ for Model II. The differences in the macroscopic properties between the two models are important and will be discussed in Section 7.5.

The criteria for transition between the different flow regimes (see Figure 4.2) for the two models (N = -1) are very similar. For instance, reverse flow passes to an undulated flow for $(a,b,c,\tilde{\eta})$ = (0,0.042,0.0149,28.6) for Model I; and (0,0.038,0.0151, 29.0) for Model II. The transition between undulated and jet-like flow occurs for $(a,b,c,\tilde{\eta})$ = (0.301,0.136, 0.0449, 24.2) and, (0.321,0.14,0.0447,24.1) for Models I and II, respectively.

7.2 Different Flow Regimes

Three different flow regimes have also been found for Model II. As b increases, the axial velocity changes from flow reversal to undulated and, finally, obtains a jet-like structure. As N increases, the region of flow reversal and undulated behavior broadens (see Figure 7.2). For example, flow reversal occurs for b < 0.038 and N = -1.0. However, for N = -0.75, flow reversal occurs for 0 < b < 0.055. Similarly, undulated

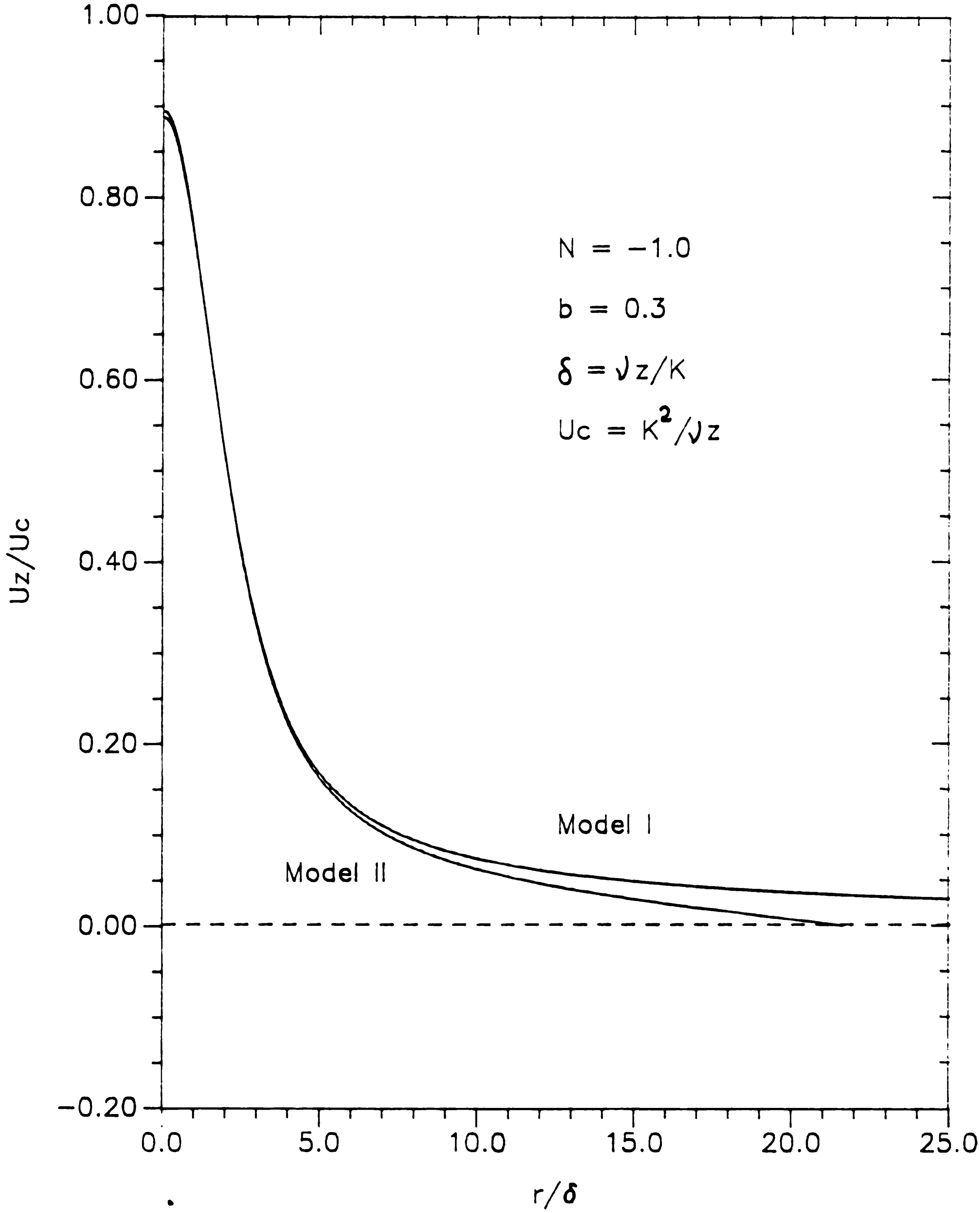

Figure 7.1 Comparison between Model I and Model II for axial velocity profile

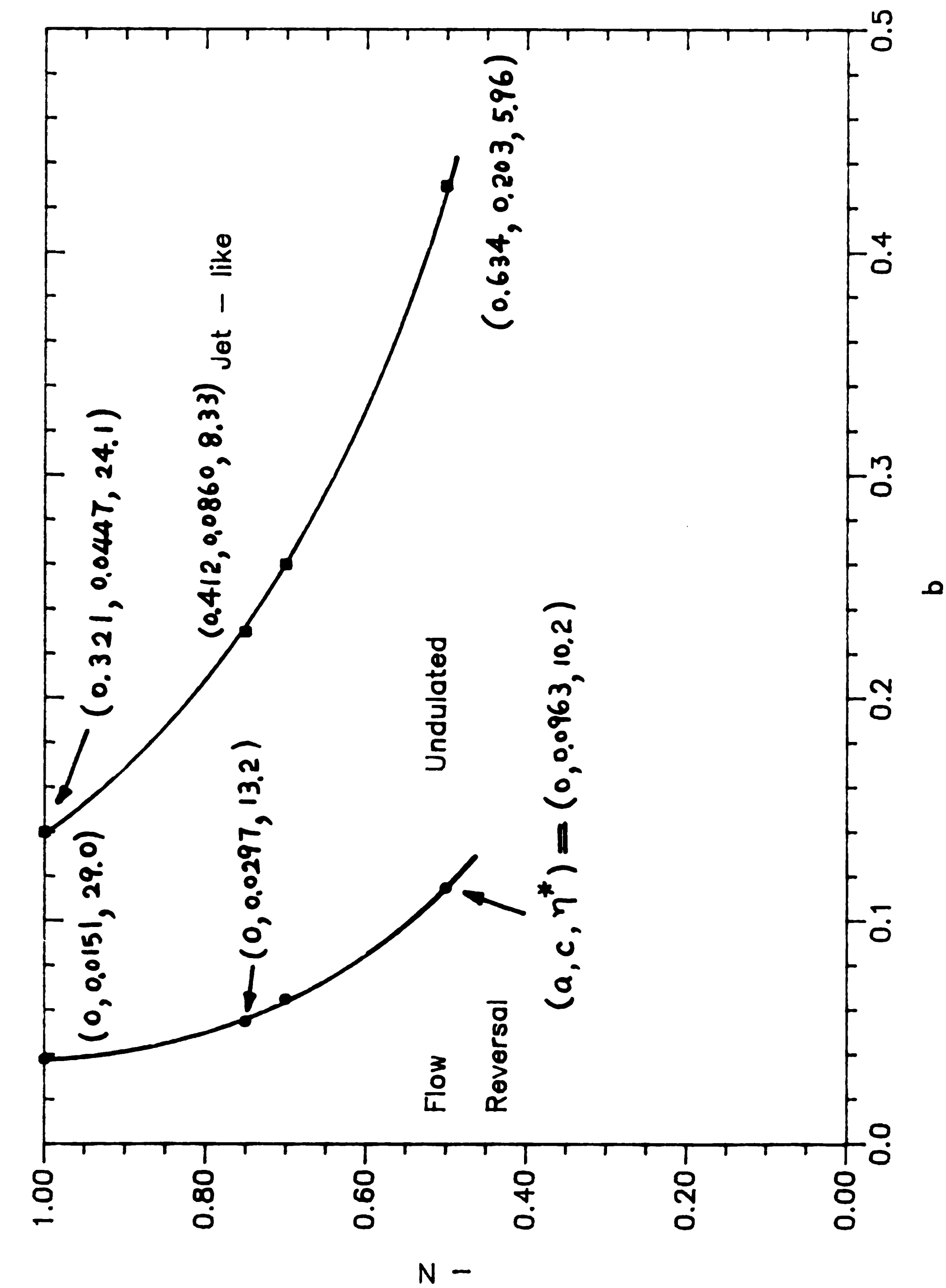

Figure 7.2 Regimes of different flow behaviour for Model II

axial velocities occur between $0.038 < b < 0.14$ for $N = -1.0$, but between $0.055 < b < 0.23$ for $N = -0.75$. As N increases from -1 to -.75, the lower limit on b for jet-like behavior increases from 0.14 to 0.23. Thus, in order to have a jet-like axial flow, a strong rotation around the axis is necessary for larger values of N. This kind of effect becomes more apparent as N increases.

7.3 General Behavior Of The Solution

Tables A.2 - A.4 in Appendix A list the values of (a,c,η^*) for different values of N and b. Figure 7.3 shows the effect of N on the parameter set (a,b,c,η^*). The general behavior is the same as Model I where 'a' and 'c' increase, but η^* decreases, as 'b' increases. 'c' is less sensitive to 'b' than 'a'. Because η^* represents the size of the viscous core, it follows from Figure 7.3 that larger values of 'b' give a more coherent vortex.

As N increases, c increases and η^* decreases. The size of the core is reduced almost 50 % when N changes from -1 to -0.75. This means that a more concentrated (or coherent) core will occur at larger values of N for fixed values of b. Because this effect is so large, it is important for Model II to be fully developed and analyzed. Once again, for fixed N, the parameters 'a', 'c', and η^* change monotonically with b. Therefore, the flow structure is uniquely determined by any one of the four dimensionless number (a,b,c,η^*) together with K, ν, and N.

Figures 7.4 - 7.6 show the general behavior of M, F, and h. The similarity functions are defined on the finite domain $0 \le \eta \le \eta^*$, so the

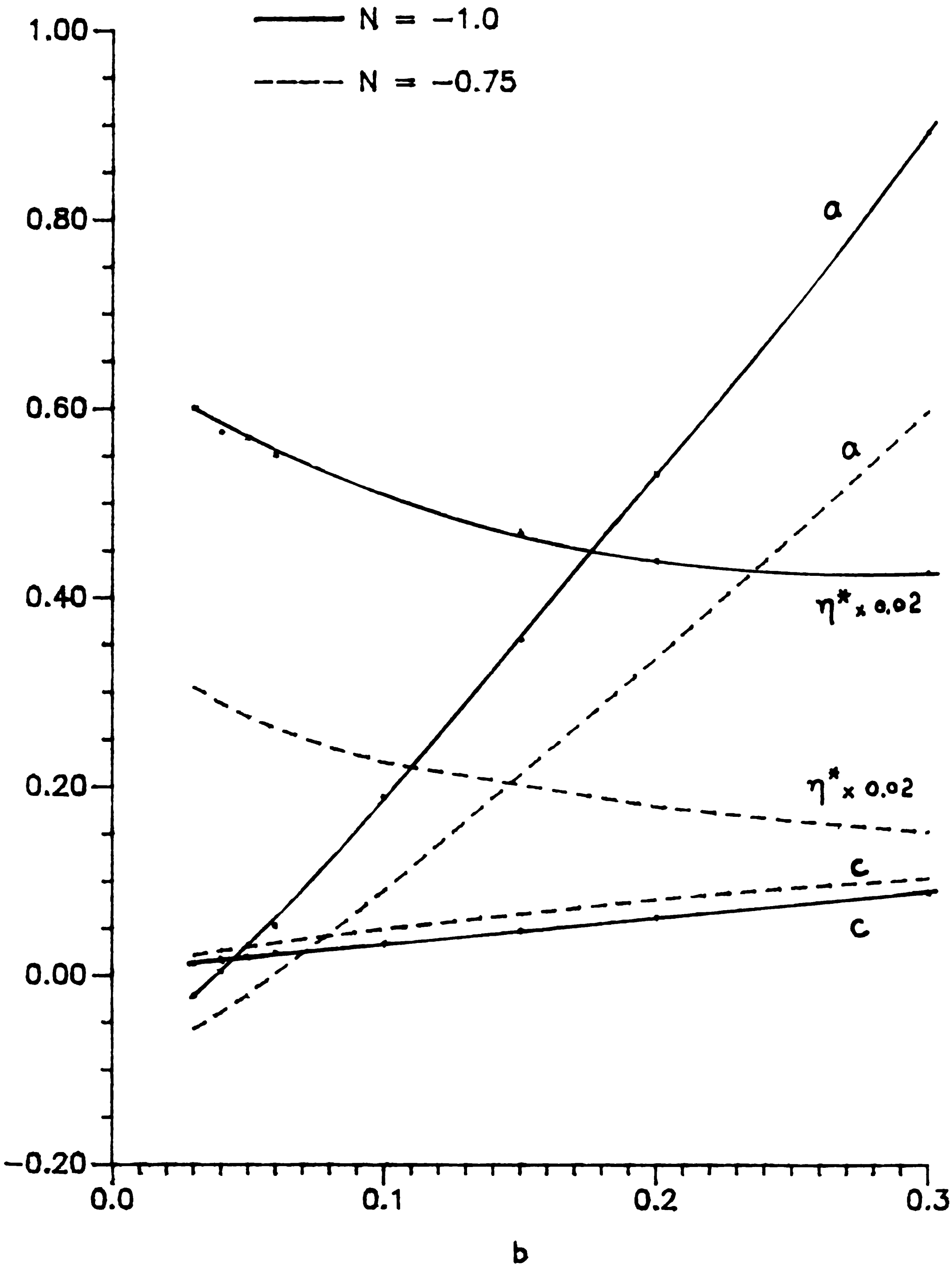

Figure 7.3 The behaviour of the solution for Model II

curves terminate at η^*. The derivatives of M, F, and h are all zero for $\eta = 0$ because of the boundary conditions (see Eqs. (3.58) - (3.59)).

Figure 7.4 shows how b affects M for N = -0.75. Comparing Figure 7.4 and 6.2 (N = -1.0, Model I), M decreases as b increases but, for Model II, goes to negative values at $\eta = \eta^*$ for any value of b. M in Model I becomes asymptotic to $1/(2\eta^2)$ at $\eta = \eta_a$. A negative value of M in Model II implies that the pressure at $\eta = \eta^*$ is higher than hydrostatic. The parameter 'c', which represents M(0), is always positive (see Figure 7.3).

The effect of b on M is significant (see Figure 7.4). For constant η, when b increases, M becomes larger at small values of η, but becomes smaller at large values of η. Because M at $\eta = \eta^*$ becomes smaller as b increases, the pressure drop across the vortex (i.e., $M(0) - M(\eta^*)$) increases with b. Thus, coherent (concentrated) vortex structures require relatively large radial pressure drops.

The behavior of F, shown in Figure 7.5, monotonically increases to a maximum value at $\eta = \eta^*$. For constant η, F increases as b increases. For fixed b and η, comparing Figure 7.5 and 6.3, F increases as N increases. Therefore, larger values of N give larger values for the circulation, or the angular momentum, at constant b and η.

The stream function h for Model II (see Figure 7.6) in the outer region is different from h for Model I (see Figure 6.4) due to the boundary conditions imposed at η^*. However, the behavior of h near the axis is similar for both models. For forward flow, h increases monotonically. For reverse flow, h is negative for small values of η

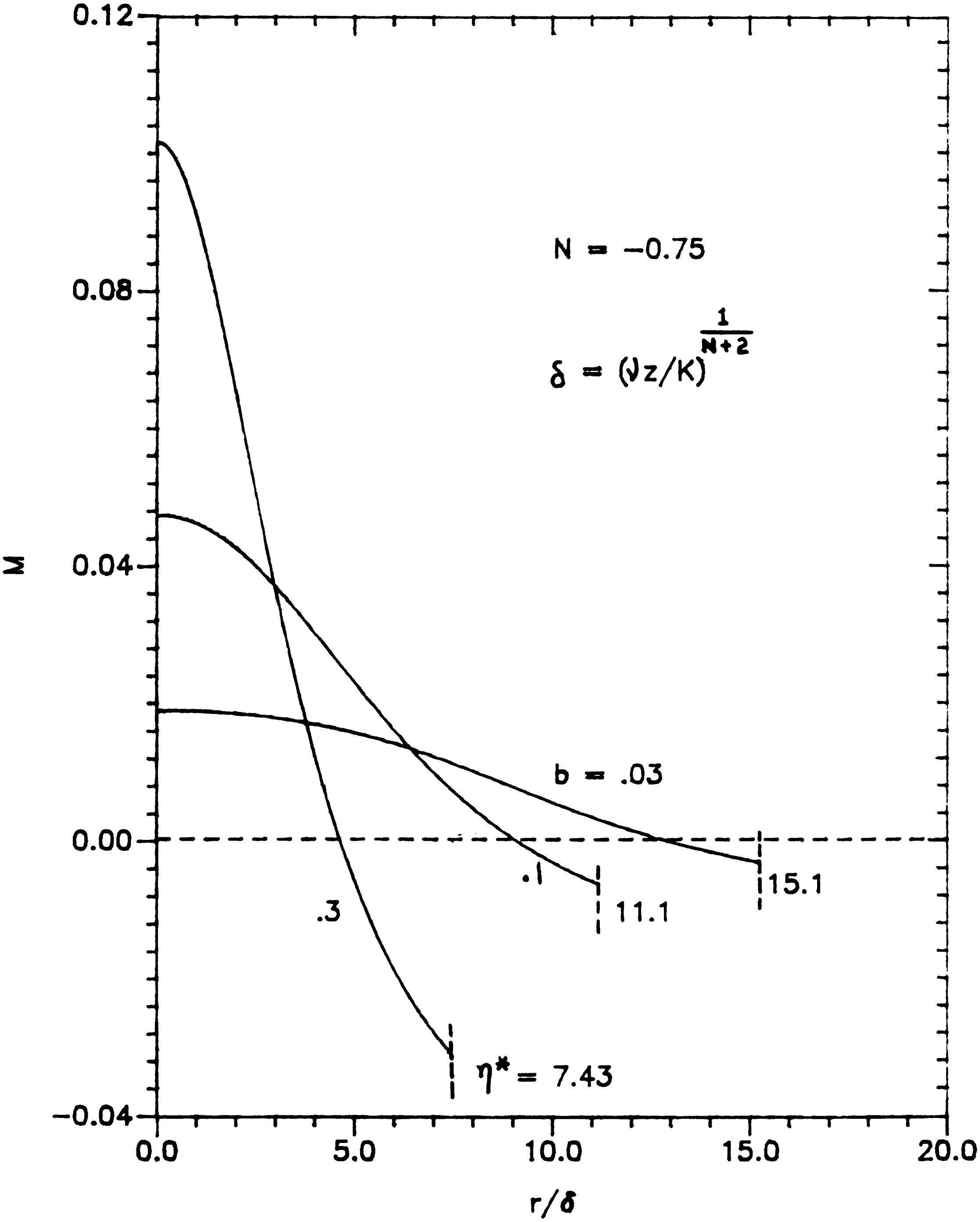

Figure 7.4 The effect of b on the behaviour of M for Model II

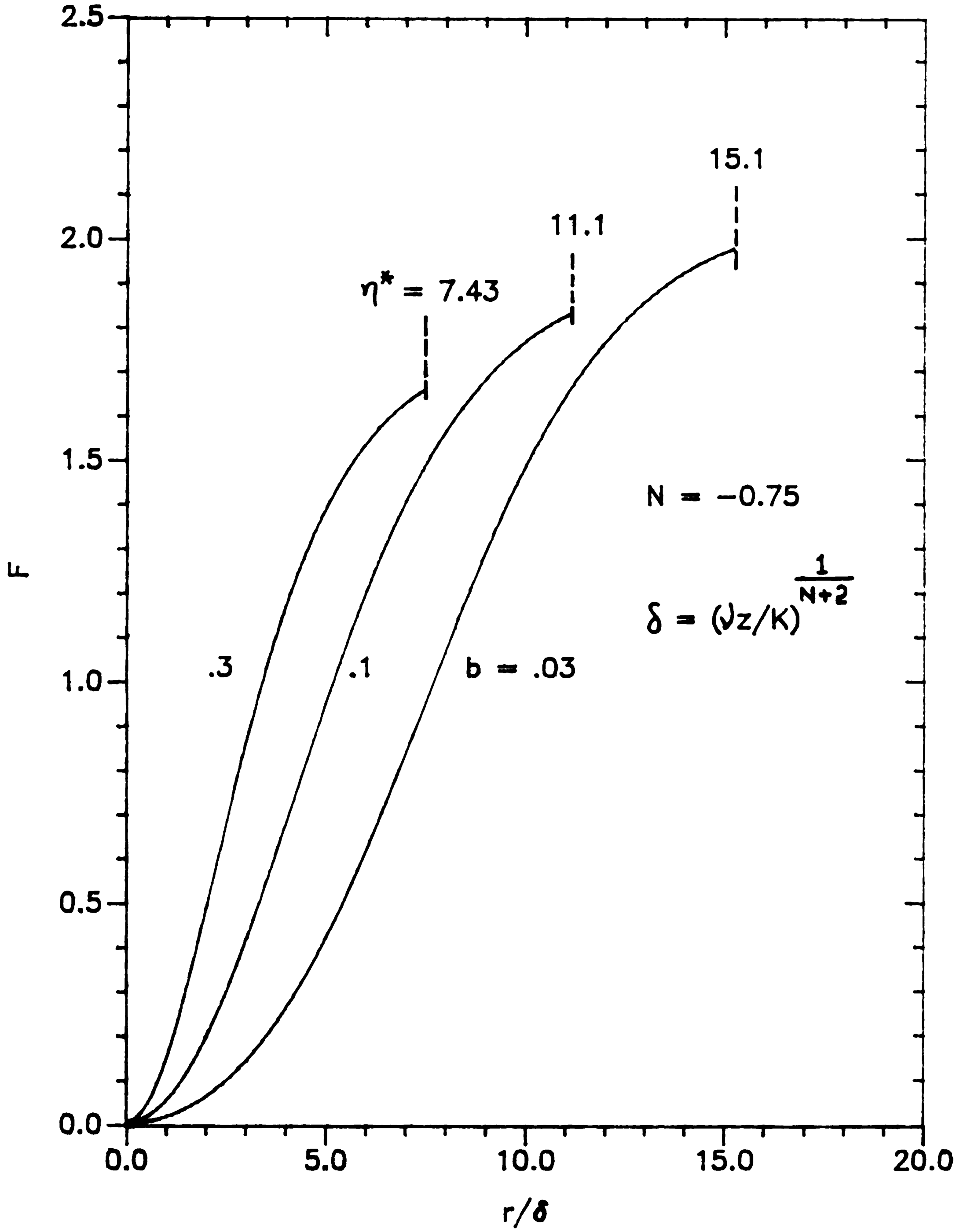

Figure 7.5 The effect of b on the behaviour of F for Model II

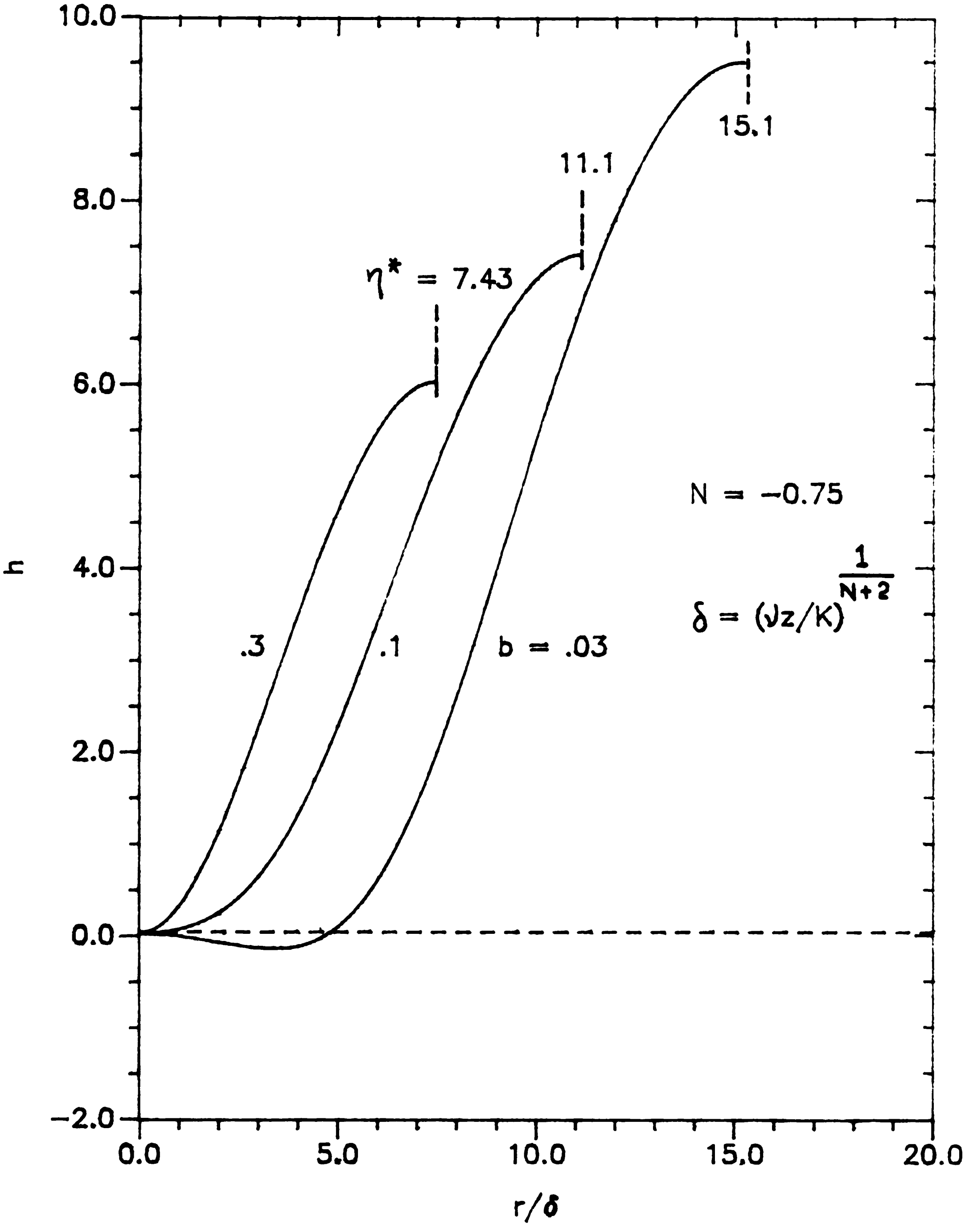

Figure 7.6 The effect of b on the behaviour of h for Model II

and positive for larger values of η. The point where $h = 0$ occurs at $\eta \approx 5$ for $N = -0.75$ and $b = 0.03$. Because $h(\eta)$ represents the local dimensionless entrainment rate (see Eq. (3.43)), $h(5) = 0$ means that the local volumetric flow rate across a surface of fixed z and $0 \leq r \leq 5\delta(z)$ is zero. Therefore, the axial velocity must be zero at some value of r between 0 and $5\delta(z)$. It can be seen from Figure 7.6 that zero axial velocity occurs at $\eta \approx 3.5$ (also see Figure 7.8) where the slope of h is zero.

One important difference between Model I and Model II is the stream function at the outer edge of the vortex core. In Model I, h is asymptotic to h_a, defined by Eq. (3.53). However, for Model II, the slope of h at $\eta = \eta^*$ equals zero because $u_z(\delta^*,z) = 0$.

For fixed N and $\eta < \eta^*$, the effect of b on h is to increase the local volumetric flow rate as b increases. However, the global entrainment rate, defined by Eq. (3.43), increases as b decreases. Thus, as the vortex core diameter increases, the volumetric flow rate becomes larger. For example, it follows directly from Figure 7.6 that $h(\eta^*) \approx 9.5$ for $b = 0.03$ and $h(\eta^*) \approx 6.0$ for $b = 0.3$. So as b increases by an order of magnitude, the core size decreases by a factor of two and the volumetric flow rate through the vortex decreases by about 30%.

7.4 Behavior Of The Velocity Field

Figure 7.7 shows that the common features of the tangential velocity profiles for different values of b and $N = -0.75$ include : a Rankine-type structure with a forced vortex near the axis and a free-vortex-like flow in the outer region; the maximum tangential velocity

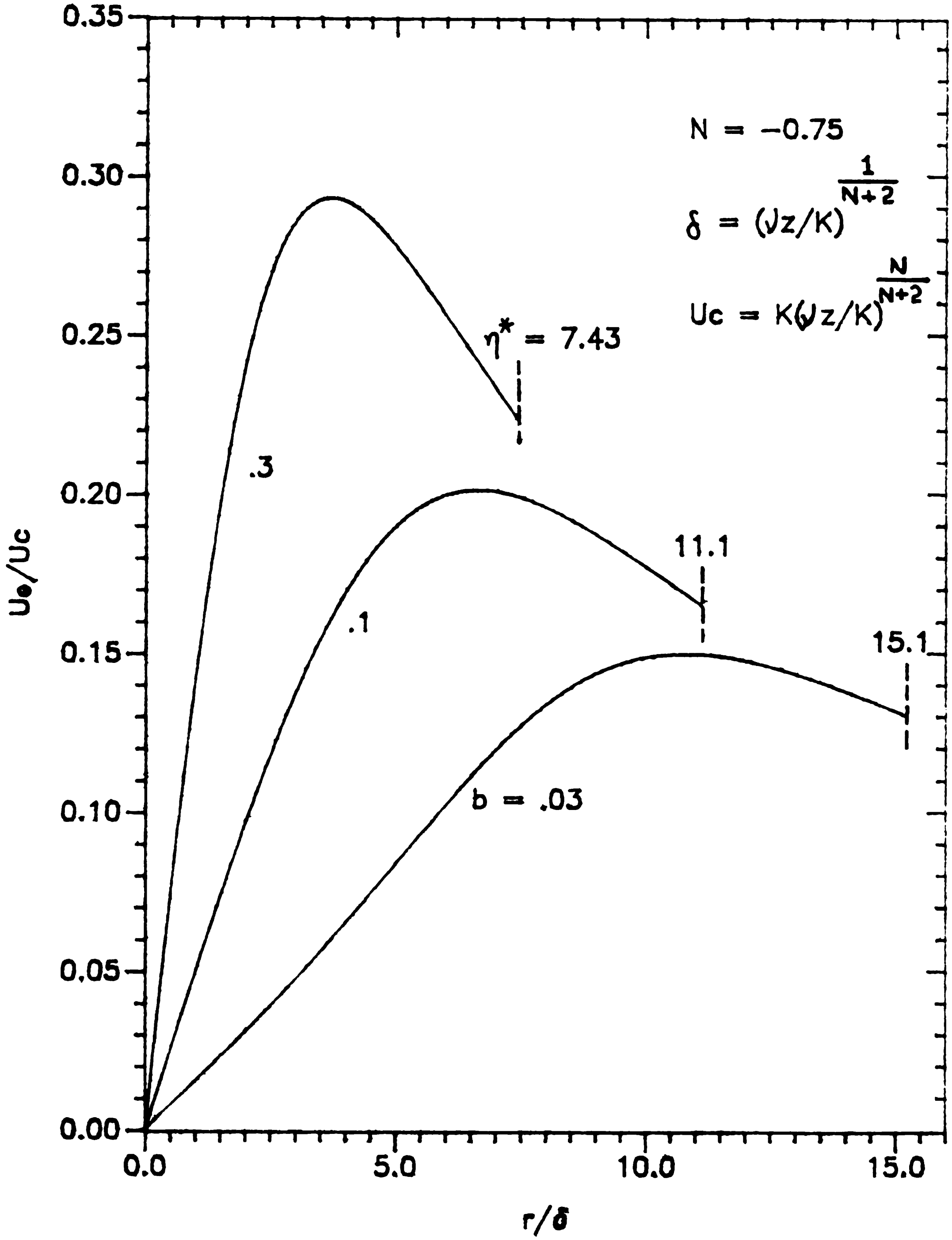

Figure 7.7 The effect of b on the tangential velocity profile for Model II

shifts to smaller values of η and becomes larger as b increases; and, the core size decreases as the rotation frequency around the axis increases (i.e., b increases). It is also noteworthy that as b increases, the fraction of the cross sectional area of the vortex in solid body rotation decreases.

The axial velocity behavior for Model II for general N has some features which are similar to Model I (see Figure 7.8). Note that reverse flow on the axis appears at smaller values of b and jet-like flow on the axis appears at larger values of b. At intermediate values of b, undulated flow exists (see Figure 7.2 for other values of N).

In the flow reversal region (Figure 7.8), zero axial velocity occurs at $\eta \approx 3.5$ for $b = 0.03$ which corresponds to the zero slope of the stream function (see Figure 7.6). The flow moves downward within $\eta < 3.5$ and moves upward for $3.5 < \eta < 15.1$. For forward flow on the axis, the flow moves upward everywhere (i.e., $0 \le \eta < \eta^*$). Note that strong rotation around the axis (large b) gives a higher axial velocity near the axis and lower axial velocity near the outer boundary. The axial velocity goes to zero at $\eta = \eta^*$ because $u_z(\delta^*,z) = 0$. Again, the comparison between Figure 7.7 and 7.8 shows that the values of η at maximum axial velocity is smaller than the values of η at maximum tangential velocity for any value of b. Thus, the position of maximum axial velocity occurs within the solid body region. Characterization of different flow regimes using the mechanical energy balance on the axis is the same for Models I and II and has already been discussed in Section 6.4.

The radial velocity behavior in Model II is very important to the understanding of light particle separation (see Chapter 9). The common

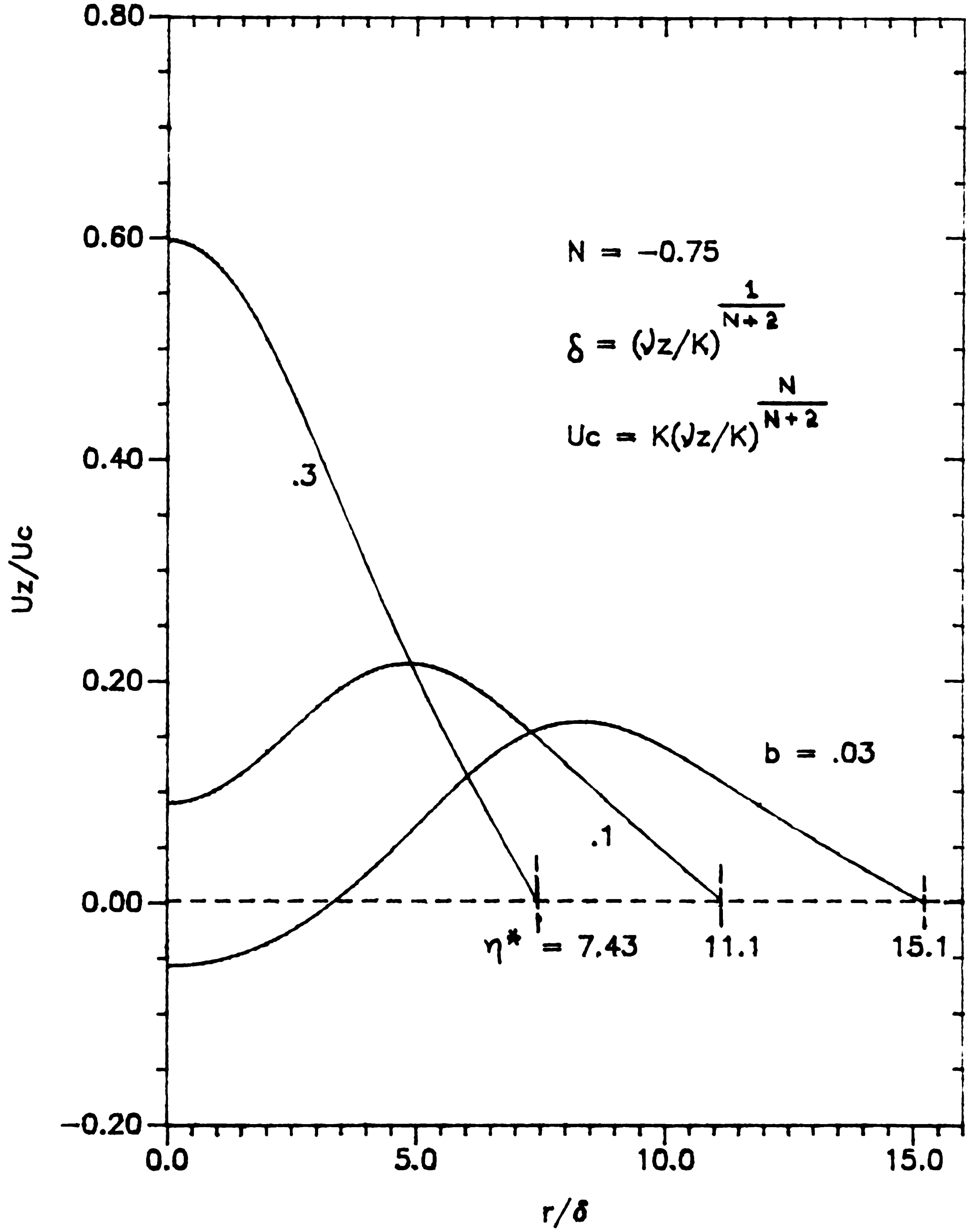

Figure 7.8 The effect of b on the axial velocity profile for Model II

features of radial velocity in Model II (see Figure 7.9) are the same as in Model I. In brief, these are :

(a). Positive radial velocity near the axis for forward flow, but negative radial velocity near the axis for reverse flow.

(b). Only one mantle ($u_r = 0$) exists in undulated or jet-like flow region, but two mantles exist in reverse flow region.

(c). The inner mantle for reverse flow is about $\eta \approx 3.0$ for $b = .03$ and $N = -0.75$. Therefore, all the flow within this mantle will move downward toward the singular point.

(d). The peak of maximum radial velocity shifts to smaller values of η as b increases.

(e). The effect of b on the radial velocity is to reduce the mantle size in the forward flow region; therefore, a strong rotation about the axis causes a small mantle to form with a very strong jet-like flow behavior over a very small vortex core.

(f). For fixed values of η, the radial velocity near the axis becomes larger when b increases. However, the radial velocity near the edge of the vortex becomes smaller when b increases.

(g). A surface of zero radial velocity (i.e., mantle) always exists within the vortex core ($\eta < \eta^*$).

7.5 Macroscopic Properties

Figures 7.10 - 7.13 show the effect of b on the macroscopic properties for the vortex (see Table 3.2). An important feature of Figure 7.10 is that the axial thrust does not determine the flow behavior uniquely. The minimum value of $\hat{F}_z$ is about 0.5 for $N = -1.0$; and, 0.45 for $N = -0.75$. For Model I, the minimum thrust is 0.58 (see

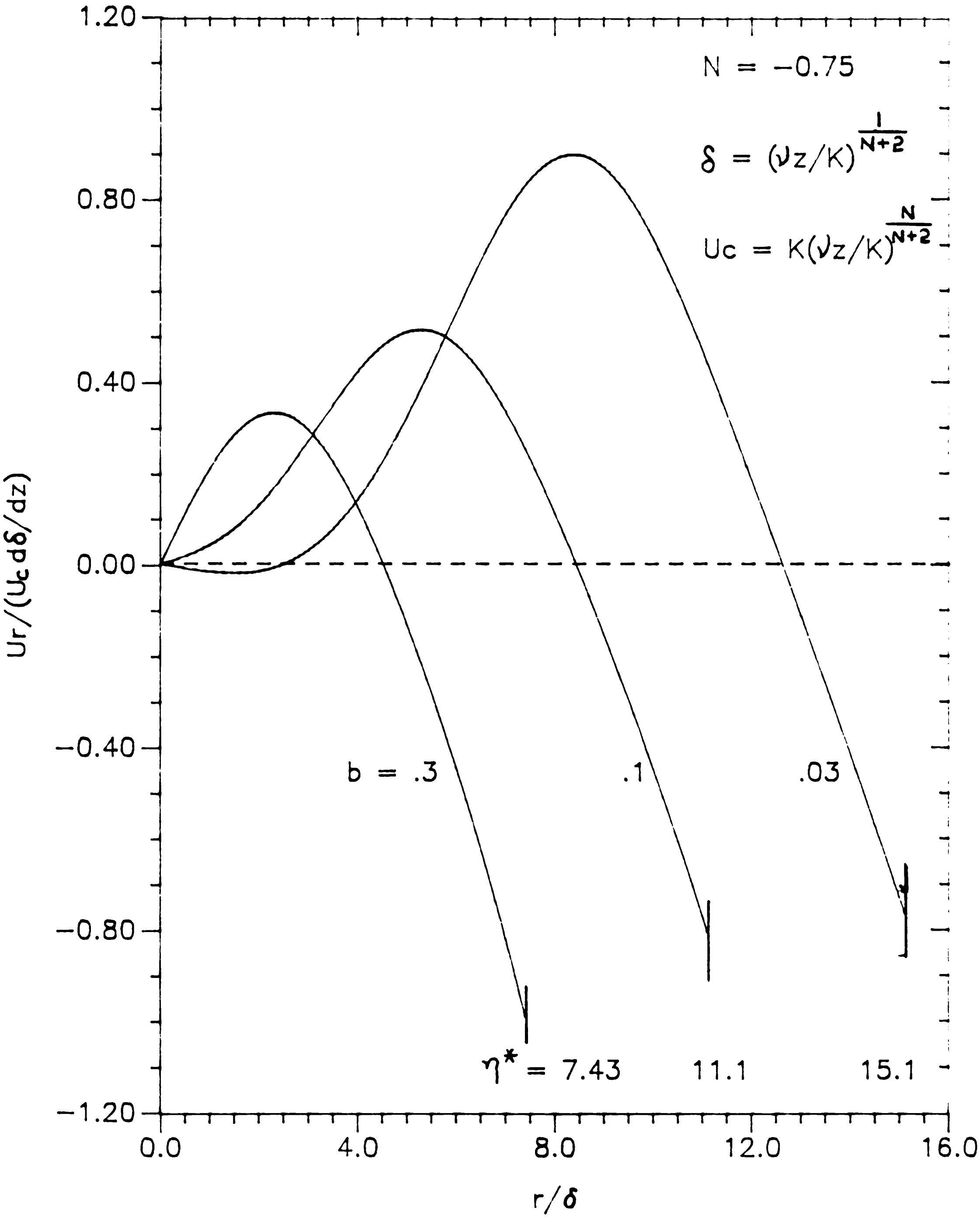

Figure 7.9 The effect of b on the radial velocity profile for Model II

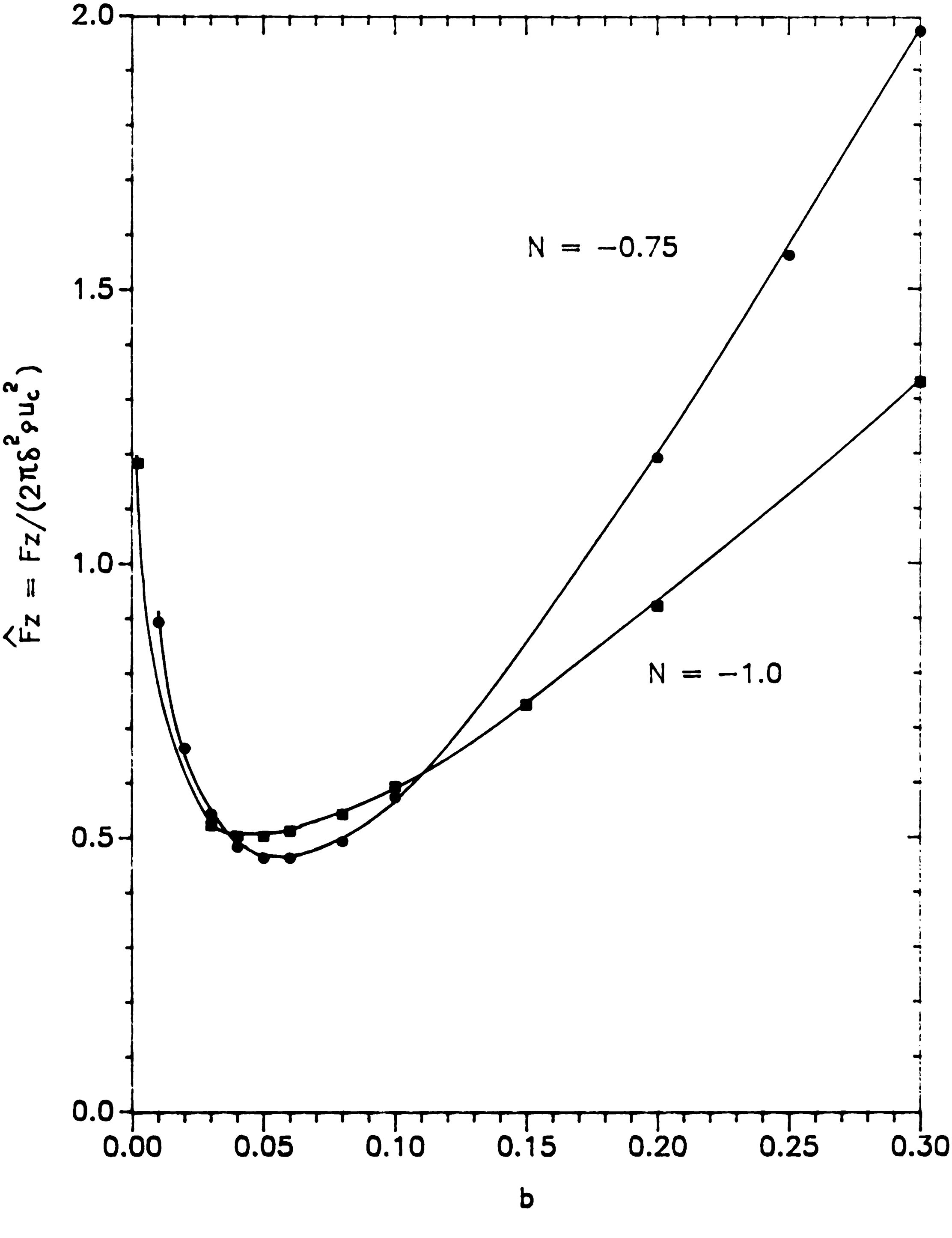

Figure 7.10 The effect of b on the macroscopic axial thrust for Model II

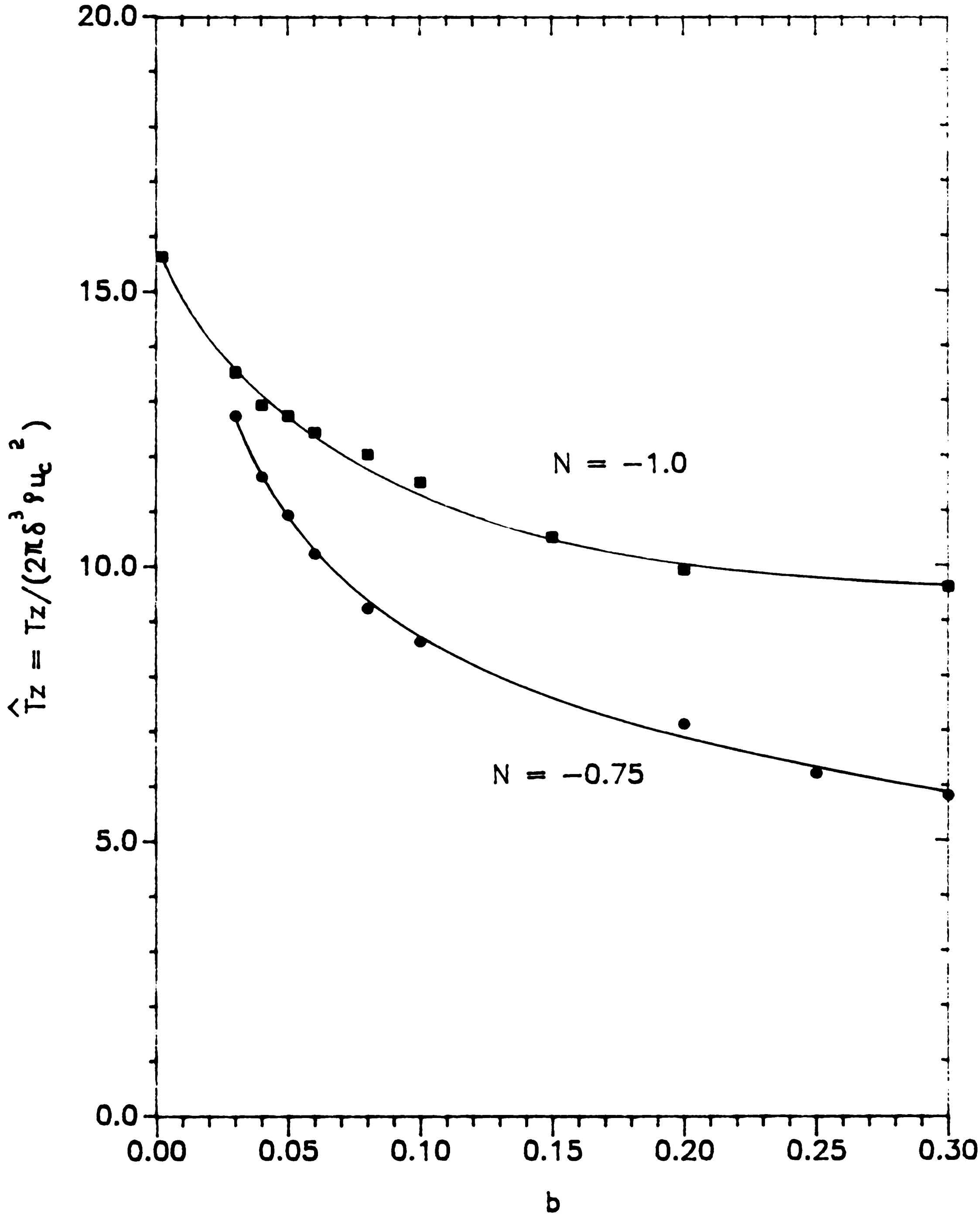

Figure 7.11 The effect of b on the macroscopic axial torque for Model II

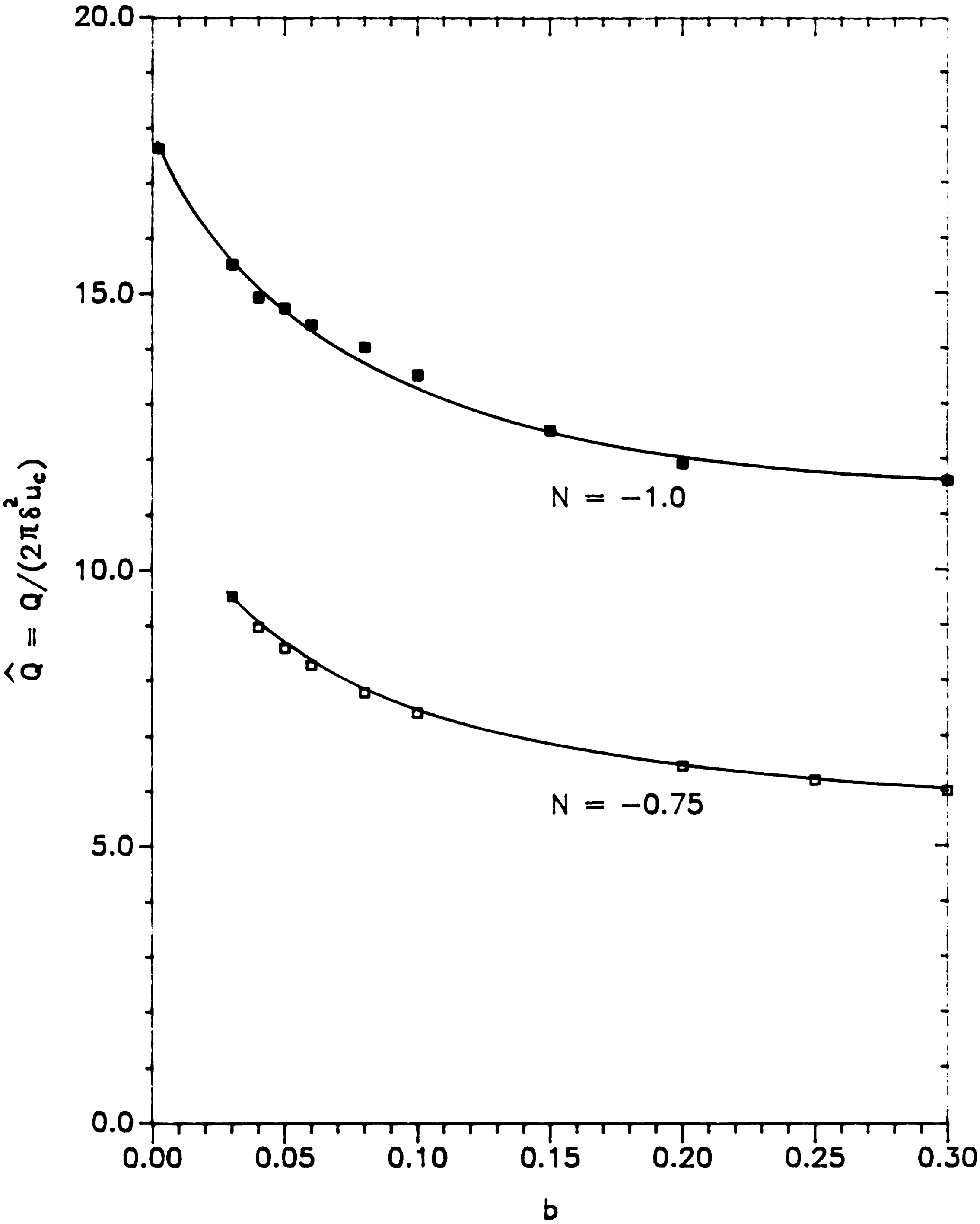

Figure 7.12 The effect of b on the volumetric flow rate for Model II

Figure 6.10). For a fixed value of the axial thrust above the minimum value, two values of b are possible. For example, with N = -1 and $\hat{F}_z$ > 0.5, three different cases are possible : (1) For $0.50 \le \hat{F}_z \le 0.52$ (which corresponds to the transition point between flow reversal and undulated flow), two different undulated profiles are possible; (2) For $0.52 \le \hat{F}_z \le 0.70$ (which corresponds to the transition point between undulated and jet-like flows), either a flow reversal or an undulated flow behavior on the axis occurs; and, (3) When the axial thrust is larger than 0.70, either flow reversal or jet-like behavior obtains. For N = -0.75, the corresponding values for $\hat{F}_z$ are 0.45, 0.47, and 1.4, respectively.

The axial torque and the volumetric flow rate decrease monotonically as b increases (see Figure 7.11 and 7.12). The slope of these curves are steeper in the small b region. For large values of b, small changes in the axial torque and flow rate will cause large changes in b.

Although the qualitative behavior of $\hat{T}_z$ and $\hat{Q}$ for Models I and II are similar, the specific velues of these parameters are much smaller for Model II. For example, at b = 0.3 and N = -1, $\hat{T}_z$ is 14.5 for Model I but only 9.6 for Model II. If N increases to -0.75, then $\hat{T}_z$ = 5.8. The macroscopic flow rate $\hat{Q}$ decreases from 16.5 (Model I) to 11.6 (Model II, N = -1). For N = -0.75, $\hat{Q}$ = 5.9.

The axial torque $\hat{T}_z$ and the volumetric flow rate $\hat{Q}$ are both proportional to $h(\eta^*)$ (see Table 3.2). As b decreases, η^* increases (see Figure 7.3). Because $h(\eta^*)$ increases with η^*, $\hat{T}_z$ and $\hat{Q}$ become very large for $b \to 0$. On the other hand, both $\hat{T}_z$ and $\hat{Q}$ appear to approach a positive lower bound for very large values of b. For example, with b = 10 and N = -1.0, $\hat{T}_z = 5$ and $\hat{Q} = 7$. If N = -0.75 and b = 10, then $\hat{T}_z = 2.8$ and $\hat{Q} = 4$.

An important parameter for both Models I and II is the macroscopic pressure drop, $\hat{\Delta p}$. Figure 7.13 shows that for N = -1 and -0.75, $\hat{\Delta p}$ increases monotonically with an almost constant slope. For fixed b, $\hat{\Delta p}$ increases as N increases. It is noteworthy that for b > 0.05, the macroscopic pressure drop for N = -0.75 is almost 1.5 time the macroscopic pressure drop for N = -1.0. Unlike the other global properties, a one-to-one correspondance between $\hat{\Delta p}$ and b exist. Thus, as previously discussed in Chapter 6, the flow behavior is uniquely determined by specifying K, ν, N and either $\hat{\Delta p}$ or one of the local properties : a, b, c, η^*.

The dissipation of kinetic energy over the cross section of the vortex can be calculated as follows

$$\Phi = 2\pi \int_0^{\tilde{\delta}(z)} (\underline{\underline{\tau}} : \nabla \underline{u}) r dr \tag{7.1}$$

where

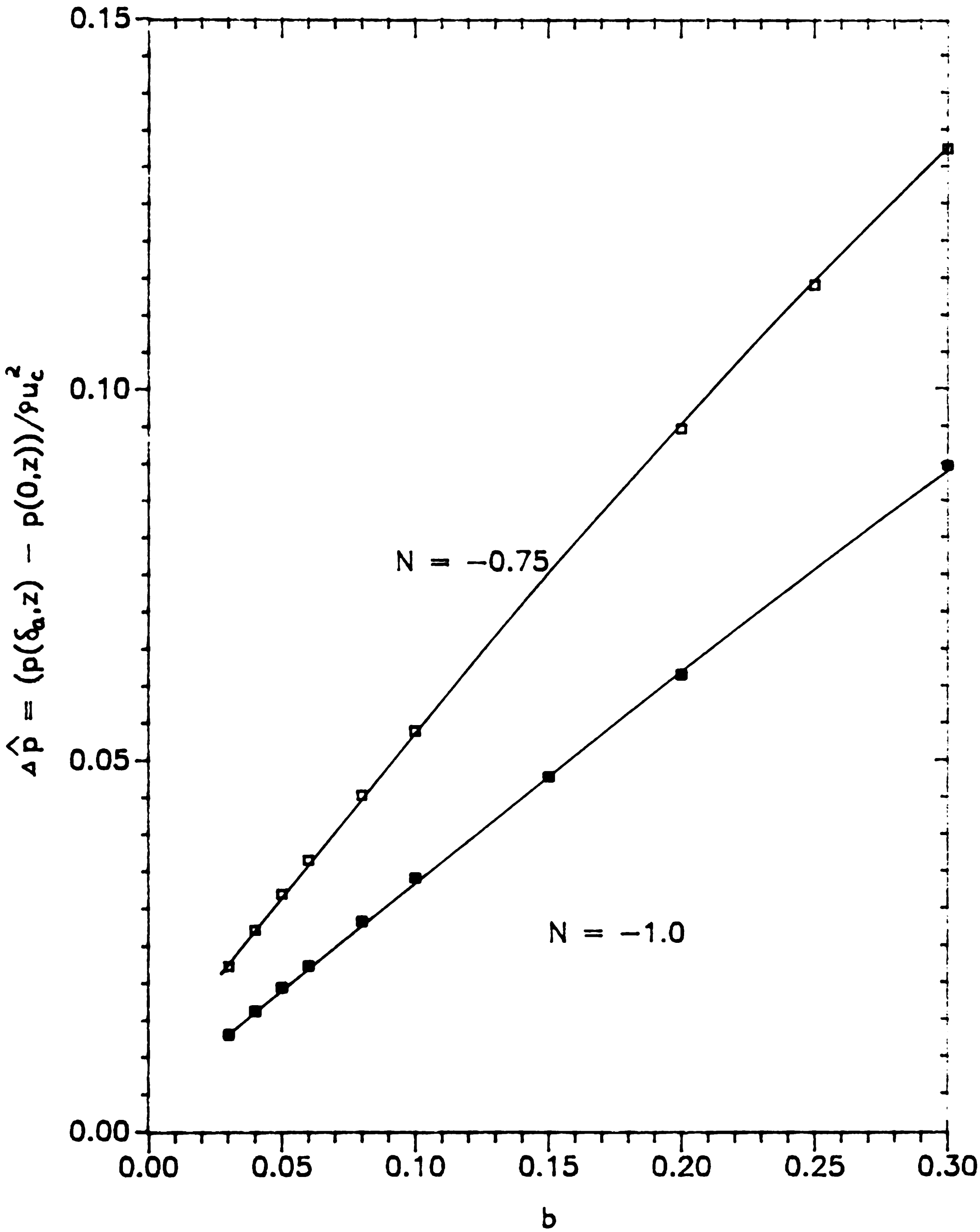

Figure 7.13 The effect of b on the macroscopic pressure drop for Model II

$$\underline{\underline{\tau}} : \nabla \underline{u} = \mu \left\{ \left[r \frac{\partial}{\partial r}\left(\frac{u_\theta}{r}\right) \right]^2 + \left[\frac{\partial u_z}{\partial r} \right]^2 \right\} \tag{7.2}$$

represents the irreversible conversion of kinetic energy into internal energy per unit volume by viscous dissipation (see p. 82 of Bird et al., 1960).

Eq. (7.1) can be written in terms of the similarity functions defined in Chapter 3. Thus, by substituting Eqs. (3.28), (3.34), (3.37), and (3.38) into Eqs. (7.1) and (7.2), it follows that

$$\hat{\Phi} = \frac{\Phi}{2\pi\mu u_c^2} = \int_0^{\eta^*} \left[\left(\frac{F'}{\eta} - \frac{2F}{\eta^2}\right)^2 + (G')^2 \right] \eta d\eta. \tag{7.3}$$

The dimensionless dissipation $\hat{\Phi}$ depends only on b and N. Figure 7.14 shows how b affects $\hat{\Phi}$ for N = -1.0 and N = -0.75. The behavior of $\hat{\Phi}$ is similar to the behavior of the macroscopic axial thrust. The values of $\hat{\Phi}$ become large for small and large values of b. The minimum value of $\hat{\Phi}$ is about 0.062 for N = -1.0 and 0.102 for N = -0.75. Although the macroscopic dissipation does not uniquely determine the flow structure, it nevertheless provides a useful characteristic of the flow.

For a fixed value of N and b, it follows directly from Eq. (7.3) that

$$\Phi = 2\pi\mu u_c^2 \hat{\Phi}(b,N) \tag{7.4}$$

where

$$u_c = K\delta^N = K\left(\frac{\nu z}{K}\right)^{\frac{N}{N+2}}.$$

Thus,

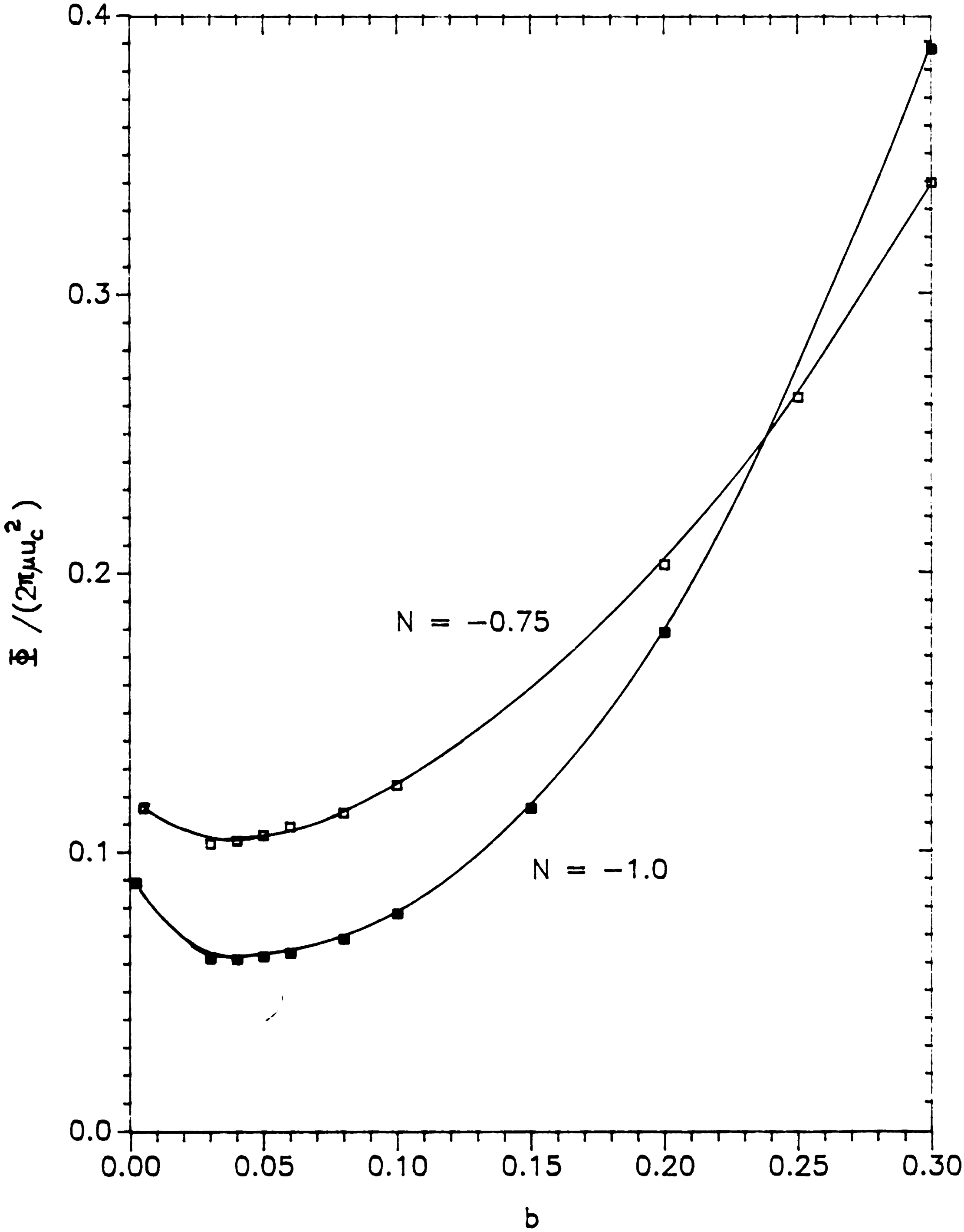

Figure 7.14 The effect of b on the macroscopic dissipation for Model II

$$\Phi \propto z^{\frac{2N}{N+2}}. \tag{7.5}$$

Eq. (7.5) implies that $\Phi \to \infty$ as $z \to 0$ for $-1 \leq N < 0$; and, $\Phi \to 0$ for $z \to \infty$. The total dissipation follows by integrating Eq. (7.4) from $z_D > 0$ to $z = L$:

$$D = \int_{z_D}^{L} \Phi dz = 2\pi\mu L u_c^{2}(L)\hat{\Phi}(b,N)\frac{N+2}{3N+2}\left[1 - \left(\frac{z_D}{L}\right)^{\frac{3N+2}{N+2}}\right] .$$

For $z_D = 0$, D is unbounded for $-1 \leq N \leq -2/3$; however, if $-2/3 < N < 0$, then $0 < D < \infty$. For $z_D > 0$ and $-1 \leq N < 0$, D is positive and bounded.

CHAPTER 8

AN ANALYSIS OF EXPERIMENTAL RESULTS IN THE LITERATURE

8.1 Experimental Results

The major assumptions of this study are constant density and viscosity, axisymmetric flow, and similarity structure. Although the similarity theory necessarily neglects the effect of wall boundary layers in confined vortex flows, the results of several experimental (and computational) studies are used to explore the possibility that the analysis can be used to quantify the core region of flooded hydrocyclones or, more generally, of confined vortex chambers containing a single fluid phase (either gas or liquid, but not both).

Several major studies of confined vortex chambers are used for the purpose of comparing theoretical and experimental (including computational) results. Figure 8.1 shows the various coordinate systems and geometries of these studies. Table 8.1 summarizes the important operating conditions for the experiments. The location of the reference coordinate $\tilde{z}$, shown in figure 8.1, defines the orientation of the viscous core and will be discussed further in Section 8.3.

Among the six papers listed in Table 8.1, Escudier et al. [1980, 1982] and Dabir [1983] are the most important because they have very complete information. Moreover, the flows in these studies were axisymmetric, although under some conditions nonaxisymmetric behavior was observed. The tangential and axial components of the velocity were

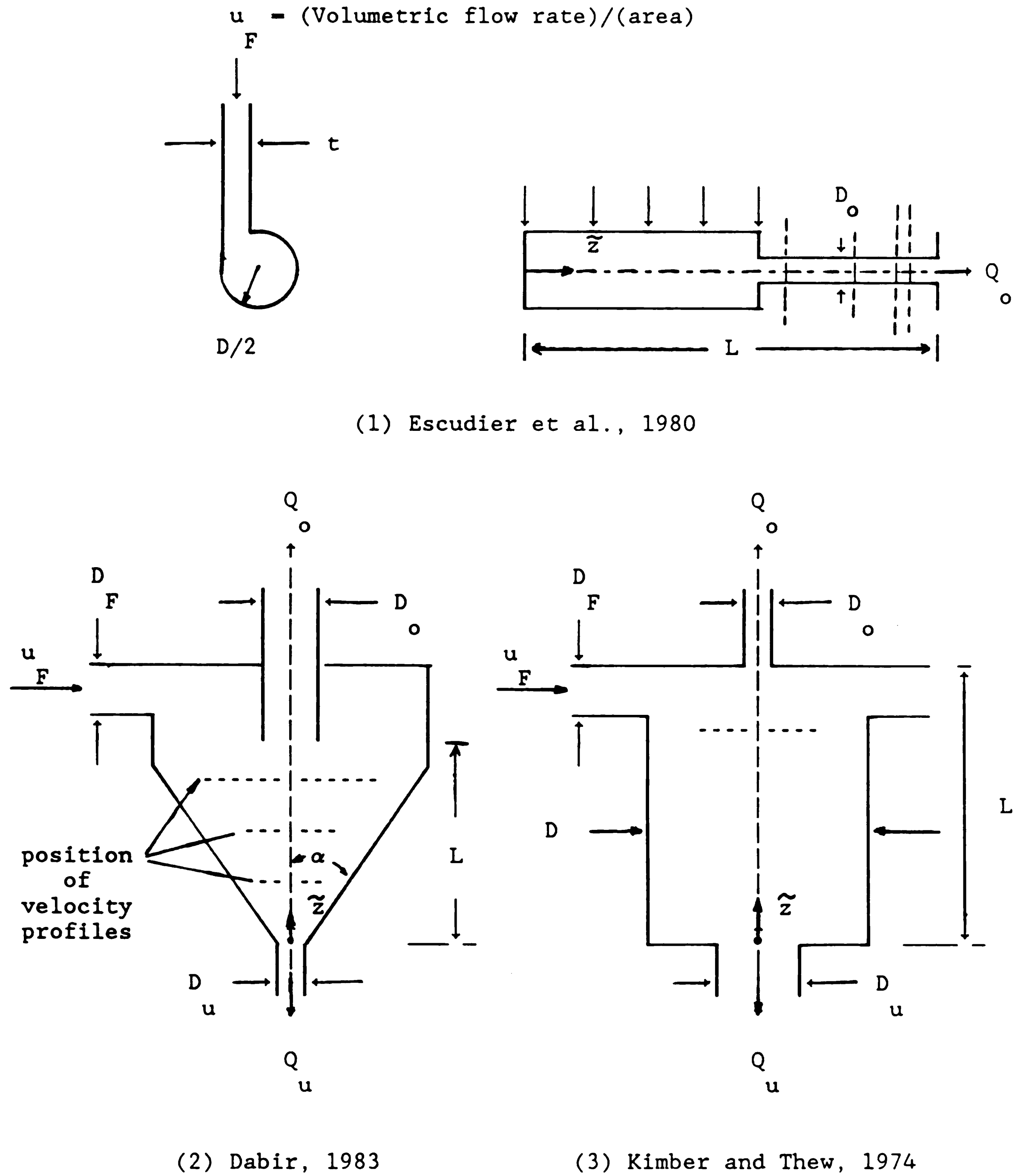

Figure 8.1 Coordinate system for various vortex chambers

Table 8.1 Flow conditions of the experimental studies

Reference	Index	Flow Conditions					Flow Regime
		u_F cm/s	Q_o cm^3/s	D mm	D_o mm	L cm	
Escudier et al. 1980 (experimental)	1a	24	400	55	40	42.5	Reverse
	1b	24	400	55	25	42.5	Undulated
	1c	24	400	55	10	42.5	Jet-like
Escudier et al. 1982 (experimental)	1d	6	100	55	18	42.5	Jet-like
	1e	12	200	55	18	42.5	Undulated
	1f	24.6	411	55	18	42.5	Undulated
	1g	51	850	55	18	42.5	Reverse
Dabir 1983 (experimental)	2a	140	500	76	25.8	35.0	Undulated
	2b	140	500	76	12.9	35.0	Jet-like
	2c	140	500	76	12.2	35.0	Jet-like
Kimber and Thew 1974 (experimental)	3	40	51	50	12.7	300	Undulated
Boysan et al. 1982 (computational)	4	1370	42000	203	64	33.0	Jet-like
Pericleous et al. 1984 (computational)	5	56.7	1250	200	80	45.2	------

obtained by using laser doppler anemometry. The velocity data are tabulated in Appendix C.

Both computational papers assume axisymmetric behavior and a model for the Reynolds stress. Boysan et al. [1982] used an algebraic Reynolds stress model and Pericleous, et al. [1984] used a modified Prandtl mixing length model. These results, which are sensitive to the inlet and boundary conditions, will also be examined for similarity in this chapter.

Because the similarity theory assumes that the viscous core is driven by a tangential velocity having the form

$$u_\theta = Kr^N, \quad r \geq \delta^*(z),$$

the experimental (and computational) data should also show this behavior. The important idea is that K and N are independent of the axial coordinate. Specific values of N and K are developed for each data set.

Figure 8.2 shows the behavior of the tangential velocity in the outer region for the data sets in Appendix C. The results of Dabir (Indices 2a,b,c) and of Escudier (Indices 1a,b,c) show that N is approximately -0.75. This is interesting because a Beltrami vortex (see Section 2.2) also shows this type of behavior. However, the vortex device studied by Kimber and Thew (Index 3) shows that $N \approx -0.6$; and, N is about -1.0 for the two computational studies (Indices 4 and 5).

It is noteworthy that N and K do not change significantly with axial position. For example, 1a represents data at $\tilde{z} = 19.35$ cm and 19.85 cm, whereas 2a represents three axial positions: $\tilde{z} = 8$, 20, and 32

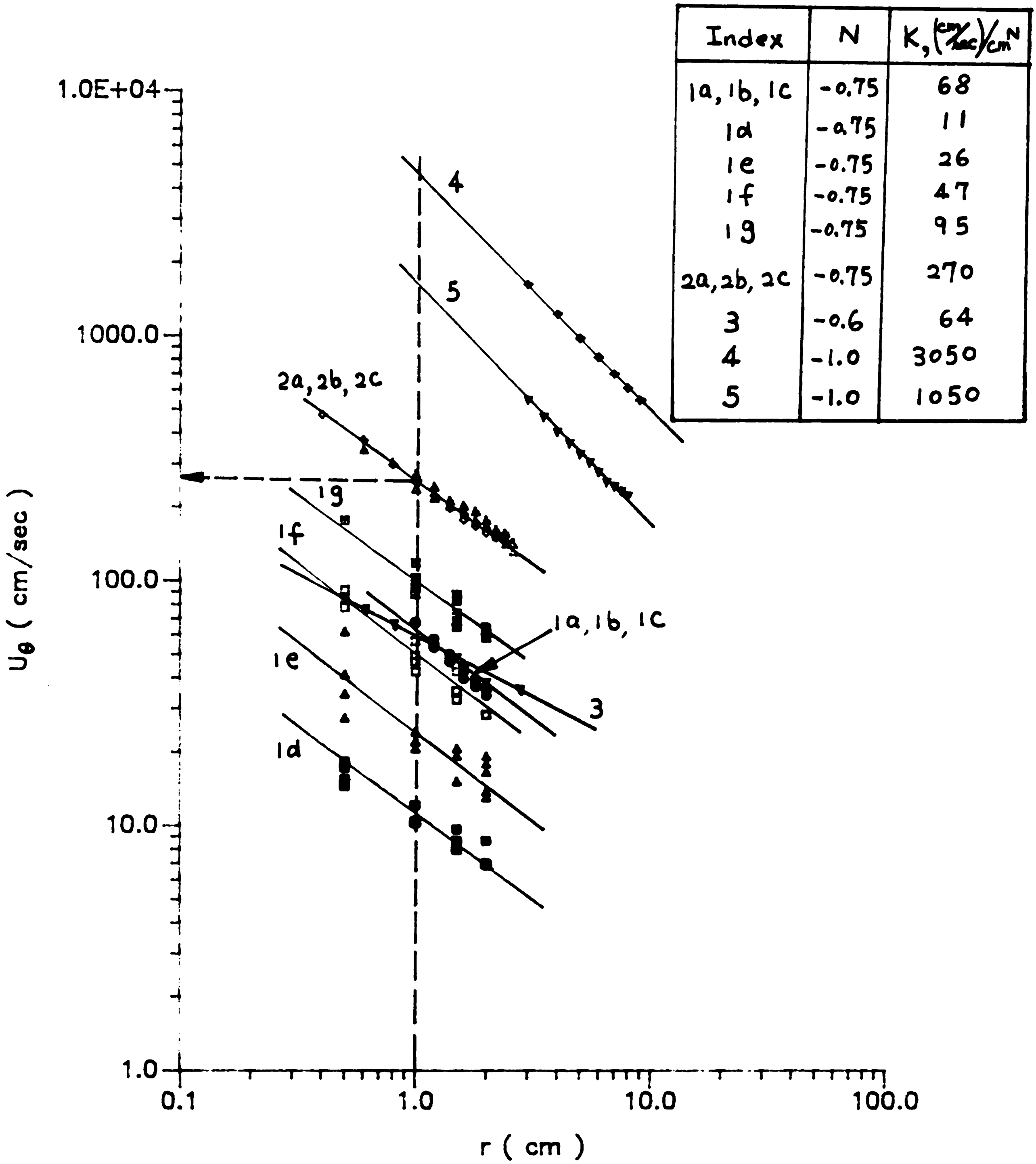

Figure 8.2 Deviation from ideal behaviour in the outer region of several experimental vortex flows

cm. For the data evaluated, N appears to be independent of the flow rate and insensitive to the contraction ratio of the vortex chamber (i.e., D_o/D). The coefficient K, however, is a strong function of Q_o, but not the contraction ratio D_o/D (see experiments 1a - 1c).

8.2 Flow Regimes

Following Eqs. (4.12) and (4.15), the values of 'a' and 'b' are defined by

$$|a| = \frac{|u_z(0,z)|}{u_\theta(\delta,z)} = \frac{|u_o|}{K\delta^N}$$

and

$$b = \frac{\left.\frac{\partial u_\theta}{\partial r}\right|_{r=0}}{\frac{K}{2}\,\delta^{N-1}}$$

$\delta(z)$ can be eliminated between the above two expressions to give

$$\phi(b,N) = \frac{|a|^{(N-1)/N}}{2b} = \frac{K(|u_o|/K)^{(N-1)/N}}{\left.(\partial u_\theta/\partial r)\right|_{r=0}} \tag{8.1}$$

The right-hand-side of Eq. (8.1) can be estimated directly from experimental (or computational) data. The left-hand-side can be calculated theoretically.

Figure 8.3 shows the behavior of $\phi(b,N)$ for $0 < b \le 0.3$ and three values of N. Table 8.2 gives representative numerical values for

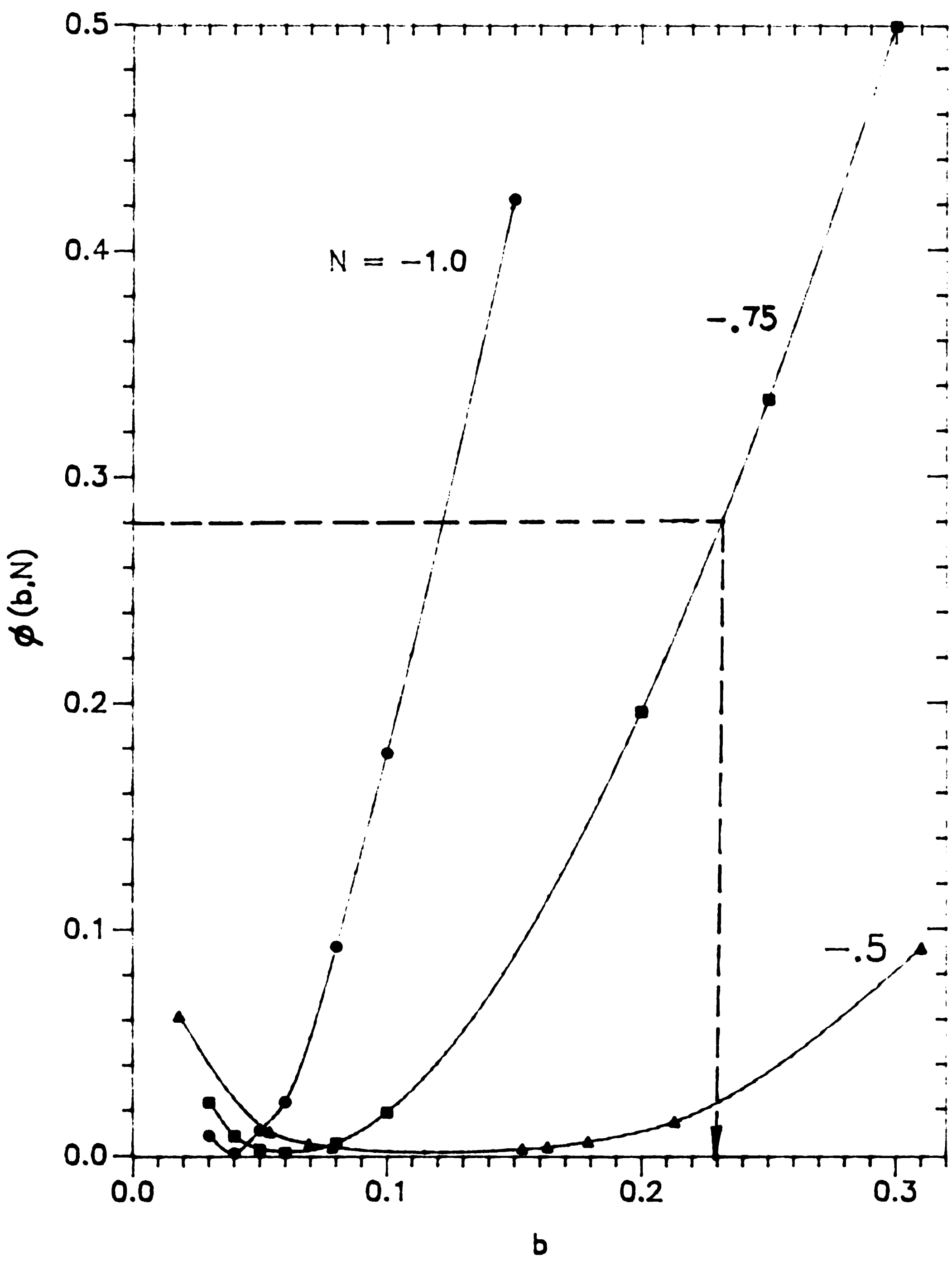

Figure 8.3 Theoretical evaluation for $\phi(b,N)$

Table 8.2 Theoretical evaluation of ϕ (N,b)

b	ϕ (N,b)		
	N = -1	-0.75	-0.5
0.03	0.00778	0.0219	0.0309
0.04	0.000186	0.0708	0.0181
0.05	0.0102	0.00124	0.0103
0.06	0.0227	0.0	0.00555
0.08	0.0915	0.00407	0.00119
0.10	0.177	0.0176	0.0
0.15	0.422	------	------
0.20	0.705	0.195	0.00881
0.25	-----	0.333	0.0305
0.30	1.33	0.498	0.0702
0.50	----	1.39	0.481

$\phi(b,N)$. Figure 8.3 or Table 8.2 can be used to determine the value of 'b' associated with a specific experimental flow. For the family of curves shown in Figure 8.3, the zero of $\phi(b,N)$ moves to larger values of b for larger values of N. For negative values of u_o (flow reversal), the value of b will be located to the left of the zero of $\phi(b,N)$; positive values of u_o (forward flow) correspond to values of b to the right of $\phi = 0$.

Figure 8.3 can be used to predict the flow behavior for each of the data sets in Appendix C. For example, the data set 1e has the following characteristics :

$$(\partial u_\theta / \partial r)|_{r=0} \approx 100\ s^{-1}\ ,\ u_o \approx 27\ cm/s\ ,$$

$$K \approx 26\ (cm/s)/cm^N\ ,\ N \approx -0.75\ .$$

Eq. (8.1) implies that $\phi = 0.28$ and, according to Figure 8.3, this corresponds to $b \approx 0.23$ for $N = -0.75$. Thus, according to Figure 8.4, a vortex flow with $b = 0.23$ has an undulated axial velocity profile. This type of profile was also observed experimentally. The values of b corresponding to the various experiments are listed in Table 8.3.

Figure 8.4 shows values of b vs. N for the experimental studies. The two solid curves represent theoretical boundaries between the three flow regimes : flow reversal, undulated, and jet-like. The symbols in Figure 8.4 correspond to the flow behavior observed in the experiments. When more than one axial position was used to determine b, an average value of b was used to develop Figure 8.3. An error range for b is given in Table 8.3. With the exception of Index 4 for which b =

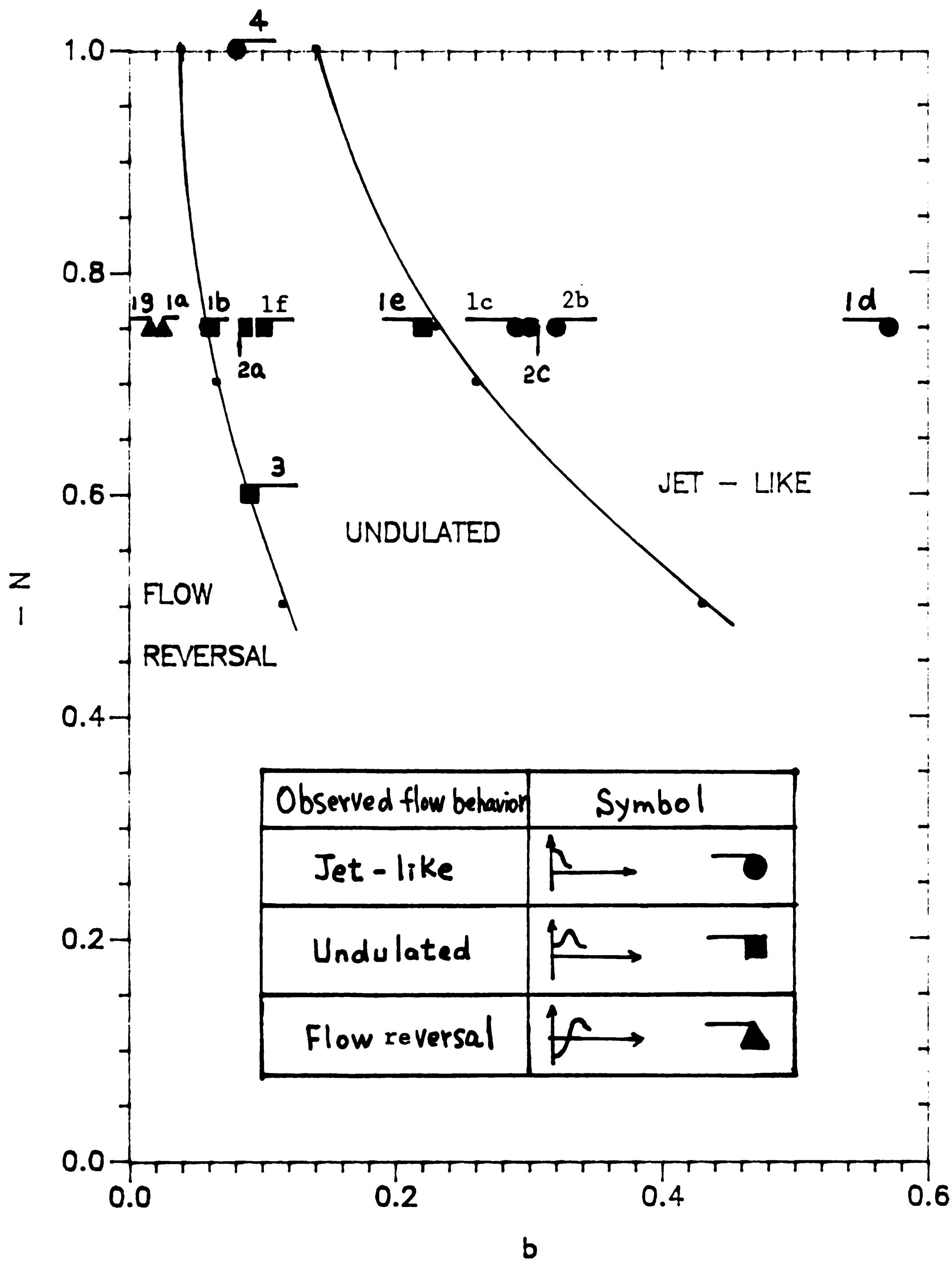

Figure 8.4 Comparison between theoretical and experimental flow behaviour

Table 8.3 Predicted values of b and flow behavior

Index	Experimental Conditions N,K see Figure 8.2				Theory	
	z cm	$(\partial u_\theta/\partial r)_{r=0}$ 1/s	u_o cm/s	Flow Structure	b	Flow Structure
1a	19.35 19.85	160	-24 -23	Reverse	0.025 ± 0.002	Reverse
1b	19.35 19.85	360	3 10	Undulated	0.06 ± 0.003	Undulated
1c	19.35 19.85	800	144 450	Jet-like	0.29 ± 0.02	Jet-like
1d	25.0 28.35 29.45	100	55 51 50	Jet-like	0.57 ± 0.03	Jet-like
1e	25.05 28.35 29.45	100	27.4 25.6 23.8	Undulated	0.22 ± 0.01	Undulated
1f	28.35 31.65	200 140	18 15	Undulated	0.10 ± 0.01	Undulated
1g	21.65 31.65	300 210	-65 -52	Reverse	0.015 ± 0.001	Reverse
2a	20 32	600 400	40 30	Undulated	0.09 ± 0.01	Undulated
2b	20 32	1000	335 375	Jet-like	0.32 ± 0.01	Jet-like
2c	20 32	1000	400 340	Jet-like	0.31 ± 0.01	Jet-like
3	295	2100	0	Undulated	0.12	Undulated
4	19.8 26.4 33.0	850	730 410 290	Jet-like	0.08 ± 0.02	Undulated

0.08±0.02, Figure 8.4 shows that the observed flow behavior is qualitatively consistent with the similarity theory. Because almost all of the calculated values of b are located in the same flow regime as predicted by the similarity theory, this research may be very useful in determining the actual flow behavior of the vortex core.

8.3 Similarity Scaling Of The Centerline Velocity

The centerline axial velocity, $u_z(0,z)$, follows from Eq. (4.12) by letting $\eta = 0$:

$$u_z(0,z) = aK(\nu z/K)^{N/(N+2)} = u_o \; . \qquad (8.2)$$

In Eq. (8.2), z is the distance from the singular point. Measurements of u_o in the laboratory are relative to an arbitrary reference point, rather than the intrinsic singular point of the theory. Because the similarity theory predicts that the magnitude of the centerline axial velocity decreases as z increases, it is necessary to orient the reference coordinate $\tilde{z}$ in the same direction as the intrinsic coordinate z. Thus, in Figure 8.1, $\tilde{z}$ must be chosen in the direction of decreasing $|u_z(o,z)|$, and this is determined experimentally.

If z_o represents the origin (i.e., singular point) of the similarity theory relative to the laboratory reference point, then z_o may be either positive or negative. Thus, with

$$z = \tilde{z} - z_o \; ,$$

Eq. (8.2) can be rewritten as

$$u_o = aK(\nu/K)^{N/(N+2)}[(\tilde{z} - z_o)]^{N/(N+2)}$$

or, equivalently, as

$$|u_o|^{(N+2)/N} = (|a|K)^{(N+2)/N}(\nu/K)(\tilde{z} - z_o) \qquad (8.3)$$

A plot of $|u_o|^{(N+2)/N}$ vs. $\tilde{z}$ will provide

$$\text{slope} = (|a|K)^{(N+2)/N}(\nu/K)$$

and

$$\tilde{z} = z_o \text{ at } |u_o|^{(N+2)/N} = 0 \text{ (extrapolated)}. \qquad (8.4)$$

Figure 8.5 shows how the above expression can be used to estimate z_o from experimental values of u_o. The table in Figure 8.5 lists the values of z_o determined in this manner. Because the data follow the predicted behavior defined by Eq. (8.3), Figure 8.5 provides additional evidence that the similarity theory can be used to describe the viscous core of confined vortex flows.

8.4 Similarity Scaling Of The Angular Momentum Profiles

The similarity theory requires the local circulation, or axial component of angular momentum, to follow the scaling law

$$\frac{ru_\theta(r,z)}{\delta(z)u_c(z)} = F\left(\frac{r}{\delta(z)}\right) .$$

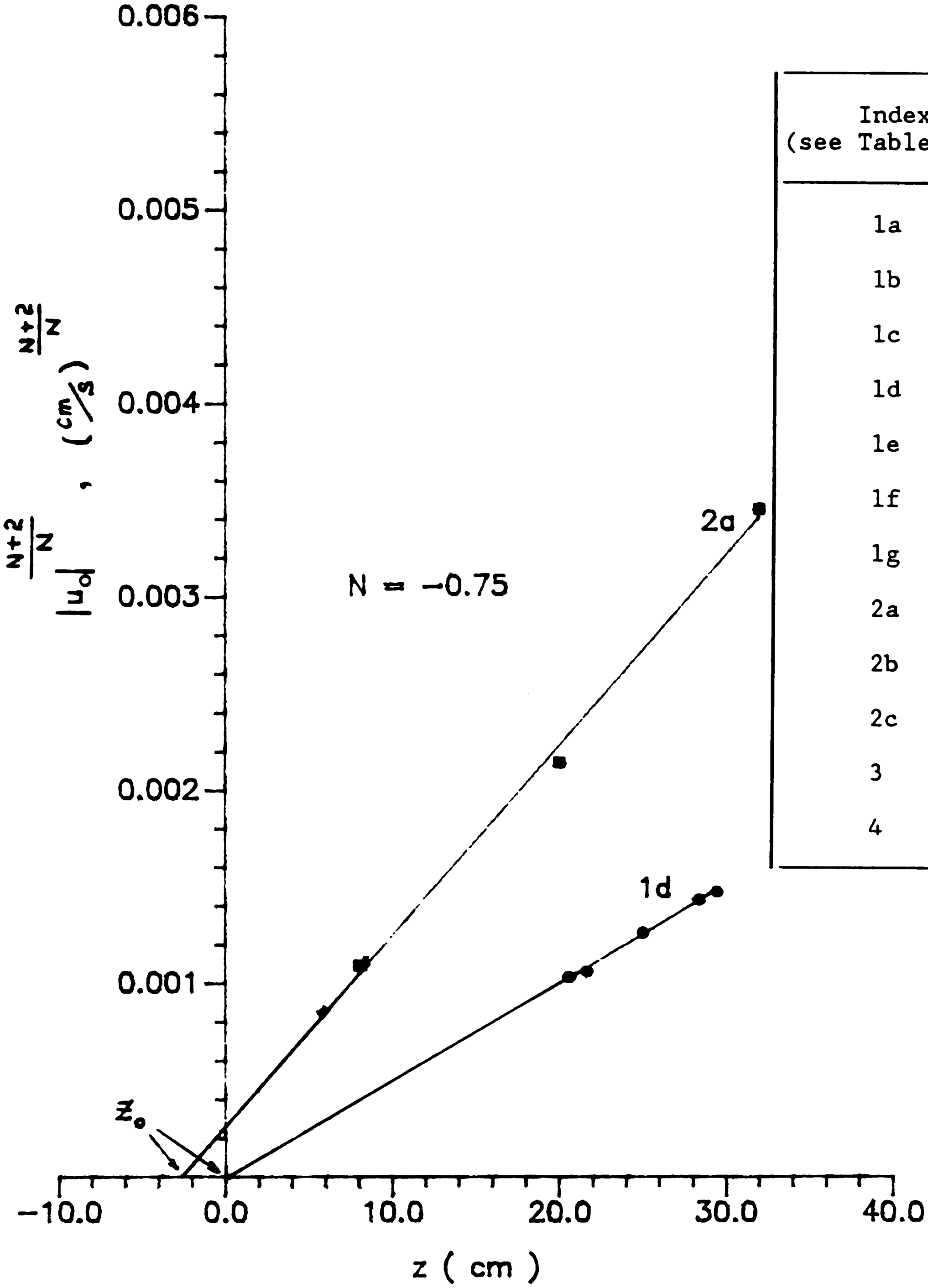

Index (see Table 8.1)	z_o , cm
1a	(2.5)
1b	2.5
1c	(2.5)
1d	0
1e	3.0
1f	3.0
1g	3.5
2a	-2.5
2b	(-2.5)
2c	(-2.5)
3	(0)
4	2.0

Figure 8.5 Similarity scaling of the centerline velocity

Because (see Eqs. (3.37) - (3.38)) $\delta u_c \propto \delta^{N+1}$ and $\delta \propto z^{1/(N+2)}$, a plot of $(ru_\theta)/(z^{(N+1)/(N+2)})$ vs. $r/(z^{1/(N+2)})$ for different values of r and z should fall on the same curve. Figure 8.6 and 8.7 show that the data for Index 1d and Index 2a (see Table 8.1) fall approximately on the same curve, which indicates that a similarity structure obtains.

All of the experimental velocity profiles used in this chapter fall outside the region about the singular point where the pressure is negative. With z^o defined by $p(0,z^o) = 0$, Eq. (4.19) in Chapter 4 can be used to determine z^o for a specific data set. For example, for the data presented in Figure 8.6, the parameter 'b' was estimated to be about 0.57 (see Table 8.3, Index 1d). From Figure 8.2, N = -0.75 and K = 11 $(cm/s)/cm^N$. A theoretical estimate for 'c' follows directly from Figure 7.3 : for b = 0.57, c = 0.13. Therefore, if $p^o \approx 1$ atm (1.01 bars) and if $K/\nu = 340\ cm^{-(N+1)}$ (see Table 8.4), then $z^o \approx 0.034$ cm (see Eq. (4.19)). The smallest value of $\tilde{z}$ used in Figure 8.6 is 10 cm >> z^o. Similarly, $z^o \approx 3.1$ cm for the data analyzed in Figure 8.7, which is much smaller than $\tilde{z} = 20$ cm.

8.5 Viscosity Estimates

Eq. (4.15) relates b to the viscosity coefficient ν. Thus, once b, K, N, z_o, and the angular velocity at the axis have been determined, the viscosity coefficient can be calculated from

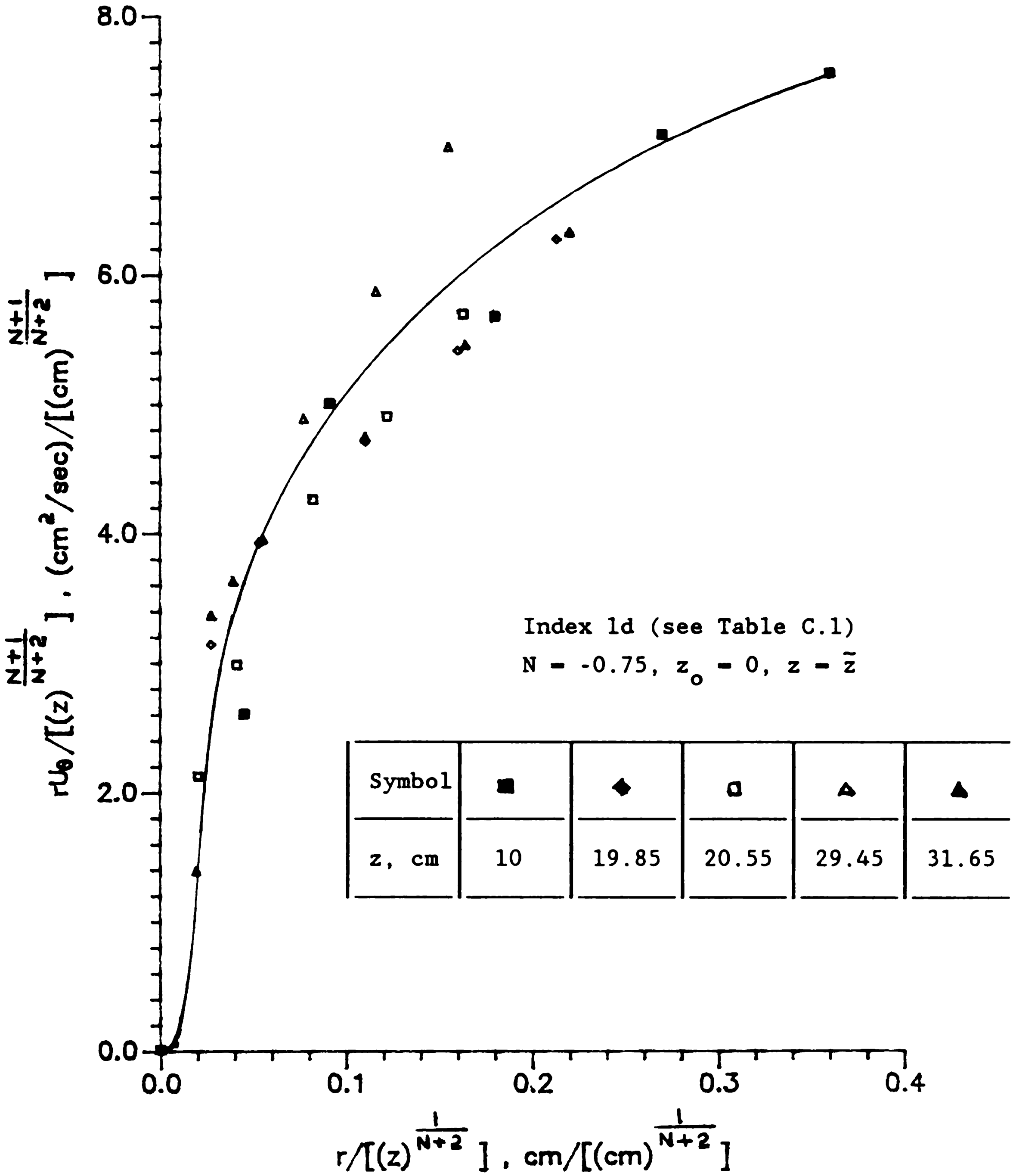

Figure 8.6 Similarity scaling of the angular momentum (data from Escudier et al., 1982)

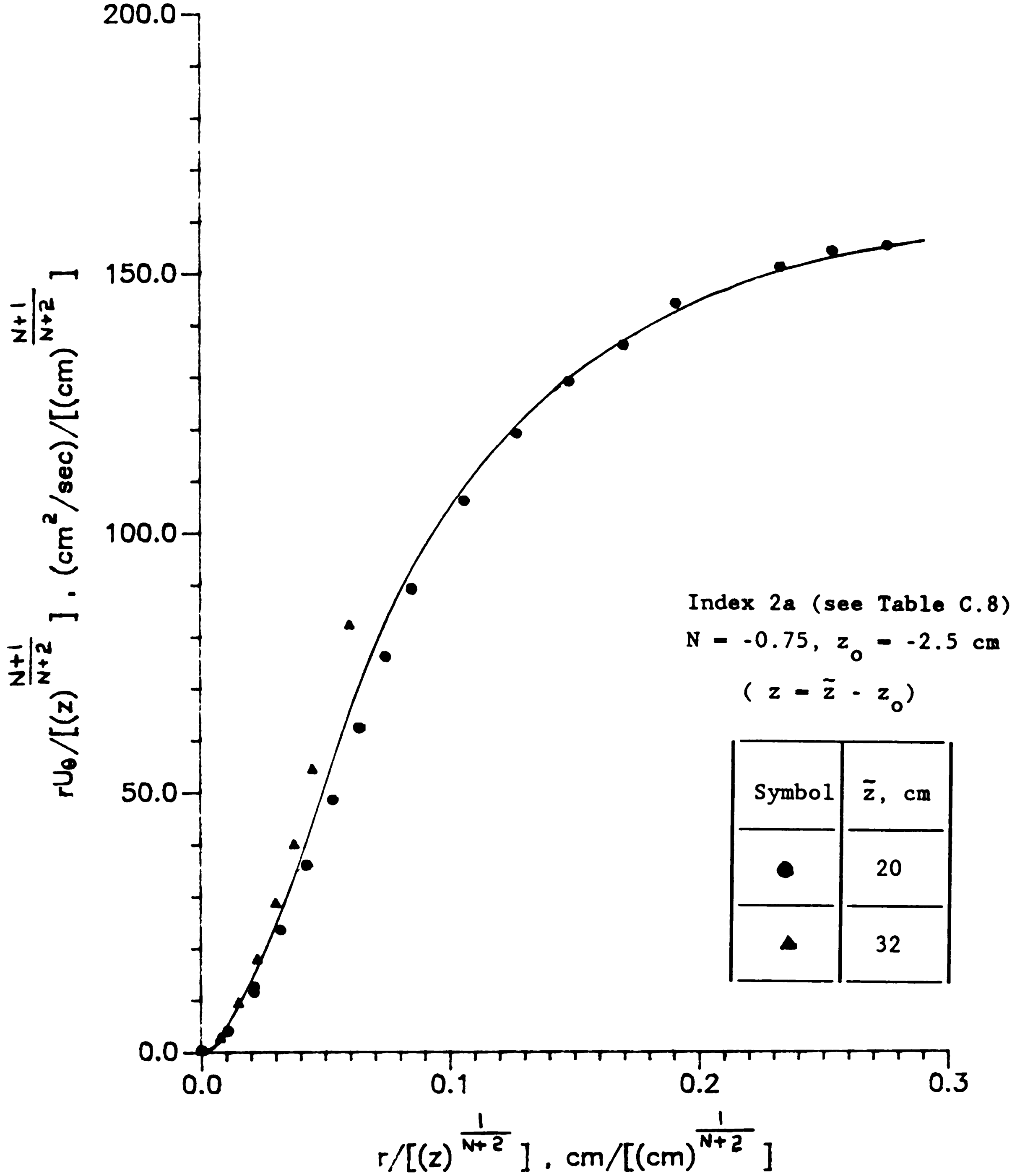

Figure 8.7 Similarity scaling of the angular momentum (data from Dabir, 1983)

$$\nu = \frac{K}{(\bar{z} - z_o)} \left(\frac{2(\partial u_\theta / \partial r)|_{r=0}}{bK} \right)^{\frac{N+2}{N-1}} .$$

Table 8.4 gives the values of ν for each experimental data set in Appendix C.

For data sets 1a - c, the viscosity coeffient was found to be about 0.11 cm^2/s. Obviously, ν cannot be interpreted as a fluid parameter inasmuch as the molecular kinematic viscosity for liquid water is about an order of magnitude smaller. Thus, the similarity theory applied to laboratory scale vortex flows should be interpreted as a mathematical model for the mean field with a Boussinesq approximation for the shear components of the Reynolds stress (see Chapter 1, Hinze, 1975).

The boundary layer approximations used in Chapter 3 only retained the $r\theta$ - and rz - components of the viscous stress. Thus, a consistent extension to the mean field equations for turbulent flows requires

$$\langle u_r' u_\theta' \rangle = - \nu_e r \frac{\partial}{\partial r} \left(\frac{\langle u_\theta \rangle}{r} \right) \tag{8.5}$$

and

$$\langle u_r' u_z' \rangle = - \nu_e \left(\frac{\partial \langle u_z \rangle}{\partial r} + \frac{\partial \langle u_r \rangle}{\partial z} \right) \tag{8.6}$$

where $\langle u_\theta \rangle$ and u_θ' represent, resp., the mean and fluctuating components of the tangential velocity. The turbulent coefficient of viscosity (or "eddy" viscosity) appearing in Eqs. (8.5) and (8.6) depends on the flow

Table 8.4 Viscosity estimates based on the similarity theory

Index	Flow Conditions K, N see Table 8.2 b see Table 8.3 z_o see Figure 8.5			Viscosity Coefficient	K/ν ,
	Flow rate Q_o , cm^3/s	Contraction Ratio D_o / D	Flow Regime	ν, cm^2/s	$cm^{-(N+1)}$
1a	400	0.73	Reverse	0.11 ± 0.01	620 ± 60
1b		0.45	Undulated		
1c		0.18	Jet-like		
1d	100	0.33	Jet-like	0.034 ± 0.003	324 ± 30
1e	200		Undulated	0.075 ± 0.07	346 ± 35
1f	411		Undulated	0.11 ± 0.01	427 ± 50
1g	850		Reverse	0.062 ± 0.004	1500 ± 100
2a	140	0.34	Undulated	1.1 ± 0.3	246 ± 70
2b		0.17	Jet-like		
2c		0.16	Jet-like		
3	40	0.25	Undulated	0.049	1300
4	1370	0.40	Jet-like	50 ± 18	60 ± 18

and may change significantly with either r or z (see, for example, Bloor and Ingham [1984]). Here, however, ν_e must be considered constant.

Table 8.4 indicates that the contraction ratio D_o/D, which determines the type of flow regime in the vortex core, does not affect the "eddy" viscosity ν_e ($= \nu$). However, as the flow rate decreases (see indices 1d - 1g), the estimated value of ν changes from 0.062 cm^2/s at $Q_o = 850$ cm^3/s to 0.034 cm^2/s at $Q_o = 100$ cm^3/s. The experiments of Dabir (Indices 2a - 2c) yield values of ν_e about an order of magnitude larger than observed by Escudier at lower flow rates. It is noteworthy that both Dabir's and Escudier's data show that ν_e may not be affected by the contraction ratio D_o/D. The experiments of Kimber and Thew (Index 3) are also consistent with the above results and give $\nu_e = 0.049$ cm^2/s for $Q_o = 40$ cm^3/s and $D_o/D = 0.25$. The computational results of Boysan (Index 4) suggest that $\nu_e \approx 50$ (± 18) cm^2/s for $Q_o = 1370$ cm^3/s.

8.6 Entrainment Rates

A dimensionless entrainment rate into the vortex can be calculated from Eq. (3.43),

$$\frac{1}{2\pi\nu}\frac{dQ}{dz} = h(\eta^*). \qquad (8.7)$$

For fixed values of N and b, $h(\eta^*)$ is uniquely determined by the similarity theory (see Chapter 7, Figure 7.6). The local volumetric flow rate Q(z) at various values of z (or $\tilde{z}$, see Figure 8.1) can be calculated from

$$Q(z) = 2\pi \int_0^{\delta^*(z)} u_z(r,z) r dr$$

where $\delta^*(z)$ corresponds to $u_z \approx 0$. The actual graphs for $u_z(r,z)$ at different axial positions presented by Escudier et al. [1980, 1982] were very small and difficult to read. Estimates for u_z obtained from these figures, which have been tabulated in Appendix C, are subject to error. A rough judgment is that Q can only be determined to within 30 % using this information.

Figure 8.8 illustrates how dQ/dz was determined from the experimental data, a process which introduces significant error. Nevertheless, a dimensionless entrainment rate was estimated by using the values of ν listed in Table 8.4; the results are shown in Figure 8.9. Figure 8.9 compares the theoretical values of $h(\eta^*)$ corresponding to (b,N) with the experimental estimate of $h(\eta^*)$ using Q(z) and ν (see Eq. (8.7)). Although the correlation between these two methods for determining $h(\eta^*)$ is less than desirable, Figure 8.6 provides a critical test of the similarity theory.

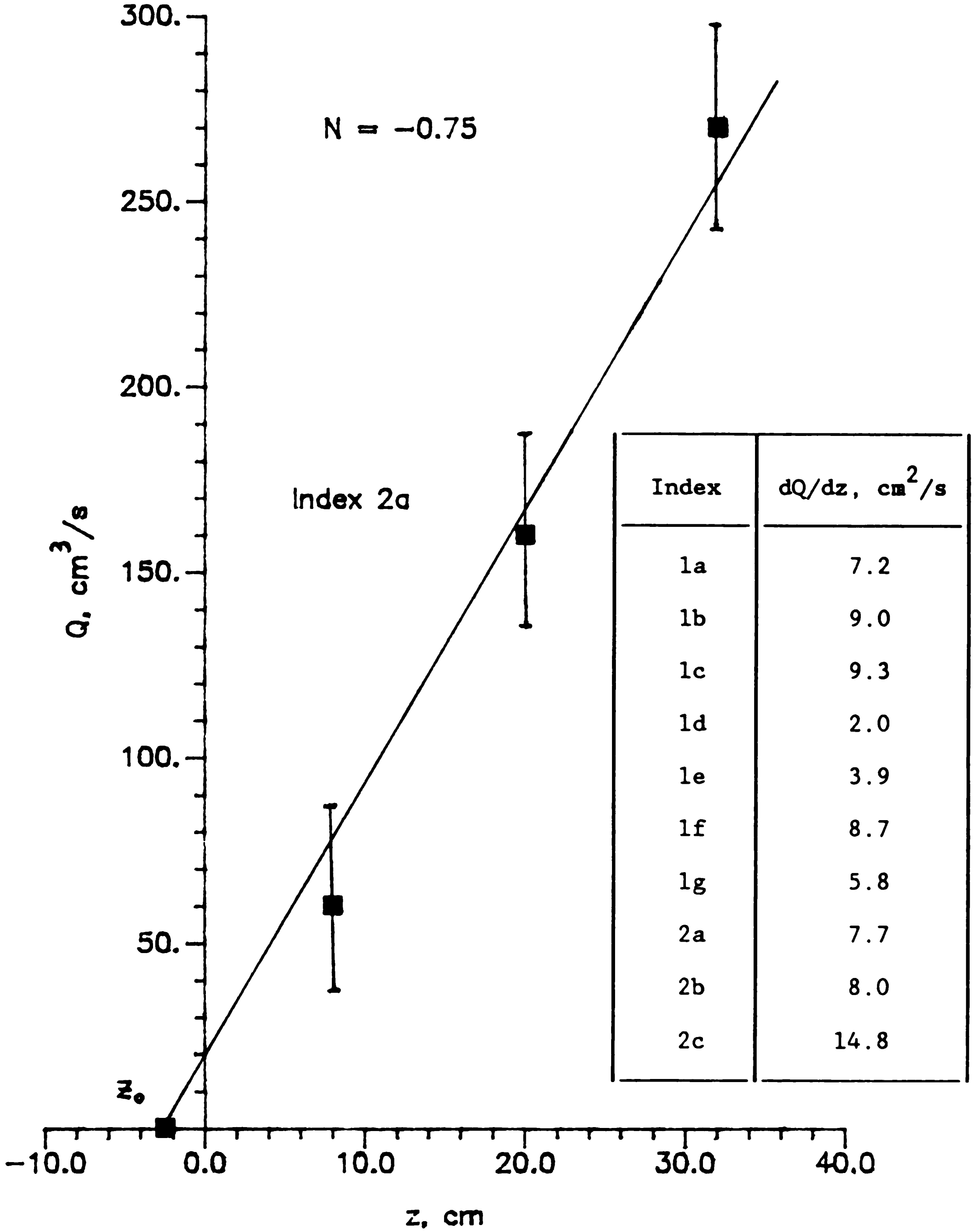

Index	dQ/dz, cm^2/s
1a	7.2
1b	9.0
1c	9.3
1d	2.0
1e	3.9
1f	8.7
1g	5.8
2a	7.7
2b	8.0
2c	14.8

Figure 8.8 Estimates of entrainment rates

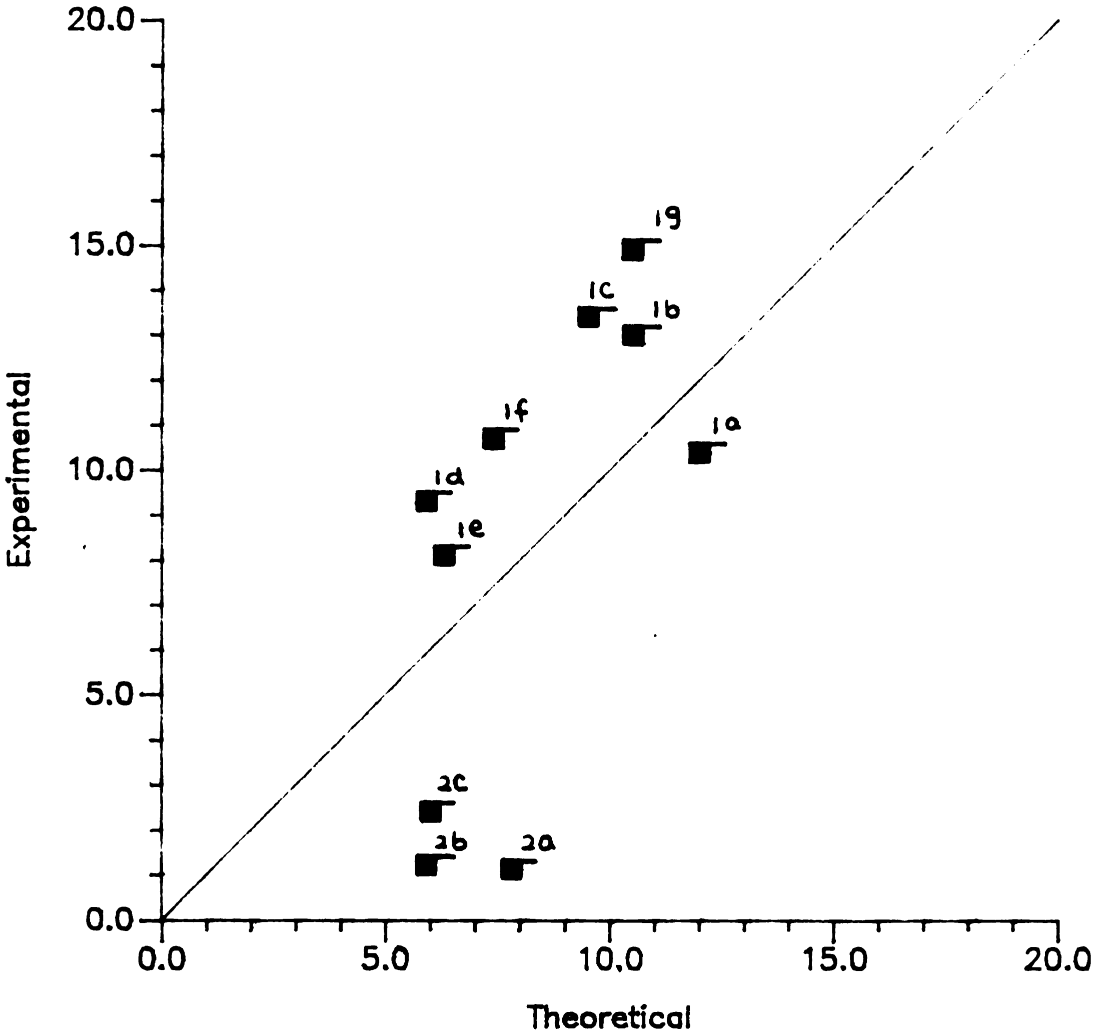

Figure 8.9 Comparison between theoretical and experimental entrainment rates

CHAPTER 9

PARTICLE EQUILIBRIUM ORBITS WITHIN THE CORE REGION OF VORTEX FLOWS

9.1 Background

An important application of swirling flows is the separation and classification of very fine particles. Oil - water separation and coal beneficiation are significant examples. Hydrocarbon contamination of the oceans by oil tankers and offshore platforms is obviously undesirable, and an efficient process for removing small amounts of crude oil from a continuous phase could lessen the enviromental impact of these energy sources. Equipment already exist for cleaning oily water but, unfortunately, these filter-coalescer systems require long residence time and are typically large in size and mass, a feature which is especially bothersome on offshore platforms where space is limited. An oily water clean-up system with a large throughput and a short mean residence time is clearly desirable and Colman et al. [1980] have suggested that hydrocyclones be used for this application.

Thew and his coelleagues (see, Colman and Thew, 1980; Colman et al., 1980; Smyth et al., 1980; Colman and Thew, 1983; Smyth et al., 1984; Thew et al., 1980; Kimber and Thew, 1974) over the past decade have been studying the possibility of using hydrocyclones for oil/water separations. To stabilize the central vortex region within the hydrocyclone, they have developed the concept of a co-axial withdrawal of fluid through the vortex finder (Colman and Thew, 1980). With this modification, they were able to increase the ratio of the overflow concentration of dispersed component (by volume) to the feed concentration from 20 : 1 to 160 : 1 in a 30 mm cylindrical hydrocyclone. The experiments were developed for Kuwait crude with density equal to 0.86 g/cm^3; mean particle diameter, 41 microns; and, feed concentration, 1000 ppm by volume. Earlier, Kimber and Thew [1974] studied the separation of Roxstone oil from water with drop sizes in the range 40 - 50 microns. They were able to separate 90 % of the oil. For the hydrocyclone design shown in Figure 8.1 (design c), Colman et al. [1980] obtained 99% separation for a drop size of 55 microns, but only 75% separation for 23 microns. They used Forties crude with the following physical properties : ρ_p = 0.84 g/cm; feed concentration = 1000 ppm. Similar effects were observed for Kuwait crude. Obviously, the particle size plays a critical role in the performance of hydrocyclones. More recent design modification have been developed at Southampton University, U.K. (see Colman et al., 1980) with some additional improvements in separation performance, but the ubiquitous drop in efficiency for particle sizes between 20-40 microns remains. Is this phenomenon a result of the specific design or an intrinsic property of the flow structure of a viscous vortex ?

The above results of Thew partly motivated the investigation of this chapter, which explores the behavior of very fine particles in a vortex flow. The model developed in Chapter 7 is used to calculate the equilibrium orbits of spherical particles and to develop some understanding of how the complex flow patterns within a viscous vortex could possibly account for the apparent low efficiency of separation of very fine particles.

Within a cyclone separator, particles with densities larger than the continuous phase migrate to the outer region and are removed by a helical flow directed toward the underflow. Likewise, particles with densities less than the continuous phase migrate toward the core of the vortex and are removed by an upward helical flow. The viscous drag on very fine particles (<< 500 microns) resist the relative migration due to differences in density and may, in some situations, balance the net centrifugal force acting on the particles. Thus, if the particle residence time within the vortex is sufficiently long, then equilibrium orbits may occur. Many investigators (see p.44 Svarovsky, 1984) have used this idea to study the effect of hydrodynamic parameters on the separation performance of heavy (i.e., $\rho_p > \rho_f$) particles inasmuch as in the outer region of the vortex field an inwardly directed radial flow drags the particles away from the conical wall. An analogous phenomenon may also occur for light particles (i.e., $\rho_p < \rho_f$) in the central core region of a hydrocyclone operating without an air core (see Dabir and Petty, 1984b; Listewnik, 1984; and, Chen and Petty, 1986).

9.2 Theory

Criner and Driesser (see p.44 Svarovsky, 1984) first proposed the concept of the equilibrium orbit. According to this concept, a particle in a hydrocyclone flow achieves an equilibrium orbit at a radial position where its terminal settling velocity equals the radial velocity of the continuous phase. If the equilibrium orbit lies inside the locus of zero axial velocity, the particle leaves the cyclone through the vortex finder (see Figure 8.1) due to the upward motion of the fluid.

Otherwise, it moves toward the underflow due to the downward motion of the fluid. In this study, several assumptions are made :

1. The axial and tangential components of the particle velocity are the same as the continuous phase;
2. The discrete particles are spherical and $\rho_p < \rho_f$;
3. Particle acceleration times are small, so the viscous drag on the particle balances the net centrifugal force on the particle everywhere in the flow field; and,
4. Stoke's law applies (see, p.59 Bird et al., 1960).

Because $\rho_p < \rho_f$, the net centrifugal force acting on the particles is directed toward the axis and has a magnitude given by

$$F_c = \frac{\pi d_p^3}{6} (\rho_f - \rho_p) \frac{u_\theta^2}{r} \geq 0. \qquad (9.1)$$

In Eq. (9.1), d_p represents the diameter of the particle with density ρ_p; ρ_f denotes the density of the continuous fluid phase. u_θ is the tangential velocity of the fluid.

The viscous drag on the particle is directed away from the axis if $u_r > u_{pr}$, and toward the axis if $u_r < u_{pr}$. The magnitude of this force, according to Stoke's law, is

$$F_v = 3\pi\mu d_p (u_r - u_{pr}) \qquad (9.2)$$

where u_{pr} represents the radial component of the particle velocity and μ is the <u>molecular</u> viscosity of the fluid. The difference between the fluid and particle velocities is often called the "terminal" velocity.

Svarovsky [p7, 1984] argues that the time needed for a particle to achieve its terminal settling velocity is very small (≈ milliseconds). Therefore,

$$F_v = F_c \tag{9.3}$$

is a good practical approximation in the entire flow field.

Eqs (9.1) - (9.3) imply that

$$u_{pr} = u_r - \tau_p \frac{u^2_\theta}{r} \tag{9.4}$$

where the characteristic time τ_p for the particle is given by

$$\tau_p = \frac{1}{18} \frac{d^2_p}{\nu} (1 - \frac{\rho_p}{\rho_f}) \tag{9.5}$$

The sign of u_{pr} obviously depends on the relative magnitudes of u_r and $\tau_p u_\theta^2/r$. Obviously, if $u_r < \tau_p u_\theta^2/r$, the particle migrates toward the axis. If on the other hand $u_r > \tau_p u_\theta^2/r$, then the particle moves away from the axis. The <u>equilibrium orbit</u> is defined by

$$u_{pr}(r_E, z_E) = 0. \tag{9.6}$$

From Eq (9.4), this implies that

$$u_r(r_E,z_E) = \tau_p \frac{[u_\theta(r_E,z_E)]^2}{r_E} \tag{9.7}$$

Eq. (9.7) defines the locus of points (r_E,z_E) in the flow domain for which Eq. (9.6) holds. The radial and tangential components of the fluid velocity can be related to the previously developed similarity theory (see Table 3.2 and Chapter 7) :

$$u_r = u_c \frac{d\delta}{dz}\left(h' - (N+2)\frac{h}{\eta}\right) \tag{9.8a}$$

$$u_\theta = u_c \frac{F}{\eta} \tag{9.8b}$$

$$u_c = K\delta^N \tag{9.8c}$$

$$\delta = \left(\frac{\nu_e z}{K}\right)^{\frac{1}{N+2}} \tag{9.8d}$$

The viscosity coefficient which affects the relaxation time τ_p is the <u>molecular</u> kinematic viscosity of the fluid. The viscosity coefficient ν_e in the similarity parameter $\delta(z)$ should be interpreted as an "eddy" viscosity (see Section 8.5).

By inserting Eqs. (9.8a) and (9.8b) into Eq. (9.7) and rearranging the result, it follows that

$$\left[\frac{\tau_p u_c}{\delta \frac{d\delta}{dz}} \right]_{z=z_E} = \left[\frac{\eta(h' - (N+2)\frac{h}{\eta})}{(\frac{F}{\eta})^2} \right]_{\eta=\eta_E} \tag{9.9}$$

The left-hand-side can be interpreted as a intrinsic Stokes' number (cf. Svarovsky, p8). It depends explicitly on the properties of the particles (d_p, ρ_p/ρ_f), the intrinsic properties of the continuous phase (μ, ρ_f), and the parameters used to characterize the vortex flow (N, K, ν_e). The right-hand-side depends explicitly on N and the dimensionless spin parameter b (see Eq. (4.15)). Thus, for a given similarity surface η_E, Eq. (9.9) gives an expression for z_E. Because $\eta = r/\delta(z)$, the corresponding value of r_E can easily be calculated as

$$r_E = \eta_E \delta(z_E) = \eta_E \left(\frac{\nu_E z_E}{K}\right)^{\frac{1}{N+2}} \tag{9.10}$$

Thus, with the Stokes number for an arbitrary similarity surface defined by

$$Sk(\eta;b,N) = \left[\frac{\eta(h' - (N+2)\frac{h}{\eta})}{(\frac{F}{\eta})^2} \right]_{\eta=\eta_E} , \tag{9.11}$$

it follows from Eq. (9.9) that

$$\tau_p K(N+2) z_E [\delta(z_E)]^{N-2} = Sk(\eta_E;b,N)$$

which easily rearranges to

$$z_E = \left(\frac{Sk(\eta_E;b,N)}{\tau_p \nu_e (N+2)} \right)^{\frac{N+2}{2N}} \left(\frac{K}{\nu_e}\right)^{\frac{2}{-N}} . \tag{9.12}$$

Thus, for a given similarity surface η_E, Eqs. (9.10) and (9.12) determine the position of the equilibrium orbit, defined by Eq. (9.6), for a given set of physical parameters : N, b, K/ν_e, $\tau_p \nu_e$. The set of points (r_E, z_E) calculated for $0 \leq \eta_E < \eta^*(b,N)$ defines the equilibrium orbit surface for a specific flow structure.

9.3 Stability Of The Equilibrium Surface

An equilibrium surface consists of all points (r_E, z_E) in the flow domain for which the terminal velocity of the dispersed phase equals the local velocity of the fluid phase. The equilibrium surface is locally stable if a particle in the neighborhood of the surface tends to move toward the surface. It is locally unstable if the particle moves away from the surface. For a given flow situation, the equilibrium surface can be very complex. It may have regions which are locally unstable and regions which are stable. Figure 9.1 illustrates the above stability definition and Figure 9.2 shows the type of behavior which occurs for forward flow and reverse flow vortices.

Figure 9.1 shows a portion of an equilibrium surface. Above the surface, the radial velocity of the dispersed phase is outward; and,

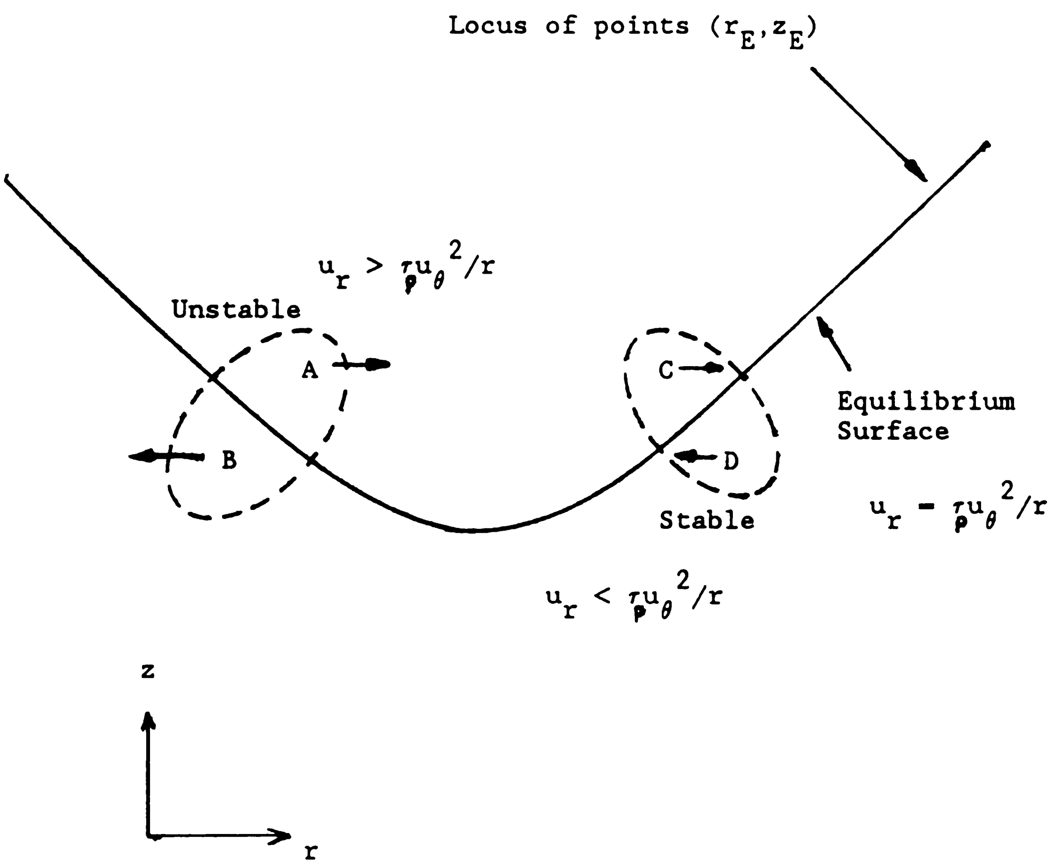

Figure 9.1 Definition of a stable and unstable equilibrium surface

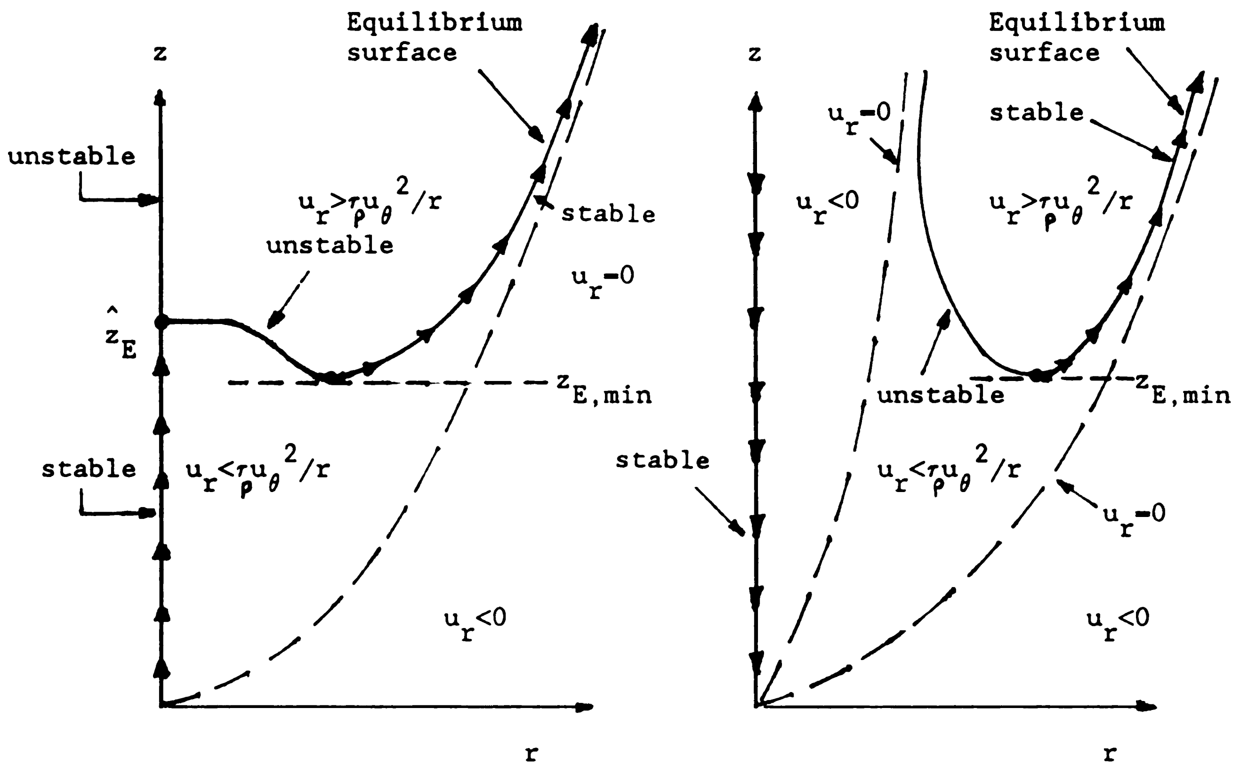

(a). Forward flow (b). Reverse flow

Figure 9.2 Stability of equilibrium surfaces for forward and reverse flow vortices below the surface, the radial velocity of the dispersed phase is inward (see Eq. (9.4)). Thus, points 'A' and 'B' are unstable because they tend to leave the local neighborhood of the equilibrium surface and, as indicated, points 'C' and 'D' are stable.

Figure 9.2 illustrates in more qualitative detail the geometry of the equilibrium surface for a forward flow vortex (a > 0) and a reverse flow vortex (a < 0). It follows directly from Eq. (9.4) that on the axis $u_{pr} = 0$, because both u_r and u_θ are zero. Because $u_r < 0$ near the axis for reverse flows (see Section 4.2), the set of points $r_E = 0$, $0 < z_E < \infty$ represents stable orbits provided a < 0 (reverse flow).

For forward flow, $u_r > 0$ near the axis and eventually exceeds $\tau_p u_\theta^2/r$ for large values of z. This value, defined as $\hat{z}_E$, follows directly from Eqs. (9.11) and (9.12) by setting $\eta_E = 0$:

$$Sk(0;b,N) = -2N\frac{a}{b^2} \tag{9.13}$$

$$\hat{z}_E = \left(\frac{-2Na/b^2}{\tau_p K(N+2)} \right)^{\frac{N+2}{2N}} \left(\frac{K}{\nu_e}\right)^{\frac{N-2}{2N}} . \tag{9.14}$$

Numerical calculations show that for $z > \hat{z}_E$, $u_r > \tau_p u_\theta^2/r$ near the axis; and, for $z < \hat{z}_E$, $u_r < \tau_p u_\theta^2/r$ near the axis.

Figure 9.2 shows multiple equilibrium orbits for a fixed axial position. Below $z_{E,min}$, the orbit is unique for both situations and occurs on the axis. For $z > z_{E,min}$ and a < 0, three orbits exist.

Stable solutions occur on the axis and on the branch near the outer surface of zero radial velocity. An unstable solution occurs near the inner surface of zero radial velocity. For $a > 0$ and $z > \hat{z}_E$, an unstable orbit occurs on the axis (as previously mentioned) and a stable solution exist near the 'mantle', defined by $u_r = 0$. For $z_{E,min} < z_E < \hat{z}_E$ and $a > 0$, three solutions exist (see Figure 9.2a). For larger values of b, this region disappears and the branch leaving the axis at $\hat{z}_E$ is stable. The surface $z_E(r_E)$ in this case has a parabolic structure.

9.4 Results

The dimensional equilibrium surface (r_E, z_E) can be constructed for a specific set of parameters b, N, K/ν_e, and $\tau_p \nu_e$. The dimensionless parameters b and N uniquely determine the similarity structure of the vortex: jet-like flow, undulated flow, or reverse flow (see Figure 7.2). Because the experimental studies of Dabir [1983] and Escudier et al. [1980, 1982] correspond to $N = -0.75$ (see Figure 8.2), this value of N is used in the parameter calculations presented here. The effect of the flow structure on the quantitative behavior of the equilibrium surface is examined for $b = 0.03$ (flow reversal), $b = 0.10$ (undulated flow), and $b = 0.30$ (jet-like flow). Although the empirical dimensional parameter K/ν_e may depend implicitly on b (see Table 8.4), a nominal value of 500 $cm^{-(N+1)}$ is used for the equilibrium orbit calculations.

The numerical value of $\tau_p \nu_e$ depends on several physical properties and, most importantly, the particle diameter d_p. Eq. (9.5) implies that

$$\tau_p \nu_e = \frac{d_p^{\,2}}{18} (1 - \rho_p/\rho_f) \frac{\nu_e}{\nu}. \tag{9.15}$$

Figures 9.3 - 9.5 show the equilibrium surfaces calculated using Eqs. (9.10) and (9.12). Three different values of $\tau_p \nu_e$ are presented for each flow situation; Table 9.1 relates these values to a specific particle size, density ratio, and ν_e/ν. The dimensionless Stokes number, defined by Eq. (9.11), parameterizes each equilibrium surface for a fixed value of $\tau_p \nu_e$. The magnitude of $Sk(\eta_E;b,N)$ at representative points are indicated on each curve.

9.5 Discussion

Figure 9.3 shows an equilibrium surface for jet-like flow ($b = 0.3$, see Figures 7.7 - 7.9). As previously discussed, stable orbits only exist on the axis for $z < \hat{z}_E$ and on the branch near the outer surface of the zero radial velocity (see Figure 9.2a). Therefore, a particle with diameter 32 microns (see Figure 9.3 for other parameters) will obtain its stable orbit through two possible ways. If the particle reaches the stable axis first, it will follow the axis and move upwards until it reaches $\hat{z}_E$. Above that point, the particle will move away from the axis; if the residence time is long enough, the particle will reach the outer equilibrium surface and continue to move upwards and away from the

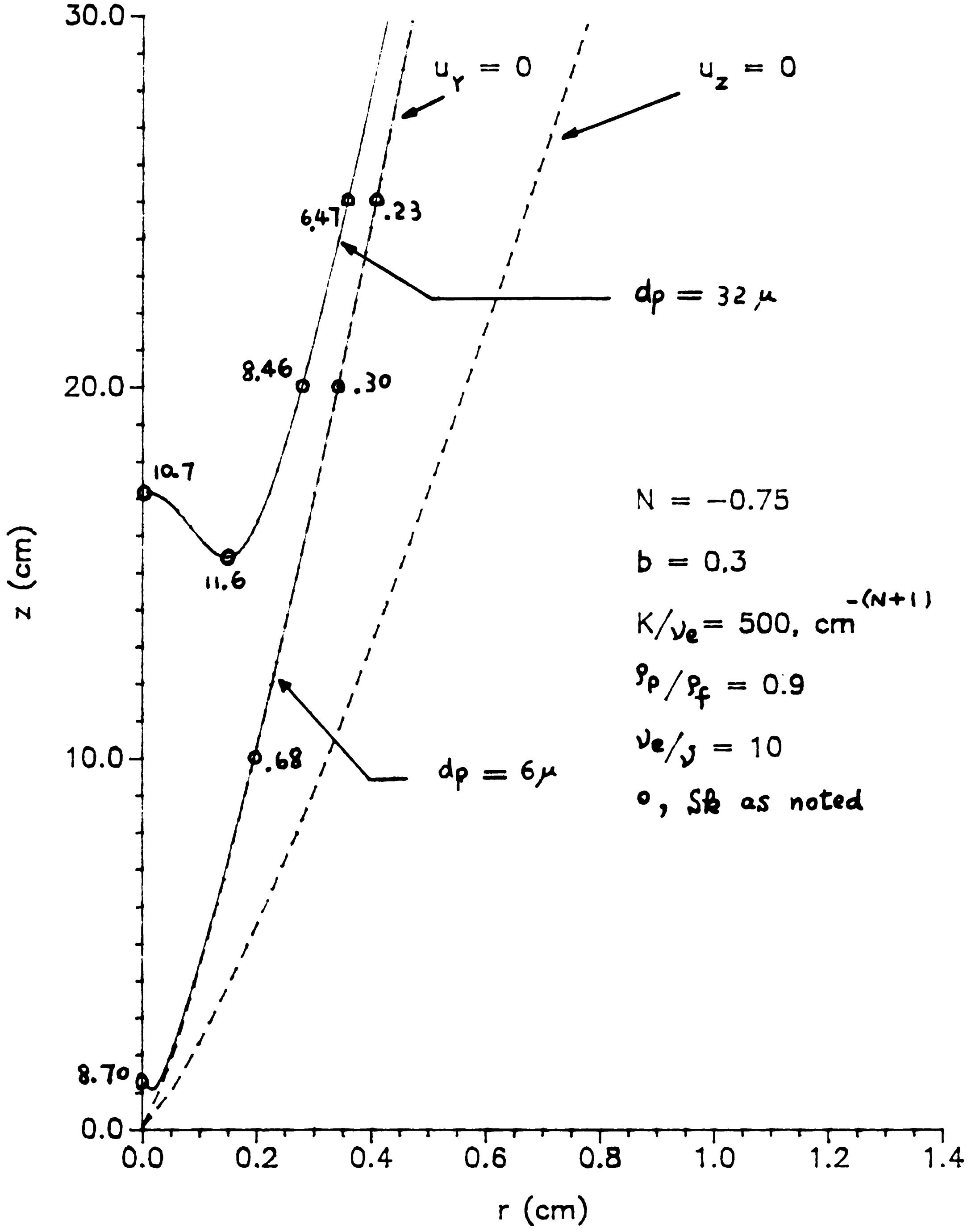

Figure 9.3 Equilibrium surfaces for jet-like flow

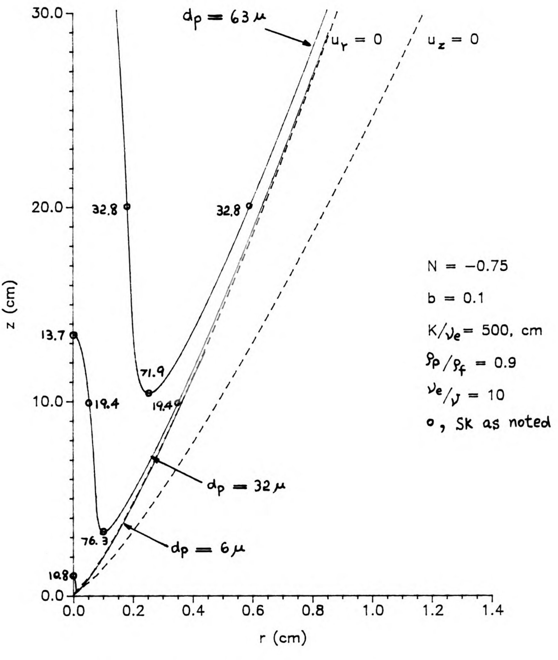

Figure 9.4 Equilibrium surfaces for undulated flow

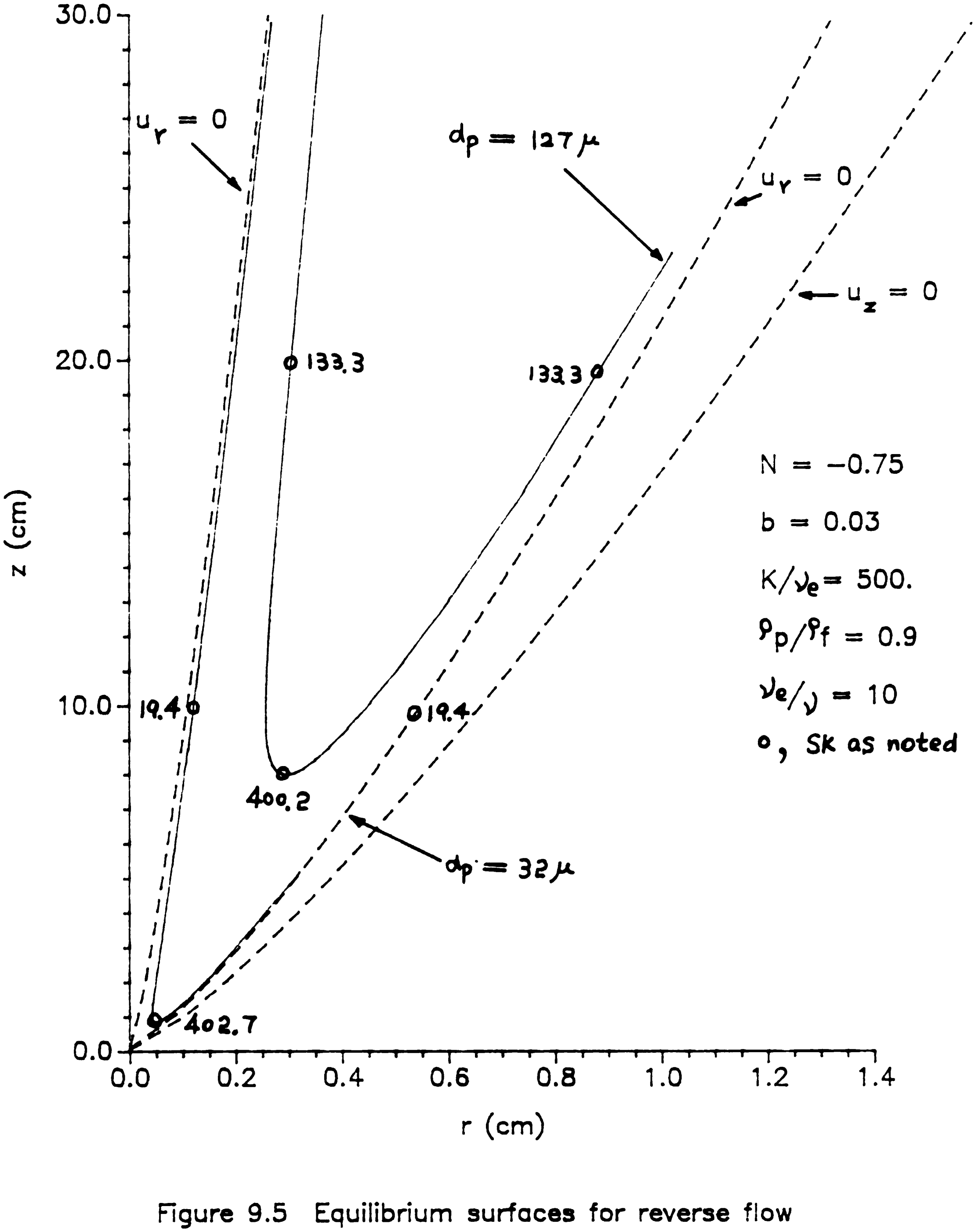

Figure 9.5 Equilibrium surfaces for reverse flow

Table 9.1 Parameter used to calculate the equilibrium surfaces

$N = -0.75$, $\rho_p/\rho_f = 0.9$,	$K/\nu_e = 500\ cm^{-1/4}$ $\nu_e/\nu = 10$	
b	$\tau_p\nu_e \times 10^8$, cm^2	d_p , microns (nominal)
0.3 jet-like flow Figure 9.3	2.21	6.3 (6)
	13.87	15.8 (16)
	55.56	31.6 (32)
0.1 undulated flow Figure 9.4	2.21	6.3 (6)
	55.56	31.6 (32)
	221.90	63.2 (63)
0.03 reverse flow Figure 9.5	55.56	31.6 (32)
	221.90	63.2 (63)
	889.01	126.5 (127)

axis. The particle may, however, move directly to the outer stable surface, depending on how it enters the vortex flow.

Figure 9.3 shows that the equilibrium surfaces for large particles are positioned at large values of z and that all the equilibrium surfaces become asymptotic to the surface of zero radial velocity. Therefore, for constant z_E, smaller particles have larger stable equilibrium orbits and are closer to the outer surface of zero radial velocity. The value of $\hat{z}_E$ (see Figure 9.2a) increases as d_p increases. For 32μ, 16μ, and 6μ size particles the corresponding values of $\hat{z}_E$ are, resp., 17.2 cm, 5.4 cm, 1.2 cm (see Figure 9.3 and Eq. (9.14)). Likewise, the values of $z_{E,min}$ decreases from 15.5 cm to 0.9 cm as d_p changes from 32 μ to 16 μ.

The intrinsic Stokes' number, defined by Eq. (9.11), can also be calculated by rearranging Eq. (9.12):

$$Sk = \tau_p \nu_e (N+2)(K/\nu_e)^{\frac{4}{N+2}} z_E^{\frac{2N}{N+2}} \tag{9.16}$$

Thus, for a fixed equilibrium surface, the value of $z_{E,min}$ (see Figure 9.2) will produce the maximum value of Sk. This occurs because N < 0. For the case shown in Figure 9.3, Sk_{max} equals 11.6 for $d_p = 32\mu$ and 8.9 for $d_p = 6\mu$.

For undulated, forward flows, the behavior of the equilibrium surface (Figure 9.4) is very similar to the equilibrium surface for jet-like, forward flows. A positive radial velocity always occurs near the axis (see Figure 7.9), which makes the existence of equilibrium orbits possible. The values of $\hat{z}_E$, compared with Figure 9.3, are only reduced slightly: 13.4 cm for 32 μ particles (17.2 cm in Figure 9.3) and 1.0 cm for 6 μ particles (1.2 cm in Figure 9.3). However, the minimum value of z_E decreases significantly from 15.5 cm to 3.2 cm for 32 μ particles when b decreases from 0.3 to 0.1.

The equilibrium surfaces for reverse flow are topologically different from jet-like and undulated flow (Figure 9.5). Because a negative radial velocity always exists near the axis (see Figure 7.9), particles in the vicinity of the axis will always move inward toward the axis. Two mantles of zero radial velocity exist for reverse flow, and equilibrium surfaces can only exist between these two surfaces. Although at $z_E > z_{E,min}$ (see Figure 9.2) three equilibrium orbits exist, only two are stable: one on the axis and the other on the branch near the outer surface of zero radial velocity. Therefore, if the equilibrium orbit concept ultimately determines the location of a particle in the flow field, then it may move either upward following the outer surface or downward following the axis. The two possibilities depend on how the particle is introduced into the vortex flow. The position of $z_{E,min}$ is about 8.0 cm for 127μ and becomes smaller as the particle size decreases. For $d_p = 32\mu$, $z_{E,min}$ is about 0.8 cm, a twenty fold decrease as the flow field changes from jet-like behavior (b = 0.3) to a reverse flow behavior (b = 0.03).

The effect of N on the equilibrium surfaces is also significant. By comparing Figures 9.6 and 9.3, the local minimum orbit occurs at $z = \hat{z}_E$ for N = -1.0, but is off the axis for N = -0.75. The size of the

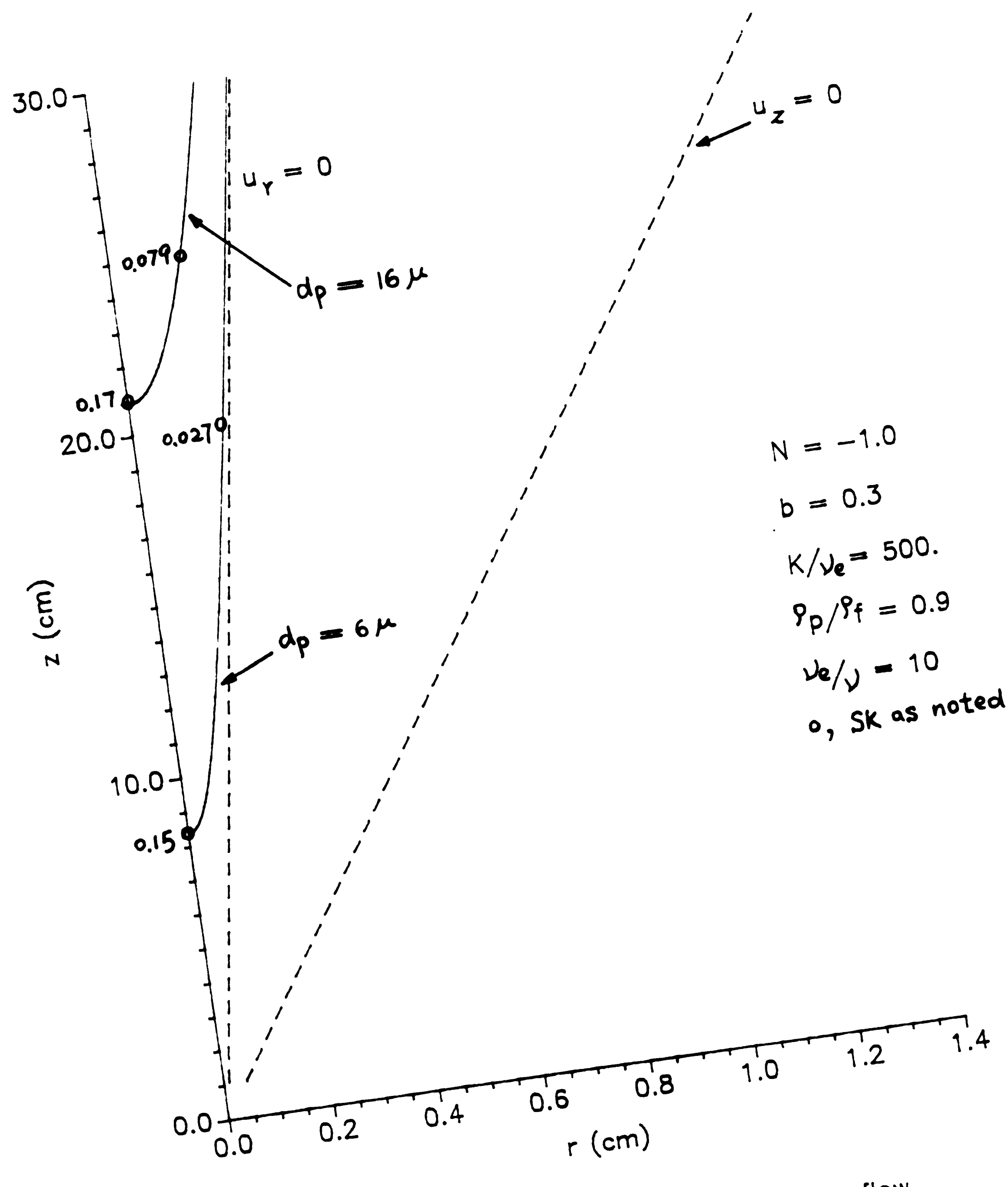

Figure 9.6 Equilibrium surfaces for jet-like flow

mantle reduces by almost half when N decreases from -0.75 to -1.0; and, the values of $\hat{z}_E$ for 6μ particles increase from 1.2 cm to 8.4 cm. Because $\tau_p \propto d_p^2$, it follows from Eq. (9.14) that

$$\hat{z}_E \propto d_p^{\frac{N+2}{-N}} .$$

Thus, for large values of N, the flow field has a much sharper classification effect on the particles. For example, if N = -1/2, then $\hat{z}_E \propto d_p^3$, which shows that the axial position of the equilibrium surfaces is relatively insensitive to particle size for small particles, but change significantly for large values of d_p.

As discussed in Chapter 7, b uniquely determines the similarity structure of the flow for a given value of N. The effect of b on the structure of the particle equilibrium surfaces is clearly seen by comparing Figures 9.3 - 9.5. For large values of b, the size of the outer mantle becomes smaller, and the particles move closer to the axis. At z_E = 30 cm and d_p = 32μ, the equilibrium radius decreases from 1.2 cm to 0.4 cm as b increases from 0.03 to 0.3. Also note that for d_p = 32μ, the local minimum equilibrium orbit $(z_E, r_E)_{min}$ changes in units of cm from (15.4, 0.15) to (0.8, 0.025) as b decreases from 0.3 to 0.03.

The equilibrium orbit theory studied in this chapter provides useful insights provided the major assumptions are satisfied. There are, however, some limitations which should be discussed. For instance, the model assumes that Stoke's law is valid, which implies that the particle Reynolds Number is less than unity (see p.68 Bradley, 1965). The particle Reynolds number, defined as

$$Re_p = \frac{d_p|u_r - u_{pr}|}{\nu} , \tag{9.17}$$

can be roughly estimated on the equilibrium surfaces where the terminal velocity equals the radial velocity of the fluid. For $d_p = 32\mu$ (0.0032 cm), b = 0.3, N = -0.75, $K/\nu_e = 500\ cm^{-0.25}$, $\rho_p/\rho_f = 0.9$, and $\nu_e/\nu = 10$, the maximum value of u_r, 2 cm/s, occurs on the similarity surface $\eta_E \approx 2$ (see Figure 7.9). This corresponds to $z_E = 15.6$ cm on the equilibrium surface (see Eq. 9.12 and Figure 9.3). Therefore, the maximum value of Re_p is about 0.64 ($\nu = 0.01\ cm^2/s$), which shows that Stoke's law is a reasonable approximation in the neighborhood of the particle equilibrium surface.

The model also assumes a balance between the centrifugal and viscous forces. Other forces, such as gravity, acting on the particle are neglected. For $d_p = 32\mu$, the maximum tangential velocity occurs for $\eta_E = 3.5$ and $z_E = 20$ cm (see Figures 7.7 and 9.3) and is about 1200 cm/s. Therefore, the centrifugal force acting on the particle at $z_E = 20$ cm, $r_E = 0.3$ cm is 0.0093 $g.cm/s^2$. The mass of the 32μ size particle ($\rho_f = 0.9\ g/cm^3$) is $1.7x10^{-8}$g, so its centrifugal acceleration (F_c/m_p) is $5.42x10^5\ cm/s^2$ or about 550 times larger than the acceleration due to gravity.

9.6 Conclusions

The following conclusions result from the calculations presented in this chapter:

A. For a fixed cyclone geometry, large particles are probably not limited by their equilibrium surfaces because they occur at relatively large values of z. However, small particles are more likely to follow their equilibrium surfaces, which approach the outer surface of zero radial velocity, or 'mantle'.

B. This model predicts the existence of equilibrium orbits for the entire range of b studied.

C. Different flow behavior will have different types of equilibrium surfaces; the location of these surfaces change significantly with b and N.

D. For forward flow on the axis, the axis is stable only when $z \le \hat{z}_E$; however, it is always stable for reverse flow because $u_r < 0$ near the axis.

E. The effect of N on the classification of particles is very significant. From Eqs. (9.14) and (9.5),

$$\hat{z}_E \propto d_p \qquad \text{for } N = -1$$

$$\hat{z}_E \propto d_p^{5/3} \qquad \text{for } N = -3/4$$

$$\hat{z}_E \propto d_p^{3} \qquad \text{for } N = -1/2$$

Thus, for larger values of N, the flow field has a much sharper classification effect on the particles. The axial position of the equilibrium surface for larger values of N is relatively insensitive to small particles but changes significantly for large particles.

F. Because 'a' is almost proportional to 'b' at large values of 'b' (see Figure 7.3) and because

$$\hat{z}_E \propto \left(\frac{a}{b^2} \right)^{\frac{N+2}{2N}}, \text{ it follows that}$$

$$\hat{z}_E \propto (b)^{-\frac{N+2}{2N}}$$

Thus as 'b' increases, $\hat{z}_E$ increases because $-1 \leq N < 0$. Therefore, a stronger rotation around the axis provides a large $\hat{z}_E$, provided b does not affect K/ν_e.

As previously discussed (see Section 9.1), the efficiency of a 3"-hydrocyclone drops sharply when the particle size approaches 20 - 40 microns. The model developed here may provide a theoretical explanation for this phenomenon because small particles are more likely to be limited by their equilibrium surfaces. Thus, in the apparatus of Colman et al. [1980], the jet-like behavior shows a very high efficiency for capturing the large particles because their trajectories in the vortex are not limited by equilibrium surfaces. However, as d_p decreases and the geometry and flow parameters remain the same, the efficiency is expected to drop as the particle size decreases because the equilibrium surface will cause the particle to miss the vortex finder.

This theory provides new information which can be used for light particle separation in vortex flows. The equilibrium surfaces can be located by knowing the properties of the particles ($d_p, \rho_p/\rho_f$), the intrinsic properties of the continuous phase (μ, ρ_f), and the parameters used to characterize the vortex flow (b, N, K, ν_e). The stability of the equilibrium surface (see Section 9.3) yields important information about the ultimate location of the particles. The results show that the stable surfaces always approach a surface of zero radial velocity for large values of z. Thus, once the above parameters have been estimated, the relationship between the separation efficiency and the hydrodynamics can be quantified. The efficiency can be improved by either adjusting the size of the outlet vortex finder or by adjusting the strength of rotation around the axis, which may be controlled by the inlet velocity. A relationship between the separation efficiency, the size of the vortex finder, and the inlet velocity could be developed experimentally and the results used to study certain aspects of this theory. It is clear from the quantitative calculations presented that a single design and set of operating conditions cannot give the same separation efficiency for all particle sizes. However, a more explicit connection between the design, the hydrodynamics, and the performance of hydrocyclones should be beneficial.

CHAPTER 10

CONCLUSIONS AND RECOMMENDATIONS

10.1 Summary Discussion

Some experimental observations, as discussed in Section 1.1, suggest that a similarity theory could be used to describe the flow structure in the core region of swirling flows. Among these observations are the algebraic decay of the centerline velocity, the free-vortex-like swirl velocity in the outer region, and the nonlinear growth of the viscous boundary layer.

Model II, motivated by these experimental observations (see Section 4.1), has the feature of variable circulation on similarity surfaces by using a more general vortex in the outer region (see Eq. (3.21)). The boundary conditions require that a zero axial velocity and free-vortex-like swirl velocity occur at the same core surface. Although these assumptions may not be true for some vortex flows, the theoretical results are consistent with many experiments (see Dabir, 1983; Escudier et al., 1982, 1984).

The results have revealed the existence of various flow structures in the vortex core. Three types of flow behavior (reverse, undulated, and jet-like flow) were identified experimentally and theoretically (see Figure 7.8). A study of the solution behavior near the axis provides *a priori* criteria for different flow regimes (see Figure 4.2 and Table 4.1), which can be determined uniquely by one of the four parameters :

local spin parameter ('b'), "excess" pressure on the axis ('c'), centerline axial velocity ('a'), and size of vortex core (η^*) as well as K, ν, and N.

The analysis of the "excess" mechanical energy and the axial forces acting on a fluid particle on the axis has revealed that transition from reverse flow to undulated flow occurs when the inertia force (F_I) is zero and the excess mechanical energy (E) is negative. However, the transition from undulated flow to jet-like flow occurs when the viscous force (F_V) and excess mechanical energy are both zero.

The parameters K and ν_e affect the behavior of the flow. As K/ν_e increases, the length scale (δ) decreases (see Eq. (3.38)) and the velocity scale (u_c) increases (see Eq. (3.37)). For $K/\nu_e = 500\ cm^{-0.25}$, $\nu_e = 0.1\ cm^2/sec$, b = 0.3, N = -0.75, z ≈ 15.6 cm, and $\eta \approx 2$ (see Section 9.5), the axial, tangential, and radial velocities are estimated as 200 cm/sec, 96 cm/sec, and 0.4 cm/sec, resp.. In general, the magnitude of the radial velocity is much smaller than the magnitude of the axial and tangential velocities. For the data evaluated (see Chapter 8), N appears to be independent of the flow rate and insensitive to the contraction ratio of the vortex chamber. The coefficient K, however, is a strong function of the flow rate (Q_o), but not the contraction ratio (D_o/D).

For N = -1, the macroscopic axial thrust (F_z) is independent of the axial coordinate. However, for N ≠ -1, the macroscopic axial thrust is zero at the singular point and increases as z increases.

Circulation is another feature which is quite different for $N = -1$ and $N \neq -1$. A constant circulation on similarity surfaces always occurs for $N = -1$ (see Section 6.1). However, for $N \neq -1$, the circulation on similarity surface (constant η) increases as z increases.

The distribution of axial component of vorticity on the axis $\omega_z(0,z)$ in this study varies along the axis and is uniquely fixed by 'b'. For $N = -1$, $\omega_z(0,z)$ is proportional to z^{-2}. However, in the theoretical study of Ingham and Bloor, 1984, the certerline vorticity is independent of z.

The tangential velocity profiles in this study always show a Rankine - type structure with a forced vortex near the axis and a free-vortex-like flow in the outer region. It is found that as b increases, the fraction of the cross sectional area of the vortex in solid body rotation decreases. the radial velocity, however, is quite different for various flow structures. This study revealed that positive radial velocities near the axis always occur for forward flow, whereas negative radial velocities result for reverse flows (see Figure 7.9).

The forward flow on the axis in this study is always against an adverse pressure gradient (see Section 4.2). There will always be a region near the singularity point for which the pressure is less than zero. This region (z^o), from previous specific calculations (see Section 4.2), is estimated to be about 8 cm for a gas vortex and 5.6 cm for a liquid vortex. In general, they are much smaller than the length of the vortex chambers for most of the experiments studied. Therefore, data for $z > z^o$ are used to compare with theoretical calculations (see Chapter 8).

Similarity scaling (see Section 1.1) implies that the total dissipation for $N = -1$ is always unbounded. However, for $N \neq -1$, this study revealed that the total dissipation is unbounded for $-1 < N \leq -2/3$ and is bounded for $-2/3 < N < 0$. As 'b' increases, the macroscopic flow rate decreases. This is also true for the macroscopic axial torque; however, the macroscopic pressure drop increases as 'b' increases. Although the macroscopic axial thrust does not uniquely determine the flow behavior, the macroscopic pressure drop determines uniquely the flow structure.

10.2 Conclusions

The major conclusions of this study can be summarized as follows :

(1). This study predicted quantitatively the various flow structures for a viscous vortex (see Figure 7.1 and 7.2). The range of b for reverse and undulated flow behavior broadens as N increases. Transition values of b for three types of flow structures become larger when N is larger (see Figure 7.2).

(2). The viscous boundary layer increases linearly with the axial coordinate for Model I ($\delta \propto z$) and is parabolic-like for Model II ($\delta \propto z^{1/(N+1)}$). Model II reduces to Model I, with only some minor differences (see Figure 7.1), when $N = -1$.

(3). The study of macroscopic properties revealed that the macroscopic axial force, F_z, did not uniquely determine the flow structure (see Figure 7.10). The macroscopic pressure drop, however, uniquely determines the flow behavior because its one-to-one relationship with the local spin parameter, b (see Figure 7.13). For fixed b, a larger value of N causes a larger macroscopic pressure drop, $\Delta\hat{p}$ (see Figure 7.13).

(4). N appears to be insensitive to the flow rate and the contraction ratio of the vortex chamber (see Figure 8.2 and Table 8.1). An interesting result is that N has a value near -0.75 for most of the experimental data analyzed and is, thereby, consistent with a theoretical analysis for Beltrami flows in the outer region.

(5). Model II, which considered flow structures induced by a more general flow ($-1 \leq N < 0$), has the feature of variable circulation on similarity surfaces. For the same similarity surface (constant η), the circulation increases as 'b' increases (see Figure 9.5). For fixed η and b, large values of N cause an increase in the circulation (see Figure 9.5).

(6). This study revealed that the macroscopic dissipation for Model I is unbounded. However, the total dissipation for Model II is unbounded for $-1 \leq N \leq -2/3$, but bounded for $-2/3 < N < 0$.

(7). The pressure on the axis always increases in the direction of increasing axial position for any type of flow behavior. A negative pressure, which exists near the singularity point, is estimated to be the same order of magnitude for gas and liquid vortices (see Section 4.2). However, it is an order of magnitude smaller than the length of many experimental vortex chambers (see Dabir, 1983; Boysan et al., 1982; and Escudier et al., 1980, 1982).

(8). The effect of N on the size of the viscous core is significant. When N increases, the size of the core decreases (see η^* in Table A.2 to A.4) for fixed b. Therefore, a more coherent core will occur at larger values of N for fixed b.

(9). When N increases, the lower limit on b for undulated and jet-like flows becomes much larger (see Figure 7.2). Therefore, in order to keep jet-like behavior, a stronger rotation on the axis (large b) is necessary for larger values of N.

(10). This study, for the first time, provides a way to understand various flow structures through the excess mechanical energy and force balances on a fluid particle on the axis (see Section 6.5). The viscous force and the substantial time derivative of excess mechanical energy ($D\hat{E}/D\hat{t}$) have to change sign when the flow transfers from jet-like to undulated behavior. However, the flow transfers from undulated to reverse behavior only if $D\hat{E}/D\hat{t}$ changes sign.

(11). The estimates of viscosity coefficient of various experiments based on this study have revealed that the viscosity coefficient cannot be interpreted as a molecular kinematic viscosity, instead it should be considered as a constant eddy viscosity (see Chapter 8).

(12). This study, for the first time, provides a possible explanation why the separation efficiency of hydrocyclones drops sharply as the particle size of a light disperse phase decreases. Because the very fine particles are more easily controlled by the equilibrium surfaces, which move far away from axis for smaller particles, they are probably missing the vortex finder, if the vortex finder is too small.

10.3 Recommendations

Based on the results developed in this research, the following recommendations for additional study are suggested.

(1). Although Model II produces many useful results, it treats the problem with some restrictions (see Chapter 3). The model has assumed that the similarity functions at the surface (i.e., locus of zero axial velocity) require the free-vortex-like swirl velocity ($u_\theta = Kr^N$, $r \geq \delta^*$) and continuity of viscous stress. The behavior of the outer flow (i.e., $r > \delta^*(z)$) is still unknown and has to satisfy these boundary conditions at the surface. These restrictions are too ad-hoc and may not exist for some flows. A study of an outer flow which can match the core behavior in Model II is recommended for development. Another recommendation is to remove the free-vortex-like swirl velocity condition at the surface of zero axial velocity. This may provide a way to match the core flow with an inviscid flow or Beltrami flow in the outer region. The relationship between the core flow and the outer flow could provide a connection with the geometry and operating conditions.

(2). This study has predicted some specific features which are important for the comparison between theoretical and experimental data. These features include : the decay of central axial velocity, free-vortex-like swirl velocity at the outer region, and the decay of the axial component of angular momentum. Therefore, it is recommended to measure the following velocities very carefully and accurately.

(a). Tangential velocity profile, which can be used to determine K and N;

(b). Central axial velocity, which is used to determine the direction of the vortex core;

(c). Angular velocity around the axis ($\partial u_\theta/\partial r|_{r=0}$), which combined with (a) and (b) can be used to determine the value of b;

(d). Axial velocity profiles, which provide an estimate of entrainment rate.

The above accurate measurements will provide a basis for the comparison between theoretical predictions and experimental results.

(3). In this study, radial velocity profiles play a very important role, esp., in the oil-water separation. Unfortunately, experimental data for radial velocity are very scarce. Because this study predicts a mantle (locus of zero radial velocity) always exists, it is very important to validate this finding. Therefore, it is strongly recommended that the experimental test, either direct measurement or visualization of radial velocity, should be carefully executed for a flooded hydrocyclone, esp., near the central core region.

(4). Although the equilibrium surfaces of light particles can be predicted from this study, the detail trajectory of particles are still unknown. Because the velocity field can be determined from this study directly, it provides a way to calculate the trajectory of dispersed particles. Based on the major assumptions in Chapter 9 and Eq. (9.4), the two differential equations for the spatial coordinates of individual spherical particles can be expressed as

$$\frac{dr_p}{dt} = u_{pr} = u_r(r_p,z_p) - \tau_p \frac{u_\theta^{\,2}(r_p,z_p)}{r_p}$$

$$\frac{dz_p}{dt} = u_{pz} = u_z(r_p,z_p)$$

Because u_r, u_z and τ_p can be calculated for any initial particle position, the particle trajectory at any time can be calculated by integrating these two non-linear differential equations. Once the trajectory of specific particles have been determined, an estimate of how long it will take for particles to reach their stable equilibrium surfaces can be made.

(5). In the study of oil-water separation, this model predicted large particles are probably not limited by the equilibrium surfaces while the small particles have more chance to be controlled by the equilibrium surfaces. Therefore, for collecting different particle sizes of oil droplets, a different design of the vortex finder is necessary. This theory also showed that the quantitative behavior of the ultimate particle location is determined by the local spin parameter, b, for fixed other parameters. Because b could be controlled by the inlet velocity for fixed geometry, it is recommended to study the relationship between inlet velocity (or flow rate) and b. The information could provide a way to improve the efficiency of oil-water separation for various particle sizes through the control of inlet velocity for fixed geometry.

APPENDIX A

SOLUTIONS $(a,b,c,\tilde{\eta})$ FOR MODEL I AND MODEL II

Table A.1 Solution (a,b,c,η_a) for Model I

b	a	c	η_a
0.03	-0.0313	0.0136	30.0
0.04	-0.0540	0.0168	28.9
0.042	0.0	0.0174	28.6
0.05	0.0226	0.0199	27.7
0.06	0.0521	0.0230	27.3
0.08	0.114	0.0289	26.6
0.10	0.179	0.0347	26.0
0.136	0.301	0.0449	24.2
0.15	0.348	0.0489	23.5
0.20	0.524	0.0627	22.5
0.30	0.886	0.0898	21.7

Table A.2 Solution (a,b,c,η^*) for Model II (N = -1.0)

b	a	c	η^*
0.03	-0.0251	0.0127	30.1
0.038	0.0	0.0151	29.0
0.04	0.00083	0.0158	28.7
0.05	0.0285	0.0190	28.4
0.06	0.0582	0.0219	27.5
0.08	0.120	0.0279	27.1
0.10	0.184	0.0337	26.8
0.14	0.321	0.0447	24.1
0.15	0.355	0.0475	23.4
0.20	0.531	0.0611	21.9
0.30	0.893	0.0881	21.3

Table A.3 Solution (a,b,c,η^*) for Model II (N = -0.75)

b	a	c	η^*
0.03	-0.0582	0.0186	15.1
0.04	-0.0406	0.0232	14.2
0.05	-0.0212	0.0276	13.5
0.055	0.0	0.0297	13.2
0.06	0.00061	0.0318	12.9
0.08	0.0431	0.0397	11.9
0.10	0.0889	0.0471	11.1
0.20	0.335	0.0786	8.79
0.23	0.412	0.0860	8.33
0.25	0.464	0.0910	8.03
0.30	0.596	0.101	7.43
0.50	1.150	0.121	5.86

Table A.4 Solution (a,b,c,η^*) for Model II ($N = -0.5$)

b	a	c	η^*
0.03	-0.123	0.0385	13.7
0.04	-0.113	0.0475	12.9
0.05	-0.101	0.0558	12.3
0.06	-0.0873	0.0636	11.8
0.08	-0.0575	0.0780	11.0
0.10	-0.0254	0.0909	10.4
0.115	0.0	0.0963	10.2
0.20	0.152	0.138	8.28
0.25	0.248	0.151	7.55
0.30	0.348	0.157	6.94
0.43	0.634	0.203	5.96
0.50	0.784	0.222	5.31

APPENDIX B

COMPUTER PROGRAMS

Table B.1 Objective of computer program and FORTRAN symbol list

Program	Objective
ABCI.FOR	This program determines $(a,c,\tilde{\eta})$ for Models I and II at given b and N
YI.FOR	This program gives Y_1 to Y_6 with respect to η for Model I and Model II
DATA1.FOR	This program sets up individual data files for non-dimensional momemtum transfer, stream function, angular momentum, pressure field, axial, tangential, and radial velocity profiles for Model I
DATA2.FOR	This program sets up individual data files for non-dimensional momemtum transfer, stream function, angular momentum, pressure field, axial, tangential, and radial velocity profiles for Model II
ORBIT.FOR	This program sets up individual data files for particle equilibrium orbits for various particle sizes

Subroutine	Description
ZSCNT	This is a subroutine in IMSL library available at Michigan State University. It solves a system of nonlinear equations by secant methods.
DGEAR	This is a subroutine in IMSL library available at Michigan State University. It solves simultaneous first-order differential equations by implicit ADAMS methods.

FORTRAN symbol list	
A	a
B	b
C	c
eta	$\tilde{\eta}$
D	Particle rsdius.
F	A vector of length N. F is given non-linear equations.
FCN	The name of a user-supplied subroutine which evaluates the system of equations to be solved.
FCN1, FCN2	Name of subroutine for evaluating functions.

FCNJ	Name of the subroutine for computing the N2 by N2 Jacobian matrix of partial derivatives.
GAMMA	$\Gamma(\eta,N,b)$
H, H1	On input, H contains the next step size in X1. On output H contains the step size used last, whether successful or not.
IER, IER1	Error parameter
INDEX, INDEX1	Input and output parameter used to indicate the type of call to the subroutine.
ITMAX	The maximum allowable number of iterations
KV	Defined by K/ν
METH, METH1	Input basic method indicator. METH = 1, implies that the ADAMS method is used. METH = 2, implies that the stiff method of Gear is used.
MITER, MITER1	Input iteration method indicator. MITER = 1, implies that the chord method is used with an analytic Jacobian.
N	The number of unknowns
N1	Power index where $U_\theta = Kr^N$.
N2	Input number of first-order differential equations.
NSIG	The number of digits of accuracy desired in the computed root
PAR	Par contains a parameter set which is passed to the user supplied function FCN.
R	Equilibrium orbit radius.

SPE	ρ_p / ρ_f
TOL	Input relative error bound.
X	A vector of length N. On input, X is the initial approximation to the root. On output, X is the best approximation to the root found by ZSCNT.
X1, X2	Independent variables. On input, X1 and X2 supply the initial value and are used only on the first call. On output, X1 nd X2 are replaced with the current value of the independent variable at which integration has been completed.
XEND, XEND1	Input value of X1 at which solution is desired next.
Y	A vector of length N2. On input, Y is an initial solutions vector, On output, Y is the best approximation which satisfies a set of simultaneous first-order differential equations.
Z	Length of confined vortex chamber.

```
C **********************************************************************
C *                                                                    *
C *                       PROGRAM : ABCI.FOR                           *
C *                                                                    *
C **********************************************************************
C *                                                                    *
C *                    SIMILARITY STRUCTURE OF AN                      *
C *          AXISYMMETRIC VISCOUS VORTEX WITH VARIABLE CIRCULATION     *
C *                                                                    *
C *                          H. C. CHEN                                *
C *                                                                    *
C *     THIS PROGRAM IS DESIGNED TO SOLVE SIX SIMULTANEOUS EQUATIONS   *
C *     WHICH ARE DEVELOPED THEORETICALLY FROM THE INTERNAL CORE FLOW  *
C *     OF CONFINED VORTEX CHAMBER.  THIS THEORY INCLUDE 6 FIRST-ORDER *
C *     SIMULTANEOUS EQUATIONS BUT WITH FOUR UNKNOWNS A,B,C,η̃ WHICH    *
C *     SHOULD BE SATISFIED WITH THREE OUTER BOUNDARY CONDITIONS FOR   *
C *     B IS SPECIFIED.  THIS PROGRAM USE SUBROUTINE ZSCNT IN THE IMSL *
C *     TO FIND OUT ZEROS FOR THREE NONLINEAR EQUATIONS.               *
C *                                                                    *
C *     ZSCNT IS A SUBROUTINE AVAILABLE IN THE IMSL , IT IS INTENT TO  *
C *     SOLVE A SYSTEM OF NONLINEAR EQUATIONS.  THE ALGORITHM IS WELL  *
C *     DESCRIBED IN THE BOOK BY W . PHILLIP, "THE SECANT METHOD       *
C *     FOR SIMULTANEOUS NON-LINEAR EQUATIONS", COMMUNICATIONS OF THE  *
C *     ACM, VOL. 2, 1959.                                             *
C *                                                                    *
C **********************************************************************

      PROGRAM ABCI
      INTEGER N,ITMAX,IER
      DOUBLE PRECISION X(3),WK(68),PAR(3),FNORM,N1,b,a1,c1,eta1
      COMMON N1,b,a1,c1,eta1
      DATA PAR/0.,0.,0./
      EXTERNAL FCN

C **********************************************************************
C *                                                                    *
C *          OPEN A DATA FILE WHICH WILL STORE DATA SOLUTION           *
C *                                                                    *
C **********************************************************************

      OPEN(UNIT=7,FILE='ABCI',STATUS='NEW')

C **********************************************************************
C *                                                                    *
C *             GIVEN INPUT PARAMETER FOR DIFFERENT CASES              *
C *                                                                    *
C **********************************************************************

      PRINT *,' INPUT N1, b'
      ACCEPT *,N1,b
```

```
      PRINT *,' INITIAL GUESS FOR a, c AND eta*'
      ACCEPT *,X(1),X(2),X(3)

      N=3
      NSIG=5
      II=0

      ITMAX=500
      WRITE(6,101) b,N1,NSIG
      WRITE(6,102) x(1),x(2),x(3)
101   FORMAT(// 7X, ' FOR THE CASE OF S = ',F10.3,'    ,N1 = ',F10.3//
   &  7X,' NSIG = ',I2)
102   FORMAT(// 10x,' initial guess for a : ',
   &  F16.7// 10X,' initial guess for c   : ',f16.7// 10x,
   &  ' initial guess for eta : ',f16.7)
      WRITE(6,103)
103   FORMAT(// '     #          a            c           eta         F(1)
   &        F(2)          F(3)      ')


      CALL ZSCNT(FCN,NSIG,N,ITMAX,PAR,X,FNORM,WK,IER)


      a1=X(1)
      c1=X(2)
      eta1=X(3)

      WRITE(6,104) IER,FNORM,X
104   FORMAT(// 2X,' IER = ',I4// 2X, ' NFORM = ',F12.4//
   &  2X,' a   = ',F12.4// 2X,' c   = ',F12.4// 2X,' eta = ',F12.4)

      CLOSE(7)
      END

C ***********************************************************************
C *                                                                     *
C *         DGEAR IS A SUBROUTINE AVAILABLE IN THE IMSL LIBRARY.        *
C *     IT FINDS APPROXIMATIONS TO THE SOLUTION OF A SYSTEM OF          *
C *     FIRST ORDER OF THE FORM Y'=F(X,Y) WITH INITIAL CONDITIONS.      *
C *     THE BASIC METHODS USED FOR THE SOLUTION ARE OF IMPLICIT LINEAR  *
C *     MULTISTEP TYPE.  THERE ARE TWO CLASSES OF SUCH METHODS AVAIL-   *
C *     ABLE TO THE USER.  THE FIRST IS THE IMPLICIT ADAMS METHODS      *
C *     (UP TO ORDER TWELVE), AND THE SECOND IS THE BACKWARD DIFFEREN-  *
C *     TIATION FORMULA (BDF) METHODS (UP TO ORDER FIVE), ALSO CALLED   *
C *     GEAR'S STIFF METHODS.                                           *
C *                                                                     *
C *         DETAIL ALGORITHM SEE REFERENCES :                           *
C *                                                                     *
C *     1.  HINDMARSH, A.C, "GEAR: ORDINARY DIFFERENTIAL EQUATION       *
```

```
C *        SYSTEM SOLVER", LAWRENCE LIVERMORE LABORATORY, REPORT          *
C *        UCID-30001, REVISION 3, DECEMBER, 1974.                        *
C *                                                                       *
C *    2.  GEAR, C.W.,NUMERICAL INITIAL VALUE PROBLEMS IN ORDINARY        *
C *        DIFFERENTIAL EQUATIONS, PRENTICE-HALL, ENGLEWOOD CLIFFS,       *
C *        NEW JERSEY, 1971.                                              *
C *                                                                       *
C ************************************************************************

      SUBROUTINE FCN(X,F,N,PAR)
      INTEGER N2,METH1,MITER1,INDEX1,IWK1(6),IER1,K
      DOUBLE PRECISION X(3),F(3),PAR(3),a2,c2,eta2,N1,b
      DOUBLE PRECISION Y(6),WK1(103),X1,TOL1,XEND1,H1
      COMMON N1,b,a2,c2,eta2
      EXTERNAL FCN1,FCNJ

      a2=X(1)
      c2=X(2)
      eta2=X(3)
      N2=6
      X1=0.001
      Y(1)=c2 - b*b*(eta2*eta2)*(X1*X1)/8.
      Y(2)=0.5*a2*X1*X1+N1*(eta2**2)/(8.*(N1+2))*(-c2+a2*a2/2.)*
     &      (X1**4)
      Y(3)=a2+N1*(eta2*eta2)/(2.*(N1+2))*(-c2+a2*a2/2)*X1*X1
      Y(4)=N1*eta2*eta2/(N1+2)*(-c2+a2*a2/2)*X1
      Y(5)=0.5*b*(eta2**(1-N1))*X1*X1 - a2*b/(16.*(N1+2))*
     &      (eta2**(3-N1))*(X1**4)
      Y(6)=b*(eta2**(1-N1))*X1-a2*b/(4.*(N1+2))*
     &      (eta2**(3-N1))*(X1**3)
      TOL1=.0001
      H1=0.0001
      METH1=1
      MITER1=0
      INDEX1=1


      DO 10 K=1,100
         XEND1=FLOAT(K)*0.01

         CALL DGEAR(N2,FCN1,FCNJ,X1,H1,Y,XEND1,TOL1,METH1,MITER1,
     &               INDEX1,IWK,WK1,IER1)

         IF(IER1 .GT. 128) GO TO 20
 10   CONTINUE

      S1=Y(3)
      S2=Y(5)
      S3=Y(6)
      F(1)=eta2**(N1)/((-2.*N1)**0.5) - S1
```

```
      F(2)=1. - S2
      F(3)=N1+1.0 - S3
C ***********************************************************************
C *                                                                     *
C *        II WILL AUTOMATICALLY COUNT THE NUMBER OF ITERATION          *
C *                                                                     *
C ***********************************************************************

      II=II+1

      WRITE(6,205) II,X,F
 205  FORMAT(/ 2X,I3,1X,6F12.5)
      IF (ABS(F(1)) .GT. 0.00001) GO TO 50
      IF (ABS(F(2)) .GT. 0.00001) GO TO 50
      IF (ABS(F(3)) .GT. 0.00001) GO TO 50
      STOP
  20  CONTINUE
      STOP
  50  RETURN
      END


      SUBROUTINE FCN1(N2,X1,Y,YPRIME)
      INTEGER N2
      COMMON N1,b,a,c,eta
      DOUBLE PRECISION Y(N2),YPRIME(N2),X1,N1,b,a,c,eta
      YPRIME(1)=-(eta**(2.*N1))*Y(5)*Y(5)/(X1**3)
      YPRIME(2)=X1*Y(3)
      YPRIME(3)=Y(4)
      YPRIME(4)=-Y(4)/X1 - eta*eta*(2.*N1/(N1+2)*Y(1)
     &    - N1/(N1+2)*Y(3)*Y(3) + Y(2)*Y(4)/X1
     &    + (eta**(2.*N1))/(N1+2)*(Y(5)**2)/(X1*X1))
      YPRIME(5)=Y(6)
      YPRIME(6)=Y(6)/X1+eta*eta*((N1+1.)/(N1+2)*Y(5)*Y(3)-Y(6)*Y(2)/X1)
      RETURN
      END


      SUBROUTINE FCNJ(N2,X1,Y,PD,X)
      INTEGER N2
      COMMON N1,b,a3,c3,eta3
      DOUBLE PRECISION Y(N2),PD(N2,N2),X1,N1,b,a3,c3,eta3
      RETURN
      END
```

```
C ***********************************************************************
C *                                                                     *
C *                        PROGRAM : YI.FOR                             *
C *                                                                     *
C ***********************************************************************
C *                                                                     *
C *                         VORTEX MODEL I                              *
C *                                                                     *
C *     THIS PROGRAM IS DESIGNED TO CALCULATE THE RELATIONSHIP OF SIX   *
C *     DEPENDENT VARIABLES --- Y1, Y2, Y3, Y4, Y5, Y6 --- WITH RESPECT *
C *     TO DIMENSIONLESS RADIAL DISTANCE.                               *
C *                                                                     *
C ***********************************************************************

      PROGRAM YI
      INTEGER N,METH,MITER,INDEX,IWK(6),IER,K,KK
      DOUBLE PRECISION Y(6),WK(103),X,TOL,XEND,H,N1,B,A,C
      COMMON N1,B,A,C
      EXTERNAL FCN,FCNJ

C ***********************************************************************
C *                                                                     *
C *              OPEN A DATA FILE TO STORE DATA SOLUTION                *
C *                                                                     *
C ***********************************************************************

      open(unit=7,file='YI',status='new')

C ***********************************************************************
C *                                                                     *
C *           GIVEN N1,A,B,C FROM PREVIOUS PROGRAM TO CALCULATE         *
C *           SOLUTION FOR EACH CASE                                    *
C *                                                                     *
C ***********************************************************************

      PRINT *,' INPUT N1,A,B,C '
      ACCEPT *, N1,A,B,C

      N=6
      X=0.001
      WRITE(7,101) N1
      Y(1)=C - (B*B)*(X*X)/8.
      Y(2)=A/2.*X*X+N1*(-C+A*A/2.)*(X**4)/(8.*(N1+2))
      Y(3)=A+N1*(-C+A*A/2.)*X*X/(2.*(N1+2))
      Y(4)=N1/(N1+2)*(-C+A*A/2.)*X
      Y(5)=B/2.*X*X-B*A/(16.*(N1+2))*(X**4)
      Y(6)=B*X-B*A/(4.*(N1+2))*(X**3)

      WRITE(7,102) A,B,C
```

```
      WRITE(7,201)
      TOL=.0001
      H=0.0001
      METH=1
      MITER=0
      INDEX=1
      DO 1 KK=1,500
      DO 10 K=1,10
         XEND=FLOAT(K)*0.01 +(KK-1)*0.1
         CALL DGEAR(N,FCN,FCNJ,X,H,Y,XEND,TOL,METH,MITER,INDEX,IWK,WK,IER)
         IF(IER.GT.128) GO TO 20

10    CONTINUE

      WRITE(7,202) X,Y
1     CONTINUE
      CLOSE(7)
      STOP
20    CONTINUE

101   FORMAT(//2X,' THEORETICAL SOLUTIONS FOR N = ', F9.4//
   *    2X,'          A                B                C')
102   FORMAT(// 2X,3F15.5)
201   FORMAT(/// 2X,'       E          Y1         Y2          Y3
   *       Y4         Y5         Y6')
202   FORMAT(2X,7F10.4)
      STOP
      END

      SUBROUTINE FCN(N,X,Y,YPRIME)
      INTEGER N
      DOUBLE PRECISION Y(N),YPRIME(N),X,N1,B,A1,C1
      COMMON N1,B,A1,C1
      YPRIME(1)=-Y(5)*Y(5)/(X**3)
      YPRIME(2)=X*Y(3)
      YPRIME(3)=Y(4)
      YPRIME(4)=(1./(N1+2)*(-2.*N1*X*Y(1) - Y(5)*Y(5)/X
   &     - (N1+2)*Y(4)*Y(2) + N1*X*Y(3)**2) - Y(4))/X
      YPRIME(5)=Y(6)
      YPRIME(6)=((N1+1.)/(N1+2)*Y(5)*X*Y(3) - Y(6)*Y(2)
   &     +Y(6))/X
      RETURN
      END

      SUBROUTINE FCNJ(N,X,Y,PD)
      INTEGER N
      DOUBLE PRECISION Y(N),PD(N,N),X
      COMMON N1,B,A2,C2
      RETURN
      END
```

```
C ********************************************************************
C *                                                                  *
C *                       PROGRAM : DATAI.FOR                        *
C *                                                                  *
C ********************************************************************
C *                                                                  *
C *                         VORTEX MODEL I                           *
C *                                                                  *
C *     THIS PROGRAM IS DESIGNED TO SET UP INDIVIDUAL DATAFILE FOR   *
C *     VORTEX MODEL I.  THE DATAFILE INCLUDES :                     *
C *                                                                  *
C *     C3H.DAT : RESULTS OF H AT GIVEN B                            *
C *     C3M.DAT : RESULTS OF M AT GIVEN B                            *
C *     C3I.DAT : RESULTS OF I AT GIVEN B                            *
C *     C3F.DAT : RESULTS OF F AT GIVEN B                            *
C *     C3HA.DAT : ASYMPTOTIC SOLUTION OF H AT LARGE RADIAL DISTANCE *
C *     C3MA.DAT : ASYMPTOTIC SOLUTION OF M AT LARGE RADIAL DISTANCE *
C *     C3FA.DAT : ASYMPTOTIC SOLUTION OF F AT LARGE RADIAL DISTANCE *
C *     C3UZ.DAT : NON-DIMENSIONAL AXIAL VELOCITY PROFILE IN         *
C *                THIS STUDY                                        *
C *     C3UT.DAT : NON-DIMENSIONAL TANGENTIAL VELOCITY PROFILE       *
C *                IN THIS STUDY                                     *
C *     C3UR.DAT : NON-DIMENSIONAL RADIAL VELOCITY PROFILE IN        *
C *                THIS STUDY                                        *
C *                                                                  *
C ********************************************************************

      PROGRAM DATA1
      INTEGER N2,METH1,MITER1, INDEX1,IWK1(6),IER1,K
      INTEGER N3,METH2,MITER2,INDEX2,IWK2(3),IER2,J
      DOUBLE PRECISION A,B,C,N1,Y(6),WK1(103),X1,TOL1,MA,FA,HA
      DOUBLE PRECISION XEND1,H1,UR2,UT2,DFA
      DOUBLE PRECISION Z(202),Z1(802),Z2(4002)
      DOUBLE PRECISION S1,S2,S3,S4,S5,S6,A1,A2,A3,UT,UT1,UR,UR1
      COMMON N1,B,A,C
      EXTERNAL FCN1,FCNJ

C ********************************************************************
C *                                                                  *
C *     OPEN INDIVIDUAL DATA FILE WHICH WILL STORE DATA SOLUTIONS    *
C *                                                                  *
C ********************************************************************

      OPEN(UNIT=1,FILE='C6HB3',STATUS='NEW')
      OPEN(UNIT=2,FILE='C6MB3',STATUS='NEW')
      OPEN(UNIT=3,FILE='C6FB3',STATUS='NEW')
      OPEN(UNIT=4,FILE='C6IB3',STATUS='NEW')
      OPEN(UNIT=5,FILE='C6UZB3',STATUS='NEW')
      OPEN(UNIT=7,FILE='C6UTB3',STATUS='NEW')
      OPEN(UNIT=8,FILE='C6URB3',STATUS='NEW')
```

```
      OPEN(UNIT=10,FILE='C6HA',STATUS='NEW')
      OPEN(UNIT=11,FILE='C6MA',STATUS='NEW')
      OPEN(UNIT=12,FILE='C6FA',STATUS='NEW')

C ***********************************************************************
C *                                                                     *
C *              GIVEN INPUT PARAMETER FOR DIFFERENT CASES              *
C *                                                                     *
C ***********************************************************************

      PRINT *,' INPUT N1,A,B,C'
      ACCEPT *,N1,A,B,C

      WRITE(6,101) N1,A,B,C
 101  FORMAT(// 7X, ' FOR THE CASE OF N1 = ',F10.3 / 10X,
    & '    A =     ',F10.5/ 10X,'    B =     ',F10.5/10X,
    & '    C =     ',F10.5)

C *********************************************************************
C *                                                                   *
C *        DGEAR IS A SUBROUTINE AVAILABLE IN THE IMSL LIBRARY.       *
C *    IT FINDS APPROXIMATIONS TO THE SOLUTION OF A SYSTEM OF         *
C *    FIRST ORDER OF THE FORM Y'=F(X,Y) WITH INITIAL CONDITIONS.     *
C *    THE BASIC METHODS USED FOR THE SOLUTION ARE OF IMPLICIT LINEAR *
C *    MULTISTEP TYPE.  THERE ARE TWO CLASSES OF SUCH METHODS AVAIL-  *
C *    ABLE TO THE USER.  THE FIRST IS THE IMPLICIT ADAMS METHODS     *
C *    (UP TO ORDER TWELVE), AND THE SECOND IS THE BACKWARD DIFFEREN- *
C *    TIATION FORMULA (BDF) METHODS (UP TO ORDER FIVE), ALSO CALLED  *
C *    GEAR'S STIFF METHODS.                                          *
C *                                                                   *
C *        DETAIL ALGORITHM SEE REFERENCES :                          *
C *                                                                   *
C *    1.  HINDMARSH, A.C, "GEAR: ORDINARY DIFFERENTIAL EQUATION      *
C *        SYSTEM SOLVER", LAWRENCE LIVERMORE LABORATORY, REPORT      *
C *        UCID-30001, REVISION 3, DECEMBER, 1974.                    *
C *                                                                   *
C *    2.  GEAR, C.W.,NUMERICAL INITIAL VALUE PROBLEMS IN ORDINARY    *
C *        DIFFERENTIAL EQUATIONS, PRENTICE-HALL, ENGLEWOOD CLIFFS,   *
C *        NEW JERSEY, 1971.                                          *
C *                                                                   *
C *********************************************************************

      N2=6
      X1=0.001
      Y(1)=C - (B*B)*(X1*X1)/8.
      Y(2)=A/2.*X1*X1+N1*(-C+A*A/2.)*(X1**4)/(8.*(N1+2))
      Y(3)=A + N1*(-C+A*A/2.)*X1*X1/(2.*(N1+2))
      Y(4)=N1/(N1+2)*(-C + A*A/2.)*X1
      Y(5)=B/2.*X1*X1 - B*A/(16.*(N1+2))*(X1**4)
```

```
      Y(6)=B*X1 - B*A/(4*(N1+2))*(X1**3)
      Z(1)=(Y(3)**2-Y(1))*X1
      SUM=Z(1)*(X1-0)/2

      TOL1=.0001
      H1=0.0001
      METH1=1
      MITER1=0
      INDEX1=1
      DO 10 K=1,100
      DO 15 KK=1,2
         XEND1=FLOAT(KK)*0.01 + FLOAT(K-1)*0.02
      CALL DGEAR(N2,FCN1,FCNJ,X1,H1,Y,XEND1,TOL1,METH1,MITER1,
     &              INDEX1,IWK1,WK1,IER1)
      UT=Y(5)/X1
      UR=-Y(2)/X1 + Y(3)*X1
      Z(KK+1+2*(K-1))=(Y(3)**2 -Y(1))*X1
      SUM=SUM+(Z(KK+2*(K-1))+Z(KK+1+2*(K-1)))*0.01/2.
15    CONTINUE

      WRITE(1,201) X1,Y(2)
      WRITE(2,201) X1,Y(1)
      WRITE(3,201) X1,Y(5)
      WRITE(4,201) X1,SUM
      WRITE(5,201) X1,Y(3)
      WRITE(7,201) X1,UT
      WRITE(8,201) X1,UR

10    CONTINUE

      X1=2.0
      N2=6
      Z1(1)=(Y(3)**2-Y(1))*X1
      TOL1=0.0001
      H1=0.0001
      METH1=1
      MITER1=0
      INDEX1=1
        DO 30 J=1,80
        DO 40 JJ=1,10
         XEND1=2.+FLOAT(JJ)*0.01 + FLOAT(J-1)*0.1

      CALL DGEAR(N2, FCN1, FCNJ, X1, H1, Y, XEND1, TOL1,
     &           METH1, MITER1, INDEX1, IWK1, WK1, IER1)

      UT1=Y(5)/X1
      UR1=-Y(2)/X1+Y(3)*X1
      Z1(JJ+1+10*(J-1))=(Y(3)**2-Y(1))*X1
      SUM=SUM+(Z1(JJ+10*(J-1))+Z1(JJ+1+10*(J-1)))*
     &    0.01/2.
```

```
40     CONTINUE

       WRITE(1,201) X1,Y(2)
       WRITE(2,201) X1,Y(1)
       WRITE(3,201) X1,Y(5)
       WRITE(4,201) X1,SUM
       WRITE(5,201) X1,Y(3)
       WRITE(7,201) X1,UT1
       WRITE(8,201) X1,UR1

30     CONTINUE

       X1=10.
       N2=6
       Z2(1)=(Y(3)**2-Y(1))*X1
       DO 50 I=1,15
       DO 60 II=1,100
       XEND1=10.+FLOAT(II)*0.01 + FLOAT(I-1)

       CALL DGEAR(N2,FCN1,FCNJ,X1,H1,Y,XEND1,TOL1,
  &              METH1,MITER1,INDEX1,IWK1,WK1,IER1)

       UT2=Y(5)/X1
       UR2=-Y(2)/X1+Y(3)*X1
       Z2(II+1+100*(I-1))=(Y(3)**2-Y(1))*X1
       SUM=SUM+(Z2(II+100*(I-1))+Z2(II+1+100*(I-1)))*
  &            0.01/2.
60     CONTINUE
       WRITE(1,201) X1,Y(2)
       WRITE(2,201) X1,Y(1)
       WRITE(3,201) X1,Y(5)
       WRITE(4,201) X1,SUM
       WRITE(5,201) X1,Y(3)
       WRITE(7,201) X1,UT2
       WRITE(8,201) X1,UR2

50 CONTINUE
201    FORMAT(2X,F10.3,F12.6)
       DO 80 I=1,250
       E=0.1*I
       HA=E**(N1+2)/(N1+2)/((-2.*N1)**0.5) - N1
       MA=E**(2.*N1)/(-2.*N1)
       FA=E**(N1+1)
       WRITE(10,201) E,HA
       WRITE(11,201) E,MA
       WRITE(12,201) E,FA
80     CONTINUE

       CLOSE(1)
       CLOSE(2)
```

```
      CLOSE(3)
      CLOSE(4)
      CLOSE(5)
      CLOSE(7)
      CLOSE(8)
      CLOSE(10)
      CLOSE(11)
      CLOSE(12)

      END


      SUBROUTINE FCN1(N2,X1,Y,YPRIME)
      INTEGER N2
      COMMON N1,B,A,C
      DOUBLE PRECISION Y(N2),YPRIME(N2),X1,N1,A,B,C
      YPRIME(1)=-Y(5)*Y(5)/(X1**3)
      YPRIME(2)=X1*Y(3)
      YPRIME(3)=Y(4)
      YPRIME(4)=(1./(N1+2)*(-2.*N1*X1*Y(1) - Y(5)*Y(5)/X1
     &     - (N1+2)*Y(4)*Y(2) + N1*X1*Y(3)**2) - Y(4))/X1
      YPRIME(5)=Y(6)
      YPRIME(6)=((N1+1.)/(N1+2)*Y(5)*X1*Y(3) - Y(6)*Y(2)
     &     +Y(6))/X1
      RETURN
      END


      SUBROUTINE FCNJ(N2,X1,Y,PD,X)
      INTEGER N2
      COMMON N1,B,A3,C3
      DOUBLE PRECISION Y(N2),PD(N2,N2),X1,N1,A3,B,C3
      RETURN
      END
```

```
C ***********************************************************************
C *                                                                     *
C *                     PROGRAM : DATAII.FOR                            *
C *                                                                     *
C ***********************************************************************
C *                                                                     *
C *                        VORTEX MODEL II                              *
C *                                                                     *
C *      THIS PROGRAM IS DESIGNED TO SET UP INDIVIDUAL DATAFILE FOR     *
C *      VORTEX MODEL I.  THE DATAFILE INCLUDES :                       *
C *                                                                     *
C *      C7H.DAT : RESULTS OF H AT GIVEN B                              *
C *      C7M.DAT : RESULTS OF M AT GIVEN B                              *
C *      C7F.DAT : RESULTS OF F AT GIVEN B                              *
C *      C7UZ.DAT : NON-DIMENSIONAL AXIAL VELOCITY PROFILE IN           *
C *                 THIS STUDY                                          *
C *      C7UT.DAT : NON-DIMENSIONAL TANGENTIAL VELOCITY PROFILE         *
C *                 IN THIS STUDY                                       *
C *      C7UR.DAT : NON-DIMENSIONAL RADIAL VELOCITY PROFILE IN          *
C *                 THIS STUDY                                          *
C *                                                                     *
C ***********************************************************************

      PROGRAM DATAII
      INTEGER N2,METH1,MITER1, INDEX1,IWK1(6),IER1,K
      INTEGER N3,METH2,MITER2,INDEX2,IWK2(3),IER2,J
      DOUBLE PRECISION A,B,C,N1,Y(6),WK1(103),X1,TOL1,MA,FA,HA
      DOUBLE PRECISION XEND1,H1,UR2,UT2,DFA
      DOUBLE PRECISION S1,S2,S3,S4,S5,S6,A1,A2,A3,UT,UT1,UR,UR1
      COMMON N1,B,A,C
      EXTERNAL FCN1,FCNJ

C ***********************************************************************
C *                                                                     *
C *      OPEN INDIVIDUAL DATA FILE WHICH WILL STORE DATA SOLUTIONS      *
C *                                                                     *
C ***********************************************************************

      OPEN(UNIT=1,FILE='C7HB3',STATUS='NEW')
      OPEN(UNIT=2,FILE='C7MB3',STATUS='NEW')
      OPEN(UNIT=3,FILE='C7FB3',STATUS='NEW')
      OPEN(UNIT=5,FILE='C7UZB3',STATUS='NEW')
      OPEN(UNIT=7,FILE='C7UTB3',STATUS='NEW')
      OPEN(UNIT=8,FILE='C7URB3',STATUS='NEW')

C ***********************************************************************
C *                                                                     *
C *            GIVEN INPUT PARAMETER FOR DIFFERENT CASES                *
C *                                                                     *
C ***********************************************************************
```

```
      PRINT *,' INPUT N1,A,B,C,ETA'
      ACCEPT *,N1,A,B,C,ETA

      WRITE(6,101) N1,A,B,C,ETA
101   FORMAT(// 7X, ' FOR THE CASE OF N1 = ',F10.3 / 10X,
   &  '    A =      ',F10.5/ 10X,'    B =      ',F10.5/10X,
   &  '    C =      ',F10.5/ 10X,'     ETA =      ',F10.5)

C ***********************************************************************
C *                                                                     *
C *       DGEAR IS A SUBROUTINE AVAILABLE IN THE IMSL LIBRARY.          *
C *    IT  FINDS APPROXIMATIONS TO THE SOLUTION OF A SYSTEM OF          *
C *    FIRST ORDER OF THE FORM Y'=F(X,Y) WITH INITIAL CONDITIONS.       *
C *    THE BASIC METHODS USED FOR THE SOLUTION ARE OF IMPLICIT LINEAR   *
C *    MULTISTEP TYPE.  THERE ARE TWO CLASSES OF SUCH METHODS AVAIL-    *
C *    ABLE TO THE USER.  THE FIRST IS THE IMPLICIT ADAMS METHODS       *
C *    (UP TO ORDER TWELVE), AND THE SECOND IS THE BACKWARD DIFFEREN-   *
C *    TIATION FORMULA (BDF) METHODS (UP TO ORDER FIVE), ALSO CALLED    *
C *    GEAR'S STIFF METHODS.                                            *
C *                                                                     *
C *       DETAIL ALGORITHM SEE REFERENCES :                             *
C *                                                                     *
C *    1.  HINDMARSH, A.C, "GEAR: ORDINARY DIFFERENTIAL EQUATION        *
C *        SYSTEM SOLVER", LAWRENCE LIVERMORE LABORATORY, REPORT        *
C *        UCID-30001, REVISION 3, DECEMBER, 1974.                      *
C *                                                                     *
C *    2.  GEAR, C.W.,NUMERICAL INITIAL VALUE PROBLEMS IN ORDINARY      *
C *        DIFFERENTIAL EQUATIONS, PRENTICE-HALL, ENGLEWOOD CLIFFS,     *
C *        NEW JERSEY, 1971.                                            *
C *                                                                     *
C ***********************************************************************

      N2=6
      X1=0.001
      Y(1)=C - (B*B)*(X1*X1)/8.
      Y(2)=A/2.*X1*X1+N1*(-C+A*A/2.)*(X1**4)/(8.*(N1+2))
      Y(3)=A + N1*(-C+A*A/2.)*X1*X1/(2.*(N1+2))
      Y(4)=N1/(N1+2)*(-C + A*A/2.)*X1
      Y(5)=B/2.*X1*X1 - B*A/(16.*(N1+2))*(X1**4)
      Y(6)=B*X1 - B*A/(4*(N1+2))*(X1**3)

      TOL1=.0001
      H1=0.0001
      METH1=1
      MITER1=0
      INDEX1=1
      DO 10 K=1,100
      DO 15 KK=1,2
         XEND1=FLOAT(KK)*0.01 + FLOAT(K-1)*0.02
```

```
         CALL DGEAR(N2,FCN1,FCNJ,X1,H1,Y,XEND1,TOL1,METH1,MITER1,
     &              INDEX1,IWK1,WK1,IER1)
      UT=Y(5)/X1
      UR=-(N1+2)*Y(2)/X1 + Y(3)*X1
15    CONTINUE

      WRITE(1,201) X1,Y(2)
      WRITE(2,201) X1,Y(1)
      WRITE(3,201) X1,Y(5)
      WRITE(5,201) X1,Y(3)
      WRITE(7,201) X1,UT
      WRITE(8,201) X1,UR

10    CONTINUE

      X1=2.0
      N2=6
      TOL1=0.0001
      H1=0.0001
      METH1=1
      MITER1=0
      INDEX1=1
      ETA1=(ETA-2.)*10
      DO 30 J=1,ETA1
      DO 40 JJ=1,10
         XEND1=2.+FLOAT(JJ)*0.01 + FLOAT(J-1)*0.1

      CALL DGEAR(N2, FCN1, FCNJ, X1, H1, Y, XEND1, TOL1,
     &           METH1, MITER1, INDEX1, IWK1, WK1, IER1)

      UT1=Y(5)/X1
      UR1=-(N1+2)*Y(2)/X1+Y(3)*X1

40    CONTINUE

      WRITE(1,201) X1,Y(2)
      WRITE(2,201) X1,Y(1)
      WRITE(3,201) X1,Y(5)
      WRITE(5,201) X1,Y(3)
      WRITE(7,201) X1,UT1
      WRITE(8,201) X1,UR1

30    CONTINUE

      WRITE(1,201) X1,Y(2)
      WRITE(2,201) X1,Y(1)
      WRITE(3,201) X1,Y(5)
      WRITE(5,201) X1,Y(3)
      WRITE(7,201) X1,UT2
      WRITE(8,201) X1,UR2
```

```
 50     CONTINUE
201     FORMAT(2X,F10.3,F12.6)

        CLOSE(1)
        CLOSE(2)
        CLOSE(3)
        CLOSE(5)
        CLOSE(7)
        CLOSE(8)

        END

        SUBROUTINE FCN1(N2,X1,Y,YPRIME)
        INTEGER N2
        COMMON N1,B,A,C
        DOUBLE PRECISION Y(N2),YPRIME(N2),X1,N1,A,B,C
        YPRIME(1)=-Y(5)*Y(5)/(X1**3)
        YPRIME(2)=X1*Y(3)
        YPRIME(3)=Y(4)
        YPRIME(4)=(1./(N1+2)*(-2.*N1*X1*Y(1) - Y(5)*Y(5)/X1
     &      - (N1+2)*Y(4)*Y(2) + N1*X1*Y(3)**2) - Y(4))/X1
        YPRIME(5)=Y(6)
        YPRIME(6)=((N1+1.)/(N1+2)*Y(5)*X1*Y(3) - Y(6)*Y(2)
     &      +Y(6))/X1
        RETURN
        END


        SUBROUTINE FCNJ(N2,X1,Y,PD,X)
        INTEGER N2
        COMMON N1,B,A3,C3
        DOUBLE PRECISION Y(N2),PD(N2,N2),X1,N1,A3,B,C3
        RETURN
        END
```

```
C ***********************************************************************
C *                                                                     *
C *                       PROGRAM : ORBIT.FOR                           *
C *                                                                     *
C ***********************************************************************
C *                                                                     *
C *     THIS PROGRAM IS DESIGNED TO SOLVE EQUILIBRIUM ORBIT OF          *
C *     DIFFERENT SIZES OF PARTICLE FOR MODEL I AND MODEL II VORTEX     *
C *                                                                     *
C ***********************************************************************

      PROGRAM ORBIT
      INTEGER N,METH,MITER,INDEX,IWK(6),IER,K,KK
      DOUBLE PRECISION Y(6),WK(103),X,TOL,XEND,H,N1,B,A,C
      DOUBLE PRECISION Z1,Z2,R1,R2,ETA1,ETA2,KV,SPE
      COMMON N1,B,A,C
      EXTERNAL FCN,FCNJ

C ***********************************************************************
C *                                                                     *
C *             OPEN A DATA FILE TO STORE DATA SOLUTION                 *
C *                                                                     *
C ***********************************************************************

      OPEN(UNIT=7,FILE='ORBIT23',STATUS='NEW')
      OPEN(UNIT=8,FILE='ORBIT24',STATUS='NEW')
      OPEN(UNIT=9,FILE='ORBIT25',STATUS='NEW')

C ***********************************************************************
C *                                                                     *
C *          GIVEN N1,A,B,C FROM PREVIOUS PROGRAM TO CALCULATE          *
C *          SOLUTION FOR EACH CASE                                     *
C *                                                                     *
C ***********************************************************************

      PRINT *,' INPUT N1,A,B,C,D '
      ACCEPT *, N1,A,B,C,D
      WRITE(6,101) N1,A,B,C,D

C ***********************************************************************
C *                                                                     *
C *    THE FOLLOWING OPERATING PARAMETER CAN BE CONTROLLED BY USER.     *
C *       SPE = THE DENSITY RATIO OF PARTICLE AND FLUID PHASE           *
C *       KV = THE RATIO OF K AND KINEMATIC VISCOSITY                   *
C *       ETA1 = THE VALUE OF ETA WHERE AXIAL VELOCITY IS ZERO          *
C *       ETA2 = THE VALUE OF ETA WHERE RADIAL VELOCITY IS ZERO         *
C *                                                                     *
C ***********************************************************************
```

```
         SPE = 0.9
         KV = 500.
         ETA1 = 11.2
         ETA2 = 8.4
      DO 50 J = 1,30
      Z1 = 1.0*J
      R1 = ETA1*((Z1/KV)**(1./(N1+2)))
      WRITE(8,201) R1,Z1
 50   CONTINUE

      DO 60 K = 1,30
      Z2 = 1.0*K
      R2 = ETA2*((Z2/KV)**(1./(N1+2)))
      WRITE(9,201) R2,Z2
 60   CONTINUE

      N=6
      X=0.001
      Y(1)=C - (B*B)*(X*X)/8.
      Y(2)=A/2.*X*X+N1*(-C+A*A/2.)*(X**4)/(8.*(N1+2))
      Y(3)=A+N1*(-C+A*A/2.)*X*X/(2.*(N1+2))
      Y(4)=N1/(N1+2)*(-C+A*A/2.)*X
      Y(5)=B/2.*X*X-B*A/(16.*(N1+2))*(X**4)
      Y(6)=B*X-B*A/(4.*(N1+2))*(X**3)

      TOL=.0001
      H=0.0001
      METH=1
      MITER=0
      INDEX=1

      DO 10 K=1,2000
         XEND=FLOAT(K)*0.01
         CALL DGEAR(N,FCN,FCNJ,X,H,Y,XEND,TOL,METH,MITER,INDEX,IWK,WK,IER)
      UT=Y(5)/X
      UR=-Y(2)/X + Y(3)*X/(N1+2)
      GAMMA=X*UR/(UT**2)
      Z=(D*2/3*(KV**(2./(N1+2)))*(((1-SPE)/(2.*GAMMA))**0.5))
     &   **((N1+2)/(-N1))
      R=X*((Z/KV)**(1./(N1+2)))
      IF(GAMMA .LT. 0) GO TO 300

      WRITE(7,201) R,Z
 10   CONTINUE
300   CONTINUE
      CLOSE(7)
      CLOSE(8)
      CLOSE(9)

101   FORMAT(//2X,' THEORETICAL SOLUTIONS FOR N = ', F10.4/
```

```
&       10X,'  A = ',F10.5/ 10X,'  B = ',F10.4/ 10X,'  C = ',F10.4/
&       10X,'  D = ',F10.4)
201   FORMAT(2X,2F12.6)
      STOP
      END


      SUBROUTINE FCN(N,X,Y,YPRIME)
      INTEGER N
      DOUBLE PRECISION Y(N),YPRIME(N),X,N1,B,A1,C1
      COMMON N1,B,A1,C1
      YPRIME(1)=-Y(5)*Y(5)/(X**3)
      YPRIME(2)=X*Y(3)
      YPRIME(3)=Y(4)
      YPRIME(4)=(1./(N1+2)*(-2.*N1*X*Y(1) - Y(5)*Y(5)/X
&         - (N1+2)*Y(4)*Y(2) + N1*X*Y(3)**2) - Y(4))/X
      YPRIME(5)=Y(6)
      YPRIME(6)=((N1+1.)/(N1+2)*Y(5)*X*Y(3) - Y(6)*Y(2)
&         + Y(6))/X
      RETURN
      END


      SUBROUTINE FCNJ(N,X,Y,PD)
      INTEGER N
      DOUBLE PRECISION Y(N),PD(N,N),X
      COMMON N1,B,A2,C2
      RETURN
      END
```

APPENDIX C

TABULAR EXPERIMENTAL DATA USED

Table C.1 Experimental data set 1a

Reference : Escudier, et al., [1980]

Experimental conditions : (see Figure 8.1)

$Q_F = 400\ cm^3/sec,\ u_F = 24\ cm/sec$

$\frac{D_o}{D} = \frac{40}{55},\ \frac{Q_o}{Q_u} = \infty$

$\tilde{z} = 19.35$ cm (from Figures 9 and 10 of Escudier)											
r,cm	0	.2	.4	1.0	1.2	1.4	1.6	1.8	2.0	2.6	N = -0.75
u_θ, cm/s	0	32	64	67	58	50	44	39	37	33	K = 68 cm^{1-N}/s
u_z, cm/s	-24	-12	0	29	-	-	9	-	4	0	$\left.\frac{\partial u_\theta}{\partial r}\right\vert_{r=0} = 160$

$\tilde{z} = 19.85$ cm (from Figures 9 and 10 of Escudier)										
r,cm	0	.2	.4	1.0	1.2	1.4	1.6	1.8	2.0	N = -0.75
u_θ, cm/s	0	32	64	67	58	50	44	39	37	K = 68 cm^{1-N}/s
u_z, cm/s	-23	-11	0	25	-	-	8	-	4	$\left.\frac{\partial u_\theta}{\partial r}\right\vert_{r=0} = 160$

Table C.2 Experimental data set 1b

Reference : Escudier, et al., [1980]

Experimental conditions : (see Figure 8.1)

$Q_F = 400\ cm^3/sec,\ u_F = 24\ cm/sec$

$\frac{D_o}{D} = \frac{25}{55},\quad \frac{Q_o}{Q_u} = \infty$

$\tilde{z} = 19.35$ cm (from Figures 9 and 10 of Escudier)

r,cm	0	.1	.2	1.0	1.2	1.4	1.6	1.8	2.0	2.6	$N = -0.75$
u_θ,cm/s	0	36	72	67	53	46	39	36	34	33	$K = 68\ cm^{1-N}/s$
u_z,cm/s	3		45	35	28	25	20	15	10	2	$\left.\frac{\partial u_\theta}{\partial r}\right\rvert_{r=0} = 360$

$\tilde{z} = 19.85$ cm (from Figures 9 and 10 of Escudier)

r,cm	0	.1	.2	1.0	1.2	1.4	1.6	1.8	2.0	$N = -0.75$
u_θ,cm/s	0	36	72	67	53	46	39	36	34	$K = 68\ cm^{1-N}/s$
u_z,cm/s	10		80	35	28	20	15	6	0	$\left.\frac{\partial u_\theta}{\partial r}\right\rvert_{r=0} = 360$

Table C.3 Experimental data set 1c

Reference : Escudier, et al., [1980]

Experimental conditions : (see Figure 8.1)

$Q_F = 400\ cm^3/sec,\ u_F = 24\ cm/sec$

$$\frac{D_o}{D} = \frac{10}{55},\quad \frac{Q_o}{Q_u} = \infty$$

$\tilde{z} = 19.35$ cm (from Figures 9 and 10 of Escudier)

r,cm	0	.1	.2	1.0	1.2	1.4	1.6	1.8	2.0	2.6	$N = -0.75$
u_θ**,cm/s**	0	80	160	67	55	48	42	38	35	33	$K = 68\ cm^{1-N}/s$
u_z**,cm/s**	144		72	33	28	25	22	19	15	0	$\left.\frac{\partial u_\theta}{\partial r}\right\vert_{r=0} = 800$

$\tilde{z} = 19.85$ cm (from Figures 9 and 10 of Escudier)

r,cm	0	.1	.2	1.0	1.2	1.4	1.6	1.8	2.0	$N = -0.75$
u_θ**,cm/s**	0	80	160	67	55	48	42	38	35	$K = 68\ cm^{1-N}/s$
u_z**,cm/s**	450		72	40	32	24	16	8	0	$\left.\frac{\partial u_\theta}{\partial r}\right\vert_{r=0} = 800$

Table C.4 Experimental data set 1d

Reference : Escudier, et al., [1982]

Experimental conditions : (see Figure 8.1)

$Q_F = 100\ cm^3/sec,\ u_F = 6\ cm/sec$

$\frac{D_o}{D} = \frac{18}{55},\ \frac{Q_o}{Q_u} = \infty$

$\tilde{z}$ = 1 cm (from Figures 5 of Escudier)							
r, cm	0	0.25	0.50	1.0	1.5	2.0	N = -0.75
u_θ, cm/s	0	19	15	10	8.5	6.9	K = 11 cm^{1-N}/s
u_z, cm/s	-	-	-	-	-	-	$\left.\frac{\partial u_\theta}{\partial r}\right\|_{r=0}$ = -

$\tilde{z}$ = 10 cm (from Figures 5 of Escudier)								
r, cm	0	0.25	0.50	1.0	1.5	2.0	2.8	N = -0.75
u_θ, cm/s	0	19	18	10	8.6	6.9	6.0	K = 11 cm^{1-N}/s
u_z, cm/s	-	14	8	6	3	2	0	$\left.\frac{\partial u_\theta}{\partial r}\right\|_{r=0}$ = -

$\tilde{z}$ = 19.85 cm (from Figures 5 of Escudier)

r, cm	0	0.25	0.50	1.0	1.5	2.0	N = -0.75
u_θ, cm/s	0	29	17	10	7.9	6.9	K = 11 cm^{1-N}/s
u_z, cm/s	-	22	11	8	6	0	$\left.\frac{\partial u_\theta}{\partial r}\right\|_{r=0}$ = -

$\tilde{z}$ = 20.55 cm (from Figures 5 of Escudier)

r, cm	0	0.25	0.50	1.0	1.5	2.0	N = -0.75
u_θ, cm/s	0	27	17	10	7.9	6.9	K = 11 cm^{1-N}/s
u_z, cm/s	62	-	-	-	-	-	$\left.\frac{\partial u_\theta}{\partial r}\right\|_{r=0}$ = -

$\tilde{z}$ = 29.45 cm (from Figures 5 of Escudier)

r, cm	0	0.1	0.2	0.25	0.50	1.0	1.5	1.6	2.0	N = -0.75
u_θ, cm/s	0	10	20	21	14	10	7.9	7.7	6.9	K = 11 cm^{1-N}/s
u_z, cm/s	50	-	-	40	36	20	2	0		$\left.\frac{\partial u_\theta}{\partial r}\right\|_{r=0}$ = 100

$\tilde{z}$ = 31.65 cm (from Figures 5 of Escudier)

r, cm	0	0.1	0.2	0.25	0.50	1.0	1.5	1.6	2.0	N = -0.75
u_θ, cm/s	0	10	20	14	18	12	9.6	9.4	8.0	K = 11 cm^{1-N}/s
u_z, cm/s	48	-	-	48	45	25	4	0		$\left.\frac{\partial u_\theta}{\partial r}\right\|_{r=0}$ = 100

Table C.5 Experimental data set 1e

Reference : Escudier, et al., [1982]

Experimental conditions : (see Figure 8.1)

$Q_F = 200\ cm^3/sec,\ u_F = 12\ cm/sec$

$\frac{D_o}{D} = \frac{18}{55},\ \frac{Q_o}{Q_u} = \infty$

$\tilde{z}$ = 1 cm (from Figures 5 of Escudier)							
r,cm	0	0.25	0.50	1.0	1.5	2.0	N = -0.75
u_θ**,cm/s**	0	65	34	21	15	13	K = 26 cm^{1-N}/s
u_z**,cm/s**	-	-	-	-	-	-	$\left.\frac{\partial u_\theta}{\partial r}\right\|_{r=0} = -$

$\tilde{z}$ = 10 cm (from Figures 5 of Escudier)								
r,cm	0	0.25	0.50	1.0	1.5	2.0	2.8	N = -0.75
u_θ**,cm/s**	0	69	34	21	15	13	12	K = 26 cm^{1-N}/s
u_z**,cm/s**	-	25	10	6	4	1	0	$\left.\frac{\partial u_\theta}{\partial r}\right\|_{r=0} = -$

$\tilde{z}$ = 19.85 cm (from Figures 5 of Escudier)

r,cm	0	0.25	0.50	1.0	1.5	2.0	N = -0.75
u_θ,cm/s	0	75	62	22	19	14	K = 26 cm^{1-N}/s
u_z,cm/s	-	40	30	20	10	0	$\left.\frac{\partial u_\theta}{\partial r}\right\|_{r=0}$ = -

$\tilde{z}$ = 20.55 cm (from Figures 5 of Escudier)

r,cm	0	0.25	0.50	1.0	1.5	2.0	N = -0.75
u_θ,cm/s	0	82	41	24	21	17	K = 26 cm^{1-N}/s
u_z,cm/s	-	-	-	-	-	-	$\left.\frac{\partial u_\theta}{\partial r}\right\|_{r=0}$ = -

$\tilde{z}$ = 29.45 cm (from Figures 5 of Escudier)

r,cm	0	0.1	0.2	0.25	0.50	1.0	1.5	1.6	2.0	N = -0.75
u_θ,cm/s	0	10	20	48	34	24	19	18	17	K = 26 cm^{1-N}/s
u_z,cm/s	23.8	30	50	60	75	30	10	0		$\left.\frac{\partial u_\theta}{\partial r}\right\|_{r=0}$ = 100

$\tilde{z}$ = 31.65 cm (from Figures 5 of Escudier)

r,cm	0	0.1	0.2	0.25	0.50	1.0	1.5	1.6	2.0	N = -0.75
u_θ,cm/s	0	12	24	17	27	22	21	21	19	K = 26 cm^{1-N}/s
u_z,cm/s	-	-	-	40	55	15	0			$\left.\frac{\partial u_\theta}{\partial r}\right\|_{r=0}$ = 120

Table C.6 Experimental data set 1f

Reference : Escudier, et al., [1982]

Experimental conditions : (see Figure 8.1)

$Q_F = 411\ cm^3/sec,\ u_F = 24.6\ cm/sec$

$$\frac{D_o}{D} = \frac{18}{55},\quad \frac{Q_o}{Q_u} = \infty$$

$\tilde{z}$ = 1 cm (from Figures 5 of Escudier)							
r,cm	0	0.25	0.50	1.0	1.5	2.0	N = -0.75
u_θ,cm/s	0	162	91	49	32	28	K = 47 cm^{1-N}/s
u_z,cm/s	-	-	-	-	-	-	$\left.\frac{\partial u_\theta}{\partial r}\right\|_{r=0} = -$

$\tilde{z}$ = 10 cm (from Figures 5 of Escudier)								
r,cm	0	0.25	0.50	1.0	1.5	2.0	2.8	N = -0.75
u_θ,cm/s	0	162	84	46	32	28	27	K = 47 cm^{1-N}/s
u_z,cm/s	-	60	10	5	5	2	0	$\left.\frac{\partial u_\theta}{\partial r}\right\|_{r=0} = -$

$\tilde{z}$ = 19.85 cm (from Figures 5 of Escudier)

r, cm	0	0.25	0.50	1.0	1.5	2.0	2.8	$N = -0.75$
u_θ, cm/s	0	162	77	46	35	28	26	$K = 47\ cm^{1-N}/s$
u_z, cm/s	-	120	60	40	30	20	0	$\left.\frac{\partial u_\theta}{\partial r}\right\|_{r=0} = -$

$\tilde{z}$ = 20.55 cm (from Figures 5 of Escudier)

r, cm	0	0.25	0.50	1.0	1.5	2.0	$N = -0.75$
u_θ, cm/s	0	169	91	56	42	28	$K = 42\ cm^{1-N}/s$
u_z, cm/s	-	-	-	-	-	-	$\left.\frac{\partial u_\theta}{\partial r}\right\|_{r=0} = -$

$\tilde{z}$ = 29.45 cm (from Figures 5 of Escudier)

r, cm	0	0.1	0.2	0.25	0.50	1.0	1.5	2.0	$N = -0.75$
u_θ, cm/s	0	-	-	84	70	42	35	28	$K = 47\ cm^{1-N}/s$
u_z, cm/s	17	-	-	30	80	140	0		$\left.\frac{\partial u_\theta}{\partial r}\right\|_{r=0} = 200$

$\tilde{z}$ = 31.65 cm (from Figures 5 of Escudier)

r, cm	0	0.1	0.2	0.25	0.50	1.0	1.5	2.0	$N = -0.75$
u_θ, cm/s	0	-	-	84	71	42	35	28	$K = 47\ cm^{1-N}/s$
u_z, cm/s	15	-	-	25	80	150	20	0	$\left.\frac{\partial u_\theta}{\partial r}\right\|_{r=0} = 140$

Table C.7 Experimental data set 1g

Reference : Escudier, et al., [1982]

Experimental conditions : (see Figure 8.1)

$Q_F = 850\ cm^3/sec,\ u_F = 51\ cm/sec$

$$\frac{D_o}{D} = \frac{18}{55},\quad \frac{Q_o}{Q_u} = \infty$$

$\tilde{z}$ = 1 cm (from Figures 5 of Escudier)							
r, cm	0	0.25	0.50	1.0	1.5	2.0	N = -0.75
u_θ, cm/s	0	290	200	100	82	61	K = 95 cm^{1-N}/s
u_z, cm/s	-	-	-	-	-	-	$\left.\frac{\partial u_\theta}{\partial r}\right\vert_{r=0}$ = -

$\tilde{z}$ = 10 cm (from Figures 5 of Escudier)							
r, cm	0	0.25	0.50	1.0	1.5	2.0	N = -0.75
u_θ, cm/s	0	320	175	87	58	44	K = 95 cm^{1-N}/s
u_z, cm/s	-	-	-	-	-	-	$\left.\frac{\partial u_\theta}{\partial r}\right\vert_{r=0}$ = -

$\tilde{z}$ = 19.85 cm (from Figures 5 of Escudier)

r, cm	0	0.25	0.50	1.0	1.5	2.0	N = -0.75
u_θ, cm/s	0	335	175	93	64	58	K = 95 cm^{1-N}/s
u_z, cm/s	-	175	80	40	20	0	$\left.\frac{\partial u_\theta}{\partial r}\right\|_{r=0}$ = -

$\tilde{z}$ = 20.55 cm (from Figures 5 of Escudier)

r, cm	0	0.25	0.50	1.0	1.5	2.0	N = -0.75
u_θ, cm/s	0	320	204	117	87	64	K = 95 cm^{1-N}/s
u_z, cm/s	-62	-	-	-	-	-	$\left.\frac{\partial u_\theta}{\partial r}\right\|_{r=0}$ = -

$\tilde{z}$ = 29.45 cm (from Figures 5 of Escudier)

r, cm	0	0.1	0.2	0.25	0.50	1.0	1.5	1.6	2.0	N = -0.75
u_θ, cm/s	0	25	50	131	131	96	73	70	58	K = 95 cm^{1-N}/s
u_z, cm/s	-	-	-	80	180	20	0			$\left.\frac{\partial u_\theta}{\partial r}\right\|_{r=0}$ = 250

$\tilde{z}$ = 31.65 cm (from Figures 5 of Escudier)

r, cm	0	0.1	0.2	0.25	0.50	1.0	1.5	1.6	2.0	N = -0.75
u_θ, cm/s	0	21	42	52	93	87	67	65	58	K = 95 cm^{1-N}/s
u_z, cm/s	-52	-30	-5	0	100	190	40	0		$\left.\frac{\partial u_\theta}{\partial r}\right\|_{r=0}$ = 210

Table C.8 Experimental data set 2a

Reference : Dabir, [1983]

Experimental conditions : (see Figure 8.1)

$Q_F = 500\ cm^3/sec,\ u_F = 140\ cm/sec$

$$\frac{D_o}{D} = \frac{25.8}{76},\quad \frac{Q_o}{Q_u} = \infty$$

$\tilde{z}$ = 8 cm (from Figures 5.9 and 5.10 of Dabir)											
r,cm	0	.1	.2	.4	.8	.9	1.0	1.2	1.4	1.6	N = -0.75
u_θ,cm/s	0	40	80	160	245	230	220	195	172	150	K = 270 cm^{1-N}/s
u_z,cm/s	60	65	70	80	10	0					$\left.\frac{\partial u_\theta}{\partial r}\right\rvert_{r=0} = 400$

$\tilde{z}$ = 20 cm (from Figures 5.9 and 5.10 of Dabir)													
r,cm	0	.1	.2	1.0	1.2	1.4	1.6	1.8	2.0	2.2	2.4	2.6	N = -0.75
u_θ,cm/s	0	40	80	235	218	200	185	172	163	150	140	130	K = 270 cm^{1-N}/s
u_z,cm/s	40	48	56	50	30	15	0						$\left.\frac{\partial u_\theta}{\partial r}\right\rvert_{r=0} = 600$

$\tilde{z}$ = 32 cm (from Figures 5.9 and 5.10 of Dabir)													
r,cm	0	.1	.2	1.0	1.2	1.4	1.6	1.8	2.0	2.2	2.4	2.6	N = -0.75
u_θ,cm/s	0	40	80	235	215	200	190	175	165	153	147	140	K = 270 cm^{1-N}/s
u_z,cm/s	30	35	40	60	40	20	15	10	6	3	0		$\left.\frac{\partial u_\theta}{\partial r}\right\vert_{r=0} = 400$

Table C.9 Experimental data set 2b

Reference : Dabir, [1983]

Experimental conditions : (see Figure 8.1)

$Q_F = 500\ cm^3/sec$, $u_F = 140\ cm/sec$

$$\frac{D_o}{D} = \frac{12.9}{76}\ ,\quad \frac{Q_o}{Q_u} = 4$$

$\tilde{z} = 20$ cm (from Figures 4.1 and 4.2 of Dabir)

r,cm	0	.1	.2	.6	.8	1.0	1.2	1.4	1.6	1.8	2.0	2.2	$N = -0.75$
u_θ,cm/s	0	100	200	340	300	260	230	200	190	180	175	160	$K = 270\ cm^{1-N}/s$
u_z,cm/s	375	340	320		60	50	35	20	5				$\left.\frac{\partial u_\theta}{\partial r}\right\rvert_{r=0} = 1000$

$\tilde{z} = 32$ cm (from Figures 4.1 and 4.2 of Dabir)

r,cm	0	.1	.2	.6	.8	1.0	1.2	1.4	1.6	1.8	2.0	2.2	$N = -0.75$
u_θ,cm/s	0	100	200	340	300	280	250	220	200	190	175	160	$K = 270\ cm^{1-N}/s$
u_z,cm/s	335	320	280		50	40	25	15	10	-	0	0	$\left.\frac{\partial u_\theta}{\partial r}\right\rvert_{r=0} = 1000$

Table C.10 Experimental data set 2c

Reference : Dabir, [1983]

Experimental conditions : (see Figure 8.1)

$Q_F = 500\ cm^3/sec,\ u_F = 140\ cm/sec$

$\frac{D_o}{D} = \frac{12.2}{76},\quad \frac{Q_o}{Q_u} = \infty$

$\tilde{z}$ = 20 cm (from Figures 5.14 and 5.15 of Dabir)											
r,cm	0	.2	.4	.6	.8	1.0	1.2	1.4	1.6	1.8	N = -0.75
u_θ,cm/s	0	-	-	-	-	-	-	-	-	-	K = 270 cm^{1-N}/s
u_z,cm/s	400	340	220	120	50	-	30	20	15	0	$\left.\frac{\partial u_\theta}{\partial r}\right\|_{r=0} = 1200$

$\tilde{z}$ = 32 cm (from Figures 5.14 and 5.15 of Dabir)													
r,cm	0	.2	.4	.6	.8	1.0	1.2	1.4	1.6	1.8	2.0	2.2	N = -0.75
u_θ,cm/s	0	200	470	370	295	250	220	195	176	165	155	148	K = 270 cm^{1-N}/s
u_z,cm/s	340	320	210	100	40	-	25	-	20	15	10	-	$\left.\frac{\partial u_\theta}{\partial r}\right\|_{r=0} = 1000$

Table C.11 Experimental data set 3

Reference : Kimber and Thew [1974]

Experimental conditions : (see Figure 8.1)

$Q_F = 51\ cm^3/sec,\ u_F = 40\ cm/sec$

$\frac{D_o}{D} = \frac{12.7}{50},\ \frac{Q_o}{Q_u} = \infty$

$\tilde{z}$ = 295 cm (from Figures 6 of Kimber and Thew)								
r,cm	0	.05	.10	.5	1.0	1.5	2.0	N = -0.6
u_θ**,cm/s**	0	50	100	84	64	48	38	K = 64 cm^{1-N}/s
u_z**,cm/s**	0	-	-	-	-	-	-	$\left.\frac{\partial u_\theta}{\partial r}\right\|_{r=0} = 1000$

$\tilde{z}$ = 50 cm (from Figures 6 of Kimber and Thew)		
r,cm	0	N = -0.6
u_θ**,cm/s**	0	K = -- cm^{1-N}/s
u_z**,cm/s**	-100	$\left.\frac{\partial u_\theta}{\partial r}\right\|_{r=0}$ = ---

Table C.12 Experimental data set 4

Reference : Boysan et al. [1982]

Experimental conditions :

$Q_F = 42000\ cm^3/sec,\ u_F = 1370\ cm/sec$

$$\frac{D_o}{D} = \frac{64}{203},\quad \frac{Q_o}{Q_u} = \infty$$

$\tilde{z} = 6.6$ cm (from Figures 3 of Boysan)											
r,cm	0	.5	1.0	3.0	4.0	5.0	6.0	7.0	8.0	9.0	N = -1.0
u_θ,cm/s	0	420	850	1600	1200	970	810	690	610	540	K=3050 cm^{1-N}/s
u_z,cm/s	283	150	0	-200	-100	-30	0				$\left.\frac{\partial u_\theta}{\partial r}\right\vert_{r=0} = 850$

$\tilde{z} = 13.2$ cm (from Figures 3 of Boysan)											
r,cm	0	.5	1.0	3.0	4.0	5.0	6.0	7.0	8.0	9.0	N = -1.0
u_θ,cm/s	0	420	850	1600	1200	970	810	690	610	540	K=3050 cm^{1-N}/s
u_z,cm/s	250	140	0	-190	-95	-30	0				$\left.\frac{\partial u_\theta}{\partial r}\right\vert_{r=0} = 850$

$\tilde{z} = 19.8$ cm (from Figures 3 of Boysan)											
r,cm	0	.5	1.0	3.0	4.0	5.0	6.0	7.0	8.0	9.0	N = -1.0
u_θ,cm/s	0	420	850	1600	1200	970	810	690	610	540	K=3050 cm^{1-N}/s
u_z,cm/s	165	120	0	-180	-90	-25	0				$\left.\frac{\partial u_\theta}{\partial r}\right\|_{r=0} = 850$

$\tilde{z} = 26.4$ cm (from Figures 3 of Boysan)											
r,cm	0	.5	1.0	3.0	4.0	5.0	6.0	7.0	8.0	9.0	N = -1.0
u_θ,cm/s	0	420	850	1600	1200	970	810	690	610	540	K=3050 cm^{1-N}/s
u_z,cm/s	90	60	0	-170	-80	-25	0				$\left.\frac{\partial u_\theta}{\partial r}\right\|_{r=0} = 850$

$\tilde{z} = 33.0$ cm (from Figures 3 of Boysan)											
r,cm	0	.5	1.0	3.0	4.0	5.0	6.0	7.0	8.0	9.0	N = -1.0
u_θ,cm/s	0	420	850	1600	1200	970	810	690	610	540	K=3050 cm^{1-N}/s
u_z,cm/s	65	40	0	-170	-70	-20	0				$\left.\frac{\partial u_\theta}{\partial r}\right\|_{r=0} = 850$

Table C.13 Experimental data set 5

Reference : Pericleous et al. [1984]

Experimental conditions :

$Q_F = 1250$ cm^3/sec, $u_F = 56.7$ cm/sec

$$\frac{D_o}{D} = \frac{80}{200}, \quad \frac{Q_o}{Q_u} = \infty$$

$\tilde{z} = 25$ cm (from Figure 4 of Pericleous)													
r,cm	0	3.0	3.5	4.0	4.5	5.0	5.0	6.0	6.5	7.0	7.5	8.0	N = -1.0
u_θ,cm/s	0	540	460	400	360	325	300	275	250	240	230	220	K=1050 cm^{1-N}/s
u_z,cm/s	-	-	-	-	-	-	-	-	-	-	-	-	$\left.\frac{\partial u_\theta}{\partial r}\right\|_{r=0}$ = ---

APPENDIX D

COMPONENTS OF THE STRESS TENSOR FOR AXISYMMETRIC, INCOMPRESSIBLE FLOWS OF A NEWTONIAN FLUID

Table D. Components of the stress tensor for axisymmetric, incompressible flows of a Newtonian fluid (cylindrical coordinates)

$$\tau_{rr} = 2\mu \frac{\partial u_r}{\partial r}$$

$$\tau_{\theta\theta} = 2\mu \frac{u_r}{r}$$

$$\tau_{zz} = 2\mu \frac{\partial u_z}{\partial z}$$

$$\tau_{r\theta} = \tau_{\theta r} = \mu r \frac{\partial}{\partial r} \left(\frac{u_\theta}{r} \right)$$

$$\tau_{\theta z} = \tau_{z\theta} = \mu \frac{\partial u_\theta}{\partial z}$$

$$\tau_{zr} = \tau_{rz} = \mu \left[\frac{\partial u_z}{\partial r} + \frac{\partial u_r}{\partial z} \right]$$

List of References

Binnie, A.M., and Teare, J.D., 1956, "Experiments on the Flow of Swirling Water Through a Pressure Nozzle and an Open Trumpet," Proc. Roy. Soc. A, 325, 78.

Binnie, A.M., 1957, "Experiments on the Slow Swirling Flow of a Viscous Liquid Through a Tube," Quart. J. Mech. and Applied Math 10, 276.

Bird, R.B., Stewart, W.E., and Lightfoot, E.N., 1960, Transport Phenomena, John Wiley and Sons, Inc.

Bloor, M.I.G., and Ingham, D.B., 1975, "Theoretical Investigation of the Flow in a Conical Hydrocyclone," Trans. Inst. Chem. Engrs., 51, 36.

Bloor, M.I.G. and Ingham, D.B., 1984, "Theoretical Aspects of Hydrocyclone Flow," p.57 in Progress in Filtration and Separation 3, ed. R.J. Wakeman.

Boysan, F., Ayers, W.H., and Swithenbank, J., 1982, "A Fundamental Methematical Modeling Approach to Cyclone Design," Trans. Inst. Chem. Engrs., 60, 222.

Bradley, D., and Pulling, D.J., 1959, "Flow Patterns in the Hydraulic Cyclone and Their Interpretation in terms of Performance," Trans. Instn. Chem. Engrs. 37, 87.

Bradley, D., 1965, The Hydrocyclone, Pergamon Press.

Burgers, J. M., 1948, "A Mathematical Model Illustrating the Theory Turbulence," Adv. in Appl. Mech. Vol. I, 197, Academic press.

Burggraf, O.R., and Foster, M.R., 1977, "Continuation or breakdown in tornado - like vortices," J. Fluid Mech., 80, 685.

Chen, H.C., and Petty, C.A., 1986, "Particle Classfication Based on Equilibrium Orbits Within the Core of a Viscous Vortex," p. 223 in 8th Annual Science, Engineering & Technology Seminars, May 24-25, Houston, U.S.A.

Chigier, N.A., and Beer, J.M., 1964, "Velocity and Static-Pressure Distributions in Swirling Air Jets Issuing From Annular and Divergent Nozzles," Trans. of the ASME, December, 788.

Chigier, N.A., and Chervinsky, A., 1967, "Experimental Investigation of Swirling Vortex Motion in Jets," J. Appl. Mech., June, 443.

Colman, D.A., and Thew, M.T., 1980, "Hydrocyclone to give a highly Concentrated Sample of a Lighter Dispersed Phase," p. 209 in Hydrocyclone, Int. Conf., Cambridge, England, BHRA Fluid Eng.

Colman, D.A., Thew, M.T., and Corney, D.R., 1980, "Hydrocyclones for oil/water separation," p143 in Hydrocyclone, Int. Conf., Cambridge, England, BHRA Fluid Eng.

Colman, D.A., and Thew, M.T., 1983, "Correlation of separation results from light dispersion hydrocyclones," Chem. Eng. Res. Des., 61, 233.

Dabir, B., 1983, "Mean Velocity Measurements in a 3"-Hydrocyclone Using Laser Doppler Anemometry," Doctor of Philosophy Dissertation, Michigan State University.

Dabir, B. and Petty, C.A., 1984a, "Laser Doppler Anemometry Measurements of Tangential And Axial Velocities in a Hydrocyclone Operating Without an Air Core," p. 15 in Proceedings of BHRA 2nd Int'l Conf. on Hydrocyclones, Sept. 19-21 (1984), Bath, England.

Dadir, B., and Petty, C.A., 1984b, "Measurements of Mean Velocity Profiles in a Hydrocyclone Using Laser Doppler Anemometry," Chem. Eng. Commu. 48, 377.

Donaldson, C. D., 1956, "Solutions of the Navier-Stokes equations for two and three dimensional vortices," Ph. D. Thesis, University of Princeton University.

Donaldson, C. Dup., and Sullivan, R.D., 1960, "Behaviour of Solutions of the Navier-Stokes Equations for a Complete Class of Three-Dimensional Viscous Vortices," Proc. 1960 Heat Transfer and Fluid Mech. Inst., p. 16, Standford University Press.

Donaldson, C. Dup., and Snedeker, R.S., 1962, "Experimental Investigation of the Structure of Vortices in Simple Cylindrical Vortex Chambers," Aero. Res. Ass. of Princeton, Inc. Rep. No. 47.

Durst, F., Melling, A., and Whitelaw, J.H., 1976, Principles and Practice of Laser Doppler Anemometry, Academic Press.

Escudier, M.P., Bornstein, J., and Zehnder, N., 1980, "Observations and LDA Measurements of Confined Turbulent Vortex Flow," J. Fluid Mech. 98 part 1, 49.

Escudier, M.P., Bornstein, J., Zehnder, J., and Maxworthy, T., 1980, "The Classification of Confined Vortex Flow Regions," Proc. Symp. on Vortex Flows, ASME winter annual meeting, Chicago. (Paper E2).

Escudier, M.P., Bornstein, J., and Maxworthy, T., 1982, "The Dynamics of Confined Vortices," Proc. R. Soc. Lond. A 382, 335.

Escudier, M.P., and Zehnder, N., 1982, "Vortex-flow regimes," J. Fluid Mech. 115, 105.

Fontein, F.J., and Dijksman, C., 1953, "Recent Developments in Mineral Dressing," p229 in Proc. of Sym. on Mineral Dressing (London: The Institution of Mining and Metallurgy).

Foster, M.R., and Duck, P.W., 1982, "The inviscid stability of Long's vortex," Phys. Fluids, 25, 1715.

Gear, C.W., 1971, Numerical initial value problems in ordinary differential equations, Prentice - Hall company.

Gouldin, F.C., Depsky, J.S., and Lee, S.L., 1985, "Velocity Field Characteristics of a Swirling Flow Combustor," AIAA J. 23, 95.

Gupta, A.K., Lilley, D.G., and Syred, N., 1984, Swirl Flows, Abacus Press, England.

Hall, M.G, 1966, "The Structure of Concentrated Vortex Cores," Progress in Aeronautical Sciences, 7, Pergamon Press.

Hinze, J.O., 1975, Turbulence, 2nd Ed., McGraw - Hill Company.

IMSL, 1984, International Methematical Subroutine Library.

Kelsall, D.F., 1952, "A Study of the Motion of Solid Particles in a Hydraulic Cyclone," Trans. Instn. Chem. Engrs. 30, 87.

Kerr, N.M., and Fraser, D., 1965, "Swirl Part I: Effect on axisymmetrical turbulent jets," J. Inst. Fuel, 38, 519.

Kimber, G.R., and Thew, M.T., 1974, "Experiments on oil/water separation with hydrocyclones," E1-1, First European Conference on Mixing and Centrifugal SEparation, SEpt. 9-11, Cambridge, England.

Knowles, S.R., 1971, "Photographic Fluid Velocity Measurement in a Hydrocyclone," M. Eng. Thesis, Dept. of Chem. Eng., McMaster University, Hamilton, Ontario.

Knowles, S.R., Woods, R.D., and Feuerstein, I.A., 1973, "The Velocity Distribution Within a Hydrocyclone Operating Without an Air Core," Can. J. Chem. Eng. 51, 263.

Lapidus, L., and Seinfeld, J.H., 1971, Numerical Solution of Ordinary Differential Equations, Academic Press.

Lewellen, W.S., 1971, "A Review of Confined Vortex Flows," N.A.S.A. Contractor Rep. No. 1772.

Listewnik, J., 1984, "Some Factors Influencing the Performance of De-oiling Hydrocyclones for Marine Applications," p.191 in Hydrocyclone, Int. Conf., Cambridge, England, BHRA Fluid Eng.

Long, R.R., 1956, "Sources and sink at the axis of a rotating liquid," Quart. J. Mech. Appl. Math. 9, 385.

Long, R.R., 1958, "Vortex motion in a viscous fluid," J. Meteorology, 15, 108.

Long, R.R., 1961. "A Vortex in an Infinite Viscous Fluid," J. Fluid Mech., 11, 611.

Lugt, H.J., 1983, Vortex Flow in Nature and Technology, John Wiley & Sons, New York.

Morton, B.R., 1966, "Geophysical Vortices," Prog. in Aero. Sci. 7, 145.

Morton, B.R., 1969, "The strength of vortex and swirling core flows," J. Fluid Mech. 38, 315.

Nuttal, J.B., 1953, "Axial Flow in a Vortex," Nature 172, 582.

Pedley, T.J., 1969, "The viscous vortex induced by a sink on the axis of a circulating fluid in the presence of a plane free surface," J. Fluid Mech., 36, 219.

Pericleous, K.A., Rhodes, N., and Cutting, G.W., 1984, "A Mathematical Model for Predicting the Flow Field in a Hydrocyclone Classifier," p. 27 in Hydrocyclone, Int. Conf., Cambridge, England, BHRA Fluid Eng.

Petty, C.A., 1985, Lecture notes in rotating flow course, Michigan State University.

Phillip, W., 1959, "The secant method for similtaneous non-linear equations," Comm. of the ACM, 2.

Qing, X.H., 1983, "Velocity and Turbulence Distributions in Cyclone," Doctor of Philosophy Dissertation, Technical University of Danmark.

Rajaratnam, N., 1976, Turbulent Jets, Elsevier Scientific Publishing Company.

Ramas, J.I., and Somer, H.T., 1985, "Swirling Flow in a Research Combustor," AIAA J. 23, 241.

Rhode, D.L., and Lilley, D.G., 1983, "Mean Flowfields in Axisymmetric Combustor Geometries with Swirl," AIAA J. 21, 593.

Rott, N., 1958, "On the Viscous Core of a Line Vortex," Z. Angew. Math. Phys., 1Xb, 543.

Serrin, J., 1972, "The swirling vortex," Phil. Trans. R. Soc. Lond. A 271, 325.

Smyth, I.C., Thew, M.T., Debenhan, P.S., and Colman, D.A., 1980, "Small-scale experiments on hydrocyclones," p. 189 in hydrocyclone, Int. Conf., Cambridge, England, BHRA Fluid Eng.

Smyth, I.C., Thew, M.T., and Colman, D.A., 1984, "The effect of split ratio on heavy dispersion liquid-liquid separation in hydrocyclones," p. 177 in hydrocyclone, Int. Conf., Cambridge, England, BHRA Fluid Eng.

Sullivan, R.D., 1959, "A Two-cell Vortex Solution of the Navier-Stokes Equations," J. Aerosp. Sci. 26, No. 11, 767.

Svarovsky, L., 1984, Hydrocyclones, Holt, Rinehart and Winston Ltd.

Swift, W.L., Barna, P.s., and Dalton, C., 1980, Vortex Flows, ASME Annual Meeting, Chicago, U.S.A.

Thew, M.T., Silk, S.A., and Colman, D.A., 1980, "Determination and Use of Residence Time Distributions for Two Hydrocyclones," p. 225 in Hydrocyclones, Int'l. Conf., Cambridge, England, BHRA Fluid Eng.

Vu, B.T., and Gouldin, F.C., 1982, "Flow Measurements in a Model Swirl Combustor," AIAA J. 20, 642.

Wu, J.Z., 1986, "Conical turbulent swirling vortex with variable eddy viscosity," Proc. R. Soc. Lond. A 403, 235.

Yih, C.S., Wu, F., Garg, A.K., and Leibovich, S., 1982, "Conical vortices: A class of exact solutions of the Navier-Stokes equations," Phys. Fluid, 25, 2147.